

2012-05-20

Magnetic Nanoparticle Enhanced Actuation Strategy for mixing, separation, and detection of biomolecules in a Microfluidic Lab-on-a-Chip System

Ahsan Munir
Worcester Polytechnic Institute

Follow this and additional works at: <https://digitalcommons.wpi.edu/etd-dissertations>

Repository Citation

Munir, A. (2012). *Magnetic Nanoparticle Enhanced Actuation Strategy for mixing, separation, and detection of biomolecules in a Microfluidic Lab-on-a-Chip System*. Retrieved from <https://digitalcommons.wpi.edu/etd-dissertations/289>

This dissertation is brought to you for free and open access by Digital WPI. It has been accepted for inclusion in Doctoral Dissertations (All Dissertations, All Years) by an authorized administrator of Digital WPI. For more information, please contact wpi-etd@wpi.edu.

**MAGNETIC NANOPARTICLE ENHANCED ACTUATION STRATEGY
FOR MIXING, SEPARATION, AND DETECTION OF BIOMOLECULES
IN A
MICROFLUIDIC LAB-ON-A-CHIP SYSTEM**

AHSAN MUNIR

Thesis submitted to the Faculty of Worcester Polytechnic Institute
in partial fulfillment for the requirements of the degree of

Doctor of Philosophy
in
Chemical Engineering

Doctoral Committee
Dr. Susan Zhou, Chair
Dr. Nickolas Kazantzis, Chemical Engineering
Dr. Cosme Furlong, Mechanical Engineering



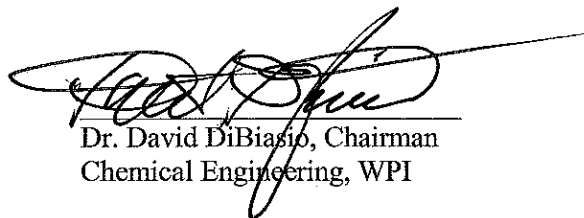
**MAGNETIC NANOPARTICLE ENHANCED ACTUATION STRATEGY
FOR MIXING, SEPARATION, AND DETECTION OF BIOMOLECULES
IN A
MICROFLUIDIC LAB-ON-A-CHIP SYSTEM**

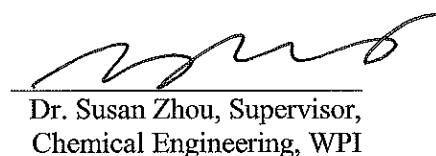
AHSAN MUNIR

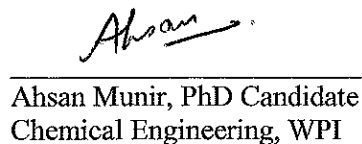
THESIS SUBMITTED TO THE FACULTY OF WORCESTER POLYTECHNIC INSTITUTE
IN PARTIAL FULFILLMENT FOR THE REQUIREMENTS OF THE DEGREE OF

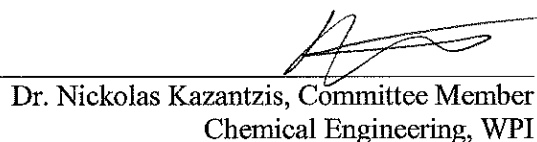
DOCTOR OF PHILOSOPHY
IN
CHEMICAL ENGINEERING

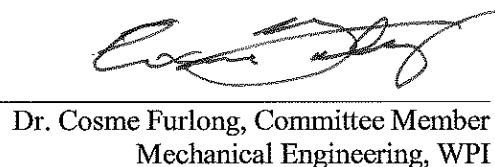
DOCTORAL COMMITTEE


Dr. David DiBiasio, Chairman
Chemical Engineering, WPI


Dr. Susan Zhou, Supervisor,
Chemical Engineering, WPI


Ahsan Munir, PhD Candidate
Chemical Engineering, WPI


Dr. Nickolas Kazantzis, Committee Member
Chemical Engineering, WPI


Dr. Cosme Furlong, Committee Member
Mechanical Engineering, WPI



May 14, 2012
Worcester, Massachusetts

Abstract

Magnetic nanoparticle (MNP) combined with biomolecules in a microfluidic system can be efficiently used in various applications such as mixing, pre-concentration, separation and detection. They can be either integrated for point-of care applications or used individually in the area of bio-defense, drug delivery, medical diagnostics, and pharmaceutical development. The interaction of magnetic fields with magnetic nanoparticles in microfluidic flows will allow simplifying the complexity of the present generation separation and detection systems. The ability to understand the dynamics of these interactions is a prerequisite for designing and developing more efficient systems. Therefore, in this work proof-of-concept experiments are combined with advanced numerical simulation to design, develop and optimize the magnetic microfluidic systems for mixing, separation and detection. Different strategies to combine magnetism with microfluidic technology are explored; a time-dependent magnetic actuation is used for efficiently mixing low volume of samples whereas tangential microfluidic channels were fabricated to demonstrate a simple low cost magnetic switching for continuous separation of biomolecules.

A simple low cost generic microfluidic platform is developed using assembly of readily available permanent magnets and electromagnets. Microfluidic channels were fabricated at much lower cost and with a faster construction time using our in-house developed micromolding technique that does not require a clean room. Residence-time distribution (RTD) analysis obtained using dynamic light scattering data from samples was successfully used for the first time in microfluidic system to characterize the performance. Both advanced multiphysics finite element models and proof of concept experimentation demonstrates that MNPs when tagged with biomolecules can be easily manipulated within the microchannel. They can be precisely

captured, separated or detected with high efficiency and ease of operation. Presence of MNPs together with time-dependent magnetic actuation also helps in mixing as well as tagging biomolecules on chip, which is useful for point-of-care applications. The advanced mathematical model that takes into account mass and momentum transport, convection & diffusion, magnetic body forces acting on magnetic nanoparticles further demonstrates that the performance of microfluidic surface-based bio-assay can be increased by incorporating the idea of magnetic actuation. The numerical simulations were helpful in testing and optimizing key design parameters and demonstrated that fluid flow rate, magnetic field strength, and magnetic nanoparticle size had dramatic impact on the performance of microfluidic systems studied.

This work will also emphasize the importance of considering magnetic nanoparticles interactions for a complete design of magnetic nanoparticle-based Lab-on-a-chip system where all the laboratory unit operations can be easily integrated. The strategy demonstrated in this work will not only be easy to implement but also allows for versatile biochip design rules and provides a simple approach to integrate external elements for enhancing mixing, separation and detection of biomolecules. The vast applications of this novel concept studied in this work demonstrate its potential of to be applied to other kinds of on-chip immunoassays in future. We think that the possibility of integrating magnetism with microfluidic-based bioassay on a disposable chip is a very promising and versatile approach for point-of care diagnostics especially in resource-limited settings.

Acknowledgement

First of all, I would like to thank Professor Susan Zhou for giving me this wonderful opportunity to join her research group and then provided excellent guidance and support throughout my doctoral studies. She was always very supportive of new ideas and encouraged creative thinking and problem solving. I could not have asked for a better advisor, mentor, and friend.

In addition, I would like to thank the members of my doctoral committee, Professor Nickolas Kazantzis, and Professor Cosme Furlong, who have contributed to my growth as a researcher.

I also like to thank my lab members, Dr. Jianlong Wang, and Zanzan Zhu. I have thoroughly enjoyed and valued working with them. The enormity of their contribution to this work is also priceless. Dr. Wang has always been a great mentor and friend to me, his encouragements, and suggestions have always helped me through all the stages of my doctoral work.

I would also like to thank the staff, faculty, and graduate students group of the department of chemical engineering of WPI for their continuous support throughout.

Finally, I thank my parents, in-laws, brothers, and sisters. The completion of more than twenty-two continuous years of schooling would not have been ever possible without their unconditional love, duas, and support.

And last but not the least; I would like to thank my wonderful wife for her ongoing support during the extremely busy and difficult times during my graduate career. She stood by me throughout the trials and tribulations, and has always been there to listen and support me.

Ahsan Munir

Table of Contents

Abstract	iii
Acknowledgement	v
List of Publication	viii
List of Figures	x
List of Tables	xx
1. INTRODUCTION.....	1
1.1 MICROFLUIDICS TO LAB-ON-A-CHIP	2
1.2 MAGNETISM AND MICROFLUIDICS	4
1.3 MOTIVATION.....	6
1.4 SCOPE AND OUTLINE OF THE THESIS.....	8
2. LITERATURE REVIEW & BACKGROUND.....	12
2.1 MICROFLUIDIC LAB-ON-A-CHIP UNIT OPERATIONS.....	12
2.1.1 <i>Mixing in microfluidics</i>	12
2.1.2 <i>Magnetic Separation/ Isolation/Trapping</i>	30
2.1.3 <i>Magnetic particle-based Detection</i>	36
2.1.4 <i>Overview of Magnetic Microfluidic Strategy</i>	44
2.2 MAGNETIC MICROFLUIDICS THEORY & CONCEPTS	46
2.2.1 <i>Magnetic Particles</i>	46
2.2.2 <i>Microfluidics Theory</i>	61
3. DESIGN & ANALYSIS.....	67
3.1 MAGNETIC NANOPARTICLE ENHANCED MIXING USING TIME DEPENDENT MAGNETIC FIELD	67
3.1.1 <i>State of the Art</i>	67
3.1.2 <i>Model Development</i>	69
3.1.3 <i>Magnetic Force Validation</i>	79
3.1.4 <i>Results & Discussion</i>	81
3.1.5 <i>Conclusion</i>	103
3.2 DYNAMICS OF MAGNETIC NANOPARTICLE CAPTURING & MAGNETIC BIOSEPARATION ..	105
3.2.1 <i>State of the Art</i>	105
3.2.2 <i>Model Development</i>	107
3.2.3 <i>Results & Discussion</i>	114
3.2.4 <i>Conclusion</i>	125
3.3 MAGNETIC NANOPARTICLE ENHANCED MICROFLUIDIC SURFACE-BASED BIOASSAY	127
3.3.1 <i>State of the Art</i>	127
3.3.2 <i>Model Development</i>	130
3.3.3 <i>Results & Discussions</i>	138
3.3.4 <i>Conclusion</i>	152
3.4 MAGNETICALLY ACTUATED SCHEME FOR TAGGING BIOMOLECULES WITH MAGNETIC NANOPARTICLES IN A MICROFLUIDIC SYSTEM	154

3.4.1	<i>State of the Art</i>	154
3.4.2	<i>Model Development</i>	157
3.4.3	<i>Results & Discussion</i>	168
3.4.4	<i>Conclusion</i>	180
4.	PROOF-OF-CONCEPT EXPERIMENTATION & VALIDATION	182
4.1	EXPERIMENTAL MATERIALS & METHODS	182
4.1.1	<i>Magnetic Microfluidic Platform Setup</i>	182
4.1.2	<i>Microfluidic chip fabrication</i>	184
4.1.3	<i>Magnetic Nanoparticles</i>	187
4.1.4	<i>Calibration Curve</i>	188
4.2	IN SITU ANALYSIS OF CAPTURING DYNAMICS OF MAGNETIC NANOPARTICLES IN A MICROFLUIDIC SYSTEM	190
4.2.1	<i>State of the Art</i>	190
4.2.2	<i>Materials & Methods</i>	193
4.2.3	<i>Results & Discussion</i>	203
4.2.4	<i>Conclusion</i>	218
4.3	INVESTIGATION OF MAGNETICALLY ACTUATED SEPARATION USING TANGENTIAL MICROFLUIDIC CHANNELS AND MAGNETIC NANOPARTICLES	220
4.3.1	<i>State of the Art</i>	220
4.3.2	<i>Materials & Methods</i>	223
4.3.3	<i>Results & Discussion</i>	227
4.3.4	<i>Conclusion</i>	238
4.4	INVESTIGATION OF MAGNETIC NANOPARTICLE-ASSISTED MIXING STRATEGY IN A MICROFLUIDIC CHANNEL USING RESIDENCE TIME DISTRIBUTION (RTD) ANALYSIS.....	240
4.4.1	<i>State of the Art</i>	240
4.4.2	<i>Materials & Method</i>	242
4.4.3	<i>Results & Discussion</i>	247
4.4.4	<i>Conclusion</i>	255
5.	CONCLUSION	256
6.	OUTLOOK	258
7.	REFERENCES	261

I. LIST OF PUBLICATIONS

- 1) MUNIR, A., WANG, J. L., ZHU, Z. Z. & ZHOU, H. S. 2012. In situ analysis of capturing dynamics of magnetic nanoparticles in a microfluidic system, *Special Issue on Advanced Sensing Systems and Multifunctional Materials* (submitted)
- 2) MUNIR, A., WANG, J. L., ZHU, Z. Z. & ZHOU, H. S. 2012. Experimental investigation of magnetically actuated bio-separation using tangential microfluidic channels and magnetic nanoparticles, *IET Nanobiotechnology* (in submission process)
- 3) MUNIR, A., WANG, J. L., ZHU, Z. Z. & ZHOU, H. S. 2012. FEM analysis of magnetically actuated technique for tagging biomolecules with magnetic nanoparticles in a microfluidic system, *Microfluidics and Nanofluidics* (in submission process)
- 4) MUNIR, A., WANG, J. L., ZHU, Z. Z. & ZHOU, H. S. 2012. Experimental investigation of magnetic nanoparticle-assisted mixing strategy in a microfluidic channel using residence time distribution (RTD) analysis, *IEEE Transactions on Nanotechnology* (in process)
- 5) MUNIR, A., WANG, J. & ZHOU, H. S. 2009. Dynamics of capturing process of multiple magnetic nanoparticles in a flow through microfluidic bioseparation system. *IET Nanobiotechnology*, 3, 55-64.
- 6) MUNIR, A., WANG, J. L., LI, Z. H. & ZHOU, H. S. 2010. Numerical analysis of a magnetic nanoparticle-enhanced microfluidic surface-based bioassay. *Microfluidics and Nanofluidics*, 8, 641-652.
- 7) MUNIR, A., WANG, J. L., ZHU, Z. Z. & ZHOU, H. S. 2011a. Mathematical Modeling and Analysis of a Magnetic Nanoparticle-Enhanced Mixing in a Microfluidic System Using Time-Dependent Magnetic Field. *IEEE Transactions on Nanotechnology*, 10, 953-961.
- 8) MUNIR, A., WANG, J. L., ZHU, Z. Z. & ZHOU, H. S. 2011b. Residence time distribution analysis of magnetic nanoparticle-enhanced mixing using time-dependent magnetic actuation in microfluidic system. *Microfluidics and Nanofluidics*, 10, 735-747.
- 9) WANG, J. L., MUNIR, A., LI, Z. H. & ZHOU, H. S. 2009a. Aptamer-Au NPs conjugates-enhanced SPR sensing for the ultrasensitive sandwich immunoassay. *Biosensors & Bioelectronics*, 25, 124-129.
- 10) WANG, J. L., MUNIR, A., LI, Z. H. & ZHOU, H. S. 2010a. Aptamer-Au NPs conjugates-accumulated methylene blue for the sensitive electrochemical immunoassay of protein. *Talanta*, 81, 63-67.
- 11) WANG, J. L., MUNIR, A. & ZHOU, H. S. 2009b. Au NPs-aptamer conjugates as a powerful competitive reagent for ultrasensitive detection of small molecules by surface plasmon resonance spectroscopy. *Talanta*, 79, 72-76.
- 12) WANG, J. L., MUNIR, A., ZHU, Z. Z. & ZHOU, H. S. 2010b. Magnetic Nanoparticle Enhanced Surface Plasmon Resonance Sensing and Its Application for the Ultrasensitive Detection of Magnetic Nanoparticle-Enriched Small Molecules. *Analytical Chemistry*, 82, 6782-6789.
- 13) WANG, J. L., ZHU, Z. Z., MUNIR, A. & ZHOU, H. S. 2010c. Magnetic Nanoparticles (MNPs) enhanced biosensing by Surface Plasmon Resonance (SPR) for portable devices. In: TOMIZUKA, M., YUN, C. B., GIURGIUTIU, V. & LYNCH, J. P. (eds.) *Sensors and Smart Structures Technologies for Civil, Mechanical, and Aerospace Systems 2010*.

- 14) WANG, J. L., ZHU, Z. Z., MUNIR, A. & ZHOU, H. S. 2011. Fe₃O₄ nanoparticles-enhanced SPR sensing for ultrasensitive sandwich bio-assay. *Talanta*, 84, 783-788.
- 15) ZHU, Z. Z., WANG, J. L., MUNIR, A. & ZHOU, H. S. 2010. Electrocatalytic activity of Pt nanoparticles on bamboo shaped carbon nanotubes for ethanol oxidation. *Electrochimica Acta*, 55, 8517-8520.
- 16) ZHU, Z. Z., WANG, J. L., MUNIR, A. & ZHOU, H. S. 2011. Direct electrochemistry and electrocatalysis of horseradish peroxidase immobilized on bamboo shaped carbon nanotubes/chitosan matrix. *Colloids and Surfaces A-Physicochemical and Engineering Aspects*, 385, 91-94.

II. LIST OF FIGURES

Figure 1.1 Schematic of Bio-analytical protocol employed in laboratory using magnetic particles: A) Magnetic nanoparticles employed in mixing, separation, and detection process (B) Surface Plasmon Resonance (SPR) detection instrument with conceptual schematic.	5
Figure 1.2 Schematic of Magnetic Nanoparticles functionalized with different biomolecules.....	7
Figure 1.3 Conceptual view of proposed Lab-on- a-Chip toolbox containing different unit operation such as mixing, separation, and detection.....	9
Figure 2.1.1 Basic designs in parallel lamination; (a) T-mixer, (b) Y-mixer	16
Figure 2.2 Droplet micro-mixer; (a) experimental results, (b) schematic representation of mixing process [91].....	19
Figure 2.3 Magnetic micro-particles (a) 1 μm Dyna-beads, (b) schematic diagram of functionalized magnetic particles [29].....	31
Figure 2.4 Table of elements indicating the magnetic properties of the element in their solid state	47
Figure 2.5 Magnetic hysteresis loop of a ferromagnetic material	51
Figure 2.6 Superparamagnetic behavior of a group of a freely suspended ferromagnetic nanocrystals (<10 nm) in the absence and presence of an external magnetic field	52
Figure 2.7 Qualitative illustration of the behavior of the coercivity as the magnetic particle size increase [183].....	53
Figure 2.8 (a) Schematic representation of superparamagnetic particles at zero magnetic fields, (b) Under presence of external magnetic field, the nanoparticles moments align in the preferential direction, (c) Hysteresis free variation of B with changing H for superparamagnetic particles.	54
Figure 2.9 Three main methods of synthesizing magnetic particles for lab-on-a-chip applications. (a) Single magnetic core, (b) mutli-core magnetic beads composed of magnetic nanocrystals, (c) magnetic nanoparticles assembled around polymer core (strawberry), (d) SEM image of a monodisperse magnetic particle (2.8 μm)[182].....	55
Figure 2.10 Selected functionalization routes for magnetic nanoparticles[184]	56
Figure 2.11 Magnetization curve of a Dynabead MyOne.....	58
Figure 2.12 Schematic illustration of forces acting on magnetic particles in a solution exposed to magnetic field.....	60

Figure 3.1(a) Schematic of time dependent magnetic micromixer, and (b) 2D axial cross-section of the microchannel with two inlets and one outlet. 70

Figure 3.2 Schematic of 2D axial cross-section of microchannel with one inlet and one outlet for RTD analysis..... 71

Figure 3.3 Magnetic force profile along the z-lines above the current carrying conductor. The location $x=20\mu\text{m}$ and $x=60\mu\text{m}$ corresponds to the inner and outer edges of the right conductor respectively. Simulation results from COMSOL Model were found to be in good approximation with experiment and simulation result from Suzuki et al[122]..... 80

Figure 3.4 Mixing efficiency at the outlet of the micro-channel for different magnetic nanoparticle size..... 82

Figure 3.5 Concentration Index in the micro-channel under varying inlet velocity: (a) Concentration index at the outlet of the microchannel, and (b) Cross-sectional plot of concentration at the outlet of microchannel after 60 sec. Black Solid line represent the ideal concentration which is desirable at the outlet. 83

Figure 3.6 Concentration profile in the micro-channel under different switching frequency: (a) Surface concentration plot of micro-channel at different frequencies given in Hz, (b) Cross-sectional plot of concentration at the outlet of microchannel after 30 sec. Black Solid line represent the ideal concentration which is desirable at the outlet..... 85

Figure 3.7 Effect of scaling (microchannel width) on the inlet flow velocity: (a) $W=30\ \mu\text{m}$, (b) $W=60\ \mu\text{m}$, and (c) $W=120\ \mu\text{m}$. Average concentration is recorded at the outlet of microchannel for a time interval of 30 sec. 87

Figure 3.8 Effect of scaling (microchannel width) on the switching frequency: (a) $W=30\ \mu\text{m}$, (b) $W=60\ \mu\text{m}$, and (c) $W=120\ \mu\text{m}$. Average concentration is recorded at the cross-ectional outlet of microchannel after 30 sec. Error bars represent standard deviation(SD). 89

Figure 3.9 Concentration profile in the micro-channel under different mixing scenario: (a) without magnetic actuation, (b) passive mixing without magnetic actuation, (c) with magnetic actuation, and (d) passive mixing with magnetic actuation. 90

Figure 3.10 Effect of magnetic actuation techniques on residence time distributions (RTD). Nine different magnetic actuation scenarios (a-i) were considered and variance was computed for RTD curves with (circle) and without (triangle) magnetic field effect. 95

Figure 3.11 Variation of RTD curve with switching frequency. (a) Effect of switching frequency of magnetic actuation on residence time distributions (RTD). (b) Plot of variance versus switching frequency. Frequency zero implies the scenario when magnetic field was not used in the simulation..... 97

Figure 3.12 Variation of RTD curve with magnetic nanoparticle size. (a) Effect of magnetic nanoparticle diameter on residence time distributions (RTD). (b) Plot of variance versus magnetic nanoparticle diameter. Frequency zero implies the scenario when magnetic field was not used in the simulation. 98

Figure 3.13 Effect of flow velocity on residence time distributions (RTD) for scenarios with (circle) and without (triangle) magnetic field. Variance (var) was computed for conditions with and without magnetic field-assisted mixing, (b) Plot of Variance Difference versus Reynolds Number. The variance difference is computed between non-magnetic field and magnetic field scenario. 101

Figure 3.14 Top view of the microfluidic system geometry used in this study. Magnetic nanoparticles enters the system from left and are attracted and trapped due to the magnetic force from the permanent magnet placed near the vicinity. Inset (b) shows the 3D representation of the complete setup for trapping magnetic nanoparticles. 107

Figure 3.15 Magnetic field components along the axis of permanent magnet (a), Inset (b) shows the axis of magnet and the microchannel. Magnetic flux density calculations starts near the face and moves away from the magnet along its axis within the microchannel. Solid line represents finite element analysis (FEA) using COMSOL whereas dotted line represents analytical solution. 115

Figure 3.16 Magnetic field components (a, b) and magnetic force components (c, d) on a magnetic nanoparticle of 50nm diameter along the axis of the micro-channel, Solid lines represent finite element analysis (FEA) whereas dotted lines represent analytical solution 116

Figure 3.17 Simulated contours of constant magnetic vector potential (flux lines) and induced particle velocity with (a) and without (b) magnetic force using finite element model. Magnetic vector potential has a unit of Wb/m..... 118

Figure 3.18 Simulated path of magnetic nanoparticles of 50 nm and 25 nm diameter shows that the trajectory of nanoparticles also depend on point of release with position varying in y-direction from 0 to 40 μm 119

Figure 3.19 Variation of trapping efficiency of magnetic nanoparticles with the nanoparticle diameter (magnet's magnetization was kept constant at 10000 A/m).	120
Figure 3.20 Variation of trapping efficiency of magnetic nanoparticles with the inlet velocity of fluid entering the microfluidic system (magnet's magnetization was kept constant at 10000 A/m).	121
Figure 3.21 Variation of trapping efficiency of magnetic nanoparticles with the magnetization of magnet (Inlet velocity was kept constant at 100 μ m/s).	122
Figure 3.22 Simulated trajectories of magnetic nanoparticles (50 nm) under varying magnetic field obtained by varying the angular position of permanent magnet (a-i) around the microchannel. The permanent magnet is placed with reference to center solid line at different angles. Dashed lines indicate the angular position of magnet. The red lines with a black dot represent the trajectory of magnetic nanoparticles within the micorchannel.	123
Figure 3.23 Predicted values of trapping efficiency for nine different scenarios (a-i) as described in figure 3.22.	125
Figure 3.24 Schematic representation of the numerical setup. (a) Simplified cross-sectional scheme of magnetically functionalized antigen capture due to surface bound antibody in a microfluidic biosensor. The liquid enters from the left and flows under laminar conditions. The antigen is allowed to diffuse in all the direction. Wall elements other than capture area are protected against unspecific binding and in simulation are considered perfect. (b) Schematic of surface binding reaction on the capture area, where the magnetically labeled antigen, C binds to the immobilized antibody, R _T forming the antigen-antibody complex, B. (c) Dimensions of the microfluidic channel used in the simulation with the position of electric wire for magnetic field force generation.	131
Figure 3.25 Variation of total flux with change in flow velocity. Solid line represents analytical results by using expression from Sheehan et al.[232], while dash and dash-dot lines represent numerical results for hemicylinder and flat reaction surface respectively.	139
Figure 3.26 Effect of association rate constant (a), inlet concentration of antigen (b), and immobilized antibody density (c) on the concentration of bound complex B. Dash line represent the reference point. Solid and dotted lines represent a 10-fold increase and decrease in parameters respectively.	140

Figure 3.27 Effect of diffusivity on the formation of Ag-Ab complex at $t=100s$. Grey dash line represents the boundary between transport and reaction-limited region. (Parameters: $u_0= 10 \mu\text{m/s}$, $c_0=10\text{nM}$, $R_T=10^{-8}\text{mol/m}^2$, $k_{\text{on}}=10^3\text{m}^3/\text{mol.s}$, and $k_{\text{off}}=10^{-2}\text{s}^{-1}$). 142

Figure 3.28 Effect of inlet flow velocity on the reaction kinetics of formation of antigen-antibody complex at the surface of microchannel. (Parameters: $c_0=10\text{nM}$, $R_T=10^{-8}\text{mol/m}^2$, $D=10^{-11}\text{m}^2/\text{s}$, $k_{\text{on}}=10^3\text{m}^3/\text{mol.s}$, and $k_{\text{off}}=10^{-2}\text{s}^{-1}$). 143

Figure 3.29 Effect of six different configuration of magnetic field on the reaction kinetics of magnetic nanoparticle tagged antigen-antibody complex at the surface of microchannel. Dash line represents (“upper bound”) and corresponds to analytical solution without mass transfer. Solid lines represent kinetic profiles when there is mass transfer with magnetic field effect and dotted line represent (“lower bound”) and correspond to scenario when there is mass transfer as well as reaction kinetics but no magnetic field. Schematic representations of six different cases of circular current carrying wires near the channel are also shown. X and dot represent current into and out of the plane..... 145

Figure 3.30 Snapshots of microchannel taken at different times with (left) and without (right) magnetic field effect on the concentration on target antigen. White dash line indicates the sensing zone and black solid line shows the position of binding surface in the microchannel. A streamline plot at $t=100s$ shows the velocity field with (left) and without (right) magnetic field effect. Magnetic field effect causes circulation near the sensing surface (left). 147

Figure 3.31(a) Outlet concentration of target antigen tagged with magnetic nanoparticles as a function of time, (b) binding concentration of antigen-antibody complex on the sensing surface as a function of time. Solid line represents when there was no magnetic field near the sensing zone whereas dashed line represents when there was the magnetic field. 148

Figure 3.32 Variation of binding time (t_{90} , time at 90% binding) with change in nanoparticle size and diffusivity. 150

Figure 3.33 Binding concentration of antigen-antibody complex on the sensing surface as a function of time. Three different scenarios (a) straight channel without magnetic field, (b) channel with bluff body on the top without the magnetic field, and (c) straight channel with the magnetic field are shown. The target antigen concentration profile is also shown inside the channel for all the three scenarios..... 152

Figure 3.34 Schematic of time dependent magnetic tagging process: a) a three-dimensional conceptual representation of the microfluidic system, b) a 2D cross-sectional view used to develop finite element COMSOL model, and c) binding reaction between MNPs and biomolecule using antigen-antibody chemistry. 157

Figure 3.35 Magnetic body force along the z-lines above the current carrying conductor. The location $x=20\mu\text{m}$ and $x=60\mu\text{m}$ corresponds to the inner and outer edges of the right conductor respectively. 167

Figure 3.36 Simulated concentration profile of MNP-tagged-biomolecule complex formed during the bulk phase reaction between MNPs and biomolecules in the presence of magnetic actuation scheme (time of simulation=5s). The effect of switching frequency (a) 0.1 Hz, (b) 0.5 Hz, (c) 1 Hz, (d) 5 Hz, (e) 10 Hz, and (f) 15 Hz on the reaction kinetics of tagging process is analyzed for four different diameters of MNPs (i) 50nm, (ii) 80nm, (iii) 100nm, and (iv)150nm. 170

Figure 3.37 Variation of mixing cup concentration of MNP-tagged-biomolecule complex formed during the bulk phase reaction between MNPs and biomolecules in the presence of magnetic actuation scheme with time. The effect of switching frequency (a) 0.1 Hz, (b) 0.5 Hz, (c) 1 Hz, (d) 5 Hz, (e) 10 Hz, and (f) 15 Hz on the reaction kinetics of tagging process is analyzed for four different diameters of MNPs..... 171

Figure 3.38 Simulated concentration profile of MNP-tagged-biomolecule complex formed during the bulk phase reaction between MNPs and biomolecules in the presence of magnetic actuation scheme after 30s. The effect of flow velocity (a) $30\mu\text{m/s}$, (b) $50\mu\text{m/s}$, (c) $80\mu\text{m/s}$, (d) $90\mu\text{m/s}$, (e) $100\mu\text{m/s}$, and (f) $120\mu\text{m/s}$ on the reaction kinetics of tagging process is analyzed..... 174

Figure 3.39 Variation of mixing cup concentration of MNP-tagged-biomolecule complex formed during the bulk phase reaction between MNPs and biomolecules in the presence of magnetic actuation scheme with time. Effect of Reynolds number (3×10^{-4} to 12×10^{-4}) on the reaction kinetics of tagging process is analyzed. Inset (b) shows that after 5s, working with $\text{Re} \sim 5 \times 10^{-4}$ provides optimum flow conditions ($\sim 50\mu\text{m/s}$) for formation of MNP-biomolecule complex. 176

Figure 3.40 Simulated concentration profile of MNP-tagged-biomolecule complex after 10s formed during the bulk phase reaction between MNPs and biomolecules for three different scenarios (a) no active or passive mixing, (b) with passive barriers, and (c) with active magnetic actuation. 177

Figure 3.41 Streamline plots of velocity field of carrier fluid containing MNPs for three different scenarios (a) with active magnetic actuation at t= (i) 4.5s, (ii) 5s, (iii) 5.5s, and (iv) 10s, (b) with passive barriers at t=10s, and (c) no active or passive mixing at t=10s. The plot shows that velocity field is varying for magnetic actuation scheme and therefore provides better mixing. 178

Figure 3.42 Comparative Study: Variation of mixing cup concentration of MNP-tagged-biomolecule complex formed during the bulk phase reaction between MNPs and biomolecules with time for three different scenarios (a) no active or passive mixing, (b) with passive barriers, and (c) with active magnetic actuation. 179

Figure 4.1 Microfluidic platform with inlet and outlet connections through tubings, permanent magnet in the vicinity of microfluidic chip, and the objective of microscope over the ROI for recording images. The sample from outlet is taken in Zetasizer Nano for concentration analysis. 182

Figure 4.2 Components of Experimental Set up: a) Micro-peristaltic pump with inlet and outlet connections using tygon tubing, (b) LCD Digital microscope with translational stage for image acquisition. 183

Figure 4.3 Fabrication Process for developing Microfluidic Channel, a) Pouring PDMS mix over the mold, and b) Cured microchannel with wires embedded in it. 186

Figure 4.4 Straight Microchannel fabricated using PDMS and micromolding process with connection for inlet and outlet using tygon tubing and stainless steel tip as interconnect. 187

Figure 4.5 Magnetic Nanoparticles used in this work, a) TEM image of multi-domain magnetite core, and b) structure of magnetic nanoparticles with magnetic core surrounded by polysaccharide matrix. 187

Figure 4.6 Calibration Curve obtained for MNPs using scattering intensity obtained from Zetasizer Nano S. Inset shows different concentrations of MNPs used in generating calibration curve($R^2=0.9908$). 189

Figure 4.7 Microfluidic Magnetic Nanoparticle Capturing System; (a) schematic of the experimental setup, (b) snapshot of the setup showing microfluidic platform with inlet and outlet connections through tubings, permanent magnet in the vicinity of microfluidic chip, and the objective of microscope over the region of interest (ROI) for recording images. Inset shows the size of ROI and microchannel diameter, c) experimental setup showing ROI within the microchannel with neodymium magnet placed at its edge (System 8), and d) Finite Element

Model setup in COMSOL for simulating the scenario given in (c). (Length of channel=75mm)
..... 194

Figure 4.8 Calculated Magnetic Flux density at center of microchannel along the length of the
microchannel, and (b) shows the magnetic flux density in the region of interest (ROI) for
different magnetic systems. 204

Figure 4.9 Capturing Efficiency Analysis, (a) Comparison of capturing efficiency of different
magnetic systems, (b) Magnetic Flux density versus capturing efficiency plot shows that
magnetic systems producing high magnetic flux density in the microchannel have higher
efficiency for trapping MNPs. 207

Figure 4.10 (a) Variation of capturing efficiency of MNPs with flow rate of MNPs and distance
of magnet from the lower wall of microchannel, and (b) 3D plot gives the guideline for obtaining
higher capturing efficiency. A lower flow rate and magnet being closer to the microchannel is
desirable. 209

Figure 4.11 (a) Micrograph of Magnetic Nanoparticle capturing experiments in the region of
interest (ROI) at different times for four different magnetic systems, i) system 2, ii) system 6, iii)
system 7, and iv) system 8. Magnetic systems were placed near the lower wall of the
microchannel. Systems 2 & 6 were placed at 5mm from the wall whereas Systems 7 & 8 was
placed adjacent to the wall (0 mm), and (b) Pixel Intensity of the captured magnetic
nanoparticles in ROI after 25s shows that system 8 has the highest amount magnetic
nanoparticles captured in the microchannel. 211

Figure 4.12 Simulated magnetic nanoparticle concentration rate (mg/s) at the inlet and outlet of
the microchannel for different flow rate conditions. Magnetic system 8 with MNPs concentration
of 0.5 mg/ml was used in the simulation. 213

Figure 4.13 Qualitative comparison of experiments and numerical simulation for capturing
magnetic nanoparticle flowing at 1 μ l/s inside the microchannel using magnetic system 8. Initial
concentration of 0.5mg/ml was injected in the system from the right. 214

Figure 4.14 Comparison of experimental and theoretical results for capturing of magnetic
nanoparticles under varying flow rate conditions. Initial concentration of MNPs injected at the
inlet was 0.5mg/ml. 215

Figure 4.15 Simulated magnetic field intensity in Tesla (a) Magnetic System 8 (i) 2D surface plot
of Magnetic field Intensity, (ii) Magnetic field intensity along the x-axis in the center of

microchannel($y=0$) , and b) System 8 with iron grooved bar (i) 2D surface plot of Magnetic field Intensity, (ii) Magnetic field intensity along the x-axis in the center of microchannel($y=0$)	216
Figure 4.16 (a) Simulated magnetic nanoparticle concentration rate (mg/s) at the inlet and outlet of the microchannel for Magnetic system 8 with and without grooved-iron bar in the vicinity of microchannel. MNPs concentration of 0.5 mg/ml was used in the simulation, (b) Capturing efficiency computed based on incoming and outgoing mass of magnetic nanoparticles for both the system.....	217
Figure 4.17 Fabrication step used in developing leak-proof microfluidic channels.....	224
Figure 4.18 Experimental Setup of magnetic field based bio-separation using tangential microchannels and magnetic nanoparticles. Inset shows the close-up of tangential microchannel with neodymium magnet where magnetic field forces are focused in order to switch the path of magnetic nanoparticles.....	225
Figure 4.19 Calibration Curve obtained for MNPs using scattering intensity obtained from Zetasizer Nano S. Inset shows different concentrations of MNPs used in generating calibration curve.....	227
Figure 4.20 Flow of MNPs in the tangential microchannel in the absence of magnetic field. 100 μ l of MNP solution having a concentration of 1mg/ml was injected in the lower microchannel. It can be seen that no switch takes place in absence of magnetic force and MNPs enter and exit from lower channel.	228
Figure 4.21 MNPs switching between microfluidic channels using Neodymium magnet. (a) Snapshot of tangential microchannel at different times. Magnetic Nanoparticles were injected in the lower microchannel, and (b) Closeup of tangential microchannel after 18s shows that due to magnetic field force generated by neodyium magnet magnetic nanoparticles switches its path and comes out from upper microchannel.....	230
Figure 4.22 Concentration of MNPs eluted from upper and lower microchannel when 100 uL of 1mg/ml MNPs were injected through lower microchannel at flow rate of 5 μ l/s in the absence and presence of magnetic field (Neodyium magnet, N52).	233
Figure 4.23 Variation of percentage of MNPs eluting from lower (O) and upper (Δ) microchannel at different flow rates in the presence and absence of magnetic field. MNPs initial concentration was 1mg/ml and 100 μ l of the sample was injected from lower microchannel. Error bar represent the standard deviation obtained after three injections.	235

Figure 4.24 Magnetic field based separation of a mixture of Polystyrene (60nm) and MNPs (200nm) injected from lower microchannel at a flow rate of 5 μ l/s, (a) average diameter of sample eluted from upper microchannel, (b) average diameter of sample eluted from lower microchannel, and (c) Percentage of MNPs eluted from upper and lower microchannel. 237

Figure 4.25 Fabrication step used in developing leak-proof microfluidic channels..... 243

Figure 4.26 Microfluidic Magnetic Nanoparticle Mixing System: (a) Schematic representation of the setup showing the microchannel with electromagnet for generating magnetic field. The MNP solution is injected near the inlet from the right and flows under laminar conditions. The samples are collected at discrete time values and analyzed using Zetasizer Nano to obtain concentration-time curves, (b) In order to generate RTD curves, MNP with known concentration is injected for a very short time interval (Dirac pulse) into the microchannel from inlet and the response function is recorded at the microchannel output, and (c) snapshot of the setup showing microfluidic platform with inlet and outlet connections through tubings, electromagnet assembly in the vicinity of microfluidic chip with power switch to control magnetic field, and the objective of microscope over the region of interest (ROI) for recording images..... 244

Figure 4.27 (a) Micrograph of magnetic nanoparticle concentration in the region of interest (ROI) with the microchannel at discrete time intervals, and (b) Oscillating magnetic field in the form of square-wave that is turned on and off at different times. Four pulses of magnetic field are generated to cause disturbances in MNP solution coming from right and moving towards left. 250

Figure 4.28 Concentration-time curves of magnetic nanoparticle solution obtained with (circle) and without (square) magnetic actuation. MNP solution was injected for a very short time period into the de-ionized (DI) water flowing at rates of (a) 1 μ l/s, (b) 0.6 μ l/s, and (c) 0.3 μ l/s..... 251

Figure 4.29 Residence time distribution (RTD) curves of magnetic nanoparticle solution obtained with (circle) and without (square) magnetic actuation. MNP solution was injected for a very short time period into the de-ionized (DI) water flowing at rates of (a) 1 μ l/s, (b) 0.6 μ l/s, and (c) 0.3 μ l/s 253

Figure 4.30 Normalized variance plot for three flow rate conditions with and without magnetic actuation..... 254

III. LIST OF TABLES

Table 2.1 Comparison of the different particle manipulation techniques (Abbreviations: MP= magnetophoresis, DEP= dielectrophoresis, MR= Mechanical Retention, and SP= superparamagnetic	39
Table 2.2 A qualitative comparison of the different magnetic manipulation methods.....	43
Table 2.3 Comparison of homogenous and heterogeneous bioassay using magnetic particles....	44
Table 2.4 Overview and Comparison of different types of Magnetism	49
Table 2.5 Properties of water at 20 °C and 1 atm	62
Table 3.1 Nine combinations of magnetic actuation configurations (a-i). Microchannel (grey) at the center is surrounded by four-electrodes numbered 1-4. Oscillating current in the form of square-wave is applied to these electrodes in various combinations.....	93
Table 3.2 Comparison of SCD and RTD Analysis and their outcome	104
Table 4.1 Specification of Magnetic System Assembly used in Capturing MNPs	195

1. INTRODUCTION

Over the past two decades, the rise of microfabrication technology and its ability to produce miniaturized Micro-Electro-Mechanical Systems (MEMS) [1, 2] has touched our daily life. These systems have the capability to measure mechanical, thermal, biological, chemical, optical and magnetic phenomena and have resulted in creating an “intelligent” microsystem capable of sensing and controlling its environment. One of the most prominent and successful examples of MEMS technology is the accelerometer. Introduced by Analog Devices in 1991, accelerometers are now a part of every automobile, their role is to control the airbag’s release in case of an accident. One of the strengths and characteristics of MEMS is their versatility and interdisciplinary nature. The range of MEMS application is significantly growing mainly due to ease of fabrication techniques, equipment, and materials that are well established in semiconductor industry.

In recent years, miniaturization and integration of biological/chemical analysis to MEMS devices has played a major role in scaling the lab-scale biological and chemical analysis systems down to chip-format often referred as Micro Total Analysis Systems (μ -TAS) or Lab-on-a-Chip (LOC) systems [3, 4]. These systems are now being realized for numerous chemical and biological analyses includes DNA analysis, clinical analysis, proteomics analysis, forensic analysis and even immunoassays and toxicity monitoring [4-7]. Fueled by the development of new fabrication methods[8-11] , innovative techniques to interface analytical systems with electro-mechanical components are continuously being developed and offer the design and fabrication of μ -TAS with a wide range of applications including drug delivery systems, monitoring devices, nucleic acid-based analysis and automatic point-of-care diagnostic micro-chips.

The development of Lab-on-a-Chip (LOC) systems is fuelled by a need to perform rapid and sensitive analyses on small sample volumes. However, at a more primary level, interest in these systems is stimulated by the fact that physical processes are easier to control when instrument dimensions are small. The main advantages of Lab-on-a-Chip (LOC) systems over traditional laboratory instrumentation, is lower fabrication costs, improvement of analytical performance regarding quality and operation time, small size, disposability, precise detection, minimal human interference and lower power consumption. Furthermore, labs on chips offer point-of-care diagnostic abilities that could revolutionize medicine and health care. Such devices are now being realized for hospitals, at the site of crime and in other areas, including a range of industrial applications and environmental monitoring.

1.1 Microfluidics to Lab-on-a-Chip

Microfluidics, which deals with the miniaturized handling of liquid samples [9, 12-14] in recent years have steadily gained interest among researchers. More innovative applications of microfluidics are emerging and an increasing diversity of techniques can be found in literature [15-17]. Continuous flow microfluidics of the first generation is joined by droplet-based approaches [18-20] , cells are cultured, transported and studied on a microfluidic chip[21] and particles are manipulated within the microfluidic system [22]. It was the field of life sciences for which the first commercial microfluidic based systems was introduced [23]. In particular, microfluidic technologies have been developed to carry out chemical and biochemical analyses. In life sciences and bioengineering applications, the need to manipulate fluids moving in microchannels has stimulated several new research ideas, such as the development of new microfabrication methods, usage of new materials such as polymer — poly(dimethylsiloxane), or PDMS for fluidic systems[8],implementation of novel components for the assembly of complex

microfluidic devices and the study of the fundamental behavior of fluids in narrow-bore channels[24]. The array of microfluidic tools and strategies developed to carry out mixing, separation, and detection, and the capability to integrate all these components on one platform has led to the development of Micro Total Analysis Systems (μ TAS) or Lab-on-a-Chip (LOC)[3, 4, 25, 26]. Such systems aim at shrinking a laboratory filled with people down to a chip the size of a credit card. In Lab-on-a-Chip (LOC) devices all necessary sample handling and analysis are performed within the microchip platform. Thus an LOC can be thought as a black-box that generates a meaningful output signal upon the introduction of a real world sample, such as biological samples, environmental samples, an aqueous droplet or blood. The advantages of miniaturized bioanalysis systems are manifold most importantly, the reduction of sample and reagent volumes and thus the reduction of overall costs [27, 28]. The unique behavior of liquids at the micro-scale allows greater control of molecular concentrations and interactions. In addition, the miniaturization leads to decreased reaction times and allows a high parallelization of reactions, which is an enormous advantage in screening-based protocols. Lab-on-a-Chip devices also allow samples to be analyzed at the point of need rather than in a centralized laboratory which is enormous application in medical diagnostics, environmental monitoring, and bio-defense. The advantages LOC systems are compelling, but designing and developing these devices that operate effectively is challenging. Commercial exploitation of these devices is slow, but is gaining speed, with many new innovative products in the market from companies like Agilent, Caliper Life Sciences and Phillips to name a few. Microfluidic technology is a technology of 21st century which is in early adolescence, and still needs innovative and groundbreaking ideas, designs, and strategies for development of complete LOC systems, providing enormous benefits and easily used by non-experts.

1.2 Magnetism and Microfluidics

Magnetism and Microfluidics are known to researchers from almost decades, but it's only few years' back that they have been integrated together [29]. However, magnetism dates back to historic times and the concepts of magnetism have time and again been successfully utilized for vast array of applications with tremendous success. Today, magnetism is well-known to be coupled with electricity and it is a science which is well developed. Electric fields have previously been combined with microfluidic, such as capillary electrophoretic separations, electroosmotic pumping and dielectrophoretic trapping [30]. Magnetic fields on the other hand are not so common in microfluidic application. It's only in recent years with advancement made in nanotechnology and microfabrication that their potential is realized. Magnetic fields offer tremendous advantages over electric field. For example, objects inside a microfluidic channel can be manipulated by an external magnet field that is not in direct contact with the fluid. Target molecules can be isolated from a sample by attaching them to small magnetic particles which are then recovered using an external magnetic field. In contrast to electric manipulation, magnetic interactions are generally not affected by surface charges, pH, ionic concentrations or temperature. The marriage of magnetism and microfluidics thus has been relatively recent. It is due to the advancement made in the nanotechnology, magnetic particles functionalized antibodies are readily available and easy and simple microfabrication protocols makes it possible to develop magnetically actuated microfluidic devices. The avenues created by this fusion has wide variety of applicability which is not only limited to physics and engineering. In fact, one of the first applications of magnetic particles and magnetic field was in a batch scale clinical biosciences application, even before microfluidics came into existence. They are used in DNA extraction[31], cell separation[32] and antibody detection[33-36]. The advantage of the magnetic

particles is their easy handling and the ever increasing choice of surface functionalization available in the market [37]. In general, bioanalytical protocols employing magnetic particles repeat a series of particle handling steps, as shown in Figure 1.1. The mixing with a sample solution is followed by the concentration of the particles via a permanent magnet. The sample solution is removed and the particles are re-suspended in the medium of the subsequent step, such as a washing solution or detection substrate. In comparison with other concentration or separation procedures, magnetic separation does not require additional elaborate equipment, but simply a field gradient generated by a permanent magnet [38] or a specially designed electromagnet[39].

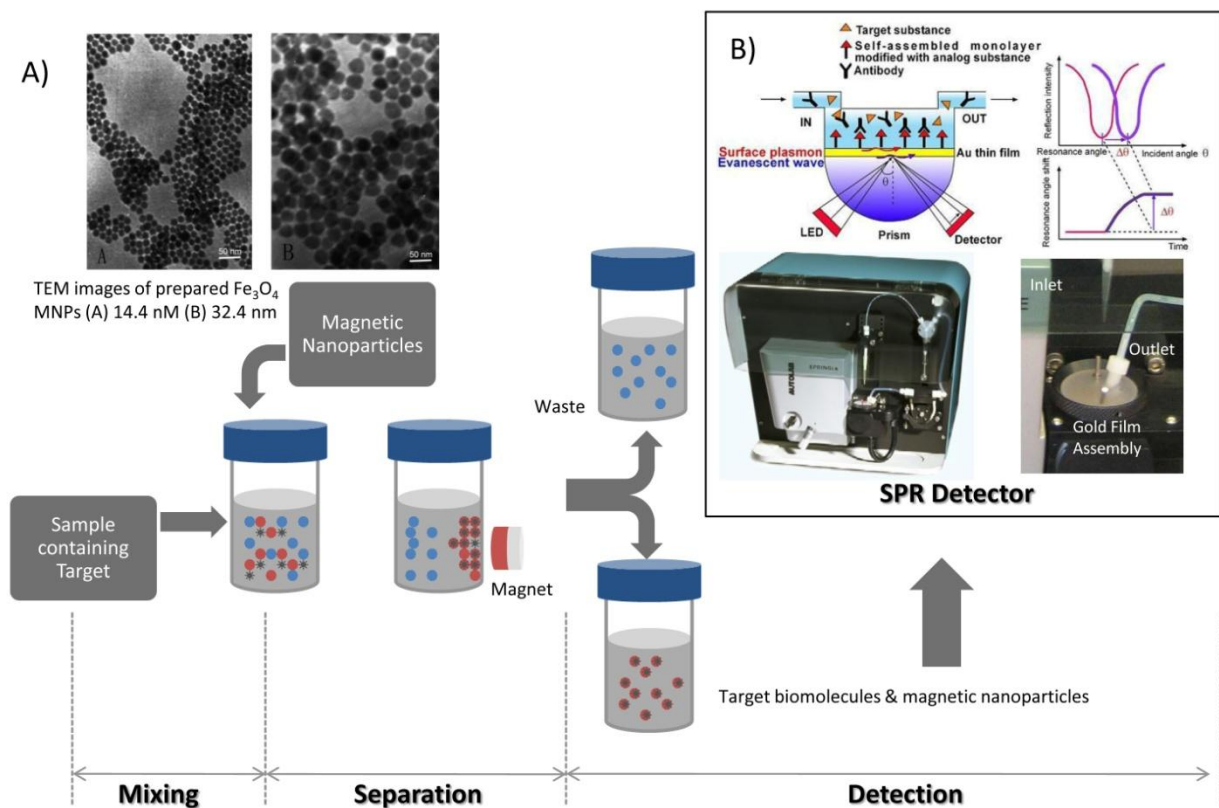


Figure 1.1 Schematic of Bio-analytical protocol employed in laboratory using magnetic particles: A) Magnetic nanoparticles employed in mixing, separation, and detection process (B) Surface Plasmon Resonance (SPR) detection instrument with conceptual schematic.

Furthermore, the magnetic particles serve not only as markers for the biomolecules of choice, but also as substrates and handles for manipulation. This multi-functionality of the magnetic particles makes them ideal candidates for being the active component in miniaturized bioanalytical systems[40]. Subsequently, LOC-type systems employing magnetic microparticles as either active or passive components are steadily gaining impact and importance, as recent publications show [29]. Some new applications stemming from this fusion include pumping and mixing of fluids, as well as the incorporation of switches and valves into lab-on-a-chip devices have been successfully developed[29]. In recent years, microfluidic bioseparation system based on magnetic particles have been successfully developed for separation, analysis and detection of biomolecules [41-47], immunoassay of proteins [48, 49], purification of DNA [50], fluid mixing [51], and cell separation[52, 53]. Magnetic forces are successfully used in these systems to transport, position, separate and sort magnetic as well as non-magnetic objects. Bio-assays have also been performed on the surface of magnetic particles trapped inside a microchannel. More recently, on-chip detection techniques based on magnetic forces [54-56] have been investigated and basic research of magnetic behavior, not possible on the large scale, has also been undertaken in the confined space of microchannels.

1.3 Motivation

Recent developments made in the development of magnetic microfluidic systems are based on functionalized magnetic beads or microparticles [29, 52, 53, 57-60] (see Figure 1.2). Compared with magnetic microparticles or microbeads, superparamagnetic iron oxide magnetic nanoparticles are more promising and interesting for a number of reasons. These particles possess better properties such as higher surface to volume ratio [37, 61, 62] for chemical binding, minimum disturbance caused due to attached biomolecules because of their extremely small size,

and moreover they are superparamagnetic [37] , i.e., their magnetization without a magnetic field is zero. This is important because unlike microparticles or microbeads they do not agglomerate and stay suspended in carrier liquid when the magnetic field is removed. This makes it easy for the removal or capture of tagged biomolecules of interest. Moreover, with no magnetic memory, the particle flow is highly predictable in microfluidic. This is an advantage, especially in complicated processing methods. The dimension of magnetic nanoparticles is also smaller or comparable to those of a biomolecules like cells, proteins, DNA as such they provide closer interaction and tagging.

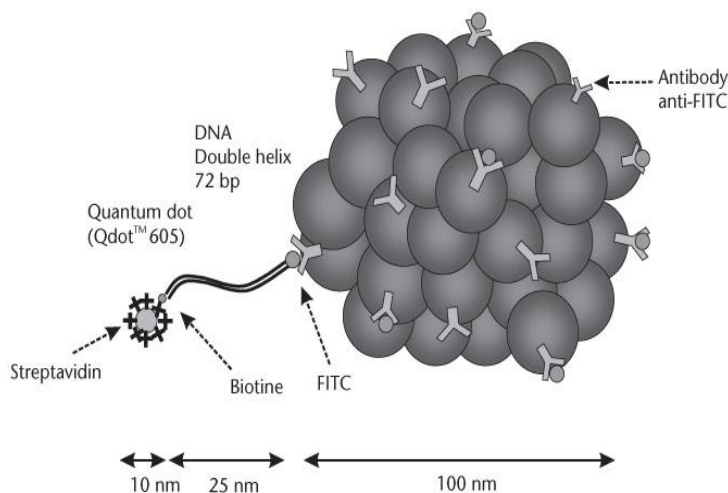


Figure 1.2 Schematic of Magnetic Nanoparticles functionalized with different biomolecules.

Another important advantage of action at a distance allows their use in microchannels with relatively simple design. It is possible to manipulate the magnetic nanoparticles using an external field. Hence, the particles may be effectively separated or sorted from a carrier fluid which otherwise flows steadily. They can be easily tagged to biomolecules for bioseparation and pre-concentration. This allows using reagents from various sources, directed to the site, as needed by the process while arresting the motion with a magnetic field. Further, as mentioned previously, due to low residual magnetism, the particles readily re-disperse into the flow upon removal of the

field. Motion of magnetic nanoparticles in a microfluidic channel can also be controlled using a time-dependent magnetic field in a manner that the particle-fluid hydrodynamic interaction causes mixing. The inherent benefits offered by magnetic actuation using magnetic nanoparticles includes: reduced reagent costs, elimination of labor intensive steps, easy automation, high purity and decreased processing time compared to conventional methods. Overall, magnetic nanoparticles offer numerous advantages and their introduction in a microfluidic Lab-on-a-chip system is expected to greatly enhance the device functionality.

1.4 Scope and Outline of the Thesis

In recent years, a wide range of methods for the handling of liquids in microfluidic systems have been proposed and developed [13, 30, 63]. In parallel, wide array of sensors, mixers, separators, ready to be integrated into complete miniaturized analytical systems, have been demonstrated, resulting in new approaches for Lab-on- a-Chip systems. In this work we propose a novel approach of using magnetic manipulation technique to carry out each unit operation in these miniaturized systems. Based on the conceptual design shown in Figure 1.3, we can envision our Lab-on-a-Chip toolbox containing different unit operation such as mixing, separation, and detection. In Figure 1.3, we can see that two streams, one consisting of target biomolecules, and the other with magnetic nanoparticles enter the microchannel. They do not mix at all due to low diffusivity without external or internal perturbation. Magnetic nanoparticle solution can be stirred using time-varying magnetic field generated by the magnetic source present in the vicinity of microchannel. This causes turbulence and enhanced mixing in order to bring tagging on chip. Once the target biomolecules are tagged with magnetic nanoparticles, they are separated from non-magnetic stream containing non-targets using magnetic field source. This process helps in pre-concentrating the solution and removing the unwanted noise.

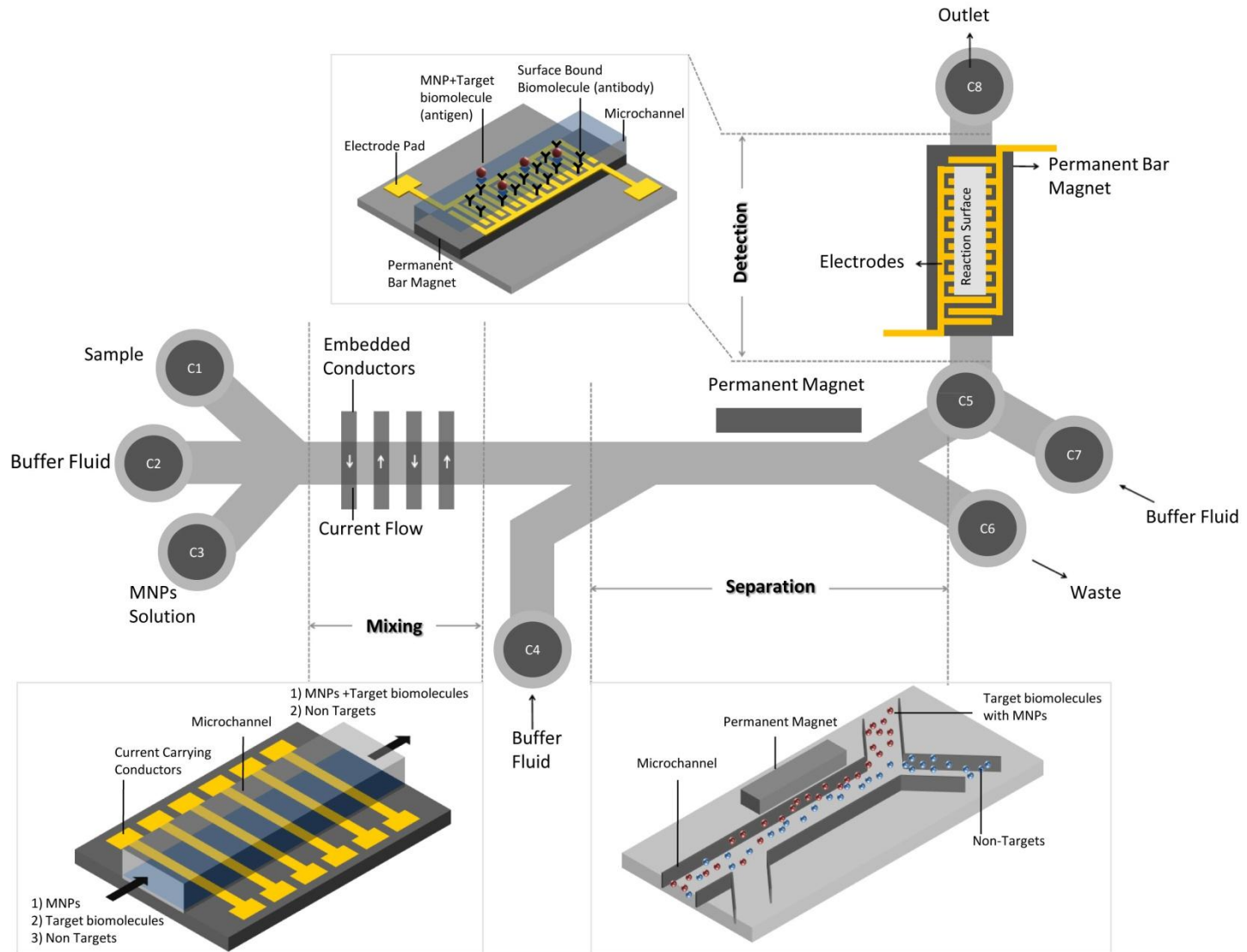


Figure 1.3 Conceptual view of proposed Lab-on-a-Chip toolbox containing different unit operation such as mixing, separation, and detection

The magnetic targets are then directed towards sensing surface and diffusion limitation for surface-based kinetics is overcome by focussing targets on surface-bound antibodies using magnetic field. These operations form the building blocks of any analytical procedure whether it is performed on miniaturized chip or in conventional laboratory. Our idea is to employ magnetic field to mix, separate, and detect biomolecules efficiently. Magnetism in the microfluidics will streamline each unit operation which is simple to develop and can easily be integrated. The overall objective of this work is to study the combination of magnetic manipulation by using magnetic nanoparticles with other elements of the microfluidic toolbox and to examine the applicability of developing a simple, fast, and sensitive miniaturized bioanalysis system. In this work we propose to combine theoretical models and proof-of-concept experiments to design and develop components of a lab-on-chip system that will significantly improve the ability to mix, separate and detect biomolecules in a manner that is more efficient than present generation microfluidic system. We will deploy iron-oxide magnetic nanoparticles enhanced magnetic actuation strategy for mixing, separation, and detection on a microfluidic platform and study important parameters that govern the efficiency of these systems. Residence-time distribution (RTD) analysis, for the first time, will be successfully applied both in theoretical and experimentation to predict the performance of microfluidic system. It will also be used to investigate and optimize design parameters used in the magnetically actuated microfluidic system. This doctoral thesis combines theory, modeling, design, fabrication, and proof-of-concept experiments to facilitate development of magnetic actuation-based microfluidic unit operations and can be classified in two broad categories:

A Design and Analysis

- i) Development of magneto-hydrodynamic finite element models (MHFEM) using COMSOL Multiphysics.
- ii) Studying magnetically enhanced mixing, separation, detection process on-chip using MHFEM.
- iii) Using Residence time distribution (RTD) analysis for characterization of magnetically enhanced mixing in microfluidic systems.
- iv) Proposing optimized process parameters for designing and developing the magnetic microfluidic systems.

B Proof-of-Concept Experiments & Validation

- i) Assembly of microfluidic platform together with fabrication of microfluidic channel using low cost, robust, and easy in-house technique to study the magnetically enhanced mixing and separation.
- ii) Investigation and evaluation of capturing and separation dynamics of MNPs in microchannels.
- iii) Characterization of mixing process in microchannel using Residence Time Distribution (RTD) analysis.

2. LITERATURE REVIEW & BACKGROUND

2.1 Microfluidic Lab-on-a-Chip Unit Operations

2.1.1 Mixing in microfluidics

Mixing is a fundamental step in most of the microfluidic systems used in biochemistry analysis where biological processes such as enzyme reactions often engage reactions that require mixing of reactants. Mixing is also essential in LOC platforms for tagging of specific entities by some labels such as magnetic particles which are used for actuation. Micro-mixers can be integrated in a microfluidic platform or utilized as a stand-alone device. However, mixing several fluids at the micro-scale is not as easy as it might seem at first glance. As discussed earlier, the Reynolds number at these dimensions is usually quite small and no turbulence takes place. Therefore, flow streamlines do not interfere with each other which results in zero mixing. Nevertheless, over small distances mixing can be performed by diffusion phenomenon. Alternatively, mixing may be enhanced by chaotic patterns, which can be induced by various schemes. Micro-mixers can be generally categorized as passive and active mixers. In passive micro-mixers where no external energy is required, the mixing process can rely on diffusion or chaotic advection. Passive mixers can be further categorized by their arrangement for the mixed phases such as lamination, injection, chaotic advection and droplet. In active micro-mixers an external field is used to generate disturbance to enhance the mixing process. Therefore, active mixers can be categorized by their type of external sources such as pressure, temperature, electrokinetics, and acoustics. Almost in all active mixers the basis of mixing is the chaotic advection of the flows. In the following sections, a brief introduction on the diffusion and chaotic advection phenomena is given and, subsequently, the review considers various types of passive and active micromixers.

2.1.1.1 Diffusion

Diffusion is the instinctive spreading of matter (particles), heat, or momentum and represents one type of transport phenomenon. It is the movement of entities from regions with higher chemical potential to lower chemical potential. One type of diffusion is the molecular diffusion (Brownian motion) in which we are dealing with transfer of the matter. Here, chemical potential can be interpreted as the concentration of molecules or particles. In fact, Brownian motion is an entropy minimizing process occurring in the presence of a non-uniform distribution of molecules. In microfluidic systems, the molecular diffusion is the dominant mechanism of mixing of mass species unless some external perturbation is applied. It is, however, mostly too slow and thus impractical in many cases, especially for large molecules. Let us estimate the characteristic time of diffusion. The reason for the diffusion is the large gradient of the concentration of the fluid molecules (or suspended particles) which exists when two different liquids have a common interface. The mathematical model of diffusion can be described by Fick's second law [64, 65]:

$$\frac{\partial C}{\partial t} = D \cdot \nabla^2 C \quad (2.1)$$

where C is the concentration for a particular fluid molecule type and D is the solute diffusion constant. For steady state diffusion (when the concentration within the diffusion volume does not change with respect to time) the Eq. 2.1, is reduced to Fick's first law, which gives the flux of the diffusing species as a function of the change in concentration in space (distance):

$$J = -D \frac{\partial C}{\partial x} \quad (2.2)$$

where J is the diffusive mass flux per unit of area (area perpendicular to x) and x is the position. D , diffusion coefficient or diffusivity, is defined as:

$$D = \frac{\kappa T}{6\pi\mu r} = \frac{\text{Driving Potential}}{\text{Resistance}} \quad (2.3)$$

where

- κ is the Boltzmann's constant ($=1.35054 \times 10^{-23}$ [J/K])
- T is the absolute temperature of the fluid
- r is the molecular radius of the solute
- μ is the dynamic viscosity of the fluid

Temperature dependency of the diffusion coefficient is associated with this fact that the Brownian motion of the particles is due to the applied forces from small liquid molecules which are excited by the temperature. The average time for the suspended entity to diffuse over a given distance is directly proportional to the square of the distance:

$$\tau \rightarrow L^2 D \quad (2.4)$$

where L is the characteristic mixing length (e.g., channel width) and τ is the time of mixing. τ can be up to the order of 10^5 seconds for particles with 1 μm diameter dispersed in water solution diffusing a distance of 100 μm . Obviously, such a diffusion time is not realistic and microfluidic devices that employ natural diffusion as their sole mixing mechanism will not be able to satisfy the rapid mixing requirement in bio-chemical analyses. Therefore, an innovative method of mixing is essential to enhance the process. As Eq.2.4 suggests, the rate of diffusion is dependent on diffusion coefficient, and the mixing length. Both viscosity and diameter are intrinsic properties of the solution and the chosen species, and thus the only remaining possibility of enhancing diffusion is to increase the contact surface and decrease the diffusion path.

2.1.1.2 Chaotic advection

In addition to diffusion, advection is another important form of mass transfer in flows. Advection is normally parallel to the main flow direction, and is not functional for the transversal mixing process. However, the so-called chaotic advection can enhance the mixing in microfluidic devices significantly. Mixing in these devices generally involves two steps; at first, a heterogeneous mixture of homogeneous domains of the two fluids is created by advection and, subsequently, diffusion between adjacent domains leads to a homogeneous mixture at the molecular level [66]. In the context of micro-mixers, the question arises on how the principle of chaotic advection can be implemented, as macroscale techniques such as employment of stirrers are not available. Chaotic advection can generally be produced by special geometries and three-dimensional structures in the mixing channel or induced by an external force in passive and active micro-mixers, respectively.

2.1.1.3 Passive micro-mixers

Because of their simple concept, passive mixers were one of the first microfluidic devices reported. Here we review the passive mixers based on their arrangement for the mixed phases.

2.1.1.3.1 Basic T-mixer and Y-mixer

As discussed earlier, fast diffusion mixing can be accomplished by decreasing the mixing path and increasing the contact surface between two liquid phases. Lamination separates the inlet streams into “n” sub-streams and then joins them into one stream. The most simple design is a channel with merely two inlets ($n = 2$); known as the T-mixer or the Y-mixer [67, 68]. Figure 2.1 illustrate the design of a typical T-mixer and Y-mixer, respectively [69].

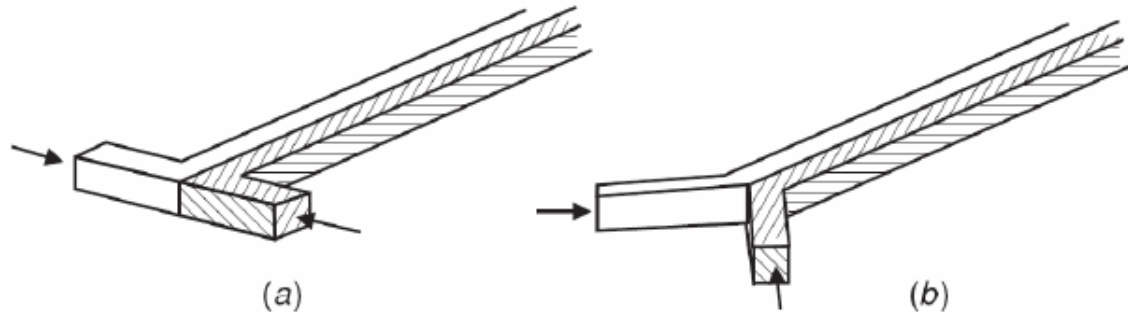


Figure 2.1.1 Basic designs in parallel lamination; (a) T-mixer, (b) Y-mixer

Since the basic T-mixer depends solely on molecular diffusion, a long mixing channel is required to accomplish the process. Nevertheless, efficient mixing may be achieved in a short mixing length at the expense of increasing the Reynolds number [70]. A chaotic regime can be induced at these high Reynolds numbers. Wong et al [71] reported a T-mixer which utilizes Reynolds numbers up to 500, where flow velocity is as high as 7.60 m/s at a pressure of up to 7 bar. However, in such micro-mixers, the high velocities on the order of 1 m/s or even higher require high supply pressures. The high pressure may be a crucial challenge for bonding and inter-connection techniques. At rather high Reynolds numbers the basic T-mixer can be further modified by implementation of some obstacles in the channel, which generate vortices and chaotic advection.

2.1.1.3.2 *Passive micro-mixers based on multi-lamination (parallel lamination)*

Multi-laminating flow configurations are the ones in which the number of sub-streams is greater than two and can be realized by different types of feed arrangements. As explained, lamination is based on the concept of decreasing the mixing path by making narrow channels [72]. Another method to make narrow paths is by fabricating inter-digital structures in the channel [73]. The flow is usually driven by pressure, but can also be generated by electrokinetic forces [74, 75].

Vortex (cyclone) mixers are another type of multi-laminating mixers where fast vortices are generated to enhance mixing with multiple inlet streams focused in a circular chamber[76, 77].

An alternative concept to reduce the mixing path for multi-lamination micromixers is hydrodynamic focusing. The basic design for hydrodynamic focusing is a relatively long channel with three inlets. The middle inlet is dedicated to the sample flow, while the solvent streams join through two encompassing inlets and act as the sheath flows. Hydrodynamic focusing technique was initially developed to enable fast mixing process. It reduces the stream width and, consequently, the mixing path. Knight et al [78] reported a prototype with a narrow mixing channel of $10\ \mu\text{m} \times 10\ \mu\text{m}$ in section. The sample fluid may be focused to a specific width by adjusting the pressure ratio between the sample flow and the sheath flows. In this way, diffusion distances are significantly reduced by compressing the fluid layer to a few micrometers, resulting in a mixing in the milliseconds range [79].

2.1.1.3.3 Passive micro-mixers based on Split-and-Recombine configurations

Split-and-Recombine (SAR) micro-mixers can improve the mixing by splitting and later joining the streams, creating sequentially multi-laminating patterns. For instance, the inlet streams may be first joined horizontally and then in the next stage vertically. SAR mixing commonly relies on a multi-step procedure. The basic operations are: splitting of a bi- or multi-layered stream perpendicular to the main orientation into sub-streams, re-direction or realignment of the sub-streams, and the recombination of these. These basic steps are usually accompanied by one or more re-shaping steps[80]. After m splitting and joining stages, 2^m liquid layers can be laminated. The process leads to a 4^{m-1} times improvement in the mixing time.

Branebjerg et al. [81] and Schwesinger et al. [82] were among the first who considered a micron-sized implementation of the SAR approach. Since then, several kinds of micro-mixers have been

realized utilizing some kind of multi-step SAR approach. The designs of SAR mixers differ in the exact geometry by which they actually achieve the fluidic arrangement. In context with micro-technological applications, the SAR concept is especially appealing, since it allows achieving fine multi-lamination with moderate pressure drops and without severe fabrication constraints. Melin et al [83] reported a simple design for a pressure-driven flow but it only worked for discrete liquid samples.

2.1.1.3.4 Injection micro-mixers

The basis of the injection mixing is similar to the SAR lamination mixer. However, instead of splitting both inlet flows, the mixer solely splits the solute flow into many sub-streams and injects them into the solvent flow. On top of one stream is an array of nozzles, which create a number of micro-plumes of the solute. These plumes enlarge the contact surface and decrease the mixing path, thereby improving the mixing efficiency. Miyake et al [84] developed an injection micro-mixer with 400 nozzles which were arranged in a square array. The mixer has an area for mixing, which is very flat and thin with micro-nozzles provided at the bottom of the mixing chamber. First, the mixing area is filled with one liquid, and the other liquid is injected into the area through the micro-nozzles, making many micro-plumes. The nozzles are positioned very closely in rows, 10-100 μm apart, in order that the plumes may quickly diffuse for this distance. Thus, effective mixing will be performed without any additional driving. Similar technique for the mixing with different nozzle shapes was reported by other researchers [85, 86].

2.1.1.3.5 Droplet micro-mixers

An alternative method for reducing the mixing path is to form droplets of the mixed liquids. The movement of a droplet leads to creation of an internal flow field which disturbs the fluid and causes mixing inside the droplet feasible. Droplets may be generated and manipulated

individually using pressure [87] or capillary effects such as thermo-capillary [88] and electro-wetting [89, 90]. Moreover, droplets may be generated by virtue of the large difference of surface forces in a narrow channel with multiple immiscible phases such as oil-water or water-gas [91]. In this micromixer, carrier liquid such as oil helps in formation of droplets of the aqueous samples. While moving through the channel, the shear force between the carrier liquid and the sample accelerates the mixing process in the droplet (Figure 2.2).

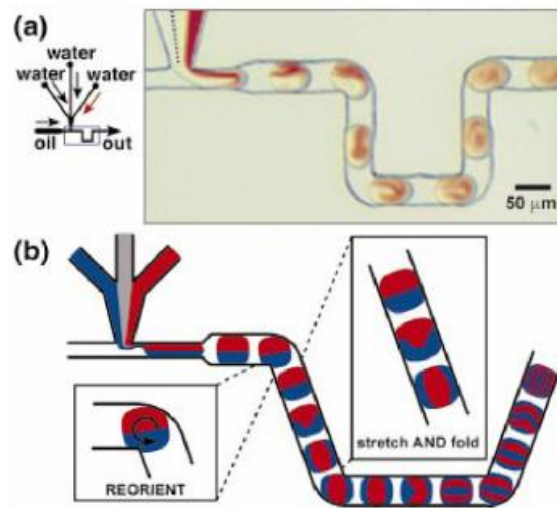


Figure 2.2 Droplet micro-mixer; (a) experimental results, (b) schematic representation of mixing process [91]

2.1.1.3.6 *Passive micro-mixers based on chaotic advection*

Chaos cannot occur in steady two-dimensional flows, but only in three dimensional and two-dimensional time-dependent flows. In two-dimensional flows, time-dependency may be considered as an added third dimension. Time dependency may be induced by external forces, which is the principle of active mixing class. In passive micro-mixers the basic idea is to modify the configuration and shape of the channel in a way that leads to splitting, stretching, and folding of the flow. Here, we classify the passive chaotic mixers based on the range of flow Reynolds

number; high, intermediate and low. However, it is not always possible to dedicate a particular design to a specific range of Reynolds number.

Chaotic advection at high Reynolds numbers ($Re > 100$)

A simple method is to insert obstacle structures in the mixing micro-channel in order to induce the chaotic advection. Various configurations and arrangements have been reported. Lin et al [92] used seven cylinders of 10 μm diameter placed in a narrow channel (50 $\mu\text{m} \times 100 \mu\text{m} \times 100 \mu\text{m}$) to enhance mixing. The mixing was performed with Reynolds numbers ranging from 200 to 2000 and a reaction time was 50 μs . Wang et al [93] reported a mixer using the same type of obstacles with different arrangements and carried out a numerical investigation of the mixing at high Reynolds numbers. The mixing channel was 300 μm in width, 100 μm in depth and 1.2-2 mm in length, and the diameter of the obstacle was 60 μm . It was revealed that obstacles in a channel at low Reynolds numbers cannot generate eddies or re-circulations. However, simulation results showed that obstacles could enhance the mixing performance at high Reynolds numbers.

An alternative method to generate chaotic advection is by utilizing zigzag channels to produce re-circulation. Mengeaud et al [94] used a micro-channel with a width of 100 μm , a depth of 48 μm and a length of 2 mm. In conducting a numerical investigation, they adopted the periodic steps of the zigzag shape as the main optimization parameter. Reynolds number was varied ranging from 0.26 to 267 and a critical Reynolds number of 80 were found. Below this number the mixing process relied entirely on diffusion whereas as at higher Reynolds numbers, mixing was performed by the generated re-circulations at the turns along the channel. The re-circulations could induce a transversal component of the velocity, which enhances the mixing process.

Chaotic advection at intermediate Reynolds numbers ($10 < Re < 100$)

Most of the micro-mixers in this category are based on the modified three dimensional twisted channels, but there may be some exceptions as well. For instance, Hong et al [95] presented an in-plane micro-mixer with two-dimensional modified Tesla structures. The Coanda effect in this structure leads to chaotic advection and enhances mixing noticeably. The mixer performs well at Reynolds numbers higher than 5. Liu et al [96] reported a three-dimensional serpentine mixing channel comprised of a series of C-shaped segments placed in perpendicular planes. The micro-mixer has two inlet channels joined in a T-junction and a sequence of six mixing segments. It was observed that the mixer is that the mixing time is short at higher Reynolds numbers; chaotic advection only occurred at Reynolds numbers ranging from 25 to 70. Park et al [97] presented the results for mixing two fluids in a three-dimensional passive rotation micro-mixer using the break-up process). The complex channel rotates and separates the two fluids by partitioning walls, and consequently, generates smaller blobs exponentially. In practical experiments, over 70% mixing was achieved at $Re=1, 10$ and 50 , only after passing through a 4 mm long channel. Vijayendran et al [98] reported a three-dimensional serpentine mixing channel where the channel was designed as a series of L-shaped segments in perpendicular planes. The mixer was experimentally tested at Reynolds numbers of 1, 5 and 20. The results indicated that better mixing was achieved at higher Reynolds numbers. Jen et al [66] proposed various designs of twisted micro-channel providing a third degree of freedom for chaotic advection. Mixing of methanol and oxygen was numerically investigated at different velocities (0.5- 2.5 m/s).

Chaotic advection at low Reynolds numbers ($Re < 10$)

One of the most promising types of the passive micro-mixers falls in this category which works based on the idea of placing micro-structured objects within the flow passage on one side of the

channels. Stroock et al [99] was the first to investigate this concept and since then, much effort has been dedicated to improve their proposed mixers. Stroock et al [99-101] pointed out different ways of creating secondary re-circulating flows in a channel. They considered geometries with grooved channel walls, such that at least one of the walls contains ridges standing at a tilted angle with the main flow direction. Two different groove patterns were considered; obliquely oriented and staggered ridges. They referred to later one as the staggered herringbone mixer (SHM). One way to induce a chaotic pattern is to subject volumes of fluid to a repeated sequence of rotational and extensional local flows. This sequence of local flows in the SHM may be obtained by varying the shape of the grooves as a function of axial position in the channel: The alteration in the orientation of the herringbones between half cycles exchanges the positions of the centers of rotation and the up and down-welling in the transverse flow. When a pressure-driven fluid flows over such a surface, the grooves can be viewed as if they induce a slip flow in a particular direction. Confined to a channel, the flow develops re-circulation patterns, which leads to an exponential increase of specific interface, therefore to fast mixing. The SHM mixing is superior to similar channels without inserted structures or with straight ridges only. SHM can work well at a Reynolds numbers ranging from 1 to 100. The effect of chaotic advection in a channel with grooves was numerically investigated by Wang et al [102] and Aubin et al. [103] using CFD methods. They showed that an exponential stretching of the fluid interface occurs where with simple linear grooves (straight ridges), the interface area increases more slowly.

2.1.1.4 Active micro-mixers

As discussed earlier, in active micro-mixers an external field is used to generate disturbance to enhance the mixing process. Most of the active mixers rely on the chaotic regime induced by

virtue of the induced periodic perturbation. In the following, various active mixers classified by the type of employed external sources are presented.

2.1.1.4.1 Micro-impellers

Traditionally, stirring with impellers is the most common way to perform mixing of large volumes. However, several miniaturized stirrers have been developed for mixing of the liquids in micro-scale [104-106]. In macroscopic stirrers, the stir-bar or propeller rotation causes turbulence by increasing the local velocity. In microscale, the stir-bar helps mixing by providing more interfacial area rather than inducing turbulence. Claimed advantages of such mixers are the possibility to match the impeller diameter to the mixing volume, carry out large-area mixing, undergo mixing on-demand (switch on/off), and the flexibility of the mixing approach regarding the choice of liquids. A micro-stir-bar with a span of 400 μm was fabricated and placed at the interface between two liquids in a PDMS channel by Ryu et al [105]. An external magnetic field provided by a rotating magnet in a hotplate/stirrer drives the stirrer remotely. Experimental results proved that nearly complete mixing is achieved instantly.

2.1.1.4.2 Pressure field disturbance

Pressure disturbance was one of the earliest methods used in active micro-mixers where an integrated or an external micropump drives and stops the flow in the channel to divide the mixed liquids into multiple serial segments and make the mixing process independent of convection. The performance of this mixer was evaluated and mixing was found to proceed quickly in the mixing channel[107]. Another method to achieve pressure disturbance is the generation of pulsing velocity by alternating switches of the flows from a high to a low flow rate, periodically. In this way, a pulsation of the whole stream is achieved promoting axial mixing. Glasgow and Aubry [108] reported a simple T-mixer and detailed CFD simulations with a pulsed side flow at

a small Reynolds number of about 0.3. When both inlets have constant flow rates, the mixing zone is confined to a narrow band around the horizontal interface. Time pulsing of one inlet flow rate distorts the interface to an asymmetrically curved shape which changes with time. Therefore, liquid transport is promoted and mixing is improved. The degree of mixing was 22%, being 79% larger than for constant flows. The periodicity and the number of pulsing streams have a significant effect on the mixing efficiency. The best results were obtained for two pulsed inlet flows having a phase difference of 180° with the same amplitude and frequency. CFD simulations showed the bending of the fluid interface along the channel cross-section and associated stretching and folding in the direction of the flow. The corresponding degree of mixing was considerably increased to 59%. However, such devices require a complex computer controlled source-sink system.

2.1.1.4.3 Acoustic/Ultrasonic disturbance

Acoustic (ultrasonic) actuation may be utilized to stir the fluids in active micromixers [109-111]. However, ultrasonic mixing may be a challenging issue in applications for biological analysis owing to the temperature rise due to acoustic energy. Many biological fluids are sensitive to high temperatures. Moreover, ultrasonic waves around 50 kHz are harmful to biological samples by virtue of the possible cavitations. The non-destructive ultrasonic mixer reported by Yasuda et al.[110] used loosely focused acoustic waves to induce stirring movements where the wave was generated by a piezoelectric zinc oxide thin film. The actuator was driven by a programmable function generator providing a 500 kHz/3.5 MHz sine waves and programmed waveforms corresponding to the thickness-mode resonance of the piezoelectric film. The mixer performed without any consequential temperature increase and could be used for fluids sensitive to the temperature. An air bubble in a liquid can perform as an actuator, when it is energized by an

acoustic field. The bubble surface behaves like a vibrating membrane and this type of actuation is mainly dependent on the bubble resonance characteristics. Bubble vibration due to a sound field generates friction forces at the air/liquid interface which leads to a bulk fluid flow around the air bubble (known as cavitations or acoustic micro-streaming). Liu et al [112] used acoustic streaming around an air bubble for mixing where streaming was induced by the field generated by an integrated PZT actuator. Fluidic movements led to the global convection flows with “Tornado” pattern in the vicinity of the bubbles. The time required to fully mix the whole chamber was approximately 45 s. Yaralioglu et al [111] also used acoustic streaming to perturb the flow in a conventional Y-mixer.

2.1.1.4.4 Electro-hydrodynamic (EHD) disturbance

Electro-hydrodynamic effect has been used to generate chaotic flows in micromixers [113-115]. A simple geometry mixer was proposed, which works based on the EHD force when the fluids to be mixed have different electrical properties and are subjected to an electric field [113]. The electrodes are arranged so that the electric field is perpendicular to the interface between the two fluids, creating a transversal flow. Two fluids of identical viscosity and density, but with different electrical conductivities and permittivity's were used for experiments. Each fluid enters the microfluidic chamber in its own inlet channel. As soon as they meet, a jump in electrical conductivity and/or permittivity is generated at the interface between the two fluids, which has no effect as long as the electric field is absent. However, as the fluids enter the electric field influence zone close to a pair of facing electrodes, they are subjected to an electrical force, which creates a transversal secondary flow across the interface between the two fluids, therefore destabilizing the interface and enhancing the mixing process. By alternating the voltage and

frequency on the electrodes, efficient mixing was obtained in less than 0.1s at a low Reynolds number of 0.02.

2.1.1.4.5 *Magneto-hydrodynamic (MHD) disturbance*

The magneto-hydrodynamic force has been utilized in an active micro-mixers reported by Bau et al [116]. This mixer uses the arrays of electrodes deposited on a conduit's wall. By applying alternating potential differences across pairs of electrodes, currents are induced in various directions in the solution. In the presence of a magnetic field, the coupling between the magnetic and electric fields induces body (Lorentz) forces in the fluid which in turn produce mixing movement in the chamber. The Lorentz force can roll and fold the liquids in a mixing chamber. After each time unit (a few seconds), the polarity of the electrodes and the direction of the Lorentz force are reverse and the dye returns to its previous initial position. After several reversals, dye continues to deform in opposite directions and eddies are formed. These concepts work only with an electrolyte solution. Since the electrodes can be patterned in various ways; relatively complex flow fields can be generated.

2.1.1.4.6 *Electro-Osmotic disturbance*

Lin et al [117] reported a T-form micro-mixer using alternatively switching electroosmotic flow. A switching DC field is utilized to generate an electroosmotic force which concurrently drives and mixes the electrolytic fluid samples. It was shown that a mixing performance as high as 97% can be obtained within a mixing distance of 1 mm downstream from the T-junction when a 6 kV/m driving voltage and a 2 Hz switching frequency are applied. Design and fabrication of a ring electroosmotic chaotic micro-mixer with integrated electrodes was reported by Zhang et al [118]. It takes two fluids from different inlets and combines them into a single channel where the fluids enter the central loop in downstream. Four microelectrodes are positioned on the outer

wall of the central loop with an angular distance of 45° . These microelectrodes impose a spatially varying electric field, and the fluids are manipulated via the electroosmotic slip boundary condition before they enter the outlet channel. Electric potentials on the microelectrodes are time-dependent, which adds the third dimension necessary for chaotic mixing. Generated electroosmosis agitates the low Reynolds number flow. Sasaki et al [119] presented a mixer based on AC electroosmotic flow, which is induced by applying an AC voltage to a pair of coplanar meandering electrodes configured in parallel to the channel. The mixing time was 0.18 s, which was 20- fold faster than that of diffusional mixing without an additional mixing mechanism. Tang et al [120] also utilized an electroosmotic flow to improve mixing where switching on or off the voltage supplied to the flow generates fluid segments in the mixing channel. This flow modulation scheme was capable of injecting reproducible and stable fluid segments into microchannels at a frequency between Hz and 1 Hz.

2.1.1.4.7 Magnetophoretic disturbance

The magnetic field-induced migration of particles in liquids is known as magnetophoresis. Recently, in addition to separation which will be discussed later in the section, magnetophoretic forces are exploited to enhance the mixing of the particles in a solution in micro-scale devices. A magnetic force driven chaotic micro-mixer was reported, in which magnetic particles are stirred by the local time-dependent magnetic field to enhance the attachment of magnetic particles onto biological molecules suspended in the medium [43, 121-124]. Serpentine channel geometry with the perpendicular electrodes arrangement was used to create the stretching and folding of material lines as demonstrated by Suzuki et.al[122]. It is claimed that good mixing was achieved in a short time (convective time of less than 10 s) and distance (mixer length of 1.3 mm).

However, manufacturing the proposed mixer requires the utilization of complex microfabrication techniques.

Each of the investigated mixers has its own specific advantages and drawbacks and there is not any particular type as the best general candidate for the mixing process in micro-scale. Therefore, one must decide on an appropriate mixer type considering various parameters such as desired functionality, fabrication costs, disposability, and operating conditions. Generally speaking, passive micro-mixers are more preferable as no external source is required to drive these devices. Integrating actuation mechanisms such as heaters, micro-conductors, power generators and controllers to provide the required external energy in active mixers, calls for employment of sophisticated fabrication techniques, which in turn adds an extra cost to the manufacturing process. This may be a challenging issue particularly for disposable devices.

However, there are some exceptions in passive mixers where fabrication of microchannels with three-dimensional configurations such as Tesla structure, staggered herringbone parts and obstacles is as complex as active mixers. Perhaps, most convenient mixers from fabrication point of view are passive mixers, which rely on lamination techniques and no complex structure or component is required to operate them. Performance of the micro-mixer can be a crucial factor in determining the proper type of mixing mechanism for a particular application. Extent of the mixing of micro-particles in bio-fluid, for instance, has a significant effect on the quality of whole magnetic isolation process. Therefore, a mixing technique with sufficient capability must be adopted for this protocol. Efficiency may also be interpreted as the mixing time or the space required (e.g., channel length) to achieve the full extent of the mixing as in most of the integrated systems, a considerable effort is dedicated to minimizing these factors. In fact, one often needs to reach a compromise between different parameters regarded as the efficiency of the mixer.

Moreover, controllability of the mixer must be factored in. While active mixers can be activated on-demand (switch on/off), in a passive mixer there is not any chance to operate the device in particular ranges of time or space. Micro-mixers are widely used in chemical, biological and medical analysis applications where one deals with variety of fluidic environments. Each type of fluids has its own intrinsic properties such as viscosity, density, electrical properties, etc. Therefore, based on the working fluid, a proper type of the mixing technique must be adopted as some of the mixers are designed to work with particular liquids. For instance, in most active mixers where the driving force is electrokinetic, the possibilities for two mixing phases are limited; MHD mixers work solely with electrolyte solutions, in EHD mixers two fluids are expected to have distinct different electrical properties such as conductivity and permittivity, electroosmotic mixers are highly dependent upon pH and the concentration of the different ion species in the solution, and finally in dielectrophoretic and magnetophoretic mixers, presence of some polarisable elements in mixing phases is essential. On the other hand, another major limiting factor for mixing phases must be taken into account for almost all passive mixers, which rely on lamination methods; if a particle laden fluid is passed through narrow channels the probability of clogging is very high. Moreover, in those mixers where embedded conductors are utilized to supply necessary electric or magnetic field for actuation, heat generation can be a challenging issue for buffers sensitive to high temperatures. The same problem is observed in acoustic micro-mixers. In addition to the type of mixing liquids, operating conditions such as pressure and bulk fluid velocity (Reynolds number) may be a crucial parameter in choosing the suitable micro-mixing mechanism. For instance, as discussed earlier, a passive micro-mixer with inserted obstacles which relies on the chaotic advection is not an appropriate candidate for mixing of flows with low velocities. Having considered the properties of buffer containing

magnetic nanoparticles and the presence of particles themselves, in this research it was decided to employ magnetophoretic forces to perform the mixing as the same type of force is used for separation and detection stage. Besides this view to ultimately integrate the mixer to the magnetic isolation chip as its particular application, it was intended to propose a mixer with flexibility of the mixing approach regarding the choice of liquids. Magnetic nanoparticles can be loaded into most fluids and be utilized as a label for actuation. After the mixing, particles can be easily separated in downstream.

2.1.2 Magnetic Separation/ Isolation/Trapping

In the field of medicine and life sciences it is often essential to separate specific biomolecules or cells out of their native environment. This is done in order to pre-concentrate samples which may be prepared for subsequent analysis in downstream or other applications [61]. Generally, there are two types of magnetic sorting or magnetic manipulation techniques. In the first type, biomolecules or cells to be isolated demonstrate adequate intrinsic magnetic property so that magnetic manipulation or separations can be performed without any modification. There are solely two types of such biological molecules in the nature, namely red blood cells (erythrocytes) containing high concentrations of paramagnetic hemoglobin, and magnetotactic bacteria containing small magnetic particles within their cells [125]. However, to separate or manipulate these molecules, an external high magnetic field gradient or force is required. In the second type, non-magnetic target entities or biological molecules have to be tagged by a magnetic label to achieve the required contrast in magnetic susceptibility between the target and the solution. Through the use of a magnetic label and a proper magnetic field, a five-order-of magnitude difference in magnetic susceptibility between a labeled and unlabeled cell may be obtained[126, 127]. These labels are often known as magnetic micro/nanoparticles. Advances in particle

synthesis methods and other associated nanotechnologies have led to availability of magnetic micro/nanoparticles, with different surface modifications, over the last decade [128-130]. These particles have many important applications in chemical and biomedical research [61] industry. The procedure of combining target molecules with magnetic particles is often referred as tagging. In this process modification of the surface of the micro/nanoparticles is done in a way that it facilitates chemical binding between target entities and particles. In this technique the surface of particles is chemically functionalized through a coating process, thereby providing a link between the particle and the target site on a cell or a biomolecule. This coating is a specific biocompatible substance and can be an antibody or an m-RNA string but the possibilities are numerous. Magnetic tagging of cells/biomolecules can be achieved not only by attaching magnetic particles to the surface [32, 126, 131] but also by introducing magnetic nanoparticles into the cell [132]. Figure 2.3 shows an example of magnetic particles with different functional groups attached to their surface, respectively.

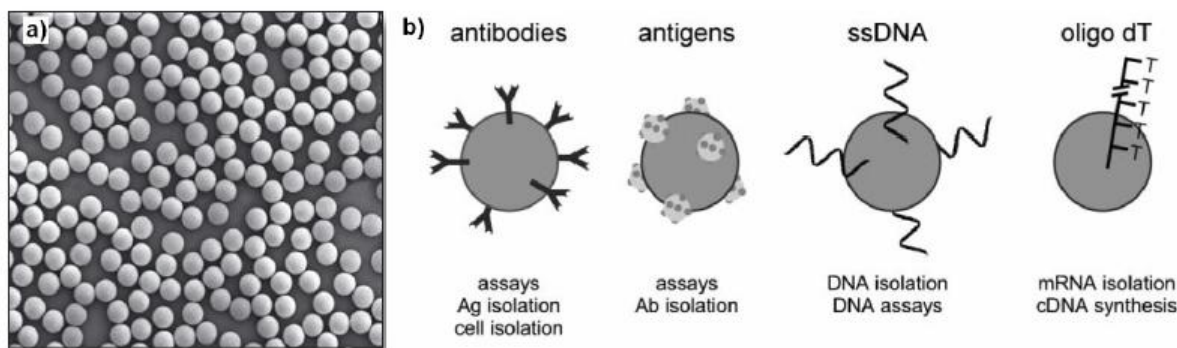


Figure 2.3 Magnetic micro-particles (a) 1 μm Dyna-beads, (b) schematic diagram of functionalized magnetic particles [29]

If magnetic particles are coated with an antibody and then mixed into a solution containing the target antigen along with other materials only the target antigens will bind to the antibodies and thus to the magnetic particles. If the magnetic particles can be subsequently separated from the

solution the target antigens will also be separated from the solution in this way. The separation step is made possible through utilizing magnetic properties of the particles. The particles used for this purpose are mostly magnetite (Fe_3O_4) or its oxidized form maghemite ($\gamma\text{-Fe}_2\text{O}_3$) and are magnetized in an external magnetic field. Such external field, generated by a permanent magnet or an electromagnet, may be used to manipulate these particles through magnetophoresis phenomenon (i.e., migration of magnetic particles in liquids). By virtue of their small size; ranging from 100 μm down to 5 nm, particles lose their magnetic properties when the external magnetic field is removed, exhibiting superparamagnetic characteristics, which means they have neither coercivity nor remanence. If the fluid mixture containing magnetically labeled cells are passed through a region where there is magnetic field, particles and therefore tagged cells will be immobilized while rest of the fluid is washed away. In fact, magnetic particles are used as a label for actuation. In the next step, magnetic field is removed and particle-cell complex is free to flow and be collected for further analysis in downstream. Commercial magnetically-activated cell separation (MACS) columns [133] (MACS system, Miltenyi Biotec GmbH, Bergisch Gladbach, Germany; MPC separator series, Dynal AS, Trondheim, Norway) are already available. The column with steel wool is placed between the poles of a magnet. The magnetic beads labeled cells will be attracted by the wool matrix and the unlabeled cell are eluted. The labeled cells can be eluted by removal of the magnet. However, these systems have several drawbacks, such as the requirement of large number of samples, long analysis times and the discontinuous separation. Another big disadvantage is that the cells will be damaged by the strong surface tension when attracted by the wool matrix. Important clinical and research applications often involve very small and valuable samples. Magnetic field based bioseparation in a microfluidic systems is receiving increased attention because of its vast applications in biomedical research, clinical

diagnostic and biotechnological sciences. Its principle involves isolating biomolecules of interest from the bulk mixture by attaching them to small magnetic particles and then recovering it by using an external magnetic field [41, 132, 134] in a continuous process. The use of microfluidic technology has provided a means to separate low volumes target molecules at faster rate. In the past few years, several microfluidic bioseparation system based on magnetic particles have been successfully developed for separation of biomolecules. The simplest and most conventional magnetic system is developed using permanent magnets. In such systems, the permanent magnets are generally placed alongside a microfluidic channel and the magnetic field gradient is adjusted by controlling the distance between the magnet and the microchannel, as well as the shape of the magnetic poles. The main advantage of using permanent magnets in such systems is the stability of the magnetic field, which at the same time is also its main disadvantage, since the generated field cannot be easily modulated. The magnetic separators with H-shape [135] or one inlet and multiple outlets (multi-phase flow) [136] or two inlet and two outlet (two-phase flow)[137-139] microchannel has been developed to separate magnetic and non magnetic microparticles as well as different magnetic particles. The only disadvantage is that magnets generate a very low gradient of magnetic field and therefore magnetic force on individual particles is too small. So low flow rates should be applied to such systems. However, for this kind of system, it is easy to apply the permanent magnetic field and does not need any complicated fabrication process of magnetic elements. Compared to permanent magnets, electromagnets offer a higher flexibility but generate lower magnetic fields. In order to maximally profit from the generated forces, the distance between the magnetic elements and the magnetic particles needs to be very small. Alternately, high gradient magnetic separator (HGMS) can generate a large magnetic force on the particles and it is much easier to implement compared

to the increase of magnetic strength have been developed. In these systems the magnetic field is generated in a multitude of ways, using wires [41, 134, 140], coils [46], tapered electrodes [141] or soft-magnetic elements that concentrate the magnetic field generated outside the chip[142]. The simplest and conventional design for high gradient magnetic separation (HGMS) is to place magnetic stainless steel wool into a tube, which is then placed between the poles of a permanent magnet [37]. With development of microfabrication techniques, integrating ferromagnetic wire into microfluidic devices attracts more and more attention and the requirements for field strength can also be reduced. Under the external magnetic field, the ferromagnetic wire will be magnetized. The magnetic field is deformed near the ferromagnetic wire and generates a high gradient magnetic field. Many HGMS have been developed, such as aligning magnetic strips [131] on the bottom of fluid chambers, depositing microfabricated magnetic wire in the middle of microchannel [143-145] or placing the magnetic element on one side [52] or both sides [146] of the channel. The magnetic elements will be magnetized by external magnetic field and generate a high gradient magnetic field. One big advantage of HGMS is that high field gradient will generate a large magnetic force on the particles and make the particles much easier to be separated compared to other magnetic separation methods. However, the magnetic field in the system is not uniform and high magnetic field and field gradient were generated near the magnetic elements. Particles will be attracted by the magnetic elements and it needs one more step to release the particles by removing the external magnetic field. For the cell separation application, the contact with surface of channel or magnetic elements will damage cells. The advantage of systems using electromagnets as compared to permanent magnets is the possibility of improved field control as well as the possibility of system automation. Further-on, electromagnets can be fabricated in smaller dimensions thus allowing to not only move clusters

of magnetic beads, but also single magnetic particles or single cells labeled with magnetic particles. The systems for the manipulation of magnetic microparticles can be divided into two groups: separation and trapping of the particles from a sample flow [146, 147] or guiding the transport of magnetic particles inside a channel [41, 134]. Magnetic separators that can be controlled by current have been developed to separate the magnetic particles with different magnetophoretic mobilities in a microfluidic channel using an alternating travelling magnetic field [148]. The magnetic particles can be moved step by step when the current was sent to the conductors alternatively and periodically. Ramadan et al. [57-59] also designed a magnetic device which consisted of arrays of microcoils with small conductors and with ferromagnetic pillars as magnetic cores. The magnetic pillars in the middle of each loop sharply enhanced the gradient of magnetic field. By alternatively injecting currents to the microcoils, magnetic beads can be attracted by the pillars and moved in different modes and step sizes. The first examples for microfluidic systems with electronic control of the movement of magnetic microparticles were presented by Lee et al.[140] and Deng et.al.[134]. Both these systems utilized multiple wires in order to generate consecutive magnetic field gradients, These kinds of systems are quite flexible and controllable, however, the particles can only be moved step by step and whole separation process is not continuous. Recently, various microfluidic systems have been developed, which profit from the duality (active element and mobile substrate) of the magnetic particles for performing bioseparation procedure on a chip. The systems differ in their use of the magnetic particles, which either serve as vehicles for the transport of molecules or cells to points of interest, or as traps for capturing the molecules before and during reaction followed by separation. Most microfluidic-based Lab-on-a-Chip systems employing magnetic microparticles follow hereby the procedure of macroscopic lab-bench protocols[149], which includes

incubation, washing and detection steps. We can see that the immobilization of the magnetic particles in the presence of a sample flow is an important feature of most channel based Lab-on-a-Chip solutions. However continuous flow separation is highly desirable in some application such as blood purification. Recently, magnetic microparticle based system for continuous separation of blood constituents' have been developed by Yung et al.[53]. This system takes the advantage of microfluidic continuous flow, low volumes and high gradient magnetic field using electromagnet. Although, this system exhibit high separation efficiency but it cannot be used for point-of-care applications or integrated on lab-on-chip for subsequent detection process. In this thesis emphasis is given on understanding the trapping and separation process especially when magnetic nanoparticles are employed for lab-on-a chip systems. The advantages of using magnetic nanoparticles over microparticles and understanding of the dynamics of magnetic nanoparticle trapping and separation is discussed in more detail in later chapters.

2.1.3 Magnetic particle-based Detection

Mass transfer and reaction kinetics play a key role in developing high performance microfluidic detection system for life sciences and medical diagnosis. Most of these microfluidic devices rely on recognition–binding event most typically antigen-antibody also known as “immunoassays” or “bioassays”. They are used for detecting disease markers [150], drug screening [151], protein characterization [152], and DNA detection[153]. The fluid containing the target antigen flows through the microfluidic channels and is brought in contact with the surface bound complementary antibody. The antigen-antibody complex is detected and quantified either by using fluorescent techniques [154, 155] or surface plasmon resonance [156, 157] or by electrochemical methods [158, 159]. The purpose of a bioassay is to measure the concentration of a protein or biomolecules in a biological liquid such as serum, blood or urine. The assay takes

advantage of the specific binding of an antibody (Ab) to its Antigen (Ag). One of the most known and used methods is the Enzyme-linked immunosorbent assay (ELISA). Immunoassays may be classified into two main categories, heterogeneous and homogeneous assays. A heterogeneous assay requires a step to remove unbound Ab or Ag from the reaction site, whereas a homogeneous assay does not require this additional step. Therefore a heterogeneous immunoassay generally requires several washing steps to separate a solid phase from a liquid phase. In the past, several bioassays have been developed on a microfluidic platform [49, 160, 161] in order to provide sensitive, selective, and rapid detection of biomolecules. Magnetic micro/nanoparticles have been widely used as signal reporters to detect various biomolecules [158] such as pathogenic bacteria [162], human allergen [163], and to facilitate location of cancerous cells [164]. Highly sensitive detection close to single magnetic particle is possible, if a particle is in close proximity and as long as all system dimensions including particle size and position, sensor area are scaled down proportionally[37]. There are relatively no efforts adopted where magnetic nanoparticles are employed to enhance the chemical sensitivity of surface binding reaction in a flow-through system. Microfluidic biochemical systems take advantage of small reaction volumes and short diffusion lengths, thus reducing assay times and analyte consumption and potentially results in high detection sensitivity. They have been developed for a broad range of biomedical and bio-analytical applications and the major part of these microfluidic systems is based on the application of continuous flow using external syringe pumps or capillary driven flows. In late nineties researcher proposed a microfluidic H-filter[165], a simple device that filters particles by size without the need of a membrane . The same group also proposed a T-sensor that may be used to measure analyte concentrations, diffusivities of molecules or reaction kinetics [166]. A diffusion immunoassay based on a T-sensor was also

reported by Hatch et al. in 2001[167]. This competitive assay is based on the measurement of the distribution of a labeled probe molecule diffusing into a region containing capture Ab's. Another detection methodology employing polymerase chain reaction (PCR) successfully implemented on a chip [168, 169] for molecular diagnostics. PCR is a technique used to amplify a few copies of a DNA fragment by several orders of magnitude. The method relies on thermal cycling, consisting of cycles of repeated heating and cooling of the sample. On-chip PCR decreases the cycle time due to better and faster control of the fluid temperature. More recently, Sato et al. [170] presented one of the first bead-based immunoassay systems. This multichannel system was able to process four samples in parallel with one pump unit and to complete the assay in 50 minutes. Bead-based systems present the additional benefit of a large surface-to-volume ratio and flexible surface functionalization on the bead surface [22, 171]. The following Section will focus on systems and techniques using micro and nanoparticles to perform on-chip immunoassays. One important parameter in microfluidic applications is the method used to drive the liquids through the microchannels. Three main techniques for liquid manipulation on-chip are often employed. The most evident actuation technique is the pressure driven-flow. A pressure difference between the inlet and the outlet forces the liquid to flow through the channel. The flow rate and velocity are defined by the fluidic resistance of the channel and the pressure difference. An efficient way to control the liquid velocity is using a syringe or micro pump that imposes constant flow rate. According to the Poiseuille's law, the no-slip condition at the channel walls induces a parabolic velocity profile. Electro-osmotic flow (EOF) is an electrical method to move liquids in capillaries or microchannels using based on the displacement of ions. When an electrolytic solution is introduced in a glass microchannel or a capillary, an accumulation of mobile charges occurs close to the surfaces. By applying an electric field along

the channel, these charges start moving and may drag the whole liquid due to viscous forces. EOF is characterized by a flat velocity profile. A liquid in a hydrophilic microchannel may also be moved by capillary forces. This flow actuation does not require external sources, but allows less flexible control of the flows. To perform an efficient bioassay several aspects have to be taken into account. Table 2.1 shows a comparison of the different methods considering important aspects that are required to perform an efficient bioassay on-chip using microparticles. A high force on the particle is needed for retention and fast actuation of the particles. The maximum possible distance range between the actuator and the particles is of importance to allow convenient integration into the microchip. For example, if particles have to be in direct contact with an electrode, the latter has to be directly integrated into the microchip. This results in a more complex fabrication process compared to a system where the actuator can be placed externally in proximity of the channel. Release of the particles after an experiment for subsequent detection is a very important aspect in bioanalytical LOC systems and is therefore the main limitation preventing the use of non-reversible retention systems. The ability to concentrate the particles in a restricted volume is generally an advantage for controlling the incubation process of a bioassay as well as to increase the particles interaction and the detection signal.

Table 2.1 Comparison of the different particle manipulation techniques (Abbreviations: MP= magnetophoresis, DEP= dielectrophoresis, MR= Mechanical Retention, and SP= superparamagnetic)

Strategy	Force	Re-suspension in fluid	Concentration
MP	High	Yes, if MNPs	High
DEP	Low	Yes	Low
Optical	-	Yes	-
MR	Medium	No	High
Acoustic	Low	Yes	Medium

From Table 2.1, it is clear that the magnetophoresis method is one of the most competitive actuation tools for immunoassays on-chip. One of the reasons is the relatively high force that may be exerted on magnetic particles in a very simple manner, for instance by using a passive element (like a permanent magnet). Maximizing the exposure of the magnetic particle surface to a microfluidic flow for biomolecule capture is an issue of primary importance [37]. For that purpose, manipulation of magnetic particles on-chip is often used for the retention of particles from flow or the transport of biological molecules. The next section provides details of different type of actuation mechanism used to create magnetic field gradient (i.e. permanent magnets or electromagnets).

2.1.3.1 Systems with external permanent magnets

A simple approach consists in passively trapping the magnetic particles in a microchannel by using external permanent magnets allowing the formation of a dense and static plug [49, 172]. Using this simple approach, a small-volume heterogeneous immunoassay system was demonstrated in microchannels with small paramagnetic beads (1–2- μm diameter). The assay was demonstrated as a direct interaction of fluorescein isothiocyanate (FITC) with an immobilized anti-FITC conjugated. Bronzeau et al. [49] demonstrated how several assays that can be performed simultaneously by flushing a sample solution over several plugs of magnetic beads with different surface coatings. Three plugs of magnetic beads were immobilized in a microchannel with external magnets. The beads featured surface coatings of glycine, streptavidin and protein A, respectively. Reagents were then flushed through the three plugs. Molecular binding occurred between matching Ag's and Ab's in continuous flow and was detected by fluorescence. Sensitivity of such systems using mm-sized external permanent magnets is however limited due to the high density of beads captured in the plug and the relatively poor

perfusability of the plug. An alternative method uses geometrically trapped self-assembled chains composed of a relatively low number of magnetic nanoparticles [173] in order to perform a complete on-chip sandwich immunoassay. The magnetic chains are retained over periodically enlarged cross sections of a microfluidic channel. Thereby, they strongly interact with the flow and rapidly capture the total of a low number of target molecules. As an example, the detection of murine monoclonal antigen with a detection limit of 1 ng mL^{-1} was demonstrated. This work demonstrated that an optimal interaction between the analyte flow and the magnetic particles is of importance for effective capture of the target antigens. Another simple and elegant concept using a permanent magnet for the continuous flow separation of magnetic beads was proposed by Pamme et al.[38]. This method uses a permanent magnet placed on one side of a microfluidic chamber. Beads are then introduced on the opposite side of the chamber and are then deflected towards the magnet. Using this method, separation of non-magnetic beads and magnetic beads was first demonstrated in a free flow device. Magnetic beads were also separated as a function of their sizes. More recently, this concept was used to perform a continuous flow immunoassay by Peyman et al. [174]. Magnetic beads are introduced on one side of a microfluidic chamber and are then deflected towards the permanent magnet on the opposite side. During the deflection, beads cross parallel reagents streams in which several binding and washing steps are performed. Using this method, a sandwich immunoassay was demonstrated. The main limitation of such approach comes from the short time during which a bead is immersed in each reagent resulting in a relatively high detection limit. Moreover, beads are moved in a unique direction (i.e. towards the permanent magnet) and therefore may not come back to the original liquid.

2.1.3.2 Electromagnet-based systems with integrated soft magnetic poles

The possibility to actively manipulate magnetic carriers in microfluidic channels opens the way to explore new opportunities for on-chip bioassays with enhanced performance[175, 176]. A magnetic core is used to guide the magnetic field generated by an external electromagnet and two microstructured soft magnetic tips are used to focus the magnetic field across a microchannel. This approach demonstrated a good mixing efficiency of two parallel flows in a microchannel and provided evidence of enhanced interaction between the magnetic particles and the fluid flow. Unfortunately, such type of ferromagnetic particles stay agglomerated in bead clusters after field removal. In many bioanalytical applications, individual particles should be released from the plug after analyte capture for further processing. The previous technique cannot be readily applied to superparamagnetic or low-coercivity beads, as these change their magnetic state by Néel relaxation and therefore cannot be directly applied for immunoassays. Long range transport of magnetic beads using planar integrated coils was demonstrated by Rida et al.[46]; also a wire-based system for the displacement of clouds of magnetic beads was presented[134, 177]. Manipulation of microdroplets using magnetic beads was presented by Lehmann et al. [50, 178] and this concept was used for the purification of DNA[50]. These systems are generally used to dynamically manipulate (i.e. displace) the magnetic particles in channels, capillaries or microchambers. Due to the relatively low magnetic field produced by the integrated wires or coils, the retention of magnetic particles in a flow using this principle is limited and the actuation speed is low. The combination of permanent magnets with electromagnets (coils) is only rarely applied for the manipulation of magnetic particles on-chip. It is clear that the combination of permanent magnets with electromagnet may still improve the efficiency of on-chip manipulation of magnetic particles.

2.1.3.3 Comparison of magnetic particle manipulation methods

Methods using passive elements (i.e. permanent magnets) and active electromagnets are often reported in the literature. A qualitative comparison of the different methods is summarized in Table 2.2. The combination of active and passive elements for the manipulation of magnetic beads on-chip is still not fully explored. Indeed, the main limitation for electromagnet based manipulation comes from the relatively low magnetic field produced by an external electromagnet or an integrated coil and thus the low magnetic force acting on the bead. Therefore, combination of electromagnets with permanent magnets might offer a good compromise between magnetic force and ability to dynamically actuate the beads.

Table 2.2 A qualitative comparison of the different magnetic manipulation methods.

Strategy	Force	Dynamic Actuation	Particle Release
Permanent Magnet	High	No	Medium
Integrated Magnet	Low	Yes	Low
External Magnet	Medium	Yes	High
Hybrid Magnet	High	Yes	Low

2.1.3.4 Comparison of on-chip Bioassay methods

Electrochemical detection was previously proposed by Choi et al.[45]. This method has the advantage to avoid a complex optical detection system. The detection limit of such type of system still remains relatively limited compared to optical methods, while integration of electrical detectors on-chip increase the fabrication process complexity. Non-fluorescent optical detection is generally performed for agglutination assays. Detection of aggregates for agglutination tests using small magnetic particles (typical below 500 nm) is usually performed using a turbidity measurement. This method is in general not readily applicable on-chip after

retention of the magnetic particles, as the particles have to be uniformly suspended in the medium. Moreover, for particles typically larger than 500 nm, this method does not apply as the diameter is larger than the wavelength of the light. On-chip agglutination was already detected using image treatment by counting the number of particles after field removal. This approach is mainly restricted to a lab environment because an automation of this protocol remains critical as a relatively large number of images have to be taken and analyzed to obtain valuable statistical results. The implementation of a simple method for on-chip biological detection is therefore of interest. The integration of heterogeneous assays on-chip has led to a shortening in the assay time and improvement of the detection limit compared to standard off-chip assays. Nevertheless, commercialization of such systems remains difficult. One reason for that is the need of a high number of different liquids (sample, washing buffer, detection buffer, etc.) to perform the assay on-chip, which involves complex handling of the fluids during experiment. On-chip integration of a homogeneous assay is therefore a good alternative to reduce the complexity of an on-chip protocol. Table 2.3 gives an idea of the reduction in complexity of a homogeneous assay compared to a heterogeneous assay on-chip.

Table 2.3 Comparison of homogenous and heterogeneous bioassay using magnetic particles

Strategy	Additional Tagging	Washing Steps	Sensitivity
Heterogeneous	Yes	2	Good
Homogeneous	No	0	NA

2.1.4 Overview of Magnetic Microfluidic Strategy

The development of magnetic micro/nanoparticle-based systems is gaining interest and a simple dynamic actuation system for superparamagnetic beads in a flow is clearly of interest. The importance to simplify on-chip protocols is important to reach the goal of simple devices for

point-of-care testing. The large majority of bioassays on-chip is nowadays based on heterogeneous assays requiring iterative separation and washing steps. Implementing a single step test on-chip is of interest especially for the simplification of the chip integration and the test protocol. In order to enhance the detection limits of such assay on a chip, critical phenomenon such as diffusion limitation needs to be overcome. The main concept of our device is summarized earlier in Figure 1.3. First of all, our system has to provide a fast and efficient mixing and separation method to pre-concentrate the magnetic nanoparticle tagged target biomolecules from the buffer solution. In a second step, the magnetic biomolecule needs to be focused on the sensor surface. The magnetic actuation has to be perpendicular to the flow direction in order to increase the probability for an antibody to encounter a magnetic tagged biomolecule (Antigen). An efficient detection system coupled with fast dynamic actuation of superparamagnetic particles on-chip is of primary interest for many kinds of bioassays on-chip. Optimization of the detection and actuation of the magnetic nanoparticles tagged biomolecules is therefore an important part of this thesis.

2.2 Magnetic Microfluidics Theory & Concepts

2.2.1 Magnetic Particles

Magnetic micro- and nanoparticles are of particular interest for Lab-on-a-chip applications. One of the main reasons is their ability to be manipulated in a fluid flow as well as the possibility to functionalize them with a large range of biomolecules. Moreover, by reducing the size of the particles, the available active surface per volume may be significantly increased. In this section, theoretical aspects of the main concepts behind the manipulation of magnetic particles in fluids are discussed. Magnetic particles are usually made of magnetic nanocrystals enclosed in a non-magnetic matrix of an inert and bio-compatible material such as a polymer or silicon dioxide[37]. The nanocrystals are generally composed of iron oxide such as maghemite (Fe_2O_3) or magnetite (Fe_3O_4) but they can also be made of alloys of transition metals (Ni, Fe, Co, Mg or Zn) or rare earth materials (NdFeB or SmCo). Iron oxide is preferred over pure iron due to its better stability against oxidation. Magnetite and maghemite are frequently chosen because they have the highest saturation magnetization, 80 and 100 $\text{Am}^2\text{kg}^{-1}$ respectively, which are two orders of magnitude higher than the saturation magnetization of other iron oxides. To understand the magnetic behavior of magnetic beads, it is important to refer to the basics of magnetism.

2.2.1.1 Properties of Magnetic Micro/Nanoparticles

2.2.1.1.1 *Types of magnetic materials*

Magnetic materials can be generally classified into five types of magnetism, depending on their bulk magnetic susceptibility (see Figure 2.4 and Table 2.4).


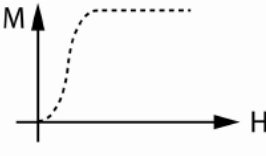
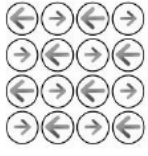
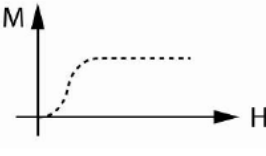



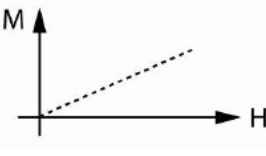


1 H																	2 He						
		<div style="display: flex; justify-content: space-around; align-items: center;"> <div style="border: 1px solid black; width: 15px; height: 15px; background-color: lightblue; margin-right: 5px;"></div> Ferromagnetic <div style="border: 1px solid black; width: 15px; height: 15px; background-color: lightpurple; margin-left: 20px; margin-right: 5px;"></div> Antiferromagnetic </div> <div style="display: flex; justify-content: space-around; align-items: center; margin-top: 5px;"> <div style="border: 1px solid black; width: 15px; height: 15px; background-color: white; margin-right: 5px;"></div> Paramagnetic <div style="border: 1px solid black; width: 15px; height: 15px; background-color: lightgreen; margin-left: 20px; margin-right: 5px;"></div> Diamagnetic </div>																					
3 Li	4 Be																	5 B	6 C	7 N	8 O	9 F	10 Ne
11 Na	12 Mg																	13 Al	14 Si	15 P	16 S	17 Cl	18 Ar
19 K	20 Ca	21 Sc	22 Ti	23 V	24 Cr	25 Mn	26 Fe	27 Co	28 Ni	29 Cu	30 Zn	31 Ga	32 Ge	33 As	34 Se	35 Br	36 Kr						
37 Rb	38 Sr	39 Y	40 Zr	41 Nb	42 Mo	43 Tc	44 Ru	45 Rh	46 Pd	47 Ag	48 Cd	49 In	50 Sn	51 Sb	52 Te	53 I	54 Xe						
55 Cs	56 Ba	57 La	72 Hf	73 Ta	74 W	75 Re	76 Os	77 Ir	78 Pt	79 Au	80 Hg	81 Tl	82 Pb	83 Bi	84 Po	85 At	86 Rn						
87 Fr	88 Ra	89 Ac	↓																				
			58 Ce	59 Pr	60 Nd	61 Pm	62 Sm	63 Eu	64 Gd	65 Tb	66 Dy	67 Ho	68 Er	69 Tm	70 Yb	71 Lu							

Figure 2.4 Table of elements indicating the magnetic properties of the element in their solid state

Magnetism originates from the spin as well as from the orbital motion of an electron around the nucleus [179]. The circulating electron produces its own orbital magnetic moment and there is also a spin magnetic moment associated with it due to the electron itself spinning on its own axis. In most materials there are almost no resultant magnetic moments, due to the electrons being grouped in anti-parallel pairs causing the magnetic moment to be cancelled (i.e. diamagnetism and paramagnetism). Diamagnetism originates from the orbital motion of electrons about the nuclei, electromagnetically induced by the application of an external magnetic field. This type of magnetism is very weak and easily overruled by paramagnetism of atoms. The paramagnetism originates from magnetic atoms or ions whose spins are isolated from their magnetic environment. This type of magnetism is also relatively weak and therefore diamagnetic and paramagnetic materials are generally referred as non-magnetic materials. In certain magnetic materials the magnetic moments of a large proportion of the electrons align, producing a macroscopic magnetization (ferromagnetic materials). Finally, magnetic materials can also be

ferrimagnetic which is generally found in compounds, such as mixed oxides, known as ferrites, from which ferrimagnetism derives its name. Table 2.4 summarized the different types of magnetic materials in the bulk form. The first three schematic representations of the magnetic moments in Table 2.4 correspond to a temperature of 0 K (i.e. ideal alignment of the electron spins). Above this temperature, the alignment of the spins is somewhat random but keeps a preferential direction. Above the Curie temperature T_c , the thermal fluctuations are so large that the spins orientation is completely random and the total magnetic moment falls to zero. Above the Curie temperature the material behaves like a paramagnetic material. Table 2.4 shows that the magnetic character of a material may be classified using its relative magnetic susceptibility χ_r . In order to easily manipulate a magnetic particle, the magnetic force acting on the latter has to be maximized; a high relative permeability of the material is therefore required. Consequently, the majority of the magnetic beads are made of ferro- or ferrimagnetic materials. For this reason, the following part of this section will focus on the ferromagnetic materials.

Table 2.4 Overview and Comparison of different types of Magnetism

Magnetism Type	Atomic and Magnetic Behavior		Susceptibility (χ_r)
Ferromagnetism			Atoms have parallel aligned magnetic moments within domain - large $ \chi_r \gg 1$ - positive Fe, $\chi_r = \sim 100'000$
Ferrimagnetism			Anti-parallel aligned magnetic moments of different types of atom do not cancel completely - large $ \chi_r \gg 1$ - positive ferrite, $\chi_r = \sim 1'000$
Antiferromagnetism			Atoms have parallel and anti-parallel magnetic moments aligned in a regular pattern - small $ \chi_r \ll 1$ - positive Cr, $\chi_r = 3.6 \cdot 10^{-6}$
Paramagnetism			Atoms have randomly oriented magnetic moments Negligible interaction between atomic magnetic moments - small $ \chi_r \ll 1$ - positive Mn, $\chi_r = 66.1 \cdot 10^{-6}$
Diamagnetism			Atoms have no magnetic moments - small $ \chi_r \ll 1$ - negative Au, $\chi_r = -2.74 \cdot 10^{-6}$

The magnetization \vec{M} of a magnetic material under an external magnetic field \vec{H} is given by:

$$\vec{M} = \chi_r \cdot \vec{H} \quad (2.5)$$

with χ_r the relative susceptibility of the material. The induced magnetic flux density $\vec{B} = \mu_0 \vec{H}$ is

increased by the magnetization \vec{M} of the material by $\mu_0 \vec{M}$ resulting in:

$$\vec{B} = \mu_0 (\vec{H} + \vec{M}) \quad (2.6)$$

Where $\mu_0 = 4\pi \cdot 10^{-7} \text{Vs} / \text{Am}$ is the permeability constant of vacuum. Combining Eqs. 2.5 and 2.6 gives:

$$\vec{B} = \mu_0(1 + \chi_r)\vec{H} = \mu_0\mu_r\vec{H} \quad (2.7)$$

where μ_r is the relative permeability of the material. The relative permeability is dependent upon the temperature and the frequency of the applied external magnetic field \vec{H} .

2.2.1.1.2 *Ferromagnetic materials*

In ferromagnetic materials, the relationship between the three vector fields ($\vec{H}, \vec{M}, \vec{B}$) is generally non-linear and history-dependent. Therefore, Eq.2.7 does not generally apply for a magnetic material; except for the initial magnetization of the material (see Figure 2.5). Ferromagnetic materials are characterized by a hysteresis loop as schematically shown in Figure 2.5. A hysteresis loop is defined by the saturation magnetization, the coercive field H_c and the remanent magnetization M_r . If the ferromagnetic material is magnetized up to its saturation from the initial state and then the magnetic field is switched off, a remanent magnetization M_r is observed. A negative coercive field H_c has to be applied to cancel the magnetization of the material. The three parameters (H_c, B_r and M_{sat}) allow describing the non-linear response of a ferromagnetic material to an external magnetic field. When a ferromagnetic material is subject to an external field, domains, having a magnetization parallel to the field, grow until reaching full magnetization (saturation) [180]. The initial permeability μ_{in} and susceptibility χ_{in} is defined by the initial induction B produced in response to an external field H :

$$\mu_{in} = 1 + \chi_{in} = \left. \frac{\delta B}{\delta H} \right|_{H \approx 0} \quad (2.8)$$

The hysteresis in the magnetization process of ferromagnetic materials can be explained by pinning of magnetic domains at impurities or grain boundaries within the material and the anisotropy of the crystalline lattice.

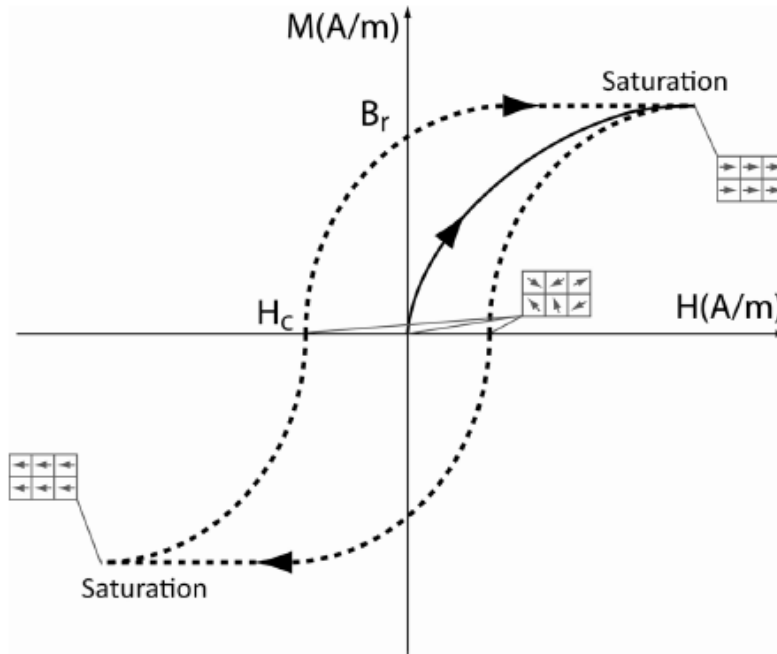


Figure 2.5 Magnetic hysteresis loop of a ferromagnetic material

2.2.1.1.3 Superparamagnetic material

A magnetic domain is a microscopic region in which the magnetic moments of atoms are grouped together and aligned. Figure 2.6 shows a picture of the magnetic domains in an iron whisker and in a thin NiFe element taken using a magneto-optical method [180]. The magnetic domain size may vary from less than ten nanometers to a few hundreds of micrometers depending on the magnetic anisotropy of the material. Prior to the exposure to an external magnetic field, a ferromagnetic material is usually unmagnetized, reflecting the randomization of the distribution of the magnetic domains.

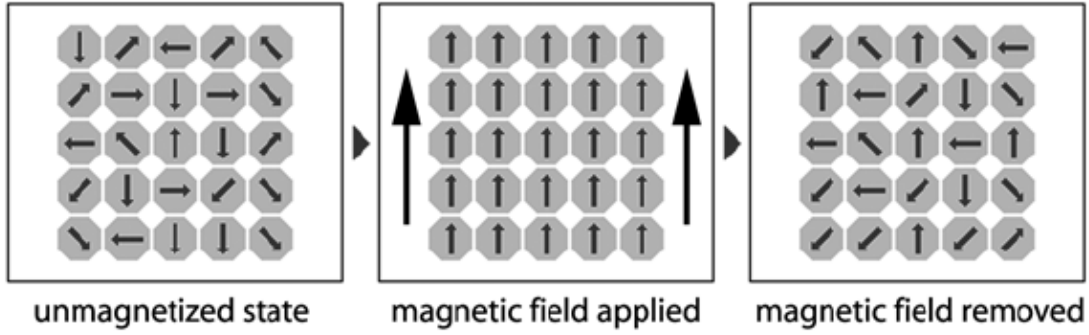


Figure 2.6 Superparamagnetic behavior of a group of a freely suspended ferromagnetic nanocrystals (<10 nm) in the absence and presence of an external magnetic field

Mono-domain nanoparticles are of particular interest for Lab-on-a-chip applications. They are single domain because they have a dimension that is typically of the order or smaller than the typical thickness of a magnetic domain wall. Mono-domain magnetic particles become superparamagnetic, i.e. their time-averaged magnetization without external magnetic field is zero when their magnetic energy is lower than about ten times the thermal energy $k_B T$, with k_B the Boltzmann constant. At room temperature, $k_B T = 4.0 \cdot 10^{-21}$ J and $K = 13.4$ kJ/m³ for maghemite (Fe₂O₃) nanoparticles [180, 181]. Therefore, finding the magnetic energy of magnetic particle using Eq. 2.9;

$$E_{mag} = \frac{4}{3} K \pi r^3 \quad (2.9)$$

We can find the maximum diameter $d_s = 18$ nm for a superparamagnetic spherical particle of maghemite. The time over which the magnetization of a particle is stable and remains in a certain state is of importance for probing the fundamental mechanism of magnetization reversal. The relaxation time τ of the moment of a particle is given by the Néel-Brown expression.

$$\tau = \tau_0 \exp\left(\frac{K \cdot V}{k_B T}\right) \quad (2.10)$$

where V is the volume of the particle and $\tau_0 \approx 10^{-9} s$. If the particle magnetic moment reverses at times shorter than the experimental time scales, the system is in a superparamagnetic state, if not, it is in the so-called blocked state [182]. Figure 2.7 gives a qualitative illustration of the behavior of the coercive field of magnetic nanoparticles as a function of their size. Particles are superparamagnetic below the critical superparamagnetic size d_s (i.e. $H_c=0$). Below d_s the thermal energy is larger than the magnetic energy and therefore the spin of the particle is free to rotate in response to the thermal energy. For particles larger than d_s , the coercive field increases to maximum at the single domain size limit d_c . Above d_c , the formation of domain walls becomes energetically favorable which results in a multi-domain structure of the particle and a decrease of the coercive field H_c .

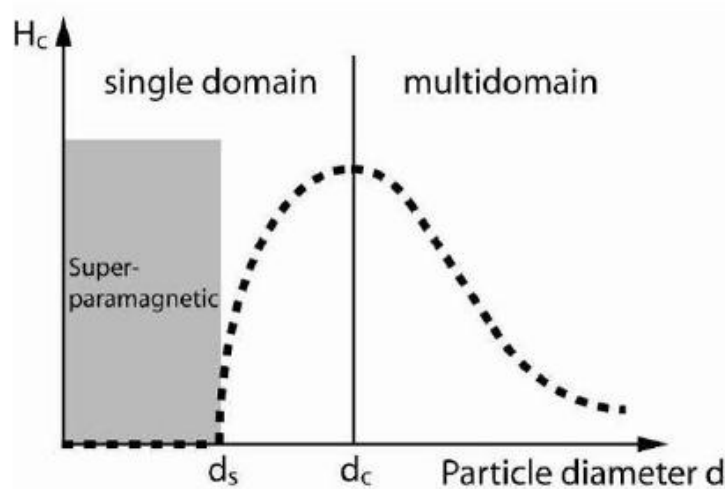


Figure 2.7 Qualitative illustration of the behavior of the coercivity as the magnetic particle size increase [183]

The majority of the magnetic nanoparticles consist of superparamagnetic nanocrystal embedded in a polymer matrix protecting the analyte from a direct contact with the metal oxide. Figure 2.8 illustrates the behavior of such multi-core superparamagnetic particles. Without an external magnetic field the magnetic moments of the iron oxide nanocrystals are randomly oriented

(Figure 2.8a). Under the application of an external magnetic field, all moments align in a preferential direction (Figure 2.8b). After switching off the external field, the particles returns to their initial state (Figure 2.8a) without having any remanence, A schematic hysteresis-free magnetization curve of a superparamagnetic bead is shown in Figure 2.8c.

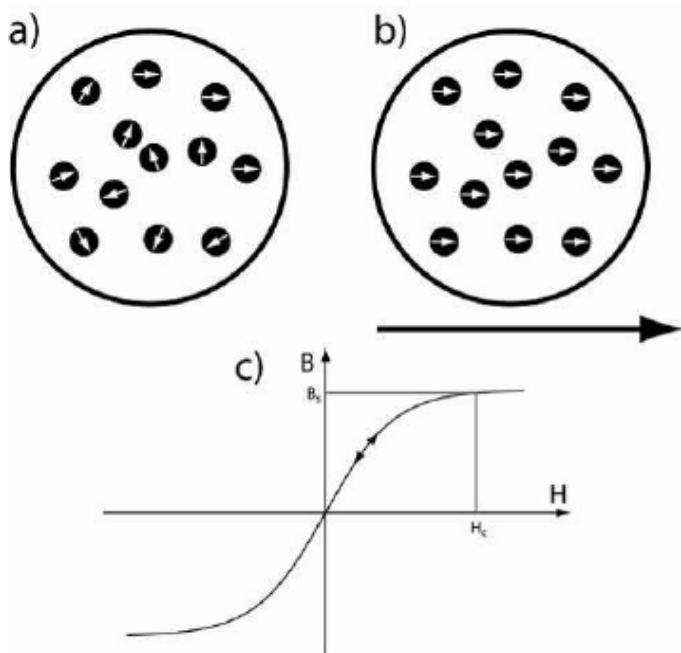


Figure 2.8 (a) Schematic representation of superparamagnetic particles at zero magnetic fields, (b) Under presence of external magnetic field, the nanoparticles moments align in the preferential direction, (c) Hysteresis free variation of B with changing H for superparamagnetic particles [182].

The benefits associated with hysteresis free superparamagnetic particles is that magnetization in absence of magnetic field helps is zero therefore in the absence of magnetic field they stay suspended in carrier liquid without agglomerating which helps in easy removal or capture of tagged biomolecules of interest. The advantage of using a polymer shell consists in the possibility of surface functionalization and subsequent immobilization of a target molecule[182]. Figure 2.9 shows the three main morphologies of composite magnetic polymer microspheres commonly used for Lab-on-a-chip applications. The magnetic particles may be composed of a

single magnetic core surrounded by an inert and preferably biocompatible material. This method is generally used for nanometer-sized superparamagnetic particles with diameters in the range of 5 – 100 nm. For the synthesis of larger superparamagnetic particles (in the range 300 nm – 10 μm), nanoparticles (generally $r < 10$ nm) are embedded in a non-magnetic polymer matrix (Figure 2.9b). An alternative method called “strawberry type” consists in assembling the magnetic nanoparticles around a polymer core and then passivating the surface using a surrounding inert polymer (Figure 2.9c). Figure 2.9d is a Scanning Electron Microscope (SEM) photograph of monodisperse magnetic beads (2.8 μm Dynabeads). Different procedures are available for the preparation and functionalization of nanocomposite microspheres [183] which is also illustrated in Figure 2.10.

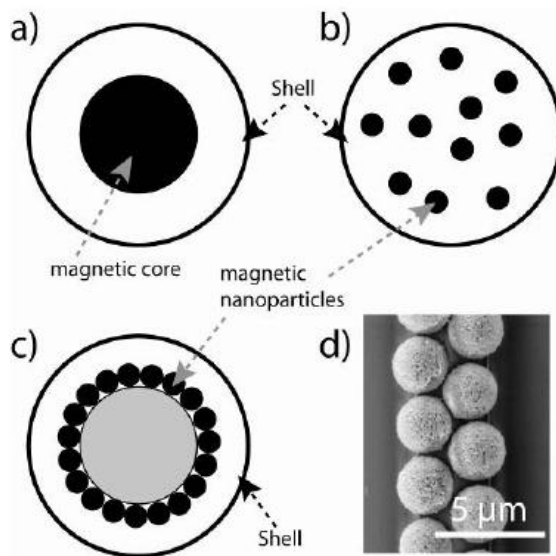


Figure 2.9 Three main methods of synthesizing magnetic particles for lab-on-a-chip applications. (a) Single magnetic core, (b) multi-core magnetic beads composed of magnetic nanocrystals, (c) magnetic nanoparticles assembled around polymer core (strawberry), (d) SEM image of a monodisperse magnetic particle (2.8 μm) [182]

In general the magnetic moment \vec{m} of a bead with negligible interaction between the nanoparticles is given by the sum of the moments of all individual nanoparticles enclosed in the polymer shell.

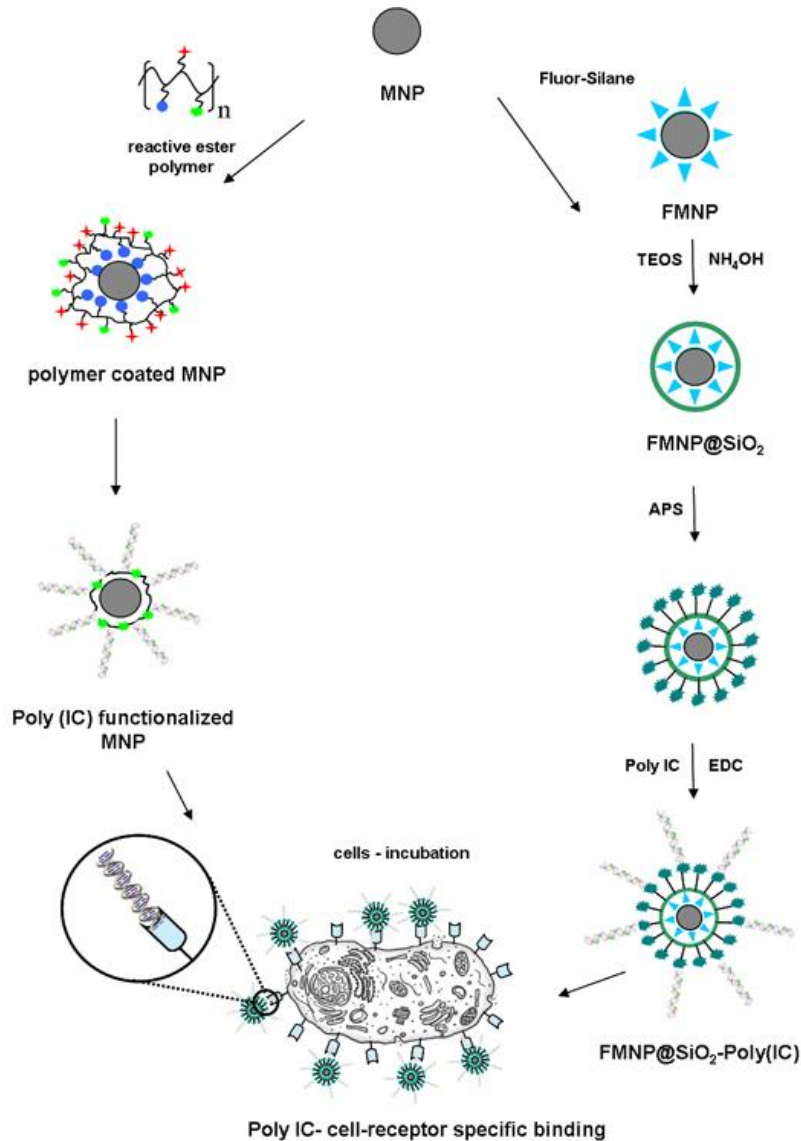


Figure 2.10 Selected functionalization routes for magnetic nanoparticles
 (Ref: <http://www.ak-tremel.chemie.uni-mainz.de/236.php>)

The magnetic moment of the composite microspheres is therefore directly related to the amount of magnetic nanoparticles in the matrix. Current techniques allow a filling factor up to $\sim 70\%$ (w/w) of Fe_3O_4 and a high saturation magnetization of $40 \text{ Am}^2\text{kg}^{-1}$ while keeping a

superparamagnetic behavior. Various types and sizes of magnetic nanoparticles can be synthesized from magnetic materials. The choice of the magnetic nanoparticles is finally dependent upon the final applications. The size of the particles is a critical parameter and may lead to the choice of a specific type of magnetic particles (i.e. single core, multicore or strawberry). The magnetic force F_{mag} is proportional to r^3 while the viscous drag force on the bead is directly proportional to its radius. Therefore decreasing the size of the bead decreases the ratio between the magnetic force and the viscous drag force, thus reducing the capacity to manipulate the particles in a liquid. Bigger particles can be manipulated easier but increasing the size reduces the surface-to-volume ratio resulting in a decrease of the specific surface available for the attachment of functional groups. The choice of the magnetic particle size is often a compromise between the biological and magnetic response therefore optimization studies needs to be performed in order to identify the correct size of magnetic particles for particular applications.

2.2.1.2 Magnetic forces on magnetic micro/nanoparticles

2.2.1.2.1 Magnetization of superparamagnetic particles

The force, F_{mag} acting on a single superparamagnetic bead, when it has acquired a magnetic moment \vec{m} in an external magnetic induction \vec{B} , is given by [61];

$$F_{mag} = (\vec{m} \cdot \nabla) \vec{B} \quad (2.11)$$

The above equation is mostly used as the basic equation for the calculation of the magnetic force, when \vec{m} is constant and has no spatial dependence, Eq 2.11 can be re-written as;

$$F_{mag} = \nabla (\vec{m} \cdot \vec{B}) \quad (2.12)$$

Figure 2.11 shows the magnetization curve of Dynabeads MyOne. Three typical regions may be distinguished. The first region is typically between 0 mT up to 10 mT, when the magnetization of

the bead is proportional to the applied magnetic flux (Figure 2.11a). In the second region the variation of magnetization of the bead is not linear with the applied magnetic flux (Figure 2.11b). The last region corresponds to saturation and therefore the magnetization of the bead is almost constant (Figure 2.11c)

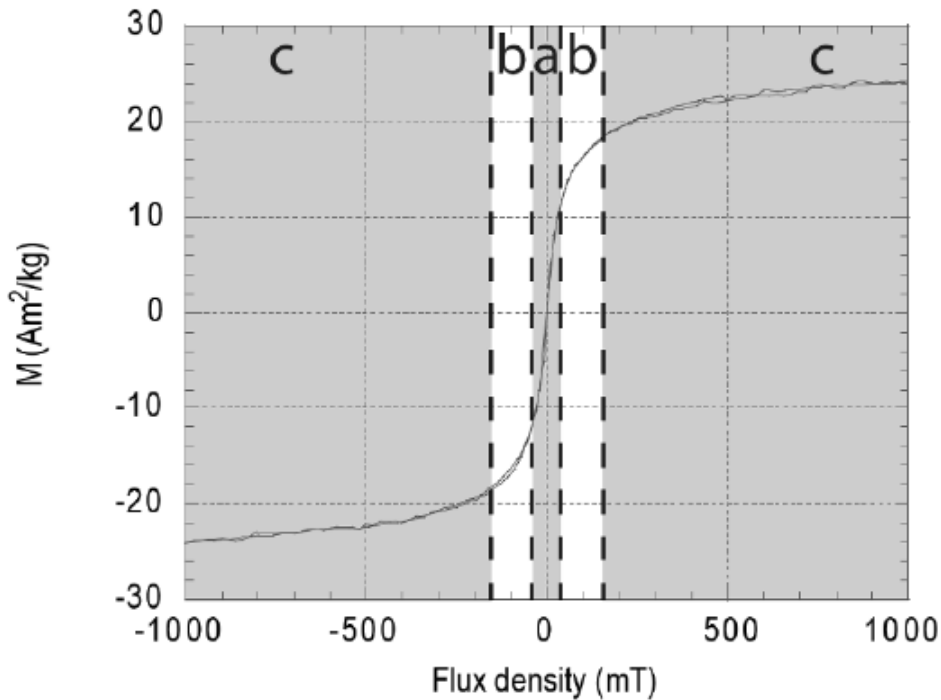


Figure 2.11 Magnetization curve of a Dynabead MyOne.

In general, the magnetization \vec{m} of the particle moving in the field is varying due to a spatially non-uniform magnetic field \vec{B} and an analytical solution of Eq.2.11 is non-trivial. Discussions of the force on magnetic dipoles or particles have been reported[29, 37], but, for our case, it is sufficient to consider two approximations: (i) weak magnetic fields where the size of the magnetic moment m of the bead is proportional to the size of the magnetic induction B (Figure 2.11a) and (ii) stronger fields where the bead moments are saturated (Figure 2.11c). In the linear region (i) of the magnetization curve, the magnetic moment of a bead in a liquid medium can be written in the following form:

$$\vec{m} = V \left(\frac{\Delta\chi}{\mu_0} \right) \vec{B} \quad (2.13)$$

where $\Delta\chi$ is the difference in susceptibility between the particle and the medium, V is the particle volume and μ_0 is the vacuum permeability. The magnetic moment \vec{m} of a non-saturated magnetic particle freely moving in a non-uniform field has the same spatial dependence as \vec{B} using standard vector calculation, we can write Eq.2.11 in the following form

$$\vec{F}_{mag} = (\vec{m} \cdot \nabla) \vec{B} = V \left(\frac{\Delta\chi}{2\mu_0} \right) \nabla \vec{B}^2 \quad (2.14)$$

The relative susceptibility of a single bead is influenced by the demagnetization factor and is therefore given by:

$$\chi_{eff} = \frac{\chi_{np}}{1 + N_d \chi_{np}} \quad (2.15)$$

where χ_{np} is the magnetic susceptibility of the nanoparticles material and N_d the demagnetization factor. The demagnetization factor is 1/3 for a spherical bead ($N_d = 1/3$). The concept of manipulating magnetic particles for LOC applications consists in using magnetic forces to transport or simply retain magnetic particles in a flow by overcoming the viscous drag force acting on the bead. Four main forces act on a magnetic bead suspended in a liquid medium, the magnetic force F_{mag} , the viscous drag force F_d , the gravity force F_g and the buoyancy force F_{buo} , as schematically shown in Figure 2.12. In general, due to the small size of the magnetic nanoparticles, the gravity force and buoyancy force may be neglected [184].

Therefore, the behavior of a magnetic bead in a liquid is mainly driven by the two opposite forces, the magnetic force F_{mag} , and the viscous drag force F_d . In equilibrium, i.e. at constant speed, we find:

$$\vec{F}_{mag} = -\vec{F}_d \quad (2.16)$$

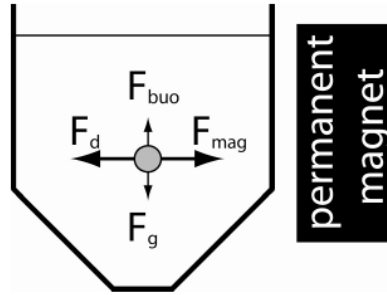


Figure 2.12 Schematic illustration of forces acting on magnetic particles in a solution exposed to magnetic field.

The drag force exerted on a magnetic nanoparticle is directly related to the flow conditions and the size of the particles. The flow conditions are linked to the Reynold's number Re , a dimensionless parameter, defined as the ratio between inertial and viscous forces,

$$Re = \frac{\text{inertial forces}}{\text{viscous forces}} = \frac{\rho a v}{\eta} \quad (2.17)$$

where a is a characteristic dimension, which may be the radius of a particles and $\rho/\eta = 1.004 \cdot 10^{-6}$ m^2/s . The flow is laminar for $Re < 2100$, where viscous forces dominate upon inertial forces. In this regime, all fluid elements move deterministically along distinct and traceable stream lines, while the turbulent regime, occurring at higher Reynolds numbers, is characterized by a random transverse motion of fluid with respect to the flow direction. The transition from one regime to the other is progressive and not clearly defined, creating a zone corresponding to a transitional regime. The Stokes flow is a particular regime of laminar flows for $Re \ll 1$. For this type of flow, the inertial forces can be neglected compared to the viscous forces, simplifying in this way the Navier-Stokes equation. As an example, a bead with a diameter of $1 \mu m$ moving at 10 mm/s using Eq.2.17 has a Reynold's number $Re = 0.5 \cdot 10^{-2}$. In these particular conditions, the viscous force on a spherical magnetic particle is given by the following equation:

$$\vec{F}_d = 6\pi\eta a\Delta\vec{v} \quad (2.18)$$

where $\Delta\vec{v}$ is the velocity of the magnetic particle with respect to the liquid medium, η is the viscosity of the medium and a the radius of the particles.

2.2.2 Microfluidics Theory

Microfluidics deals with the behaviour, precise control and manipulation of micro-litre and nano litre volumes of fluids. It is a multi-disciplinary field comprising physics, chemistry, engineering and bio-technology, with practical applications to the design of systems in which such small volumes of fluids will be used. Ascribed to the micron dimensions, microfluidics has some special characteristics such as high surface-to-volume ratio, high mass-heat transfer rate, high shear-extension rate, and low Reynolds number. Therefore, in order to understand the behaviour of micromixers, a reasonable knowledge of the theory of microfluidics is necessary. In this section a brief introduction to microfluidics and some of the key definitions is presented together with the concept of Residence Time Distribution (RTD) analysis.

2.2.2.1 Newtonian fluid

A fluid is called Newtonian when the shear stress induced by the viscosity of the fluid is directly proportional to the strain gradient:

$$\tau = \mu \frac{du}{dy} \quad (2.19)$$

The constant of proportionality μ , is the dynamic viscosity coefficient of the fluid. Water, the fluids of interest in this research, is a Newtonian fluid.

2.2.2.2 Flow regime

Laminar flow, also known as streamline flow, occurs when a fluid flows in parallel streamlines, with no disturbance between the lines. In fluid dynamics, laminar flow is a flow regime associated with high momentum diffusion, low momentum convection, and velocity and pressure

independence from time. On the contrary, turbulence or turbulent flow is a flow regime characterized by chaotic, stochastic property changes. This implies lower momentum diffusion, higher momentum convection, and quick variations of velocity and pressure in time and space. Viscous forces dominate in a laminar flow regime, while inertial forces dominate in a turbulent flow regime.

2.2.2.3 Incompressible flow

Certain fluids undergo very little change in density despite the existence of large pressures. In such circumstances when density variation in a problem is inconsequential, the fluid is called incompressible and the density is treated as a constant value in computations. Water is an incompressible fluid and Table 2.5 lists the main characteristics of water in standard conditions of pressure and temperature.

Table 2.5 Properties of water at 20 °C and 1 atm

Density ρ	Dynamic viscosity μ	Kinematic viscosity ν
998 kg/m ³	1.0 × 10 ⁻³ kg/(m.s)	1.01 × 10 ⁻⁶ m ² /s

2.2.2.4 Navier-Stokes equations

The Navier-Stokes (N-S) equations are a set of fundamental differential equations that explain the motion of the fluid substances such as liquids and gases. These equations are derived from conservation principles (i.e., conservation of mass, momentum and energy) and are the governing constitutive equations of conventional flows. The vector form of the N-S equations for an incompressible Newtonian flow is:

$$\rho \frac{\partial u}{\partial t} + \rho(u \cdot \nabla)u = -\nabla p + \eta \nabla^2 u + F_{vol} \quad (2.20)$$

Where, u is the velocity field (m/s), p is the pressure in (N/m^2) and F_{vol} is the volume force

(N/m^3). The momentum transfer from MNPs to the fluid is incorporated by setting the volume force term equal to the magnetic force acting on a single MNP multiplied with MNP number density, α , which is the number of MNP per unit volume. Therefore, the volume force acting on fluid is given by;

$$F_{Vol} = \alpha F_m \quad (2.21)$$

Eq. 2.20 couples the fluid flow equation with the magnetic field equation and depends on the instantaneous concentration of MNP solution in the microchannel which is described in more detail in later sections. MNP number density (α) is calculated using equation 2.22.

$$\alpha = \frac{6CM_{Fe_3O_4} \times 10^{-3}}{\rho_m \pi D^3} \quad (2.22)$$

Where, C is the concentration of MNPs (μM), $M_{Fe_3O_4}$ is the molar mass of Fe_3O_4 (Nm^{-2}), ρ_m is the density of MNPs (Nm^{-2}), and $F_m D$ is the diameter of MNPs (Nm^{-3}). For example, a 50 nm diameter MNP will have a volume of $6.5 \times 10^{17} \text{ cm}^3$, if the density of MNP is assumed to be 2.5 g/cm^3 (Barnes et al. 2007), the mass of MNP will be $1.64 \times 10^{-16} \text{ g}$. We know that MNPs are composed of Fe_3O_4 having molar mass of 232 g/mol , so there will be $7 \times 10^{-19} \text{ mol}$ per MNP or $4 \times 10^5 \text{ Fe}_3\text{O}_4$ per MNP, because 1 mol of Fe_3O_4 has $6.023 \times 10^{23} \text{ Fe}_3\text{O}_4$ molecules (Avogadro's number). If we know the MNP concentration which can be calculated from convection and diffusion equation of the model than we can calculate the number of MNPs per unit volume based on above computation. Therefore, for 50nm MNPs having an instantaneous concentration of $1 \mu M$ α was approximately 10^{15} MNPs/m^3 . Similar calculations are carried out for different sizes of MNPs using the generalized equation 2.22. It is also assumed that there is no particle-particle interaction (e.g.: Van der Waals forces) and even

the sedimentation effects will have negligible influence on the overall mass transport due to extremely small size of MNPs.

2.2.2.5 Steady flow

A flow is called steady when flow characteristics (e.g., velocity components) and thermodynamic properties at each position in space are invariant with time. Individual fluid particles may move, but at any particular position in domain, such particle behaves just like as any other particle when it was at that point. There is no time dependency in parameters for steady flow equations ($d/dt=0$).

2.2.2.6 No-slip condition

When a fluid flow is bounded by a solid surface, molecular interactions cause the fluid in contact with the surface to seek momentum and energy equilibrium with that surface. All liquids essentially are in equilibrium with the surface they contact. Then, all fluids at a point of contact with a solid take on the velocity of that surface which means the fluid relative velocity at all liquid-solid boundaries is zero ($V_{\text{fluid}}=V_{\text{wall}}$). In other words, the outermost molecule of a fluid sticks to surfaces past which it flows. This is called the no-slip condition and serves as the boundary condition for analysis of the fluid flow past a solid surface.

2.2.2.7 Residence Time Distribution (RTD) Analysis

The Residence-time distribution (RTD) curve is obtained by injecting a MNP solution for a very short time interval (Dirac pulse) at the inlet of the microchannel, and then the concentration of MNP at the outlet is recorded as a function of time. The RTD function also known as exit age-distribution $E(t)$ is defined quantitatively. The $E(t)$ function basically tells quantitatively, how much time different fluid elements have spent in a continuous flow system such that $E(t) \cdot dt$ is the fraction of MNP solution exiting the microchannel that have spent a time between t and

$t + dt$ in the microchannel [185, 186]. The RTD function, $E(t)$ is given by Eq.2.23, where $C(t)$ is the MNP solution concentration at the outlet, as a function of time. The MNP concentrations are recorded at different y-points along the outlet of microchannel and then average value is used as $C(t)$.

$$E(t) = \frac{C(t)}{\int_0^{\infty} C(t)dt} \cong \frac{C(t_i)}{\sum_{i=0}^{\infty} C(t_i) \cdot \Delta t_i} \quad (2.23)$$

where, $\Delta t_i (= t_{i+1} - t_i)$ is the time steps used in the simulation.

After the RTD function is obtained, parameters that are used to quantify the mixing performance are calculated based on the methods given in literature[186]. These statistical parameters are mean residence time t_m , which gives the average time the exiting fluid element spend in the microchannel; variance σ^2 , which is the measure of the spread of the distribution; and coefficient of variance or normalized variance, which provides the relative standard deviation of the distribution. These statistical parameters are mathematically given by equations 2.24-2.26.

$$t_m = \frac{\int_0^{\infty} tE(t)dt}{\int_0^{\infty} E(t)dt} = \int_0^{\infty} tE(t)dt \cong \sum_{i=0}^{\infty} tE(t)\Delta t \quad (2.24)$$

$$\text{since } \int_0^{\infty} E(t)dt = 1$$

$$\text{Variance} = \sigma^2 = \int_0^{\infty} (t - t_m)^2 E(t)dt \cong \sum_{i=0}^{\infty} (t - t_m)^2 E(t)\Delta t \quad (2.25)$$

$$\text{Normalized Variance} = \frac{\sigma^2}{t_m^2} \quad (2.26)$$

The RTD of the microchannel with magnetic actuation will deviate from an ideal plug flow mixer depending on the magneto-hydrodynamics with the microchannel. Based on computation a variance of zero would mean complete plug-flow mixing while a non-zero value will imply mixing due to non-uniform or laminar velocity and molecular diffusion. Mixing performance for all the conditions including magnetic and no magnetic field assisted mixing will be computed, compared and optimized conditions will be predicted in this thesis.

3. DESIGN & ANALYSIS

3.1 Magnetic Nanoparticle Enhanced Mixing using Time Dependent Magnetic Field

3.1.1 State of the Art

Lab-on-a-chip system that constitutes of microfluidics and nanotechnology has played a major role in recent years in shrinking the size of conventional lab-scale biological and chemical analysis to chip-format often referred to as micro-total-analysis-systems (μ TAS). These miniaturized systems offer many advantages such as rapid analysis, reduced sample and reagent volume, smaller device size for point-of-care applications and overall low cost of fabrication and development. Lab-on-a-chips are now being realized for various applications such as clinical analysis, DNA analysis, proteomics analysis, forensic analysis, immunoassays, and toxicity monitoring [4, 5, 172, 187, 188]. Nevertheless, the development of such microfluidic lab-on-a-chip system has its share of difficulties. The characteristic laminar flow regime that occurs in microscale channels makes mixing a very challenging operation and therefore needs to be addressed.

In a typical microfluidic device, mixing of two or more fluids mainly occurs by molecular diffusion, which is often much slower than convection and limits reaction times, biomolecule accumulation times and overall, separation or detection sensitivities of the devices. Therefore external or internal fluid manipulation techniques are required to enhance mass transfer and consequently mixing in microfluidic systems. Numerous experimental and theoretical studies have been published [69, 76, 189, 190] to evaluate designs and strategies. Such strategies include for instance: internal passive mixing by disturbing the fluid flows with microchannel structures[99] or by splitting and injecting the fluid flows[84, 191-193], or by confining the species in droplets[18, 19, 194, 195]. Some of the external active mixing strategies include fluid

actuation by inducing energies including electrical [119, 196-199], acoustic [200], mechanical [104, 105], ultrasonic [111] or thermal [201] in the microchannel. Although these strategies have produced excellent results, they are often difficult to fabricate or integrate. Moreover, some form of energies especially the electrical potentials applied for mixing can damage or alter the properties of the fluid solution containing cell, biomolecules or DNA [202]. Magnetic micro/nanoparticles have shown immense potential and can be advantageously tagged with biomolecule of interest for further separation and detection [41, 52, 132]. Few studies have shown that magnetic particles can also be used to enhance the mixing of fluids in microchannel [122, 203] by using embedded planar conductors at the bottom of microchannels. Although these mixing studies are encouraging and interesting but require detailed parametric analysis and optimization based on orientation of electrodes, switching frequency, magnetic nanoparticle size, and flow velocities. The major difference of proposed method from other magnetic mixing scheme (including Suzuki et.al[122]) is the choice of magnetic particles deployed in the system. In this work, magnetic nanoparticles are preferred over magnetic microparticles or magnetic beads. Magnetic nanoparticle possess several advantages such as stability over time, high surface to volume ratio for chemical binding, minimum disturbance caused by the attached biomolecules because of their extremely small size. Moreover, as the intrinsic device size is shrinking, magnetic nanoparticles will be favored over microparticles so as to reduce clogging or blockage of small size channels. The most important property that makes them unique especially related to mixing is their superparamagnetic nature, i.e., their magnetization without a magnetic field is zero. This has important outcome for applications including micromixing or bio-analysis because superparamagnetic nanoparticles tagged to the biomolecule of interest can be removed or re-suspended into the system using a magnetic field without any agglomeration and therefore, it is

very easy to switch on and off the time-dependent magnetic field and overall enhance mixing. A time-dependent magnetic field will produce oscillation in magnetic nanoparticles causing agitation in the surrounding fluid and overall enhances the mixing process. This strategy is simple to implement and can be easily integrated into lab-on-a-chip devices.

3.1.2 Model Development

In this work both Species Concentration Distribution (SCD) analysis and Residence Time Distribution (RTD) analysis is used to characterize the time-dependent magnetic actuation technique for enhancing the mixing in a microfluidic system. A schematic representation of the microfluidic channel along with corresponding co-ordinates and dimensions is shown in Figure 3.1 together with copper electrodes for creating time-dependent magnetic field. The microchannel is 60 μm deep and 600 μm long. The electrodes present at the bottom of the microchannel are 40x40 μm with the length equal to the width of the microchannel. When current is passed through the electrodes, large magnetic field gradients together with magnetic forces are established in the microchannel. The magnetic force actuates the incoming magnetic nanoparticle solution and pulls the MNPs towards the electrodes. When the electrodes are switched off, MNPs again follow bulk flow direction. By periodically turning the current on and off in the electrodes, disturbance is produced in the flow path of MNPs causing agitation in the flow which enhances the mixing. The increased mixing performance will also increase the interaction of MNPs with the target molecules.

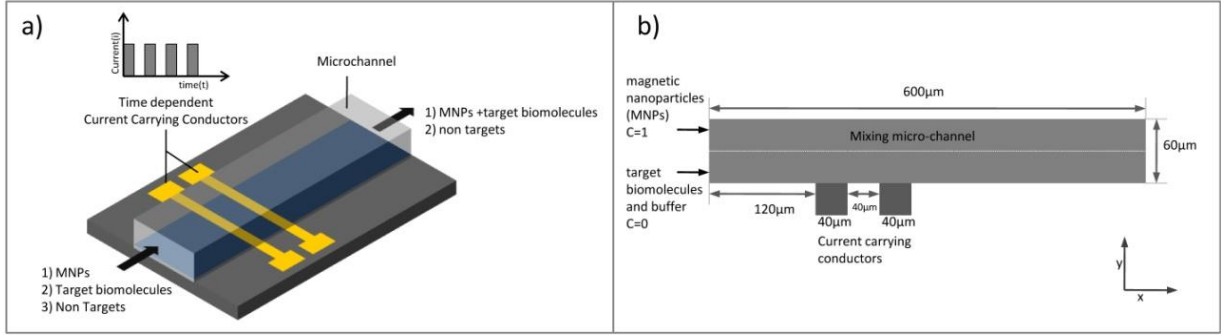


Figure 3.1(a) Schematic of time dependent magnetic micromixer, and (b) 2D axial cross-section of the microchannel with two inlets and one outlet.

Therefore, greater number of target biomolecules can be tagged with magnetic nanoparticles using conjugation chemistry [37] for further processing and analysis. The model geometry shown in Figure 3.1b is simplified two-dimensional schematic which focuses on the axial cross-section of the microchannel. Although a full three-dimensional model would be more accurate, the qualitative trend would still remain the same. For SCD analysis, two fluids are loaded in the microchannel via two inlets, the top half of the channel under consideration has a normalized concentration $C=1$ of magnetic nanoparticle solution whereas the bottom half consist of sample solution containing target biomolecules and buffer with a normalized concentration $C=0$. The total concentration of MNPs injected into the microchannel, $c=1\mu\text{M}$, which was kept constant throughout the model. In all the simulations, it is considered that MNP solution flows at a constant flow velocity from left to right with a laminar flow and for the model a parabolic flow profile is considered. It is considered that both the magnetic nanoparticle and sample solution is transported by convective flow towards the outlet and is also free to diffuse. In order to quantify the mixing performance using SCD analysis, a parameter called mixing efficiency (η_e) described by Eq. 3.1 is calculated.

$$\eta_e = \left(1 - \frac{C_{AVG} - C_\infty}{C_0 - C_\infty} \right) \times 100 \quad (3.1)$$

Where C_{AVG} is the average normalized concentration at the outlet, C_{∞} is the normalized concentration at the ideal (complete) mixing at the outlet, which will be 0.5 for our model, and C_0 is the unmixed normalized concentration of magnetic nanoparticle solution at the inlet, which is 1.0 for our model.

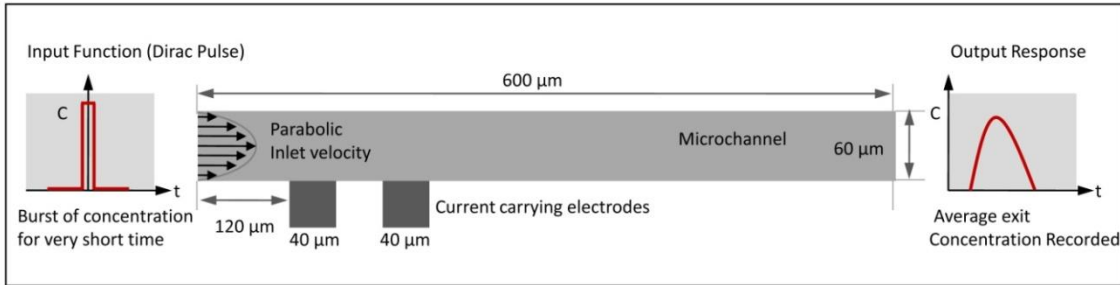


Figure 3.2 Schematic of 2D axial cross-section of microchannel with one inlet and one outlet for RTD analysis

For RTD analysis (see Figure 3.2), a solution containing MNPs enters from left and flows under laminar conditions with a parabolic inlet velocity. It is considered that the MNP solution is transported by convective flow towards the outlet and is also free to diffuse. The total concentration of MNPs equal to $1\mu\text{M}$ is injected into the microchannel and is kept constant throughout the model. In order to quantify the mixing performance, MNPs solution is injected for a very short time interval into the microchannel and the response function is recorded at the microchannel output. The equations and theory developed are based on Navier-Stokes equations for flow, convection and diffusion equation for concentration profiles, and Maxwell's equation for calculating the magnetic field. The finite element model basically solves the Maxwell's equation for time-dependent magnetic field. The computed magnetic field is coupled to fluid flow by using the magnetic volume force term acting on the nanoparticles in the Navier-Stokes equations. Finally, the concentration within the microchannel is computed using mass-transfer convection and diffusion equation. The detailed explanation of the equations and theory used in the model is described in more detail in the following sections.

3.1.2.1 Fluid Flow Equation

The magnetic nanoparticles (MNPs) of sizes ranging from 50-500 nm are assumed to be dispersed in the fluid of viscosity η ($10^{-3} \text{ kg / m} \cdot \text{s}$) and density ρ (10^3 kg / m^3) equal to that of water. The aqueous solution of MNPs is injected into the microchannel with a parabolic velocity. The early acceleration phase of MNPs within the fluid is neglected and therefore it is assumed that the MNP solution move with constant velocity. From calculation it was found that the time constant for the acceleration phase of MNPs is negligible for the scale of geometry and the size of particles used in the simulations, therefore it can be neglected and the liquid solution can overall be treated as continuum. The magnetic force acting on MNPs due to external magnetic field transfers momentum to the surrounding fluid leading to a disturbance in flow profile of carrier liquid. The flow velocity u for this incompressible fluid ($\nabla \cdot u = 0$) is described using Navier-Stokes equation,

$$\rho \frac{\partial u}{\partial t} + \rho(u \cdot \nabla)u = -\nabla p + \eta \nabla^2 u + F_{vol} \quad (3.2)$$

Where, u is the carrier fluid velocity field (m/s), p is the pressure (N/m^2), and F_{vol} is the volume force (N/m^3). The momentum transfer from MNPs to the fluid is incorporated by setting the volume force term equal to the magnetic force acting on a single MNP multiplied with MNP number density, α , which is the number of MNP per unit volume. Therefore, the volume force acting on fluid is given by;

$$F_{vol} = \alpha F_m \quad (3.3)$$

Eq. 3.3 couples the fluid flow equation with the magnetic field equation and depends on the instantaneous concentration of MNP solution in the microchannel which is described in more detail in later section. MNP number density (α) is calculated using equation 3.4.

$$\alpha = \frac{6CM_{Fe_3O_4} \times 10^{-3}}{\rho_m \pi D^3} \quad (3.4)$$

Where, C is the concentration of MNPs (μM), $M_{Fe_3O_4}$ is the molar mass of Fe_3O_4 (g/mol), ρ_m is the density of MNPs (g/cm^3), and D is the diameter of MNPs (cm). For example, a 50 nm diameter MNP will have a volume of $6.5 \times 10^{17} cm^3$, if the density of MNP is assumed to be $2.5 g/cm^3$ (Barnes et al. 2007), the mass of MNP will be $1.64 \times 10^{-16} g$. We know that MNPs are composed of Fe_3O_4 having molar mass of $232 g/mol$, so there will be 7×10^{-19} mol per MNP or $4 \times 10^5 Fe_3O_4$ per MNP, because 1 mol of Fe_3O_4 has $6.023 \times 10^{23} Fe_3O_4$ molecules (Avogadro's number). If we know the MNP concentration which can be calculated from convection and diffusion equation of the model than we can calculate the number of MNPs per unit volume based on above computation. Therefore, for 50nm MNPs having an instantaneous concentration of $1 \mu M$ α was approximately 10^{15} MNPs/ m^3 . Similar calculations are carried out for different sizes of MNPs using the generalized equation 3. It is also assumed that there is no particle-particle interaction (e.g.: Van der Waals forces) and even the sedimentation effects will have negligible influence on the overall mass transport due to extremely small size of MNPs.

3.1.2.1.1 *Boundary Conditions*

The flow of fluid at the inlet is assumed to be parabolic and moves in the direction of x-axis with zero velocity in y-direction. The average flow velocity of MNP solution is u_0 . No slip condition ($u = v = 0$) is applied along the walls of microfluidic system and at the outlet, pressure condition is set equal to zero.

3.1.2.2 Magnetic Field Equation

It is assumed that the magnetic field is described using Maxwell-Ampere's law given by;

$$\nabla \times H = J \quad (3.5)$$

Where H is the magnetic field vector (A/m) and J is the current density vector (A/m^2).

According to Gauss law for magnetic flux density, B (Vs/m^2)

$$\nabla \cdot B = 0 \quad (3.6)$$

In order to describe a relation between B and H a constitutive relation given by the following equation is used in the model.

$$B = \mu(H + M) \quad (3.7)$$

where μ is the magnetic permeability, and M is the magnetization vector. The magnetic permeability can also be expressed as $\mu_0\mu_r$, where μ_r is the relative permeability of integrated copper conductors ($\mu_r=1$) and is assumed to be constant in all the simulations, and μ_0 is the permeability in vacuum ($\mu_0 = 4\pi \times 10^{-7} N/A^2$). In order to solve Maxwell equations, the two first order partial differential equations given by Eqs. 3.5 and 3.6 are converted into a single second-order partial differential equation involving only one field variable called magnetic vector potential, A . The magnetic flux density B is represented by curl of the magnetic vector potential A according to the following equations

$$\nabla \times A = B; \nabla \cdot A = 0 \quad (3.8)$$

After substitution of Eq. 3.8 in equations Eqs. 3.4-3.7, the following vector equation is obtained:

$$\nabla \times \left(\frac{1}{\mu_0\mu_r} \nabla \times A - M \right) = J \quad (3.9)$$

It is assumed that the magnetic vector potential has a nonzero component only perpendicular to the plane A_z which basically simplifies the 2D; the externally applied current density J is calculated for the $40 \times 40 \mu\text{m}$ copper conductor. A square-shaped current with a set frequency is used to replicate the on/off behavior of current in the conductor. Heaviside step function of COMSOL (COMSOL AB., Stockholm, Sweden) is used to generate a square current pulse similar to the one produced by experimental pulse generator. The step function is expressed as $\text{flc2hs}(x, 0.1)$ and it smoothes within the interval $-0.1 < x < 0.1$. In order to implement time-dependent control signal for generating pulsating magnetic field, following equation is used.

$$J = \frac{I_0}{A} [\text{flc2hs}(\sin(2\pi ft), 0.1)] \quad (3.10)$$

Where, I_0 is the current supplied to the conductors which is equal to 1 A for all simulations, A is the surface area of the copper conductors, and f is the switching frequency in hertz. It is assumed based on literature (Suzuki et al. 2004) that the temperature rise inside the microchannel will be negligible when current between 0.5A-1A is used. Magnetic field is actuated from left to right meaning when the current in left conductor is ON, the current in the right conductor is OFF and vice versa. This is done by having a phase difference of 180° in the alternating current supplied to the conductors. The above equations are solved in magnetostatic module of COMSOL Multiphysics software and the pulsating magnetic field is obtained. The force acting on MNPs is calculated from the above magnetic field using Eq. 3.11 described in literature (Pankhurst et al. 2003).

$$F_m = \frac{V\Delta\chi}{\mu_0} (\vec{B} \cdot \nabla) \vec{B} \quad (3.11)$$

Where, V is the volume $\Delta\chi$ is the difference in magnetic susceptibility of the MNPs and the fluid which is kept constant throughout the simulation, and \vec{B} is the magnetic flux density obtained after solving Eq.3.9. The force obtained from Eq.3.11 is substituted in Eq.3.3 in order to obtain velocity profile of MNP solution.

3.1.2.2.1 *Boundary Conditions*

A magnetic insulation boundary condition ($A_z = 0$) is applied along the system boundary. The interior boundaries between the copper conductors and the air only assume continuity, corresponding to a homogeneous Neumann condition.

3.1.2.3 **Convection-Diffusion Equation**

The spatial and temporal variation of the MNP solution inside the microfluidic channel is described using the following convection-diffusion equation

$$\frac{\partial C}{\partial t} + u \cdot \nabla C = D \nabla^2 C \quad (3.12)$$

Where, C is the concentration of MNP solution in a given solution, and D is the diffusion coefficient (m^2 / s), which is assumed to be constant throughout the simulation. Moreover, it is assumed that MNPs are monodispersed and will not agglomerate to form microparticles even after application of magnetic field. Therefore, the particle velocity is assumed to remain constant and move with the velocity of fluid. This approximation is based on the fact that the time constant for acceleration phase is too small for the scale of geometry and the size of particles used in the simulation, therefore it can be neglected and the liquid solution can be treated as continuum in the model.

3.1.2.3.1 Boundary Conditions

An initial unmixed concentration of MNP solution $C_0 = 1.0 \mu\text{M}$ injected into the microchannel with the initial parabolic velocity, Convective flux is set at the outlet boundary, keeping insulation/symmetry in all the other boundaries.

3.1.2.4 Residence-Time Distribution

The Residence-time distribution (RTD) curve is obtained by injecting a MNP solution for a very short time interval (Dirac pulse) at the inlet of the microchannel, and then the concentration of MNP at the outlet is recorded as a function of time. The RTD function also known as exit age-distribution $E(t)$ is defined quantitatively. The $E(t)$ function basically tells quantitatively, how much time different fluid elements have spent in a continuous flow system such that $E(t) \cdot dt$ is the fraction of MNP solution exiting the microchannel that have spent a time between t and $t + dt$ in the microchannel. The RTD function, $E(t)$ is given by Eq.3.13, where $C(t)$ is the MNP solution concentration at the outlet, as a function of time. The MNP concentrations are recorded at different y-points along the outlet of microchannel and then average value is used as $C(t)$.

$$E(t) = \frac{C(t)}{\int_0^{\infty} C(t) dt} \cong \frac{C(t_i)}{\sum_{i=0}^{\infty} C(t_i) \cdot \Delta t_i} \quad (3.13)$$

where, $\Delta t_i (= t_{i+1} - t_i)$ is the time steps used in the simulation.

After the RTD function is obtained, parameters that are used to quantify the mixing performance are calculated based on the methods given in literature[186]. These statistical parameters are mean residence time t_m , which gives the average time the exiting fluid element spend in the microchannel; variance σ^2 , which is the measure of the spread of the distribution; and

coefficient of variance or normalized variance, which provides the relative standard deviation of the distribution. These statistical parameters are mathematically given by equations 3.14-3.16.

$$t_m = \frac{\int_0^{\infty} tE(t)dt}{\int_0^{\infty} E(t)dt} = \int_0^{\infty} tE(t)dt \cong \sum_{t=0}^{\infty} tE(t)\Delta t \quad (3.14)$$

$$\text{since } \int_0^{\infty} E(t)dt = 1$$

$$\text{Variance} = \sigma^2 = \int_0^{\infty} (t - t_m)^2 E(t)dt \cong \sum_{t=0}^{\infty} (t - t_m)^2 E(t)\Delta t \quad (3.15)$$

$$\text{Normalized Variance} = \frac{\sigma^2}{t_m} \quad (3.16)$$

The RTD of the microchannel with magnetic actuation will deviate from an ideal plug flow mixer depending on the magneto-hydrodynamics with the microchannel. Based on computation a variance of zero would mean complete plug-flow mixing while a non-zero value will imply mixing due to non-uniform or laminar velocity and molecular diffusion. In the present simulations variance values given by equation 3.15 will be calculated for different scenarios, a smaller variance value will mean narrower RTD curve, closer distribution to mean residence time, and higher mixing performance. In this way, mixing performance for all the conditions including magnetic and no magnetic field assisted mixing will be computed, compared and optimized conditions will be predicted.

3.1.2.5 Numerical Simulation

The finite element software package, COMSOL™ Multiphysics (COMSOL AB., Stockholm, Sweden) is used to solve the two-dimensional partial differential Equations obtained in our model. The finite element model consists of three application modes: incompressible Navier-

Stokes mode and magnetostatics mode to predict the convective velocity of MNP solution with and without the influence of magnetic field force, a convection-diffusion mode to predict the concentration of MNP solution within the microchannel. The meshing around the geometry is around 7 μm except near the electrodes boundary which is 5 μm in order to get more precise magnetic field results. The model is solved in transient model in one step using time-dependent solver.

3.1.3 Magnetic Force Validation

Prior to more detail parametric investigation, the magnetic force calculation in the COMSOLTM finite element model was validated using the experimental and numerical results from Suzuki et al.[122]. Magnetic force computation is the most critical step in coupling the microfluidic flow with magnetic force mixing therefore its correct estimation is essential. In order to compare results, a volume of $2.16 \times 10^{-9} \text{m}^3$ corresponding to 0.7 μm magnetic particles and a 40 x 40 μm copper conductor carrying 1A was considered in the COMSOLTM model. These parameters were used by Suzuki et al.[122]. The model setup is shown in the inset of Figure 3.3. The fluid with magnetic particles flows in the microchannel whereas at the bottom the copper conductors are used to generate magnetic field.

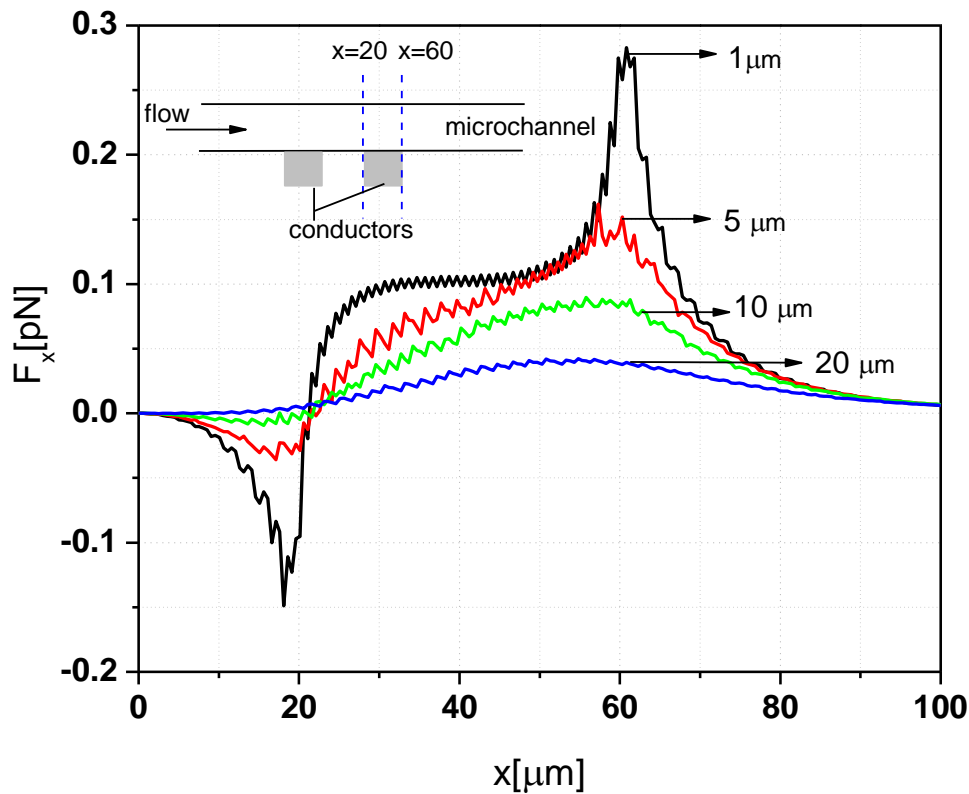


Figure 3.3 Magnetic force profile along the z-lines above the current carrying conductor. The location $x=20\mu\text{m}$ and $x=60\mu\text{m}$ corresponds to the inner and outer edges of the right conductor respectively. Simulation results from COMSOL Model were found to be in good approximation with experiment and simulation result from Suzuki et al[122].

The magnetic field force on the particles are calculated along different lines that are parallel to the x-axis ($y=1, 5, 10,$ and $20 \mu\text{m}$) starting from $180\mu\text{m}$ from the left of microchannel (central point between two conductors) and going toward right for a distance of $100 \mu\text{m}$ (see Figure 3.3). The location $x=20\mu\text{m}$ and $x=60\mu\text{m}$ corresponds to the inner and outer edges of the right conductor respectively. It can be seen from Figure 3.3 that as we move away from bottom of microchannel the x-component of magnetic force tends to decrease as well as oscillates around the central axis of the microchannel and peaks at the edges of the conductor, responsible for the oscillatory motion of the magnetic particles within the channel. Moreover, the computed

magnetic force profiles along different planes within the microchannel as well as the range of maximum magnetic forces (e.g.; 0.1-0.3 pN) obtained, agree reasonably well with experimental and simulation work performed by Suzuki et.al [122].

3.1.4 Results & Discussion

3.1.4.1 Specie Concentration Distribution (SCD) Analysis

In this section, we present the performance of time-dependent MNP-enhanced mixing under various conditions of MNP size, frequency of applied current used to generate magnetic field, inlet flow velocity and different active and passive scenarios of mixing. Time-dependent numerical results were obtained using the above described model and the performance of mixing was predicted using both concentration profiles and mixing efficiency calculation (SCD Analysis). In magnetic field equation average current of 1A was considered throughout the simulations. For the convection and diffusion equation, $D=10^{-11} \text{ m}^2/\text{s}$ is used in all the simulations. Other parameters such as fluid viscosity η ($10^{-3} \text{ kg}/\text{m}\cdot\text{s}$) and density ρ ($10^3 \text{ kg}/\text{m}^3$) were kept constant throughout. The effect of various parameters on the mixing performance is described in more detail in the following sections.

3.1.4.1.1 Effect of Magnetic Nanoparticle Size

Mixing efficiency were calculated for different MNPs size ranging from 50-300 nm for inlet flow velocity, $u_0 = 200 \text{ }\mu\text{m}/\text{s}$ and using magnetic field switching frequency, $f = 1 \text{ Hz}$ while all the other parameters were kept constant as described in previous sections. It can be seen from Figure 3.4 that as we increase the size of MNPs from 50nm to 100nm, mixing efficiency tends to increase. Further increasing the size from 100 nm to 300nm did not seem to have appreciable effect on mixing performance. We know from Eq. 3.11, that magnetic force is directly proportional to the volume of MNP, therefore larger the size of MNPs, greater will be the force

acting on it in the solution. However, in order to have enhanced mixing, oscillation of MNPs is highly desirable so that it is constantly disturbed in the flow which will only be possible if both the magnetic force and drag force are equally effective in magnetic on and off situation respectively.

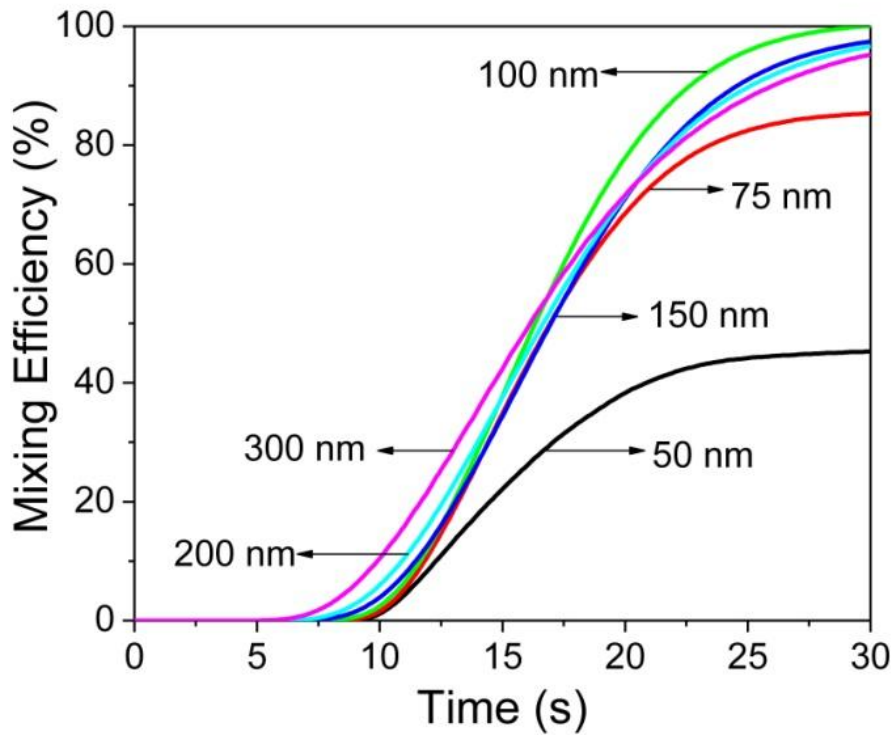


Figure 3.4 Mixing efficiency at the outlet of the micro-channel for different magnetic nanoparticle size.

Therefore, increasing the size MNPs beyond a certain critical value will make magnetic force more effective as such after the magnetic field is switched off the MNPs will not be able go back to their initial position as effectively as previous and will overall decrease the oscillation effect. For the configuration used in our model, 100 nm MNPs give the most optimized mixing performance and almost 100 % mixing is achieved in less than 20s.

3.1.4.1.2 Effect of Inlet flow Velocity

We know that mass transport can be increased by increasing the flow velocity of the incoming MNP solution. Moreover, we can further decrease the mixing time by increasing the flow velocity. In order to investigate and predict optimum mixing velocity, simulations were performed for 100 nm MNPs under magnetic field switching frequency $f = 1$ Hz. We can see from Figure 3.5 that as we increase the inlet flow velocity, it took less time to achieve 100% mixing but going beyond the 300 $\mu\text{m/s}$ mixing efficiency is not very stable and is quite oscillatory. In order to further investigate the flow velocity effect, we compute the normalized concentration profile at the cross-sectional outlet shown in Figure 3.5b.

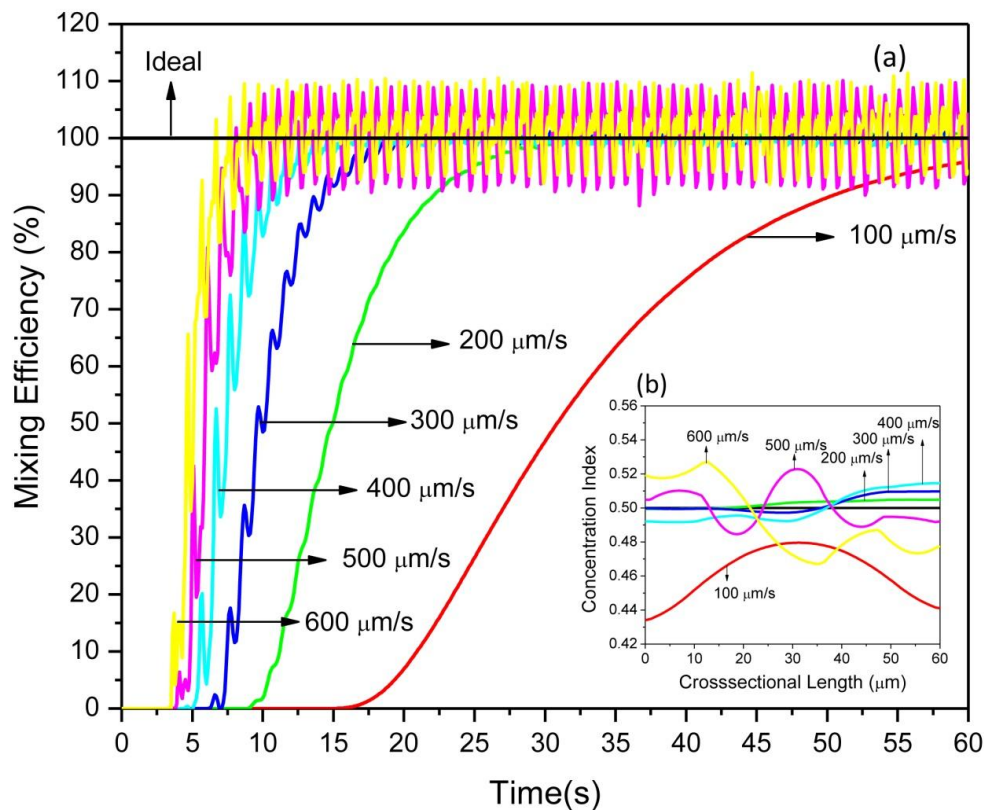


Figure 3.5 Concentration Index in the micro-channel under varying inlet velocity: (a) Concentration index at the outlet of the microchannel, and (b) Cross-sectional plot of concentration at the outlet of microchannel after 60 sec. Black Solid line represent the ideal concentration which is desirable at the outlet.

It is observed that too high inlet flow velocity, in this case $600\mu\text{m/s}$ produces large variation in concentration profile whereas too low, $u_0 = 100\mu\text{m/s}$ is unable to achieve desired mixing. Therefore, an optimum inlet velocity of $300\mu\text{m/s}$ is predicted which not only produces less variation in concentration profile but also reduces the time of mixing approximately by 50%.

3.1.4.1.3 Effect of Switching Frequency

In the microfluidic system shown in Figure 3.1, time-dependent magnetic field produced due to alternating current induces magnetic forces on the magnetic nanoparticles that disturbs the parallel streamlines in the otherwise highly ordered laminar flow. The oscillation of magnetic nanoparticles causes vertical momentum (in y-direction) to the fluid and stretch/fold streamlines of the fluids thereby enhancing the mixing performance. Therefore, the switching frequency of the current passed through the copper conductors is one of the most important factors that affect the mixing. Switching frequency can either result in very fast or very slow modulating magnetic field, therefore it needs to be optimized. Six different switching frequencies ranging from 0.1 Hz to 10 Hz were considered to optimize the mixing performance in a microchannel, keeping the other parameters such as inlet flow velocity ($300\mu\text{m/s}$), nanoparticle size (100nm), and current through the conductor (1A) constant throughout the simulations. It can be seen from Figure 3.6 that at very low switching frequency, the mixing is not really uniform. We can also see a large variation in normalized concentration at the outlet of the microchannel (see Figure 3.6b).

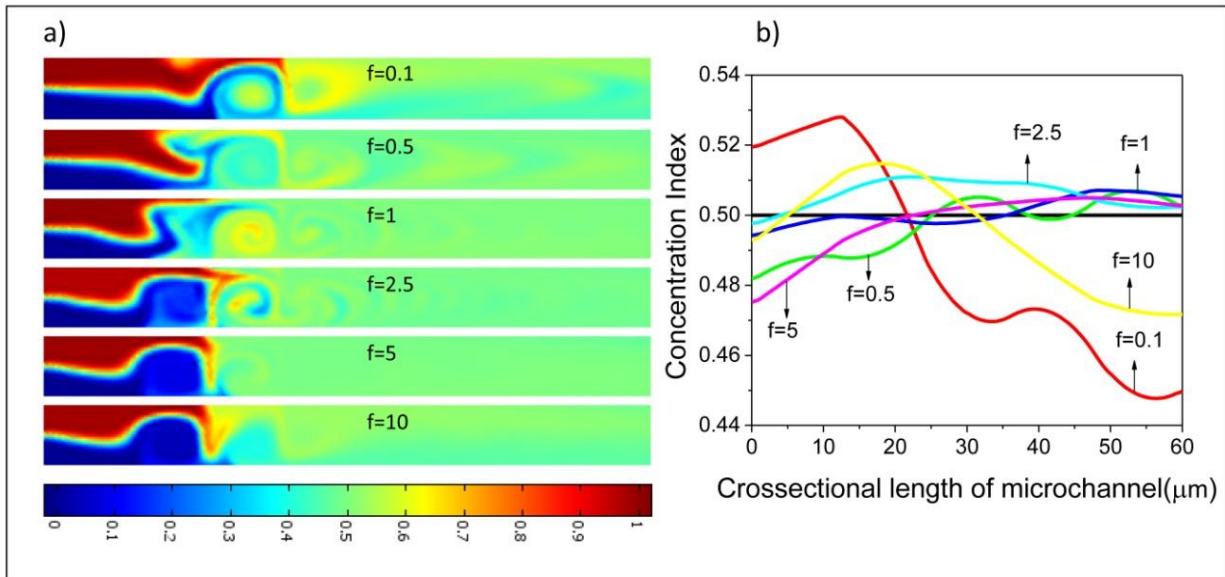


Figure 3.6 Concentration profile in the micro-channel under different switching frequency: (a) Surface concentration plot of micro-channel at different frequencies given in Hz, (b) Cross-sectional plot of concentration at the outlet of microchannel after 30 sec. Black Solid line represent the ideal concentration which is desirable at the outlet.

Ideally at the cross-section outlet the concentration should be 0.5 for perfect mixing but at low switching frequencies ($f= 0.1, 0.5$ Hz) we observe large oscillation. This may be due to the fact at very low frequency the magnetic nanoparticle solution due to attracting magnetic force are pulled towards the conductors and causes the surrounding fluid to the move to other side. Once the particles reach near the channel wall they stay there for certain time, since the frequency is low therefore the time to go back with the flow is high. This results in less oscillation and more variation in concentration profile magnetic nanoparticle solution. Similar concentration profile is observed even at very high frequency ($f= 10$ Hz). This is because, at very high frequency the magnetic force acts for a very short duration of time on nanoparticles before it is turned on/off, therefore there is very less transition of nanoparticles in the lateral directions which results in less disturbance of fluid and higher variation in concentration. There is always a critical or optimized value of switching frequency for a given configuration. For the dimensions used in these simulations, a frequency of 1 Hz is desirable because it generates more stable and uniform

mixing. These results indicate that a simple mixing scheme consisting of time-dependent magnetic field operating at critical/optimized frequency can provide efficient mixing within a very short interval of time.

3.1.4.1.4 Scaling Analysis

Scaling analysis is performed in order to determine the effect of change in geometry of the microchannel on the inlet velocity and switching frequency. Keeping all the other parameters constant and switching frequency, $f = 1 \text{ Hz}$, simulations are performed to obtain results as shown in Figure 3.7. It is found that when the width of microchannel is reduced by a factor of 2 ($W=30 \text{ }\mu\text{m}$) as compared to original device geometry ($W= 60 \text{ }\mu\text{m}$), the optimal inlet velocity to obtain high and stable mixing is around $400 \text{ }\mu\text{m/s}$ (see Figure 3.7a) whereas when the microchannel width is increased by two-fold ($W=120 \text{ }\mu\text{m}$) , low inlet flow velocity is desirable and the optimum velocity of $200 \text{ }\mu\text{m/s}$ (see Figure 3.7b) generates least variation and high mixing in a given interval of time. From the above analysis it can be seen that optimal velocity is scalable. For a narrower microchannel ($W=30 \text{ }\mu\text{m}$), MNPs require smaller lateral distance to travel , therefore in order to obtain full range of optimized oscillation in a desired time, a higher horizontal flow velocity is recommended. Similarly, If the microchannel is too wide ($W=120 \text{ }\mu\text{m}$), MNPs require longer distance to travel in y-direction due to magnetic actuation force, therefore working with smaller inlet velocity will not provide enough time to cause full range of oscillation of MNPs within the microchannel.

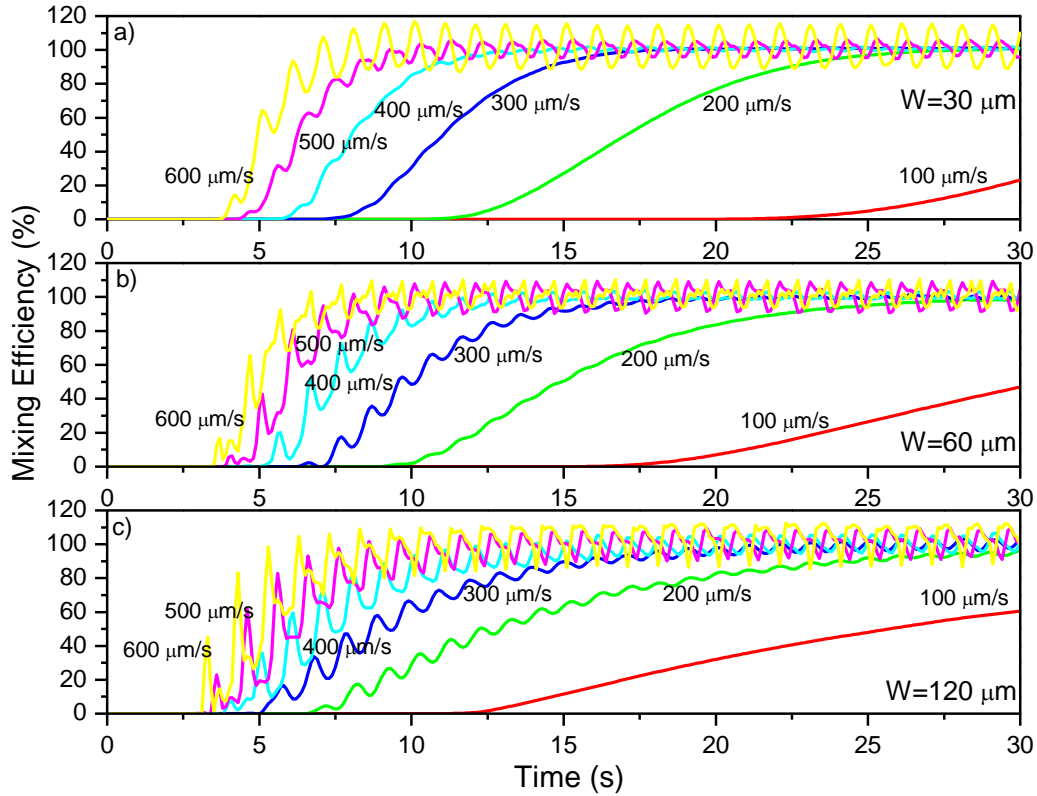


Figure 3.7 Effect of scaling (microchannel width) on the inlet flow velocity: (a) $W=30\ \mu\text{m}$, (b) $W=60\ \mu\text{m}$, and (c) $W=120\ \mu\text{m}$. Average concentration is recorded at the outlet of microchannel for a time interval of 30 sec.

Simulations are also performed to investigate the effect of scaling on the switching frequency. The optimized inlet velocity as obtained from previous results (see Figure 3.7) is kept constant together with all the other parameters described in previous sections. Switching frequency is varied from 0.1-10 Hz for different device size ($W= 30, 60,$ and $120\ \mu\text{m}$) and the average normalized concentration/concentration index together with standard deviation is predicted at the cross-sectional outlet of the microchannel. Ideally at the cross-sectional outlet the average normalized concentration should be 0.5 for perfect mixing without any standard deviation. A too high standard deviation represents non-uniform concentration whereas low standard deviation represents near-uniform concentration and better mixing. When the microchannel width is scaled

down by a factor of 2 ($W=30\ \mu\text{m}$), operating the system at low frequencies (as seen in Figure 3.8a) results in large variation of concentration at the outlet, this is true because for a narrower microchannel, MNPs require lesser time to travel lateral distance so if the magnetic force is not switched off more frequently, there is possibility that MNPs stays near the electrode and produce less cycles of full range oscillations. Based on the results given in Figure 3.8a, working with higher frequency in the range of 5-10 Hz provides better mixing and least variation in the outlet concentration. Similarly, we can see as the device geometry is scaled up, the optimum frequency required to obtain uniform concentration at the outlet should be decreased. For $60\ \mu\text{m}$ wide microchannel the optimum frequency is around 1 Hz (see Figure 3.8b) whereas for wider microchannel ($W=120\ \mu\text{m}$), a frequency of 0.1 Hz (see Figure 3.8c) gives the best mixing performance and almost near uniform concentration at the outlet. These results illustrate that optimum switching frequency is dependent on the magnetic force, inlet flow velocity and the desired travel distance of the MNPs in the lateral direction. Therefore, if the magnetic force and inlet velocity is kept constant a narrower microchannel will need higher frequency whereas wider microchannel will need smaller frequency in order to obtain good mixing.

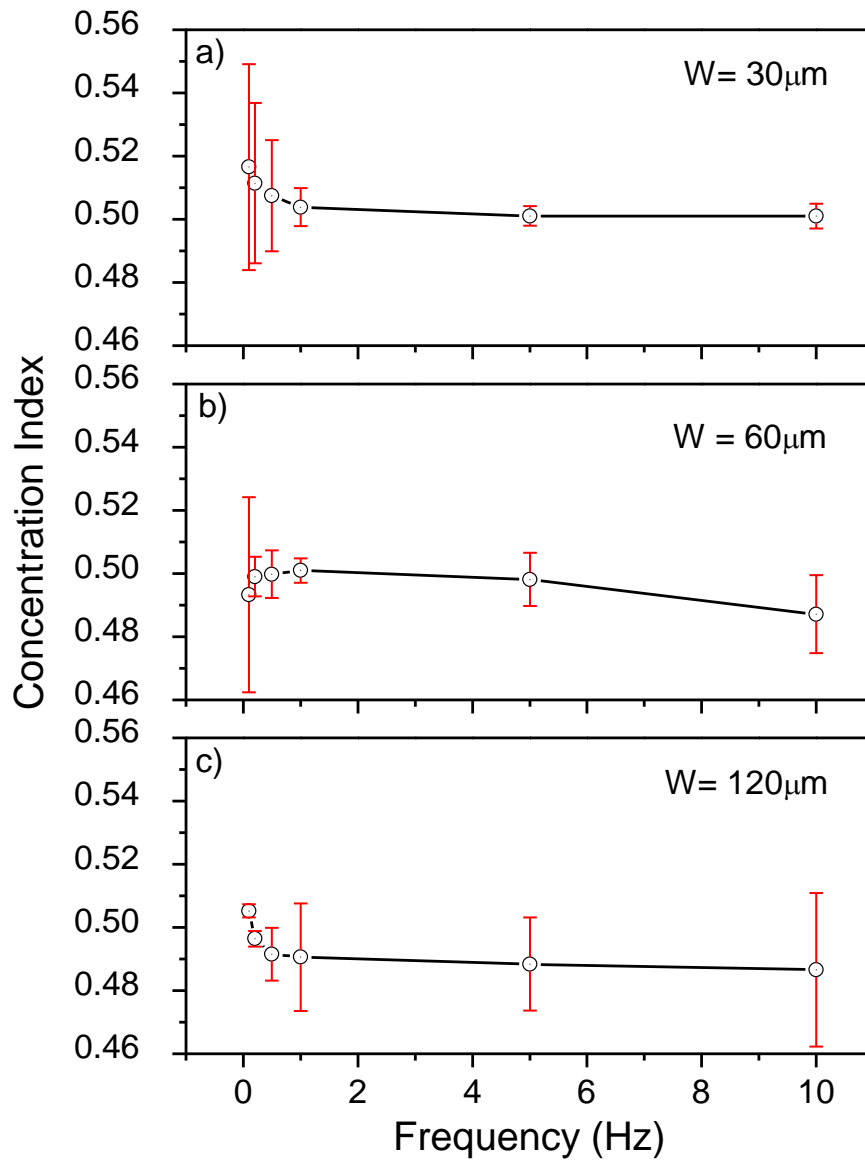


Figure 3.8 Effect of scaling (microchannel width) on the switching frequency: (a) $W=30 \mu\text{m}$, (b) $W=60 \mu\text{m}$, and (c) $W=120 \mu\text{m}$. Average concentration is recorded at the cross-sectional outlet of microchannel after 30 sec. Error bars represent standard deviation(SD).

3.1.4.1.5 Comparison of Magnetic with Passive Mixing Strategy

We further investigated and compared passive mixing method with the magnetic nanoparticle enhanced mixing. Concentration profiles shown in Figure 3.9 were obtained for scenarios with passive and magnetic actuated mixing and was compared with the condition when there are no

external mixing enhancements. As predicted, there is little or no mixing when it is only due to diffusion so external methods are needed to mix solutions in these laminar microchannels. For passive mixing, four barriers of $30\mu\text{m} \times 10\mu\text{m}$ are added (see Figure 3.9b) at the top and bottom of the channel in order to create turbulence in the flow.

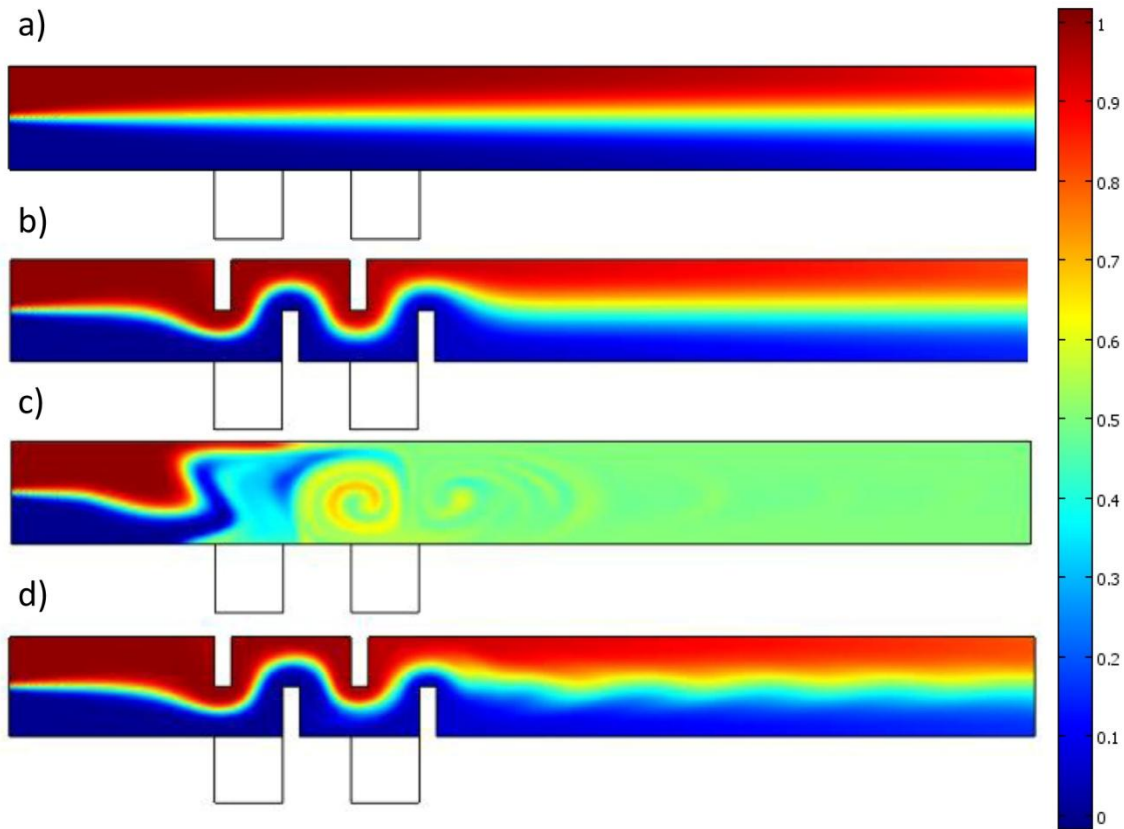


Figure 3.9 Concentration profile in the micro-channel under different mixing scenario: (a) without magnetic actuation, (b) passive mixing without magnetic actuation, (c) with magnetic actuation, and (d) passive mixing with magnetic actuation.

Slight enhancement in the mixing is observed but the solution is unable to completely mix together. Furthermore, the diffusivity of particle used in the simulation is in the order of $10^{-11} \text{ m}^2/\text{s}$, therefore either longer microchannels or more complicated barrier structures needs to be fabricated to enhance the mixing to an acceptable range. Even though passive method enhances the mixing to a certain extent but it can be seen that magnetic nanoparticle enhancement is far

better and results in almost 100% mixing in less than 20s (see Figure 3.9c). Moreover the configuration used for mixing is simple and can easily be developed without complicated fabrication processes. The size of MNPs used in this simulation is 100nm which is directed in the microchannel with an initial flow velocity of 300 $\mu\text{m/s}$. A switching frequency of 1 Hz is used to generate oscillating magnetic field. Finally, a hybrid of magnetic as well as passive method was also simulated keeping all the parameters same as above. Poor mixing was achieved as shown in Figure 3.9d. This may be due to the fact that the area needed for complete oscillation of magnetic nanoparticle is not enough for creating turbulence in the flow. Moreover, there is a change in magnetic field due to presence of barriers near the conductors which results in less force exerted on the MNPs. A slight disturbance in the flow is observed but it is not enough to mix the two solutions completely. The numerical simulation results report here indicate that magnetic nanoparticle-based strategy can be a useful simple technique for increasing mixing in microchannel, particularly for molecules that have very low diffusivity and can be used for developing rapid micromixer that can be integrated on lab-on-a-chip systems.

3.1.4.2 Residence Time Distribution (RTD) Analysis

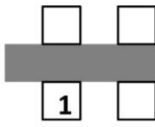
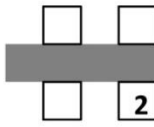
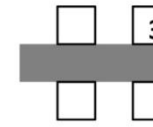
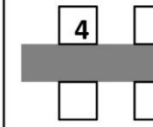

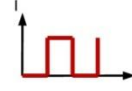
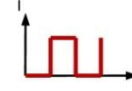
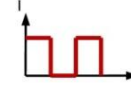

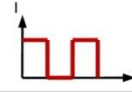
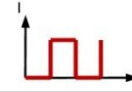
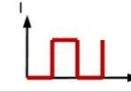

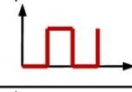
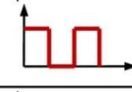
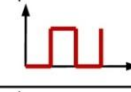
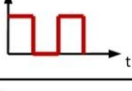
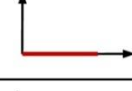
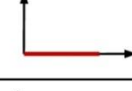
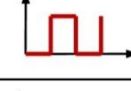

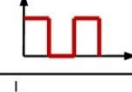
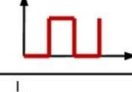
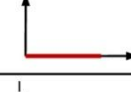
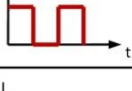






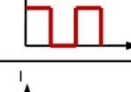

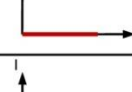
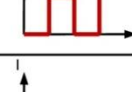





In this section, we present the performance of time-dependent MNP-enhanced mixing in microchannel under different conditions of magnetic actuation techniques, magnetic nanoparticle size, frequency of applied current used to generate magnetic field, and inlet flow velocity. Time-dependent numerical results are obtained and the performance of mixing is predicted using residence-time distribution analysis (RTD) as described earlier. In magnetic field equation average current of 1A is considered throughout the simulations. For the convection and diffusion equation, $D=10^{-11} \text{ m}^2/\text{s}$ is used in all the simulations. Other parameters such as fluid viscosity η

($10^{-3} \text{ kg / m} \cdot \text{s}$) and density ρ (10^3 kg / m^3) are kept constant throughout. The effect of various parameters on the mixing performance is described in more detail in the following sections.

3.1.4.2.1 *Effect of Magnetic Actuation configurations*

In order to investigate the magnetic nanoparticle-assisted mixing, nine different magnetic actuation configurations are incorporated in the model and compared with the base scenario when no magnetic field is deployed and the mixing is only due to convection and diffusion. As shown in Figure 3.1, magnetic field can be generated due to two copper electrodes in which electric current can be systematically turned on and off with given frequency to produce oscillating magnetic force within the microchannel. Different techniques can be adopted, either we can turn both electrodes on and off together or turn one electrode on and other off and vice-versa. Similarly, two more similar electrodes can be placed just on the opposite side of the microchannel to see if using additional electrodes have profound effect on mixing. Several combinations of techniques are possible by using four electrodes but nine most effective combinations are chosen in order to generate pulsating magnetic field to predict and optimize mixing performance. These nine combinations of magnetic actuation techniques are given in Table 3.1 together with the status of electrodes, whether they are turned on or off or not used in the simulation. The electrodes are numbered from 1 to 4 starting from bottom left and going towards upper left in anticlockwise direction. The status of electric current (ON/OFF) and combination of four electrodes produces nine scenarios (a-i) of pulsating magnetic field which is used to enhance mixing. These nine scenerios are presented in Table 3.1.

Table 3.1 Nine combinations of magnetic actuation configurations (a-i). Microchannel (grey) at the center is surrounded by four-electrodes numbered 1-4. Oscillating current in the form of square-wave is applied to these electrodes in various combinations.

Scenarios	Electrodes			
				
a				
b				
c				
d				
e				
f				
g				
h				
i				

Microchannel at the center is surrounded by four electrodes, oscillating current in the form of square-wave is applied to these electrodes in various combinations, for example; in scenario (a), all four electrodes are used where current in electrodes 1& 4 are in same phase whereas in electrodes 2 & 3 it differ by 180° . Similarly, in scenario (d) only two electrodes 1&4 are used while no current is supplied to electrodes 2& 3, and in scenario (i) only one electrode 1 is used. These nine combinations at a frequency of 1Hz are used to generate magnetic field and the effect

of the scenarios on mixing performance is investigated using RTD analysis. Other parameters such as inlet fluid velocity ($u_0 = 300 \mu\text{m/s}$), MNP size (100 nm), viscosity η ($10^{-3} \text{kg/m}\cdot\text{s}$) and density ρ (10^3kg/m^3) of the fluid are kept constant throughout the nine simulations. It can be seen from Fig.3.10 that magnetic actuation has profound effect on mixing performance. The RTD curves with magnetic actuation corresponding to all nine scenarios are compared with the RTD curve with no magnetic field effect. Earlier, Adeosun et al. [204-206] is the only group who have utilized RTD technique in microfluidics to characterize passive mixing which is similar to the scenario of the proposed work when no magnetic actuation was used. In Figure 3.10, it is found that in almost all scenarios (see Figure 3.10a-i, circle) the time-dependent magnetic actuation decreases the variance and overall enhances the mixing. This is due to large disturbance created in the flow path due to oscillating MNPs. When only molecular diffusion is responsible for mixing, large variation is observed (see Figure 3.10a-i, triangle) in mean residence time (variance=33). RTD curves together with the computed variance are used to rank the mixing performance of nine different magnetic actuation techniques. Mixing performance is considerably enhanced in scenarios c & f (see Figure 3.10c & Figure 3.10f), because smaller the variance, the narrower the RTD curve and better the mixing performance. Other scenarios provide better mixing when compared to the diffusion-based mixing but are not as efficient. Moreover, it is seen that scenario c employs all four electrodes whereas scenario f uses only two electrodes at the bottom of microchannel and therefore it will be more efficient in terms of ease of fabrication and controlling the temperature rise in the microchannel. The results from RTD curve illustrate that scenario f is the most optimized configuration which will be used later in all the simulations since increasing the number of electrodes does not have appreciable effect on the mixing quality.

The RTD results reported here indicate that magnetic nanoparticle-based strategy can be a useful simple technique for increasing mixing, particularly for molecules that have very low diffusivity.

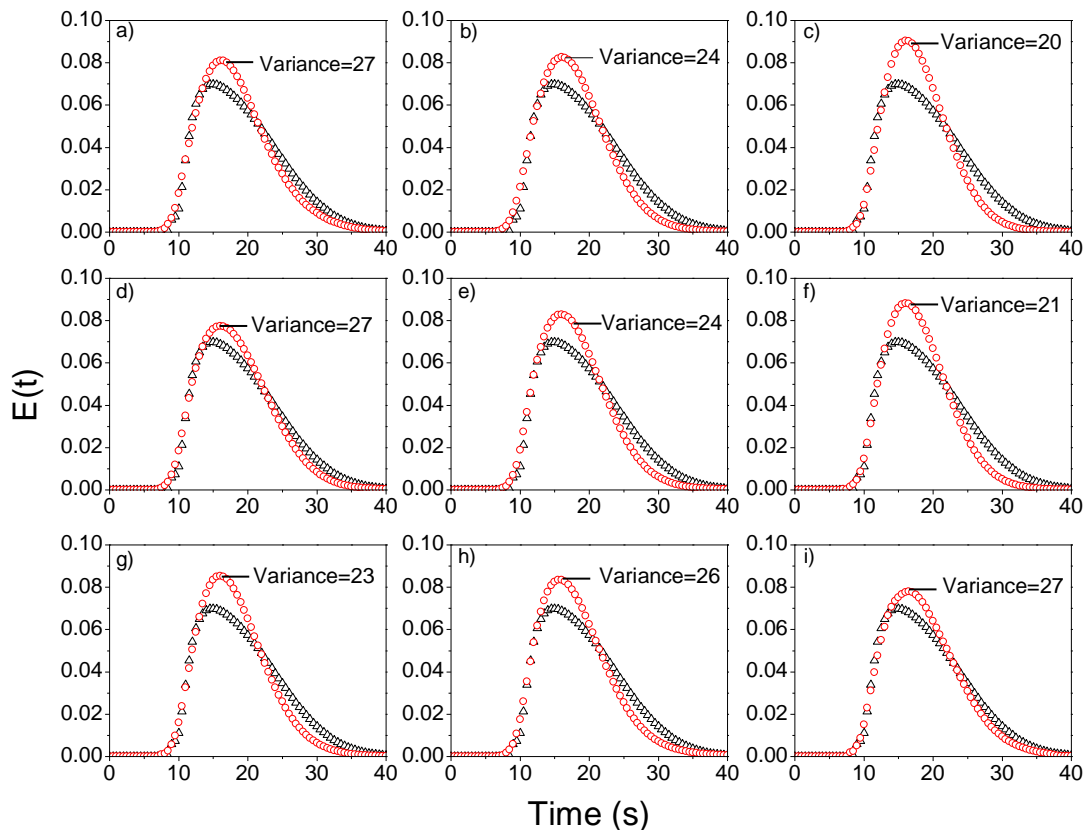


Figure 3.10 Effect of magnetic actuation techniques on residence time distributions (RTD). Nine different magnetic actuation scenarios (a-i) were considered and variance was computed for RTD curves with (circle) and without (triangle) magnetic field effect.

The major advantage of using magnetic actuation strategy over passive methods is the low fabrication cost because magnetic actuations do not require complicated microstructures for internally disturbing the fluid flows. Moreover, in passive methods the number of external parameters available to control mixing behavior is limited. For example: microchannel structure once fabricated cannot be optimized for mixing biomolecules of varying densities. Microstructures need to be re-fabricated in the microchannel with optimized design. Therefore, these systems are based on internal fabrication parameters which are often difficult to tune for

high mixing performance. Whereas, in the proposed magnetic mixing method fabrication do not play major role in mixing but it's the external actuation parameters such as magnetic field strength, magnetic field orientation, magnetic nanoparticle size etc which causes mixing. These parameters can be easily adjusted using the developed mathematical model described in more detailed in next sections before developing the actual system. Moreover, magnetically actuated mixing is much better than other active methods such as fluid actuation by energies including electrical which can damage or alter the properties of the fluid solution containing cell, biomolecules or DNA and most importantly they can be easily integrated to be used with lab-on-a-chip systems.

3.1.4.2.2 *Effect of Switching Frequency*

In the schematic of microfluidic system shown in Figure 3.2, time-dependent magnetic field due to alternating current produces magnetic forces on the MNP solution or more specifically on MNPs that disturb the parallel streamline flow in the otherwise highly ordered laminar flow. The to and fro movement of MNPs causes vertical momentum (in y-direction) to the fluid solution and stretch/fold streamlines of the fluids thereby enhancing the mixing quality. Therefore, the switching frequency of the electric current supplied to the electrodes is one of the most important parameters that affect mixing. Switching frequency of electric current can result in either very fast or very slow modulating magnetic forces; therefore needs to be optimized. The effect of switching frequency on the mixing quality is observed by using five different switching frequencies ranging from 0.1 Hz to 5 Hz, keeping the other parameters such as inlet flow velocity (300 μ m/s), nanoparticle size (100nm), and current through the conductor (1 A) constant throughout the simulations. RTD curves together with statistical variance are computed for each switching frequency and compared as shown in Figure 3.11. It can be seen that at very low (0.1

Hz) and at very high (5 Hz) switching frequency, the mixing is not appreciably enhanced when compared to scenario when no magnetic field is used. This may be due to the fact at very low frequency the MNPs due to attracting magnetic force are moved towards the electrodes and causes the surrounding fluid to move to the other side. Once the MNPs reach near the channel wall they stay there for certain time, since the frequency is low therefore the probability to go back with the flow is high.

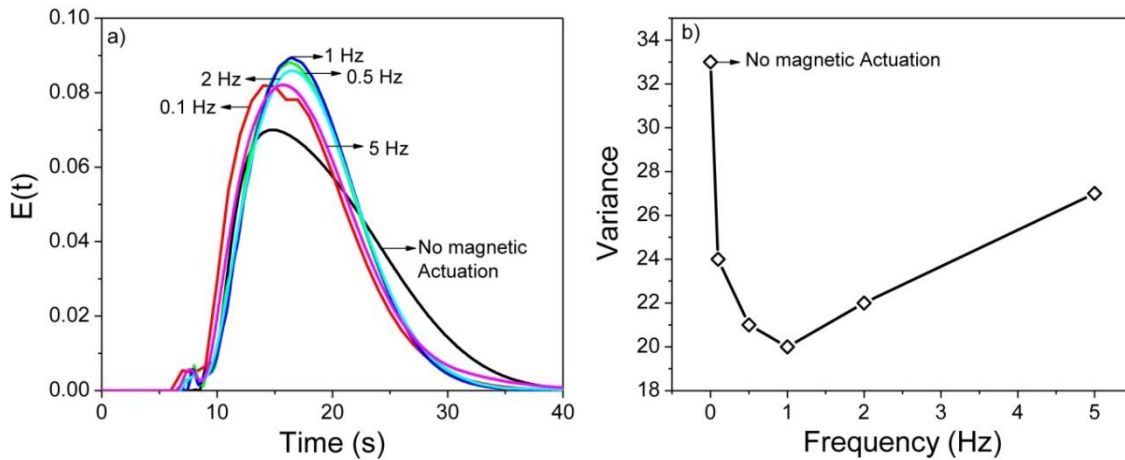


Figure 3.11 Variation of RTD curve with switching frequency. (a) Effect of switching frequency of magnetic actuation on residence time distributions (RTD). (b) Plot of variance versus switching frequency. Frequency zero implies the scenario when magnetic field was not used in the simulation.

This results in less oscillation and less mixing enhancement. Similarly at very high frequency ($f=5$ Hz) the magnetic force acts for a very short duration of time on MNPs before it is turned on/off, therefore there is very less effective transition of MNPs in the lateral directions which results in less disturbance of fluid. However, at frequencies of 0.5, 1, and 2 Hz the enhancement is more profound. It can also be seen from Fig. 10b, that switching frequency of 1 Hz gives the least amount of variation ($=20$), more narrower RTD curve(see Figure 3.11a) and highest enhancement in mixing for the scale and geometry of microchannel used in this model. Therefore, there is always a critical or optimized value of switching frequency for a given

configuration and dimensions of parameters used. For the scale and geometry used in this model, a frequency of 1 Hz is desirable because it generates more stable and efficient mixing. The RTD results indicates that enhanced mixing can be achieved within a very short interval of time using a simple scheme consisting of time-dependent magnetic field operating at critical/optimized switching frequency.

3.1.4.2.3 Effect of Magnetic Nanoparticle size

The effect of magnetic nanoparticle diameter on the mixing performance is also predicted using RTD curves. MNPs with sizes ranging from 20-300 nm are used in the simulations. Inlet flow velocity, $u_0 = 300 \mu\text{m/s}$, magnetic field switching frequency, $f = 1 \text{ Hz}$ and all the other parameters are kept constant as described in previous sections throughout the simulations. RTD curves together with variance are computed corresponding to magnetically-actuated mixing and compared with the base scenario when no magnetic field is used.

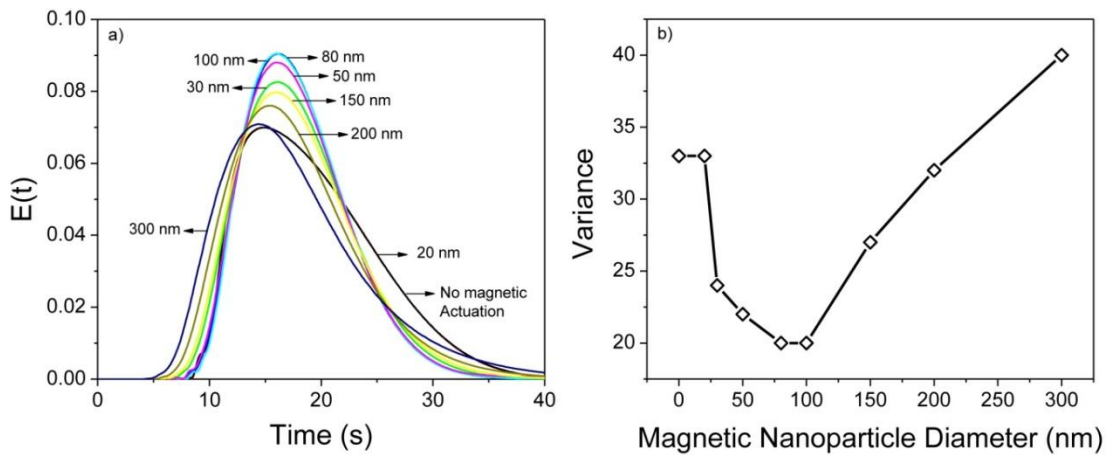


Figure 3.12 Variation of RTD curve with magnetic nanoparticle size. (a) Effect of magnetic nanoparticle diameter on residence time distributions (RTD). (b) Plot of variance versus magnetic nanoparticle diameter. Frequency zero implies the scenario when magnetic field was not used in the simulation.

It can be seen from Figure 3.12a that as we increase the size of MNPs from 20nm to 100nm, RTD curves becomes narrower as such mixing performance increases but when the MNP size is

increased beyond 100nm the RTD curves seems to spread out as such the mixing starts decreasing. This is further evident from computed variance when plotted against MNP size as seen in Figure 3.12b. The lowest variance (≈ 20) is observed when MNP size is 100nm. Decreasing the size of MNPs beyond a critical size is not effective, for example, a 20nm MNP is unable to agitate the fluid and the performance is not enhanced as compared to diffusion-based mixing. Increasing the size of MNPs to 300nm even decreases the mixing performance when compared to base scenario. As we know, the proposed system is based on continuous flow of magnetic nanoparticle solution. The fluid solution primary consists of magnetic nanoparticles and water. If no magnetic gradient exist, magnetic nanoparticles (MNPs) will just flow out of the microchannel. This happens because fluid exerts drag force on MNPs continuously. Neglecting the initial acceleration phase, the MNPs basically move with constant velocity. This approximation is based on the fact that the time constant for acceleration phase is too small for the scale of geometry and the size of particles used in the simulation. If magnetic field is applied, MNPs will experience magnetic force and if this force is more than the drag force exerted by fluid flow, MNPs will get deviated (move in lateral direction towards magnetic electrodes) from its original path. Again, if the magnetic force is switched off, MNPs will just flow with the fluid without any further deviation due to drag force. Periodically switching the magnetic force on and off will disturb the path of MNPs which will also disturb the liquid and cause mixing. Magnetic force can be made stronger by increasing the size of MNPs. If the magnetic force is too strong, large deviation will be expected in MNPs path which can be large enough to cause it to stick to side walls of microchannel. This will make drag force ineffective as it will not be strong enough to pull MNPs in horizontal direction. Therefore, overall decrease in oscillation or disturbance will be observed. Similarly, if the size becomes too small, magnetic force will be weaker and

will not be enough to cause any periodic disturbance in the flow. This will also result in decrease in overall oscillation effect and consequently mixing. Therefore, there is always a critical MNP size which will bring out optimum disturbance and mixing for a given set of conditions. Based on the results given in Figure 3.12 and for the geometrical configuration and flow condition used in the model, 100-200 nm MNPs gave the most optimized mixing performance.

3.1.4.2.4 Effect of Inlet flow Velocity

Inlet flow velocity also has significant effect on the mixing performance and needs to be optimized for a given configuration. In order to investigate and predict optimum mixing velocity, simulations are performed for 100 nm MNPs under magnetic field switching frequency $f = 1$ Hz and RTD curves are plotted and compared.

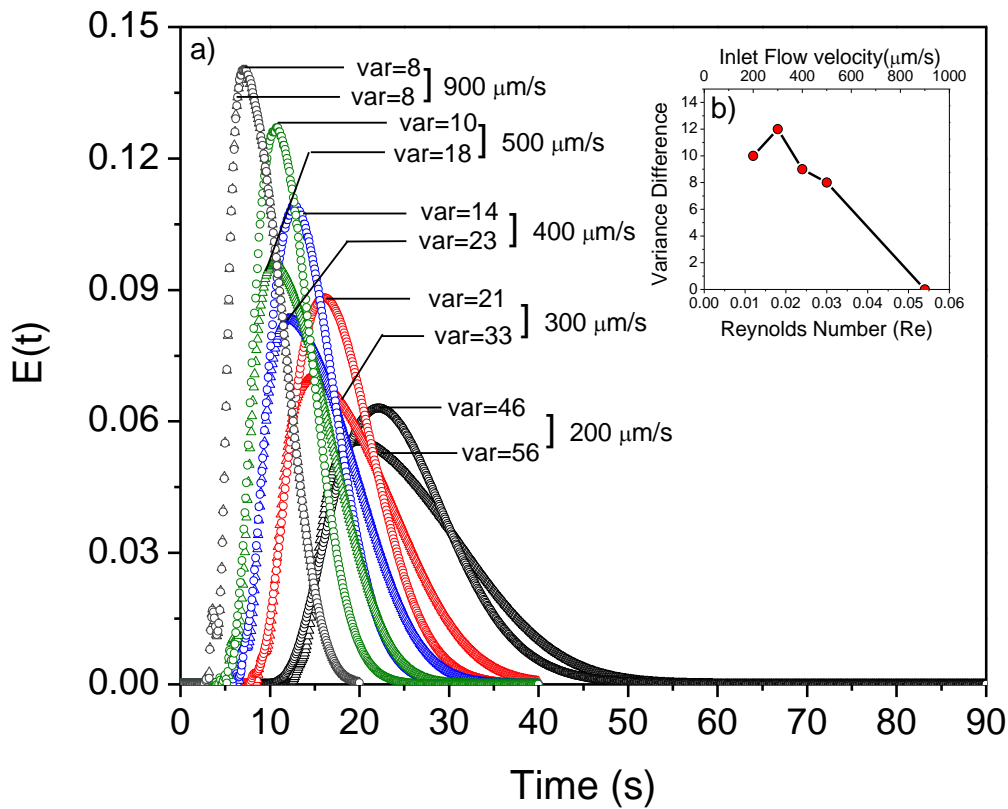


Figure 3.13 Effect of flow velocity on residence time distributions (RTD) for scenarios with (circle) and without (triangle) magnetic field. Variance (var) was computed for conditions with and without magnetic field-assisted mixing, (b) Plot of Variance Difference versus Reynolds Number. The variance difference is computed between non-magnetic field and magnetic field scenario.

When the flow conditions are changed, it can be seen from Figure 3.13 that the time fluid element spent in the microchannel also changes; therefore as the flow velocity is increased the mean residence time decreases which may also decrease the effectiveness of magnetically actuated mixing. Therefore, an optimum flow velocity for magnetically actuated mixing needs to be identified. The inlet flow velocity is changed from 200 $\mu\text{m/s}$ - 900 $\mu\text{m/s}$ and RTD curves for both no magnetic actuation and magnetic actuation are plotted as shown in Figure 3.13. It can be seen that at very high flow velocity (900 $\mu\text{m/s}$) magnetic actuation do not enhance the mixing performance and RTD curves are similar for magnetic and no magnetic scenario. The variance

calculated for these RTD curves are also similar. As the flow velocity is decreased, the effect of magnetically actuated mixing can be seen. The RTD curves for magnetic scenario when compared to no magnetic scenario becomes less spread out and the computed variance values are lower than their counterpart.

Variance differences are also computed for different flow conditions (Re ranging from 0.01-0.06) within the microchannel for both magnetic and non-magnetic scenarios. As seen from Figure 3.13b, the effect of magnetic actuation largely depends on the Reynolds Number. At higher flow velocity or Reynolds Number the Variance difference between non magnetic and magnetic scenario decreases. This means that magnetic actuation effect is less pronounced at higher flowrate for given conditions. Therefore, if the system is operated at higher flow velocity (~900 $\mu\text{m/s}$) larger magnetic field force is needed to bring out desired disturbance within the microchannel in order to enhance mixing. This can be done either by increasing the current through the electrodes or choosing larger magnetic size particles but both these conditions can have negative impact on overall mixing process. Too high current can cause excessive heating and may damage cells, DNA's or biomolecules whereas increasing the size of MNPs can lead to clogging of microchannel if the device size is expected to be small for point-of-care analysis. As this method is envisioned to enhance mixing in order to facilitate better tagging of biomolecules with MNPs in situ for lab-on-a-chip devices, the tagging process will be controlled by two important time scales, convection time scale, t_c and reaction time scale, t_r . Even though the residence time or variance (var=8) is small at high flow velocity (~900 $\mu\text{m/s}$), the tagging process will depend on how much time MNPs and biomolecules have to react. If the convection time, t_c is smaller than reaction time, t_r biomolecules and MNPs will not get enough time to interact and they will just move out of the system without being tagged. Therefore, working at lower

optimum flow velocity ($\sim 300\mu\text{m/s}$) in this case with magnetic mixing is better in order to provide sufficient reaction time for tagging biomolecules with MNPs. Moreover, working at higher flowrate will cause undesired high pressure drop within the microchannel than can have significant demerits. We can also see from Figure 3.13b, that at very low flow velocity ($\sim 200\mu\text{m/s}$), the magnetic mixing seems to be less profound. This is evident from the fact that variance difference at low Reynolds Number ($\text{Re}=0.01$) is less. This is true, because at very low flowrate magnetic field force will be more effective. If the magnetic force is too strong, large deviation will be expected in MNPs path and MNPs will travel longer distance vertically. This can cause MNPs to stick to side walls of microchannel which will make drag force ineffective to pull MNPs in horizontal direction with the fluid flow when magnetic field is turned off. Therefore, an overall decrease in oscillation or disturbance will be observed which leads to decrease in mixing. For the scale of geometry and parameters used, a flow velocity between $300\mu\text{m/s}$ - $400\mu\text{m/s}$ seems to be more effective and causes enhanced magnetically actuated mixing. It can also be seen from Figure 3.13 that at flow velocity of $300\mu\text{m/s}$, the computed variance for magnetic scenario is 21 whereas for similar condition when no magnetic field is used it is 33. This indicates that mixing due to MNPs seems to be more profound at this flow condition. Therefore, an optimum inlet velocity ranging between $300\mu\text{m/s}$ - $400\mu\text{m/s}$ is predicted for magnetically actuated mixing for the simulated geometry and conditions.

3.1.5 Conclusion

A finite element mathematical model for demonstrating an innovative time-dependent magnetically actuated mixing process for enhancing the mixing performance of a microfluidic system is successfully developed. Specie Concentration Distribution (SCD) together with Residence time distribution analysis (RTD) is used to study the dynamics of this novel mixing

process as well as predict the performance. The effect of magnetic actuation configurations, MNP size, switching frequency of magnetic field, and flow conditions is studied. It is found that orientation of electrodes as well as the direction of current to produce desirable magnetic field also play a major role on mixing performance rather than the number of electrodes.

Table 3.2 Comparison of SCD and RTD Analysis and their outcome

Parameters	SCD Analysis	RTD Analysis
Magnetic Nanoparticle Size	100 nm	80-100 nm
Inlet Flow Velocity	200-300 $\mu\text{m/s}$	300 $\mu\text{m/s}$
Switching Frequency	1	1
Electrodes Configuration	-	c & f

A two-electrode system with an optimized current can be as effective as four-electrode system. For effective time-dependent magnetically actuated mixing, an optimum switching frequency is always required that not only depends on applied magnetic field but also on convective flow velocity, channel dimension and nanoparticle size. Optimum switching frequency together with MNP size and inlet flow velocity is predicted using both the analysis and summarized in Table 3.2. Scaling analysis also illustrated that for a given magnetic force and inlet velocity, a narrower microchannel require higher frequency whereas wider microchannel will need smaller frequency in order to obtain near-uniform concentration and good mixing. Moreover, magnetically actuated mixing was compared with passive mixing strategies and was found to be very efficient and simple to develop. Overall, the developed magneto-hydrodynamic “numerical prototype” proves that time-dependent magnetic manipulation technique has an excellent potential to efficiently mix or tag MNPs with biomolecules *in situ* for further processing and will be very useful in developing efficient lab-on-a-chip systems.

3.2 Dynamics of Magnetic Nanoparticle Capturing & Magnetic Bioseparation

3.2.1 State of the Art

Magnetic field based bioseparation in a microfluidic systems is receiving increased attention because of its vast applications in biomedical research, clinical diagnostic and biotechnological sciences. Its principle involves isolating biomolecules of interest from the bulk mixture by attaching them to small magnetic particles and then recovering it by using an external magnetic field [3, 29, 41, 61, 134, 207]. In the past few years, several microfluidic bioseparation system based on magnetic particles have been successfully developed for separation, analysis and detection of biomolecules [45, 60], immunoassay of proteins [48, 172], purification of DNA [50], and cell separation [52] . However, most of the recent developments made in bioseparation is based on functionalized magnetic beads or microparticles[29, 47, 52, 147], there are relative few microfluidic systems[62] developed that have employed magnetic nanoparticles for bioseparation. Compared with magnetic microparticles or microbeads, magnetic nanoparticles are more promising and possess better properties such as higher surface to volume ratio[37, 61, 62] for chemical binding, minimum disturbance caused due to attached biomolecules [37] because of their extremely small size, and moreover they are superparamagnetic [37] , i.e., their magnetization without a magnetic field is zero. This is important because unlike microparticles or microbeads they do not agglomerate and stay suspended in carrier liquid when the magnetic field is removed. This makes it easy for the removal or capture of tagged biomolecules of interest. The dimension of magnetic nanoparticles is also smaller or comparable to those of a biomolecules like cells, proteins, DNA as such they provide closer interaction and tagging. Overall, magnetic nanoparticles offer numerous advantages and their introduction in a microfluidic system is expected to greatly enhance the device functionality.

The efficiency of magnetic bioseparation not only depends on the use of magnetic nanoparticles but also involves interplay of various other parameters such as inlet velocity of fluid containing magnetic nanoparticles, size of nanoparticles, magnetic field strength and its orientation, geometry of the device etc. In order to provide more quantitative comprehension of the capture process of magnetic nanoparticles in microfluidic system and consequently help in designing, optimizing and developing magnetic microfluidic bioseparation system, it is necessary to develop numerical model.

Numerical prototype and simulations can serve as “virtual experiments” to diagnose factors which affect magnetic nanoparticle based biomolecule separation performance. It can also help to investigate a wide range of design parameters including flow velocities, channel dimensions, geometries and nanoparticle properties and can identify key design and operational issues. There has been a few studies [138, 208-213] made in the past to study the transport of magnetic particles in microfluidic system but most of these work focused on microparticles or microbeads and was limited to the transport of only one particle in a microfluidic system. Moreover, only simple magnetic field configurations were considered without a detailed analysis and optimization strategies. Therefore, a more quantitative understanding and study of the dynamics of capture process of multiple magnetic nanoparticles is required for the design and development of the microfluidic device. For this purpose, a finite element mathematical model was developed to predict the motion of multiple magnetic nanoparticles released in the microfluidic system. The magnetic nanoparticles trajectories were computed under the influence of magnetic field and it was also shown that they varied not only because of the size but also due to position of magnetic nanoparticles from where they are launched. Parametric analysis was conducted and optimized values of inlet velocity, diameter of magnetic nanoparticles and magnetic field strength were

estimated. It was also demonstrated that the angular position of magnet around the microchannel is also critical and the device performance could further be improved by adjusting this parameter.

3.2.2 Model Development

A mathematical model was implemented to investigate the interaction of external magnetic field with the flow of magnetic nanoparticles. The two-dimensional geometrical representation of a microfluidic channel with a permanent magnet is shown in Figure 3.14a whereas Figure 3.14b shows the schematic of a 3D representation of a microfluidic magnetic bioseparation system.

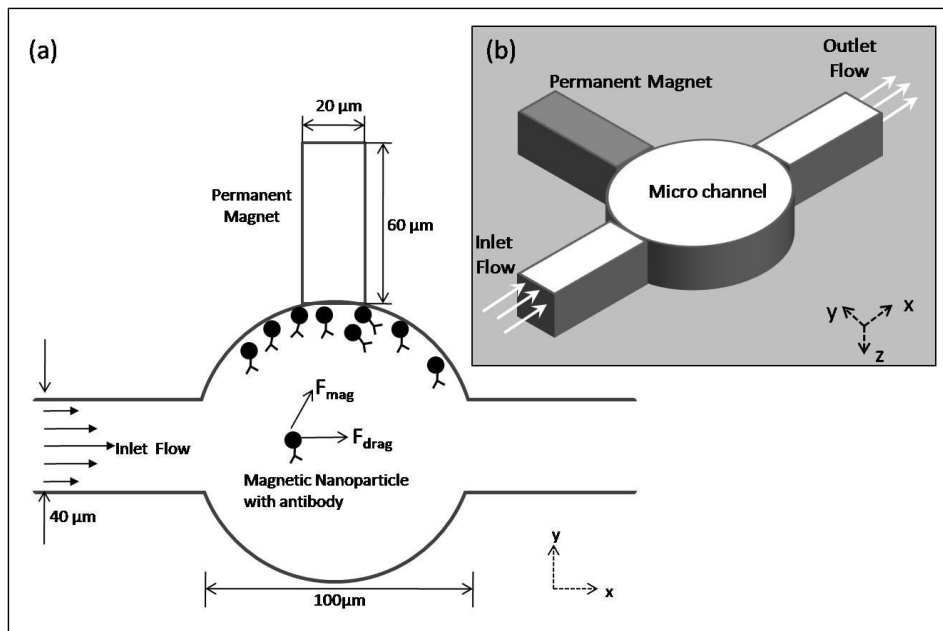


Figure 3.14 Top view of the microfluidic system geometry used in this study. Magnetic nanoparticles enter the system from left and are attracted and trapped due to the magnetic force from the permanent magnet placed near the vicinity. Inset (b) shows the 3D representation of the complete setup for trapping magnetic nanoparticles.

It was assumed that the variation in transport of magnetic nanoparticle under the influence of magnetic field will be very small in the direction perpendicular to the x-y plane due to high aspect ratio [214] of the cross-sectional geometry that is modeled. This will reduce the 3D model to a 2D approximation. Although, a complete 3D model will be more accurate because it will take into account the local deviation that will occur due to 3D geometry but will also

significantly increase the computational overhead when compared with 2D geometries. Moreover, a 2D model will serve as a simple, fast, and relatively accurate guideline for designing and optimizing microfluidic magnetic bioseparation systems. The 2D model geometry as shown in figure 3.14a consists of a channel which is 40 μm wide and 220 μm long. The channel is connected to a circular well at the center having a diameter of 100 μm . The upper of boundary of circular well is enclosed with a 20 by 60 μm permanent magnet. The magnetic nanoparticles are assumed to be dispersed in the fluid and flows from left to right as shown in Figure 3.14b. It experiences different forces inside the microchannel. These forces are magnetic forces arising from magnetic field and strong magnetic field gradient created from external permanent magnet, the drag forces due to movement of magnetic nanoparticles with respect the surrounding fluid, and the gravitational forces arising due to the gravity acting on magnetic nanoparticles. The gravitational forces will be negligible as compared with magnetic forces and drag forces due to extremely small size of magnetic nanoparticles and therefore will not be considered in the simulations. The model was set up to investigate the effect of an external magnetic field on the fluid flow with magnetic nanoparticles. The equations and theory developed are based on Navier-Stokes equations and Maxwell's equations. The model basically solves the Maxwell's equation for a static magnetic field. The computed magnetic field is coupled to fluid flow by using the magnetic volume force term acting on the nanoparticles in the Navier-Stokes equations. The detailed explanation of the equations and theory used in the model are described in the following sections.

3.2.2.1 Fluid Flow Equations

The magnetic nanoparticles with a radius r are assumed to be dispersed in the fluid of viscosity η ($10^{-3} \text{ kg/m}\cdot\text{s}$) and density ρ (10^3 kg/m^3) equal to that of water. The nanoparticles with fluid

are given a parabolic velocity at the entrance of the channel. It is assumed that the particles move with constant velocity and the early acceleration phase of magnetic nanoparticles within the fluid is neglected. This approximation is based on the fact that the time constant for acceleration phase is too small for the scale of geometry and the size of particles used in the simulation, therefore it can be neglected. The drag force on a spherical magnetic nanoparticle is given by Stokes law which is given as;

$$F_{Drag} = -6\pi\eta r(\vec{v}_f - \vec{v}_p) = -6\pi\eta r\vec{v} \quad (3.17)$$

Where, r is the radius and \vec{v}_p is the velocity of magnetic nanoparticles, \vec{v}_f is the fluid velocity with which the magnetic nanoparticles are launched into the microchannel. For the geometry used in the simulation and the range of fluid velocity given, the Reynolds's number would be much smaller than unity. For example, if the fluid of viscosity η ($10^{-3} \text{ kg/m}\cdot\text{s}$) and density ρ (10^3 kg/m^3) is given an inlet velocity \vec{v}_f ($100 \text{ }\mu\text{m/s}$) in the channel of height D ($40 \text{ }\mu\text{m}$) than the Reynold's numbers, $R = \rho D \vec{v}_f / \mu$ will be 0.004 which is smaller than unity. Therefore, the fluid flow containing the magnetic nanoparticles can be assumed to be laminar. During the movement of magnetic nanoparticles with mass m it will be subjected to change in external forces F_{Mag} arising due to magnet. According to Newton's second law of motion and Stokes law for viscous drag;

$$m \frac{\partial v}{\partial t} = F_{Mag} + F_{Drag} = F_{Mag} - 6\pi\eta r\vec{v} \quad (3.18)$$

The terminal velocity is calculated to be $\frac{F_{Mag}}{6\pi\eta r}$, and can be obtained by substituting Eg. 3.18

equal to zero. The terminal velocity of magnetic nanoparticles will be attained exponentially and the time constant can be calculated using the following equation;

$$\tau = \frac{m}{6\pi\eta r} = \frac{2\rho r^2}{9\eta} \quad (3.19)$$

The time constant is calculated for radius of nanoparticles ranging from 10 - 1000 nm used in the simulation in the fluid. It was found that the time constant varied from 0.2-22.2 ns which means that nanoparticles acquires the terminal velocity very fast and therefore, it is acceptable to neglect the acceleration phase and assume that the nanoparticles are dispersed and move with the velocity of fluid. The magnetic force due to external magnetic field acting on the nanoparticles transfers momentum to the surrounding fluid thereby changing the flow profile. The flow velocity u for an incompressible fluid ($\nabla \cdot u = 0$) is described using Navier-Stokes equation,

$$\rho \frac{\partial u}{\partial t} + \rho(u \cdot \nabla)u = -\nabla p + \eta \nabla^2 u + F \quad (3.20)$$

Where, u is the velocity field (m/s), p is the pressure (N/m^2), and F is the volume force (N/m^3). The momentum transfer from magnetic nanoparticles to the fluid is incorporated by setting the volume force equal to the magnetic force acting on the nanoparticles. The magnetic force is proportional to the magnetic field and magnetic field gradient generated from the permanent magnet. This term is very important because it couples the fluid flow equation with the static magnetic field equation and is described in more detail in the following section.

3.2.2.1.1 *Boundary Conditions*

The flow of fluid with magnetic nanoparticles was assumed to be parabolic at the inlet of the microchannel moves in the direction of x-axis with zero velocity in y-direction. The average flow velocity of the fluid with magnetic nanoparticle was u_0 . No slip condition ($u = v = 0$) was applied along the walls of microfluidic bioseparation system and at the outlet, pressure condition was set equal to zero.

3.2.2.2 Magneto-static Equations

The static magnetic field described using Maxwell-Ampere's law is given by;

$$\nabla \times H = J \quad (3.21)$$

Where H is the magnetic field vector (A/m) and J is the current density vector (A/m^2),

According to Gauss law for magnetic flux density, B (Vs/m^2)

$$\nabla \cdot B = 0 \quad (3.22)$$

In order to describe a relation between B and H a constitutive relation given by the following equation is used in the model.

$$B = \mu(H + M) \quad (3.23)$$

Where, μ is the magnetic permeability and M is the magnetization vector. The magnetic permeability can also be expressed as $\mu_0\mu_r$, where μ_r is the relative permeability of magnet (=1)

and is assumed to be constant in all the simulations and μ_0 is the permeability in vacuum ($\mu_0 = 4\pi \times 10^{-7} N/A^2$). A magnetic vector potential A is described [180] according to the following equation

$$\nabla \times A = B; \nabla \cdot A = 0 \quad (3.24)$$

After substitution of equation 3.24 in equations 3.21, 3.22, and 3.23, the following vector equation is obtained;

$$\nabla \times \left(\frac{1}{\mu_0\mu_r} \nabla \times A - M \right) = J \quad (3.25)$$

It is assumed that the magnetic vector potential has a nonzero component only perpendicular to the plane A_z which basically simplifies the 2D and it has perpendicular current equals to zero.

Based on these assumption equation 3.25 simplifies to following equation;

$$\nabla \times \left(\frac{1}{\mu_0 \mu_r} \nabla \times A - M \right) = 0 \quad (3.26)$$

The above equation is solved in magnetostatic module of COMSOL and the induced magnetization $M (M_x, M_y)$ is calculated using the arc tangent expression given by Oldenburg et al.[215];

$$M_x = \alpha \arctan \left(\frac{\beta}{\mu_0 \mu_r} \frac{\partial A_z}{\partial y} \right) \quad (3.27)$$

$$M_y = \alpha \arctan \left(\frac{\beta}{\mu_0 \mu_r} \frac{\partial A_z}{\partial x} \right) \quad (3.28)$$

The material parameters α and β are obtained using the M-H curve for Fe_3O_4 magnetic nanoparticles from literature [215] and were assumed to be constant ($\alpha = 1 \times 10^4$; $\beta = 3 \times 10^{-5}$) for the range of magnetic nanoparticles used in the simulations. It was also assumed that the magnetic nanoparticles do not interact in the surrounding fluid and the magnetic force is proportional to the induced magnetization described in equation 3.27 & 3.28 according to Rosensweig et al.[180]. The magnetic force term $F (F_x, F_y)$ is given by equation 3.29 & 3.30 and is substituted in equation 3.20 in order to provide coupling between the fluid flow and magnetic field.

$$F_x = \left(\frac{M_x}{\mu_r} \frac{\partial^2 A_z}{\partial x \partial y} \right) \quad (3.29)$$

$$F_y = \left(\frac{M_y}{\mu_r} \frac{\partial^2 A_z}{\partial y \partial x} \right) \quad (3.30)$$

3.2.2.2.1 Boundary Conditions

A magnetic insulation boundary condition ($A_z = 0$) was applied along the system boundary.

3.2.2.3 Numerical Simulation

The finite element software package, COMSOL was used to numerically solve the two-dimensional partial differential equations described in the model, and to predict the transport of magnetic nanoparticles under the influence of both magnetic and drag forces as they move from left to right as shown in Figure 3.14a. The model consists of one geometry and two application modes: incompressible Navier-Stokes and magnetostatics in COMSOL to model the transport of the magnetic nanoparticles. The meshing around the geometry was around 10 μm except for the channel which was 5 μm in order to get more precise trajectories of magnetic nanoparticles. The model was solved in two steps using two different solvers. First the magnetic field and magnetic forces generated due to permanent magnetic was solved using the magnetostatic application mode with a non-linear solver and then a time-dependent solver was used to solve incompressible Navier-Stokes application mode.

3.2.2.4 Trajectories and trapping efficiencies of Magnetic Nanoparticles

In order to obtain the trajectories of magnetic nanoparticles, the fluid phase was initially solved using the method described above in order to obtain steady state velocity profiles for both magnetic and non-magnetic cases and then nanoparticle tracing was done on a ‘frozen’ flow field using the particle tracing plot available in COMSOL. The tracing plot available in the software is based on Khan and Richardson force [216] that is derived partially using experimental results and is valid for large range of Reynolds number. The equation used in the software is based on total force that the liquid exerts on the immersed spherical particles. Using this method the trajectories of the magnetic nanoparticles launched from different positions within the microchannel were simulated. The trapping efficiency was calculated using equation 3.31 which

is based on number of particles captured, $N_{Trapped}$ and the number of particles that entered the microchannel, N

$$Trapping - Efficiency (\%) = \left(\frac{N_{Trapped}}{N} \right) \times 100 \quad (3.31)$$

It was also assumed that magnetic nanoparticles do not roll on after they hit the walls and are considered to be trapped.

3.2.3 Results & Discussion

3.2.3.1 Validation of Numerical Model

Prior to more detailed numerical investigation and parametric analysis, the finite element model was validated using the well developed analytical expressions given by Furlani et al. [208] for magnetic flux density and magnetic force using a rectangular permanent magnet. The magnet's magnetization and relative permeability of magnet was kept constant throughout the analysis. Magnetic flux density and force was calculated for 50 nm magnetic nanoparticles using both the analytical expressions as well by finite element COMSOL model developed in this work. Figure 3.15 shows the computed y-component (B_y) of magnetic flux density along the axis of permanent magnet.

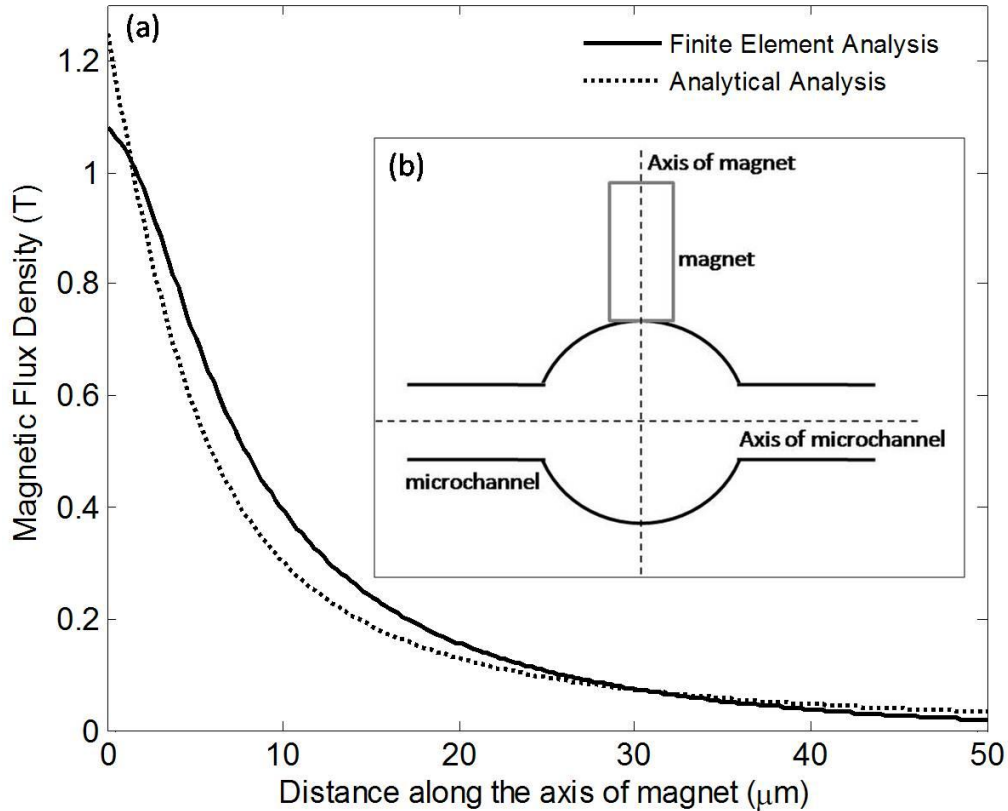


Figure 3.15 Magnetic field components along the axis of permanent magnet (a), Inset (b) shows the axis of magnet and the microchannel. Magnetic flux density calculations starts near the face and moves away from the magnet along its axis within the microchannel. Solid line represents finite element analysis (FEA) using COMSOL whereas dotted line represents analytical solution.

The numerical results agree very well with the analytical solution except for a place that lie closer to the magnet where the magnetic field experienced by nanoparticles computed analytically slightly exceed their numerically calculated values. This may be due to the fact that the magnet's edges were slightly curved for numerical calculations so as to improve convergence and reduce the numerical uncertainty. Moreover, the mesh resolution was also minimized at the corners due to curved surface thereby reducing the computational memory. It is also shown in Figure 3.15 that the magnetic flux density is high near the permanent magnet and decreases as we move away along the axis. The range of magnetic flux density (0.2-1.2 Tesla) computed

using the model and the analytical solution for the given microfluidic system was also almost of same order of magnitude as reported in real microfluidic devices [37, 47, 139].

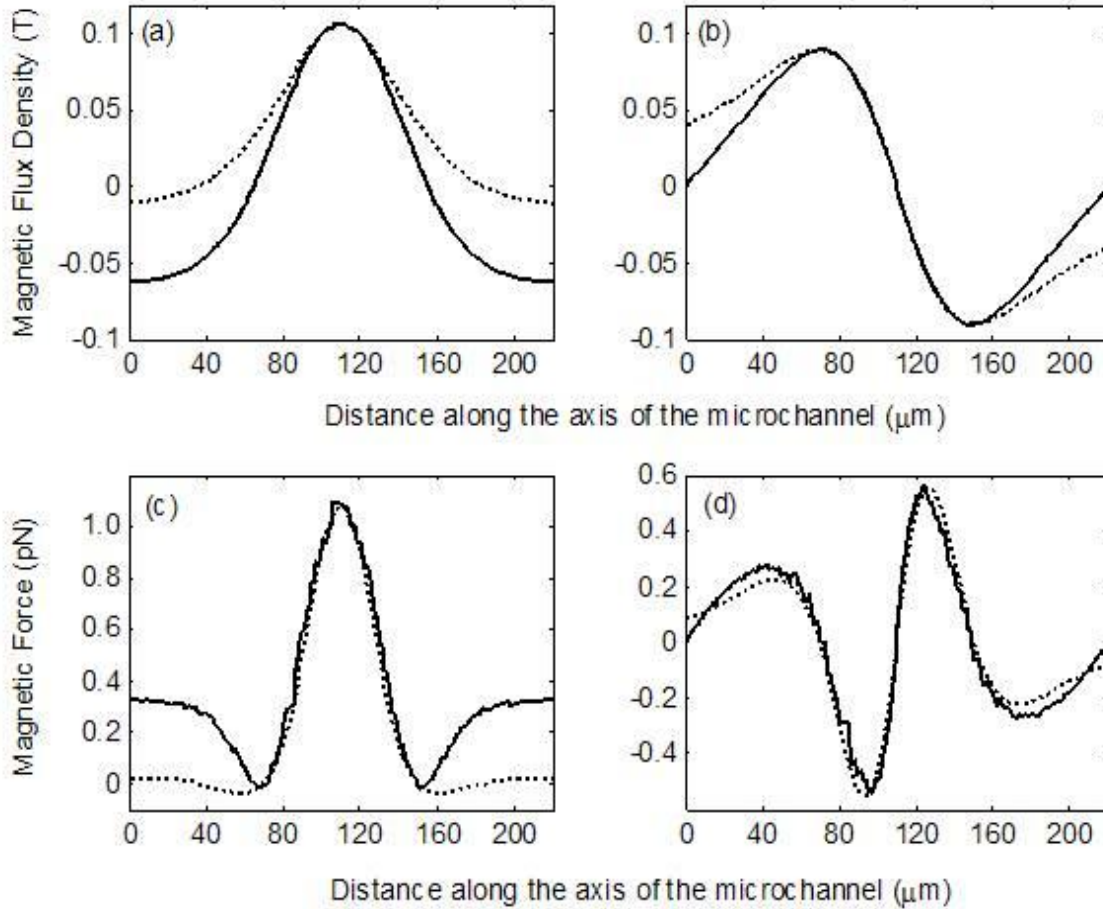


Figure 3.16 Magnetic field components (a, b) and magnetic force components (c, d) on a magnetic nanoparticle of 50nm diameter along the axis of the micro-channel, Solid lines represent finite element analysis (FEA) whereas dotted lines represent analytical solution

Figure 3.16 shows the computed magnetic flux density components (B_x , B_y) and corresponding magnetic force components (F_x , F_y) acting on nanoparticles along the axis of microchannel. It can be seen in Figure 3.16a, that B_y obtains the maximum value at the center of permanent magnet whereas B_x , as shown in Figure 3.16b oscillates around the central axis of the microchannel and peaks at the edges of the magnet. The vertical and horizontal component of magnetic force F_y and F_x as shown in Figure 3.16(c & d) has a similar profiles as their magnetic

field counterparts. The vertical component of magnetic force F_y is strongest above the center of magnet and is responsible for magnetic nanoparticle capture. Whereas, the horizontal component F_x is responsible for the oscillatory movement of the nanoparticles within the channel. For all the cases studied the numerical results were in very good agreement with the analytical predictions and indicate that the current finite element model is valid. The slight deviation that was seen in the simulations was due to the fact that numerical computation scheme employed slightly curved edges of the magnet whereas analytical expressions assumes exact rectangular permanent magnets. Moreover, the computed values of magnetic forces obtained using mathematical model was of same order of magnitude (e.g.; 0.1-1 pN) as reported by Gijs et al.[37]. The analytical equations used in this study can express simple physical principles but when the system involves coupled problems and complicated geometries, these expressions becomes too complicated and therefore, finite element based software, COMSOL was used.

3.2.3.2 Magnetic nanoparticle transport using particle tracking

Equations 3.17-3.30 as described above were used to study the transport of magnetic nanoparticles under the influence of magnetic field. It was assumed that the transport of fluid carrying magnetic nanoparticles is non-magnetic, and has a density and viscosity equal to that of water. Figure 3.17a shows the simulated induced particle velocity of nanoparticles under the influence of magnetic field whereas Figure 3.17b shows the velocity profile when there is no magnetic field. It is clearly seen that the velocity profile remains unaffected and follows a laminar flow when there is no magnetic field whereas when there is magnetic force, the velocity profile is affected and the fluid with dispersed magnetic nanoparticles tend to move towards the magnet. In order to understand the dynamics of the transport process within the channel geometry, the trajectories of magnetic nanoparticles were predicted.

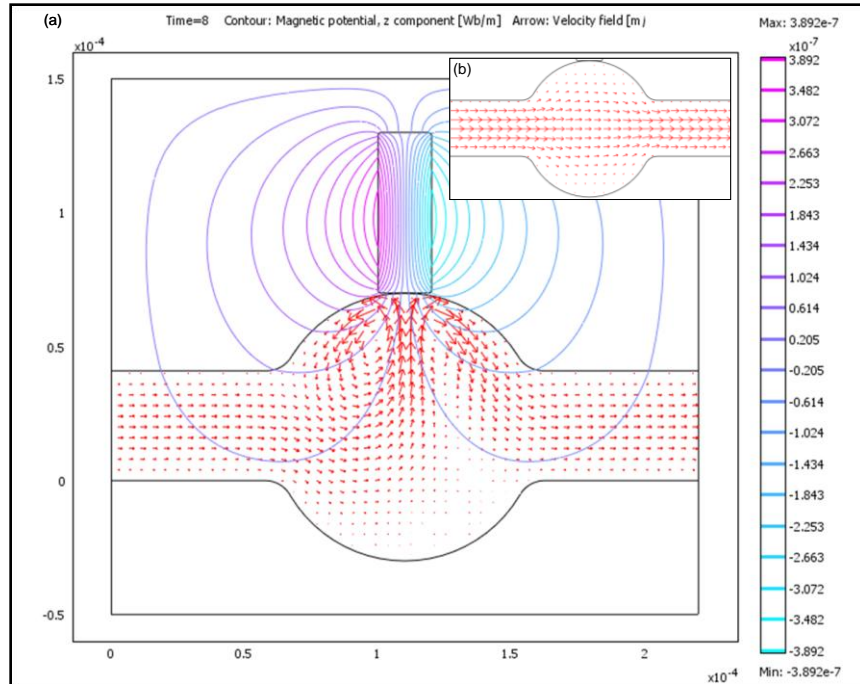


Figure 3.17 Simulated contours of constant magnetic vector potential (flux lines) and induced particle velocity with (a) and without (b) magnetic force using finite element model. Magnetic vector potential has a unit of Wb/m.

Two different diameters of magnetic nanoparticles (25 nm and 50 nm) are launched from ten different positions within the geometry ranging from 0 to 40 μm in y-direction as shown in Figure 3.18. It shows that larger nanoparticles (50 nm) had smaller trajectories and are trapped much easily as compared to smaller nanoparticles (25 nm) under similar conditions of applied magnetic field ($M=10000 \text{ A/m}$, $\mu_r=1$). This is due to the fact that magnetic forces are proportional to the size of magnetic nanoparticles. Hence, nanoparticles with larger diameter experience more magnetic force when compared to smaller nanoparticles therefore they tend to get captured much easily.

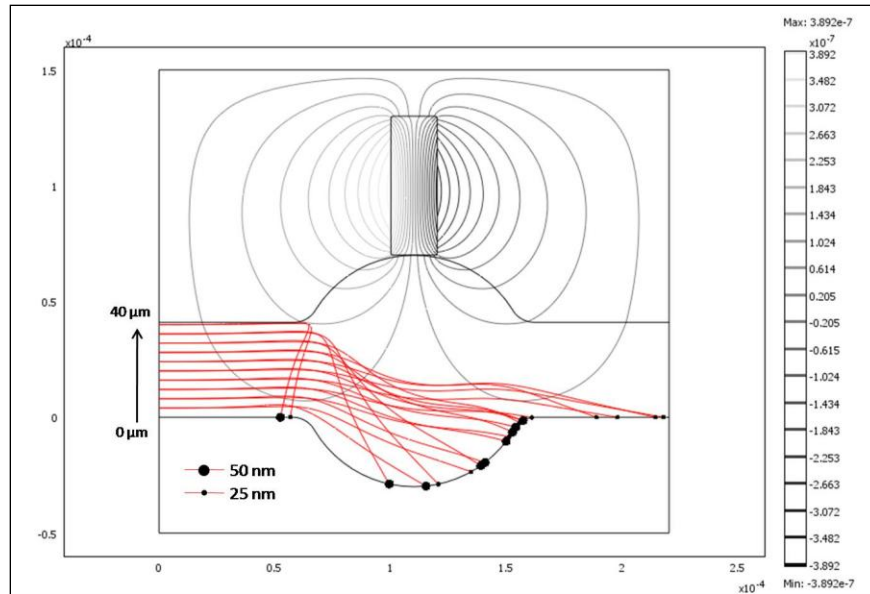


Figure 3.18 Simulated path of magnetic nanoparticles of 50 nm and 25 nm diameter shows that the trajectory of nanoparticles also depend on point of release with position varying in y-direction from 0 to 40 μm .

It is obvious that in order to trap smaller nanoparticles a higher magnetic force or more specifically higher magnetic field has to be applied across the channel. It is also observed that trajectories of nanoparticles differ dramatically with the position of the nanoparticles from where they are launched. This is due to the spatial variation of magnetic force components within the microchannel which alters the velocity profile of nanoparticles from where they are launched resulting in overall change in trajectories.

3.2.3.3 Parametric Analysis

The effects of inlet velocity of fluid, diameter of magnetic nanoparticles, and magnet's magnetization on the trapping efficiency of the microfluidic system are illustrated in this section. Figure 3.19 shows that on increasing the inlet velocity of the fluid the trapping efficiency decreases because the drag force on the magnetic nanoparticles tend to overcome the magnetic force responsible for capture thereby decreasing the overall trapping efficiency.

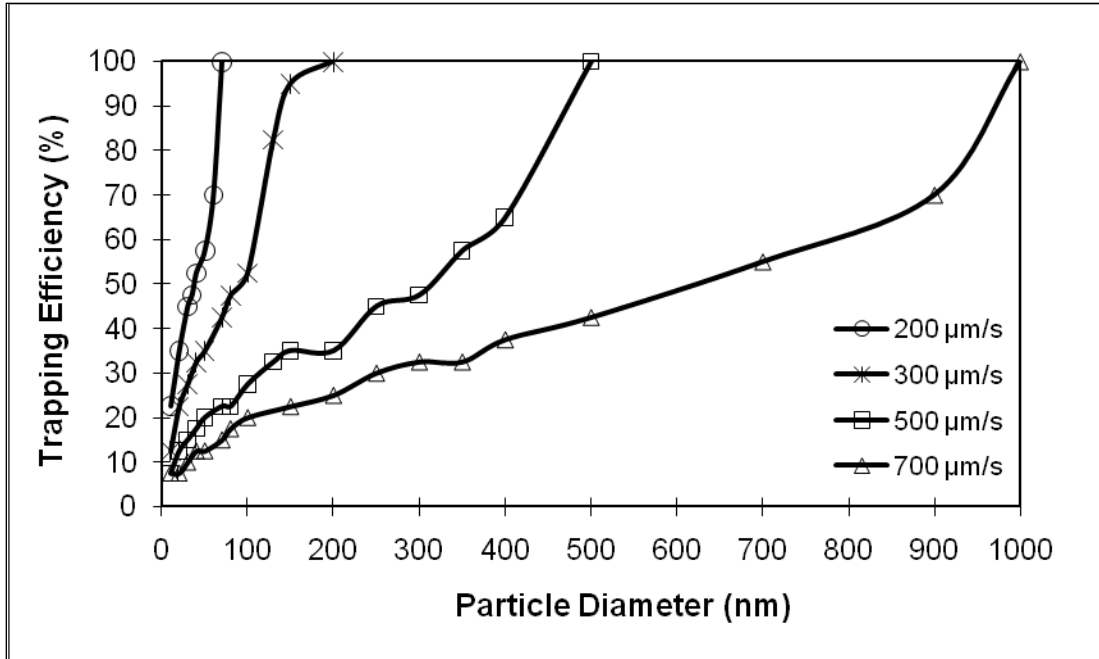


Figure 3.19 Variation of trapping efficiency of magnetic nanoparticles with the nanoparticle diameter (magnet's magnetization was kept constant at 10000 A/m).

This is also true when the diameter of magnetic nanoparticles tends to decrease. Overall, the inlet velocity of fluid is inversely and diameter of nanoparticles is directly proportional to the trapping efficiency. It was concluded from the analysis (Figure 3.19 and Figure 3.20) that in order to capture magnetic nanoparticles of 100 nm or less, the inlet velocity of fluid with which magnetic nanoparticles are launched in the given system should not exceed 100 $\mu\text{m/s}$. This is critical when designing a microfluidic bioseparation device because a too high inlet velocity would tend to decrease the trapping efficiency whereas too low might slow down the overall separation process which would make it unlikely to be used for point-of-care analysis. Therefore, the prediction of a more optimum range of inlet velocities of fluid carrying the magnetic nanoparticles will be important in designing an efficient microfluidic bioseparation device.

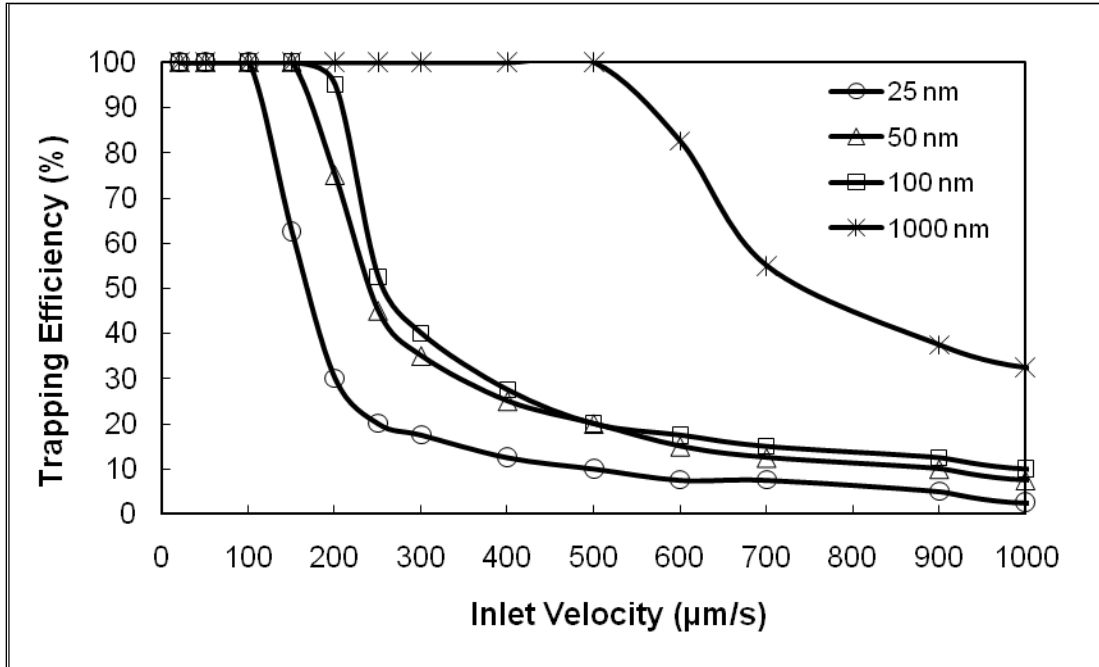


Figure 3.20 Variation of trapping efficiency of magnetic nanoparticles with the inlet velocity of fluid entering the microfluidic system (magnet’s magnetization was kept constant at 10000 A/m).

It was also observed from the analysis that larger nanoparticles/microparticles (1000 nm) tends to get captured even at higher inlet velocity (1000 µm/s). Magnetic field characterized by magnet’s magnetization also play an important role in optimizing the performance of microfluidic bioseparation system. Therefore, the effect of magnet’s magnetization on the trapping efficiency is also studied and illustrated in Figure 3.21. The inlet launch velocity of 100 µm/s was used in these simulations because it is the most optimum velocity obtained from the above analysis for trapping magnetic nanoparticles of less than or equal to 100 nm. It was seen from Figure 3.19 that higher value of magnet’s magnetization is required in order capture smaller magnetic nanoparticles and vice versa. For example, in order to capture magnetic nanoparticle of 50 nm completely in the simulated microchannel, the most optimum magnetic field strength should be equal to or greater than 6000 A/m whereas if a 10 nm magnetic nanoparticle is used in

the separation scheme than magnet's magnetization should not be smaller than 12000 A/m. In this way a range of most optimum magnetic field strength can be predicted using the model.

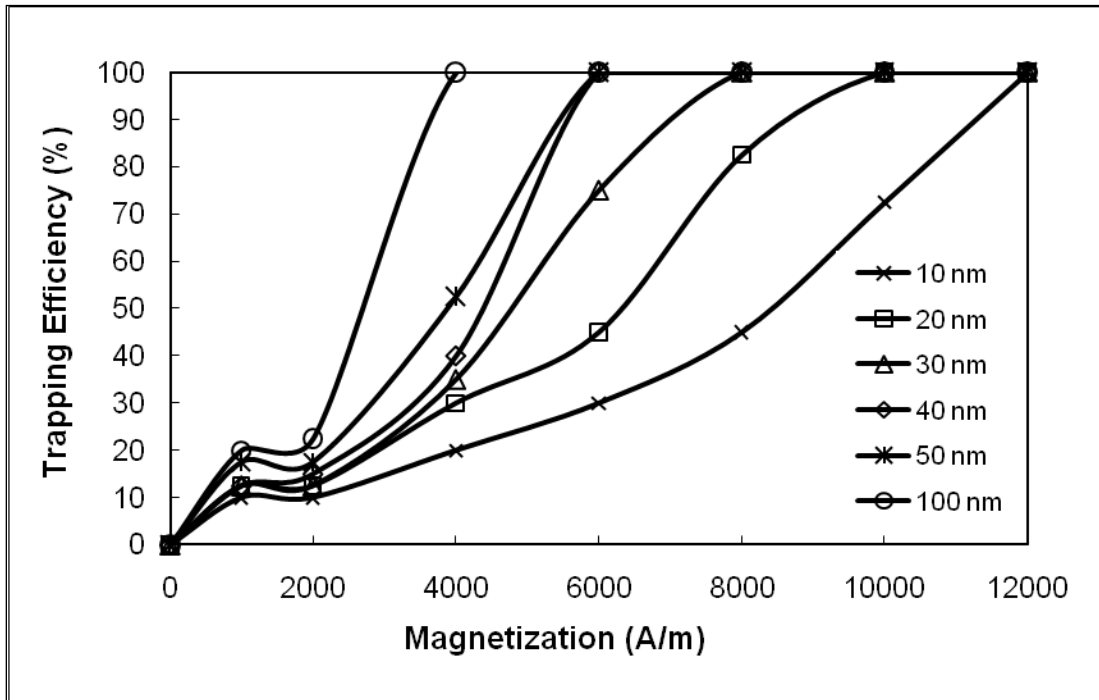


Figure 3.21 Variation of trapping efficiency of magnetic nanoparticles with the magnetization of magnet (Inlet velocity was kept constant at 100 μ m/s).

Based on the above analysis it can be seen that inlet velocity of fluid carrying the magnetic nanoparticles, the diameter of magnetic nanoparticles and the magnetic field strength are three most important parameters that can be optimized in order to enhance the performance of microfluidic bioseparation system. For example, if 50 nm magnetic nanoparticle is to be used in the bioseparation scheme, based on the above analysis the most optimum values of inlet velocity of fluid and magnet's magnetization would be 100 μ m/s and 6000 A/m respectively. Despite the successful prediction of these optimized values one should note that there are other factors which contribute significantly to further enhance the device performance.

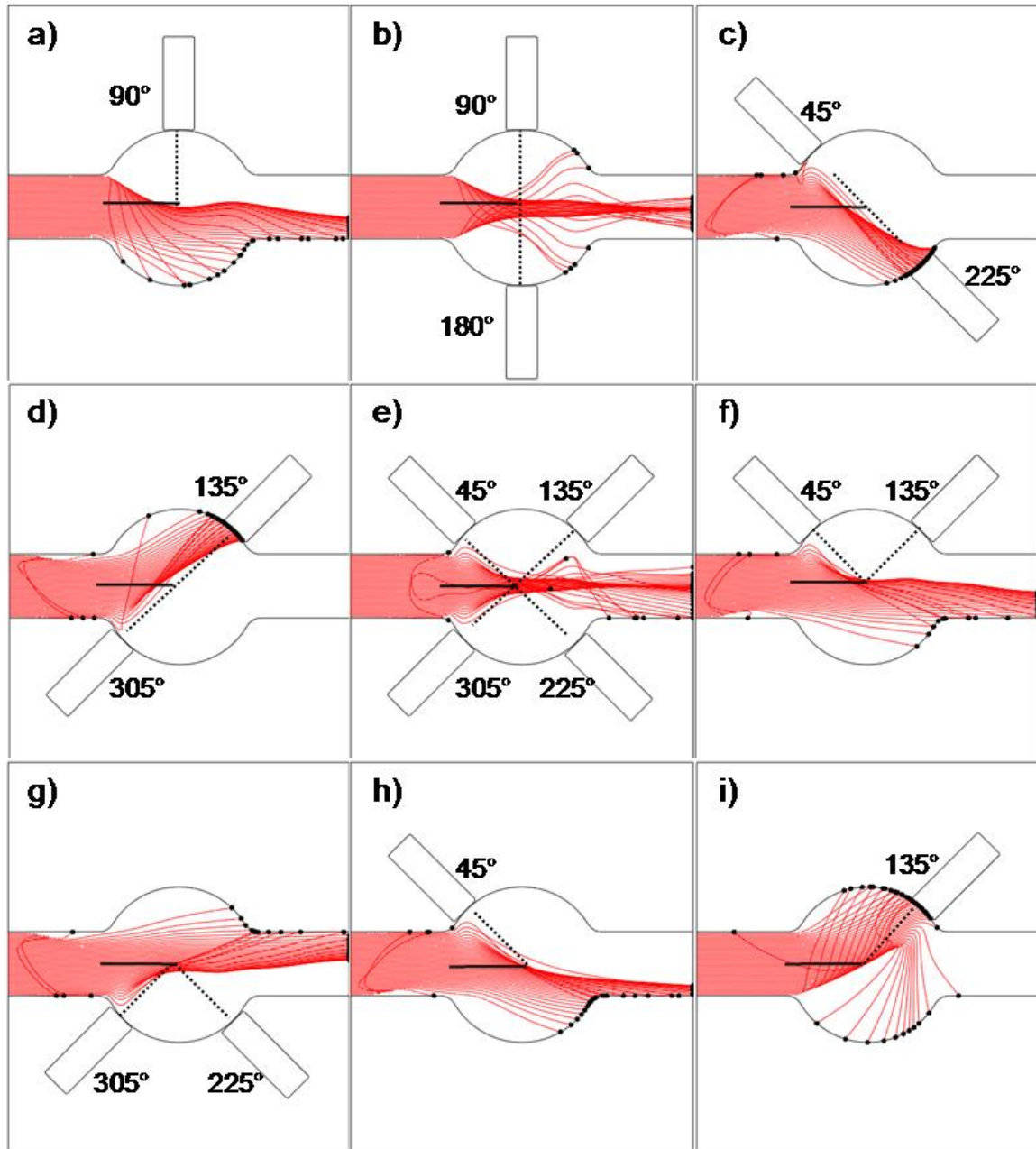


Figure 3.22 Simulated trajectories of magnetic nanoparticles (50 nm) under varying magnetic field obtained by varying the angular position of permanent magnet (a-i) around the microchannel. The permanent magnet is placed with reference to center solid line at different angles. Dashed lines indicate the angular position of magnet. The red lines with a black dot represent the trajectory of magnetic nanoparticles within the microchannel.

Parameter such as position of permanent magnet around the microchannel is also critical in dictating the resulting bioseparation efficiency. In order to demonstrate that magnet's position around the microchannel also play an important role, nine different scenerios were chosen based

on the number of magnets as well as on their angular position with respect to microchannel inlet. Figure 3.22(a-i) shows nine different angular position of magnet and the trajectories of magnetic nanoparticles of 50 nm diameter launched at a initial velocity of 100 $\mu\text{m/s}$. The magnetization value of the permanent magnets used in the simulations was kept constant at 4000 A/m. Figure 3.22(e) illustrate the scenerio were four magnet's are used, Figure 3.22 (b,c,d,f,and g) illustrate the scenerios were two magnets are used,whereas only one magnet is used in scenerios shown in Figure 3.22(a,h,and i). The trapping efficiency for all the nine scenerios were calculated and presented in Figure 3.23. It is seen that the trapping efficiency was largely dependent on the angular position of magnet around the microchannel rather than on the number of magnets. Even employing four magnets resulted in a smaller (20%) trapping efficiency as seen from Figure 3.23 (e). It was also demonstrated that when two magnets were kept at inclined position with respect to inlet flow as seen in Figure 3.23 (c and d) the trapping efficiency was 100% but when these magnets are kept perpendicular to the flow the trapping efficiency was very small (17.5%) because the magnetic force from opposite magnets tend to cancel out each other and the drag force dominates resulting in more magnetic nanoparticles being flushed out or removed. It is futher seen that 100% trapping efficiency can be achieved even with one magnet. This is done by placing it at angle of 135° with respect to inlet flow as seen from Figure 3.23 (i). From the earlier analysis, it was found that 6000 A/m of magnet's magnetization was sufficient to capture completely 50 nm particles flowing with an inlet fluid velocity of 100 $\mu\text{m/s}$ when the magnet was kept perpendicular to the inlet flow but if the same magnet is kept an angular position of 135° with respect inlet flow, 4000 A/m or 33% less magnetic field strength would be required. This further proves that the angular position of magnet is very important and the device performance could further be improved by adjusting the angular position of permanent magnet

around the microchannel which is equivalent to optimizing the spatial variation of magnetic field gradient in the channel.

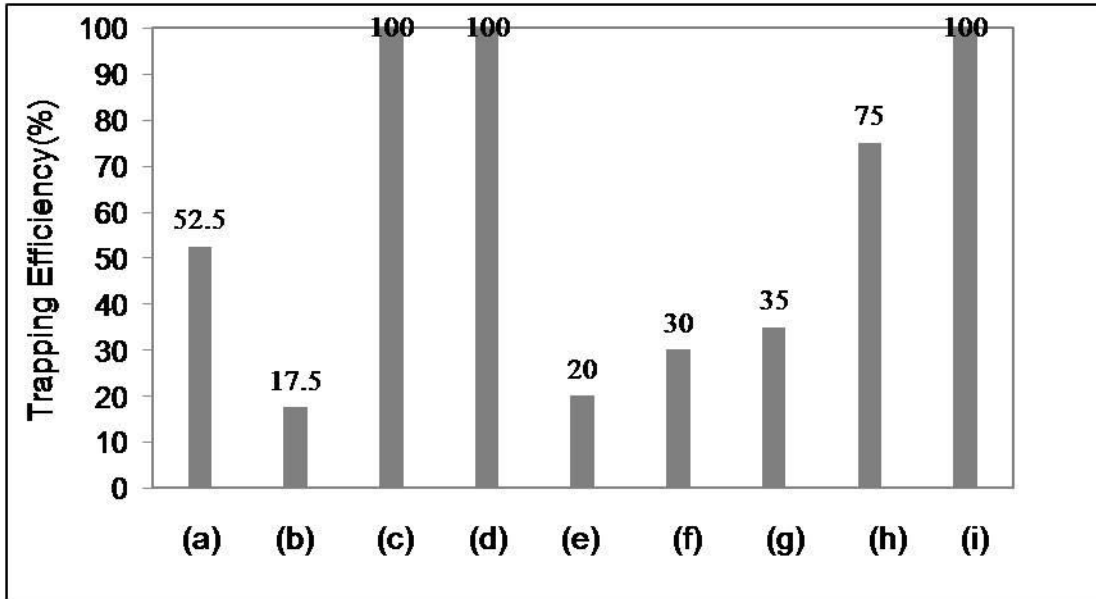


Figure 3.23 Predicted values of trapping efficiency for nine different scenarios (a-i) as described in figure 3.22.

3.2.4 Conclusion

A model for predicting the capture and transport of multiple magnetic nanoparticles in a microfluidic system is presented in this work. The model is based on coupling fluid flow with the magnetic field and solved using finite element technique. The model was used to study the effect of various parameters such as inlet flow velocity, size of magnetic nanoparticles, magnetic field strength on the capture efficiency. It also predicted the trajectories and demonstrated that the capturing process is not only altered by the size of but also by the position of magnetic nanoparticles in the microchannel. The model helped in successfully predicting the optimized values of inlet velocity, nanoparticle size and magnetic field strength and demonstrated that the device performance could further be improved by adjusting the angular position of permanent magnet around the microchannel. The quantitative analysis and predictive capability of this

model can be used to design microfluidic magnetic separation devices that will enhance clinical diagnostic and biomolecular assay development.

3.3 Magnetic Nanoparticle enhanced microfluidic Surface-based Bioassay

3.3.1 State of the Art

Mass transfer and reaction kinetics play a key role in developing high performance microfluidic detection system for life sciences and medical diagnosis. Most of these microfluidic devices rely on recognition–binding event most typically antigen-antibody and are used for detecting disease markers [150], drug screening [151], protein characterization [152], and DNA detection[153]. The fluid containing the target antigen flows through the microfluidic channels and is brought in contact with the surface bound complementary antibody. The antigen-antibody complex is detected and quantified either by using fluorescent techniques [154, 155] or surface plasmon resonance [156, 157] or by electrochemical methods [158, 159]. In the past, several bioassays have been developed on a microfluidic platform [49, 161, 217] in order to provide sensitive, selective, and rapid detection of biomolecules. The small length scales and the flow conditions often used in these microfluidic devices lead to low Reynold’s numbers ($R = uL / \nu$ where u is the velocity of fluid, L is the length of microchannel and ν is the kinematic viscosity), which is normally less than 1. Therefore, molecular diffusion becomes the only method to deliver antigen to the surface bound antibodies, as such, the binding reaction is limited by mass transport [218]. Moreover, the diffusivity of biomolecules such as DNA, protein, cells etc is of the order of 10^{-11} – 10^{-14} m²/s and their corresponding time to diffuse a distance of 100 μm is approximately 10^3 – 10^6 seconds, which is significantly long so greater channel length would be required to bring different biomolecules together through pure diffusion. In order to overcome the mass transport limitations researchers in the past have adopted several mechanical and physical strategies for replenishing the target antigen to the sensor surface. It was also demonstrated in the past that the integration of active and passive micromixers [69, 98, 99] considerably improved the biosensor

performance. Several other strategies such as periodic pulsing in serpentine channels [219] and bubble-based mixing [220] also showed significant improvement. While these approaches efficiently improved the mixing performance, complicated design and high fabrication cost are required, thus limiting its usage in applications that are driven by cost and time. Other passive schemes based on decreasing the diffusion length [72] by using narrow channels and creating consecutive splitting and recombining scheme[221] have also shown great potential but limitation with these passive configurations is the clogging of narrow channel in a high throughput application. Recently, magnetic micro/nanoparticles have been widely used as signal reporters to detect various biomolecules [158] such as pathogenic bacteria [162], human allergen [163], and to facilitate location of cancerous cells [164]. There have been promising developments [54-56] made in last few years in the detection of magnetic particles based on giant magnetoresistive sensor (GMR). Highly sensitive detection close to single magnetic particle is possible [222], if a particle is in close proximity and as long as all system dimensions including particle size and position, sensor area are scaled down proportionally[37, 54]. There are relatively no efforts adopted where magnetic nanoparticles are employed to enhance the chemical sensitivity of surface binding reaction in a flow-through system. The ability to manipulate magnetic nanoparticles externally using magnetism over the section of microchannel provides the motivation of enhanced reaction rate. The target bio-molecule labeled with MNPs can be attracted towards the binding surface using the magnetic force, resulting in reduced diffusion times and increased recognition binding, which is beneficial for higher signal and better sensitivity. In addition, magnetic nanoparticles possess several advantages such as stability over time, high surface to volume ratio for chemical binding, minimum disturbance caused by the attached biomolecules because of their extremely small size, and moreover they are

superparamagnetic, i.e., their magnetization without a magnetic field is zero [37, 61]. Overall, magnetic nanoparticles provide a simple solution for rapid and enhanced biosensing on a microfluidic format since no complicated microfabrication is required to define geometrical constrictions for reducing diffusion barriers. It is important to recognize that design of microfluidic detection system is a truly multidisciplinary, multiphysics, and multiscale engineering problem that involves convection, diffusion and binding reaction. Therefore, in order to study the interaction between these complex phenomena and propose optimized design parameters for development of efficient microfluidic devices, several computational studies [65, 223-227] have been reported. While these strategies considerably improved the reaction kinetics but often involved optimizing the design of the channel or the shape of the sensing area which can consequently impose high fabrication cost due to complicated geometry. In this work we present simpler and novel approach based on magnetic nanoparticles to improve the performance of surface-based bioassay. In order to enhance the diffusional transport, the target antigens are tagged with magnetic nanoparticles and then focused and directed towards the sensing zone by using magnetic field force. This causes more interaction of antigens and surface-bound antibodies resulting in increased binding and consequently enhancement in binding kinetics. In order to quantify the effect of convection, diffusion, and magnetic field on the surface binding kinetics and consequently help in designing, optimizing and developing sensitive surface-based microfluidic biosensor that addresses the need for faster bio-assays, a finite element “numerical prototype” is developed. The simulation performed using the developed model at the concept stage will provide an excellent estimate of the potential to use magnetic nanoparticles for rapid surface-based bioassays.

3.3.2 Model Development

This work demonstrates a magnetic nanoparticles-based approach that can be exploited to enhance the performance of recognition-binding event in a microfluidic detection system. The theoretical model developed here predicts the bulk transport of antigen tagged with magnetic nanoparticles (MNPs) and predicts the association profile of a binding event between bulk antigen and surface immobilized antibody in the capture area, also called as sensing zone. The numerical scheme was setup on the basis of the reported experimental configurations [223, 225] in which the sample to be analyzed is directed to the sensing area by convective flow and then finally to the binding site by diffusion. In this study a single microchannel with the capture area is considered. A schematic representation of the microfluidic channel and integrated sensing surface, along with corresponding co-ordinates and dimensions, is given in Figure 3.24. The microchannel considered for simulation is 20 μm deep and 200 μm long with a sensing zone 30 μm long located at the center of the microchannel. The capture area present in the microchannel is immobilized with surface bound antibodies of a given surface density. It is assumed in the model that the antigen will not be lost by sticking to the walls elsewhere other than at the capture site because the walls are considered to be treated with protein-repellent reagent. The target antigens are combined with functionalized MNPs according to the reaction shown in Fig. 1(b), providing a magnetic identity to the target which can be manipulated using a magnetic field generated due to electric wires present in the vicinity of the capture area around the microchannel.

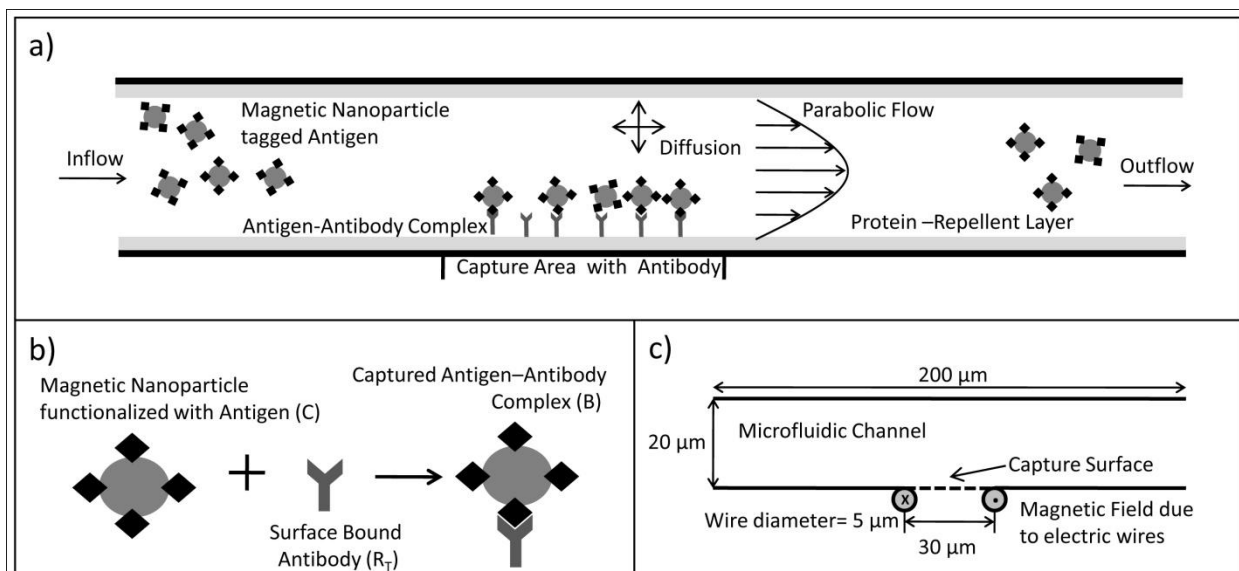


Figure 3.24 Schematic representation of the numerical setup. (a) Simplified cross-sectional scheme of magnetically functionalized antigen capture due to surface bound antibody in a microfluidic biosensor. The liquid enters from the left and flows under laminar conditions. The antigen is allowed to diffuse in all the direction. Wall elements other than capture area are protected against unspecific binding and in simulation are considered perfect. (b) Schematic of surface binding reaction on the capture area, where the magnetically labeled antigen, C binds to the immobilized antibody, R_T forming the antigen-antibody complex, B. (c) Dimensions of the microfluidic channel used in the simulation with the position of electric wire for magnetic field force generation.

The magnetic nanoparticles (MNPs) together with target antigen experience attractive magnetic force which pulls the target antigen towards the capture site as such more interaction of antigen and surface-bound antibodies occurs, resulting in enhancement of binding event. The model geometry shown in Figure 3.24c is simplified into a two dimensional problem by focusing on the axial cross-section of the microchannel. Although a full three dimensional simulation would be more accurate, the qualitative trend would be the same. In all the simulations, it is considered that antigen-MNP complex solution flows into the microchannel at a constant flow velocity. The flow of an aqueous solution of antigen-MNP complex inside a small channel is laminar and for the model a parabolic flow profile is considered. The antigen-MNP complex is transported by convective flow towards the sensing zone and is free to diffuse in order to bind with surface immobilized antibody which is accounted by applying a ligand-receptor model for quantifying association and dissociation events. In order to quantify the sensing performance of biosensor,

we define equilibrium time, the time when 90% of the target antigen complex gets bounded with surface immobilized antibodies. This time is predicted for different conditions of magnetic field and non-magnetic field influenced binding events and an optimized configuration is proposed for enhancing the performance and ultimately improving the efficiency of microfluidic biosensor-based molecular detection. The binding kinetics, magnetic field effect and the convection-diffusion model is described in more detail in the following.

3.3.2.1 Fluid Flow Equation

The magnetic nanoparticle of 50 nm diameter is assumed to be tagged with target antigens which are dispersed in the fluid of viscosity η ($10^{-3} \text{ kg/m}\cdot\text{s}$) and density ρ (10^3 kg/m^3) equal to that of water. The aqueous solution of antigen-MNPs is given a parabolic velocity at the entrance of the channel. It is assumed that the particles move with constant velocity and the early acceleration phase of antigen-MNP complex within the fluid is neglected. This approximation is based on the fact that the time constant for acceleration phase is too small for the scale of geometry and the size of particles used in the simulation, therefore it can be neglected and the liquid solution can be treated as continuum in the model. The magnetic force due to external magnetic field acting on the antigen-MNP complex transfers momentum to the surrounding fluid thereby changing the flow profile. The flow velocity u for this incompressible fluid ($\nabla \cdot u = 0$) is described using Navier-Stokes equation,

$$\rho \frac{\partial u}{\partial t} + \rho(u \cdot \nabla)u = -\nabla p + \eta \nabla^2 u + F_{vol} \quad (3.32)$$

Where, u is the carrier fluid velocity field (m/s), p is the pressure (N/m^2), and F_{vol} is the volume force (N/m^3). The momentum transfer from MNPs to the fluid is incorporated by setting the volume force $[F_{vol} = \alpha F_m]$ term equal to the magnetic force acting on a single MNP

multiplied with MNP number density, α , which is the number of MNP per unit volume. This term is very important because it couples the fluid flow equation with the static magnetic field equation. The magnetic force is proportional to the magnetic field, magnetic field gradient, magnetic susceptibility of nanoparticles and the fluid, and the volume of nanoparticles. It is assumed that volume does not change much when the nanoparticles are functionalized with antigens. Moreover, It was assumed in the model that the density of magnetic nanoparticle is low in the incoming suspension, therefore particle-particle interaction (for e.g.: due to Van der Waals forces) will be negligible. This assumption is based on the experimental work performed by Choi et al.[228]. Similarly, due to extremely small size of incoming magnetic nanoparticle tagged antigen (~ 50 nm) the sedimentation effects will have negligible influence on the overall mass transport. The magneto-static equation used in the model is described in more detail in the following section.

3.3.2.1.1 *Boundary Conditions*

The flow of fluid with antigen-MNP complex is assumed to be parabolic at the inlet of the microchannel, and moves in the direction of x-axis with zero velocity in y-direction. The average flow velocity of the fluid with magnetic nanoparticle was u_0 . No slip condition was applied along the walls of microfluidic system and at the outlet, pressure condition is set equal to zero.

3.3.2.2 **Magneto-static Equation**

It is assumed that the magnetic field is governed by magneto-statistics and the static magnetic field is described using Maxwell-Ampere's law given by;

$$\nabla \times H = J \tag{3.33}$$

Where H is the magnetic field vector (A/m) and J is the current density vector (A/m^2),

According to Gauss law for magnetic flux density, B (Vs/m^2)

$$\nabla \cdot B = 0 \quad (3.34)$$

In order to describe a relation between B and H a constitutive relation given by the following equation is used in the model.

$$B = \mu(H + M) \quad (3.35)$$

Where, μ is the magnetic permeability and M is the magnetization vector. The magnetic permeability can also be expressed as $\mu_0\mu_r$, where μ_r is the relative permeability of wire (=1) and is assumed to be constant in all the simulations and μ_0 is the permeability in vacuum ($\mu_0 = 4\pi \times 10^{-7} \text{ N/A}^2$). In order to solve Maxwell equations, the two first order partial differential equations given by Eq. 3.34 and 3.35 are converted into a single second-order partial differential equation involving only one field variable called magnetic vector potential A . The magnetic flux density B is represented by curl of the magnetic vector potential A according to the following equations

$$\nabla \times A = B; \nabla \cdot A = 0 \quad (3.36)$$

After substitution of Eq. 3.36 in equations Eq. 3.33, 3.34, and 3.35, the following vector equation is obtained;

$$\nabla \times \left(\frac{1}{\mu_0\mu_r} \nabla \times A - M \right) = J \quad (3.37)$$

It is assumed that the magnetic vector potential has a nonzero component only perpendicular to the plane A_z which basically simplifies the 2D; the externally applied current density J was calculated for a wire diameter of $5\mu\text{m}$ carrying 1A surface current throughout the simulation. The above equations are solved in magnetostatic module of COMSOL Multiphysics software (COMSOL AB., Stockholm, Sweden). The force on antigen-MNP complex is assumed to be equivalent to the force acting on spherical magnetic nanoparticle having a point-like dipole

moment. The force acting on dilute suspension of magnetic nanoparticles is described using the following equation given in literature [61].

$$F_m = \frac{V\Delta\chi}{\mu_0} (\vec{B} \cdot \nabla) \vec{B} \quad (3.38)$$

Where, V is the volume of nanoparticles, $\Delta\chi$ is the difference in magnetic susceptibility of the nanoparticle and the fluid which is kept constant throughout the simulation, and \vec{B} is the magnetic flux density obtained after solving Eq.3.37, The force obtained from Eq.3.38 is substituted in Eq.3.32 in order to obtain velocity profile of antigen-MNP complex suspension.

3.3.2.2.1 Boundary Conditions

A magnetic insulation boundary condition ($A_z = 0$) is applied along the system boundary. The interior boundaries between the wires and the air only assume continuity, corresponding to a homogeneous Neumann condition.

3.3.2.3 Convection-Diffusion Equation

The spatial and temporal variation of the antigen-MNP complex inside the microfluidic channel is described using the following convection-diffusion equation

$$\frac{\partial C}{\partial t} + u \cdot \nabla C = D \nabla^2 C \quad (3.39)$$

Where, u is the velocity field (m/s) obtained from the Navier-Stokes equation, C is the bulk concentration (mol/m^3) of antigen-MNP complex in a given solution, and D is the diffusion coefficient (m^2/s) of the solute which is assumed to be constant throughout the simulation.

3.3.2.3.1 Boundary Conditions

An initial concentration C_0 of antigen-MNP complex is given at the inlet boundary and convective flux was set at the outlet boundary, keeping insulation/symmetry in all the other boundaries.

3.3.2.4 Binding Kinetics Equation

The binding reaction at the capture site between the antigens tagged with magnetic nanoparticles C (mol/m^3) and the immobilized antibody R_T (mol/m^2) is schematically shown in Figure 3.24b and can be described by following reversible surface reaction;



$$\frac{\partial B}{\partial t} = k_{on}C(R_T - B) - k_{off}B \quad (3.41)$$

Where, B is the bound antigen-antibody complex (mol/m^2), k_{on} is the association rate constant ($M^{-1}s^{-1}$), and k_{off} is the dissociation rate constant (s^{-1}). Effect of association and dissociation rate constant on the binding kinetics was investigated by keeping the same affinity constant and results obtained are described in more detail in the later section.

3.3.2.5 Ideal case

Analytical solution can be obtained for the given mathematical problem in an ideal case, where there is no transport or diffusion limitation. It can be considered that the target antigen-MNP complex concentration is constant and in excess as compared to the number of immobilized antibodies inside the microfluidic channel. Therefore, we can assume it to be C_0 (mol/m^3). The rate of formation antigen-antibody complex is given by Eq.3.41. If there is no bound complex initially, the analytical solution of given partial differentiation equation becomes;

$$B = \frac{C_0 \cdot R_T}{C_0 + \frac{k_{off}}{k_{on}}} \left[1 - \exp\left(-\frac{t}{\tau}\right) \right] \quad (3.42)$$

$$\text{Where, } \tau = \frac{1}{k_{on}C_0 + k_{off}} \quad (3.43)$$

Therefore, the fraction of bound antigen-antibody complex will only be a function of rates constant k_{on} , k_{off} and initial antigen concentration C_0 , and is

$$\frac{B}{R_T} = \frac{C_0}{C_0 + \frac{k_{off}}{k_{on}}} \left[1 - \exp\left(-\frac{t}{\tau}\right) \right] \quad (3.44)$$

This equation is the “upper bound” and corresponds to the fastest binding event between antigen and antibody. Convection and diffusion effects tend to slow down the kinetics. In addition, the equilibrium can be calculated from Eq. 3.44 which is obtained when the time is put infinity and the fraction of bound complex will be;

$$\frac{B}{R_T} = \frac{C_0}{C_0 + \frac{k_{off}}{k_{on}}} \quad (3.45)$$

Eq.3.45 is used to calculate the fraction of bound complex when both convection and diffusion are present.

3.3.2.6 Numerical Simulation

The finite element software package, COMSOLTM Multiphysics (COMSOL AB., Stockholm, Sweden) is used to numerically solve the two-dimensional partial differential equations described in the model above. The model consists of four application modes: incompressible Navier-Stokes mode and magnetostatics mode to predict the convective velocity of antigen-MNP solution with and without the influence of magnetic field force, a convection-diffusion mode to

predict the bulk concentration of antigen-MNP complex within the microchannel, and a one dimensional geometry is defined under diffusion mode to predict the bound surface concentration of antigen-antibody complex. The meshing around the geometry is around 5 μm except near the sensing surface which was 1 μm in order to get more precise results. The model is solved in two steps using two different solvers. The magnetic fields are first solved using the non-linear solver and then Navier-Stokes and convection-diffusion equations are solved simultaneously with a time-dependent solver. The model predicts the bound antigen-antibody complex and association profile for different sets of conditions. The fraction of bound complex is obtained for different conditions by dividing the bound complex concentration with equilibrium concentration for “ideal case” as defined in the above section.

3.3.3 Results & Discussions

3.3.3.1 Validation of Numerical Model

The model developed in this work is based on coupling of mass transport with the surface binding reversible reaction. In order to compare the analytical results described in literature [229, 230] we assumed in our model that the reaction kinetics is irreversible and infinitely fast. The diffusivity of $10^{-11} \text{ m}^2/\text{s}$ and inlet MNP complex concentration of 10nM was kept constant throughout. It was found (see Figure 3.25) that the numerical results seems to agree very well with analytical results for hemicylinder reaction surface in the microchannel but for flat surface numerical solution gave higher values of total flux.

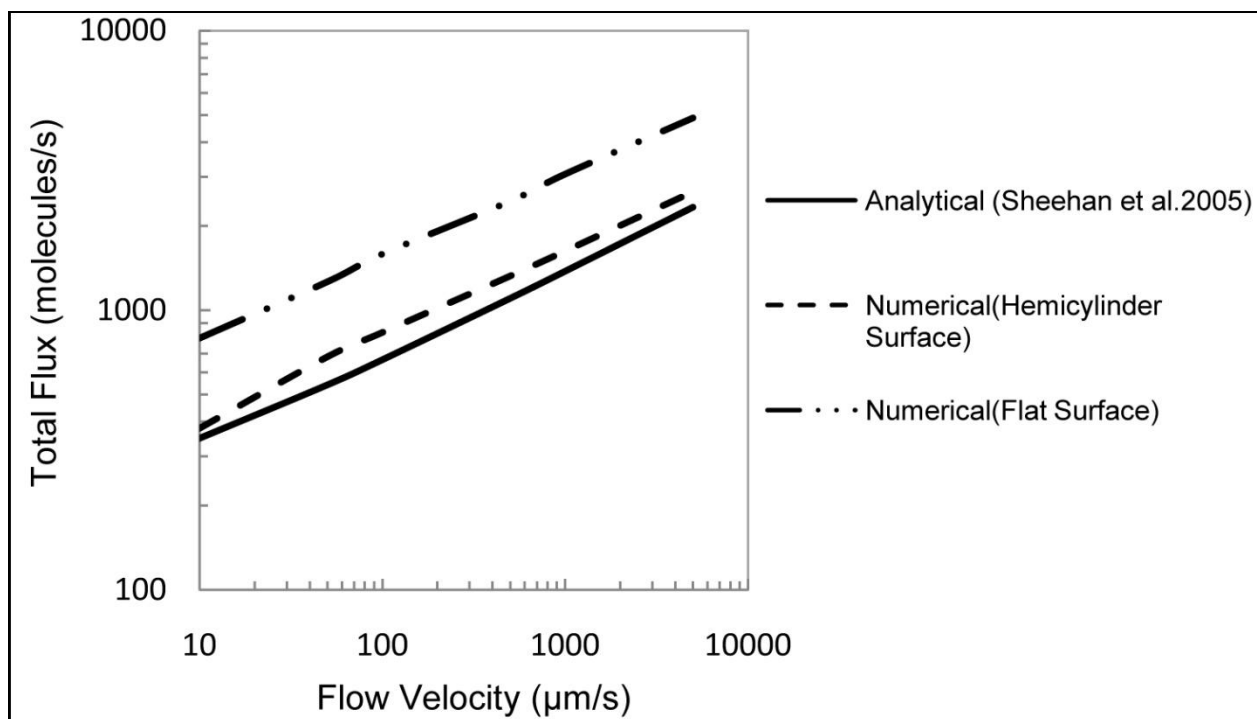


Figure 3.25 Variation of total flux with change in flow velocity. Solid line represents analytical results by using expression from Sheehan et al.[230], while dash and dash-dot lines represent numerical results for hemicylinder and flat reaction surface respectively.

This is true because the flat surface ($W = 30\mu\text{m}$) did not alter the velocity profile of incoming targets and offered more surfaces for binding reaction, whereas hemicylinder surface ($W = \pi R, R = 10\mu\text{m}$) altered the velocity profile for the given dimension of the microchannel (height=20, width=20, and length=200 μm) and consequently due to altered velocity it offered fewer surfaces for binding. Overall, the trend of total flux obtained for a steady state agree very well and increases with incoming flow velocity. The numerical model also gave comparable results with numerical models given in the literature [225, 226, 231] for incoming antigen-MNP complex in the microchannel without magnetic field effect.

3.3.3.2 Parametric Analysis

The model is further used to evaluate the influence of key parameters on the performance of surface kinetics-based flow through biosensors. The affinity constant, K_a ($= k_{on} / k_{off}$) between the target antigen and immobilized antibody plays an important role on the performance of a biosensor. Therefore, the effect of surface binding reaction constant on the detection performance is investigated for a 120-seconds-long capture step.

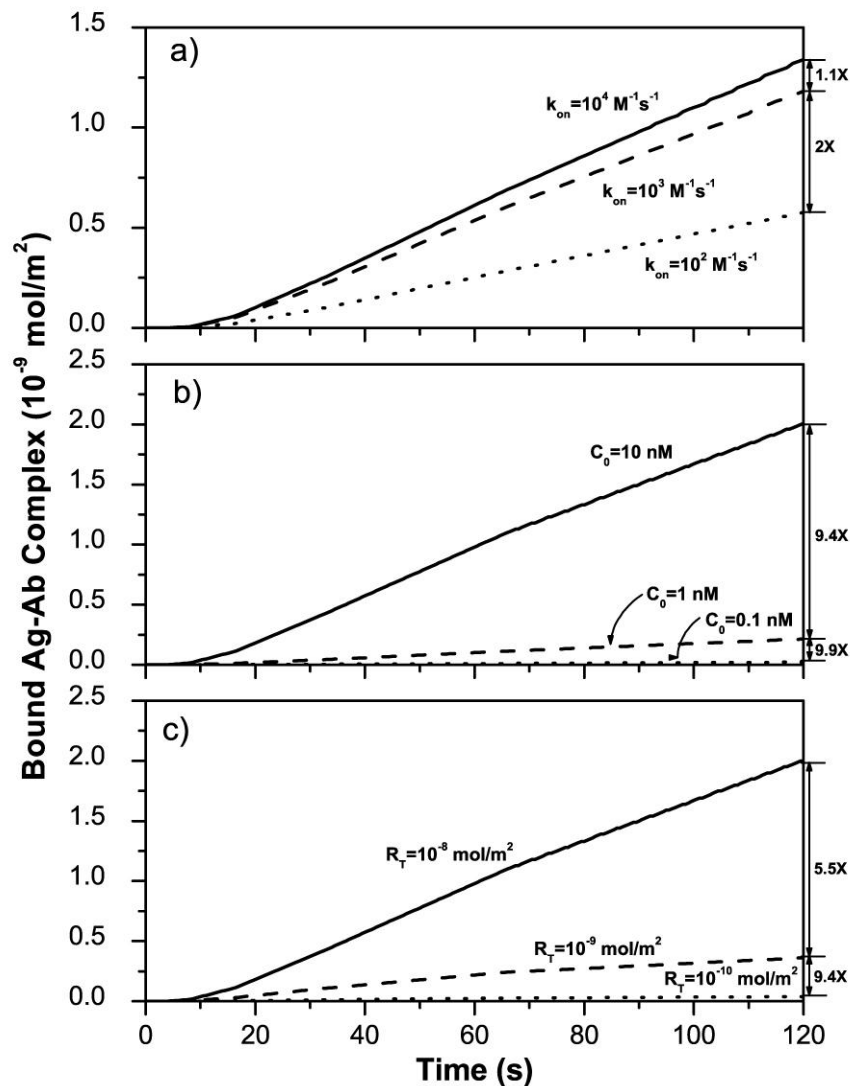


Figure 3.26 Effect of association rate constant (a), inlet concentration of antigen (b), and immobilized antibody density (c) on the concentration of bound complex B. Dash line represent the reference point. Solid and dotted lines represent a 10-fold increase and decrease in parameters respectively.

The association rate constant, k_{on} is changed from 10^2 to 10^4 ($M^{-1}s^{-1}$) with 10^3 ($M^{-1}s^{-1}$) chosen as reference point as shown in Figure 3.26a. The affinity constant, K_a is kept constant at $10^8 M^{-1}$ throughout the simulations and is comparable to the values reported in literature [65, 232, 233]. It is observed that the bound complex concentration, B increased by a factor of 1.1X and decreased by 2.0X when association rate constant is increased and decreased respectively by an order of 10 around the reference point. This suggests that the association rate at lower k_{on} is less diffusion limited. The effect of inlet concentration of antigen tagged with magnetic nanoparticle and antibody surface density on bound complex concentration is also investigated and shown in Figure 3.26b-c. We observed that when the inlet concentration is increased or decreased by an order of 10, there is linear increase or decrease of bound complex concentration. This trend is not observed when antibody density is changed around the reference point; instead there is smaller increase and larger decrease in bound complex concentration. This suggests that the antigens are deficient or limiting for the surface reaction of antigen and antibody in a microfluidic channel. Therefore in order to enhance the surface reaction and consequently reduce the detection time of microfluidic biochip, it is important to maximize the mass transport of antigen in the vicinity of the reactive surface. Similar trend was observed by Friedrich et al. [226] where only 10% of the target molecule reaches the sensor surface in order to bind to recognition molecule. This means that majority of the target antigens will flow without interacting with the surface-bound antibodies and the molecules that reach the surface due to high affinity will bind instantaneously. Therefore, in order to alleviate this problem, strategy based on increasing the mass transfer in a microchannel and consequently enhancing the surface kinetics is highly desirable.

3.3.3.3 Influence of Convection and Diffusion

The velocity of fluid entering the microchannel and the diffusion constant of the target antigens are important in optimizing the mass transport. For most of the practical microfluidic biochips the diffusion coefficients fall in the transport limited regime. Therefore, in order to investigate the effect of diffusivity on the formation of antigen-antibody MNP complex, diffusion coefficient was varied keeping all other parameters constants and the simulated results at $t=100s$ is presented in Figure 3.27.

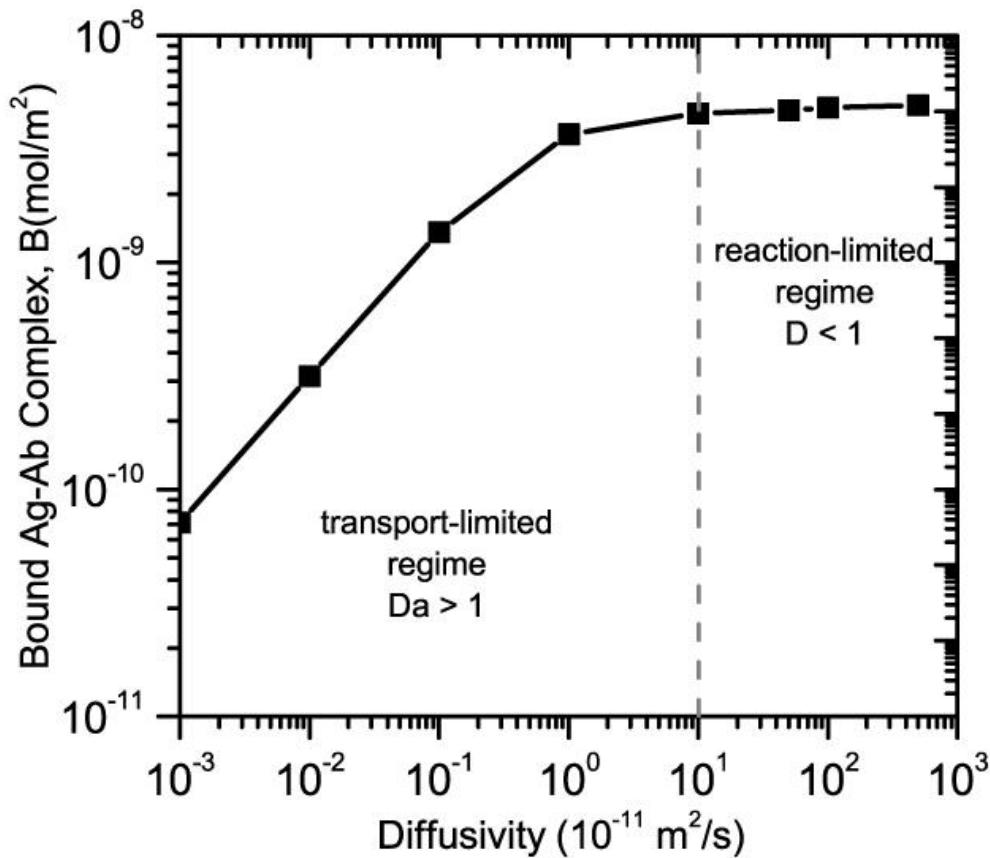


Figure 3.27 Effect of diffusivity on the formation of Ag-Ab complex at $t=100s$. Grey dash line represents the boundary between transport and reaction-limited region. (Parameters: $u_0=10 \mu\text{m}/\text{s}$, $c_0=10\text{nM}$, $R_T=10^{-8} \text{mol}/\text{m}^2$, $k_{on}=10^3 \text{m}^3/\text{mol}\cdot\text{s}$, and $k_{off}=10^{-2} \text{s}^{-1}$).

It was found that for low values of diffusivity ($< 10^{-10} \text{ m}^2/\text{s}$) the detection performance is limited by transport process, whereas at higher values the performance is dictated by reaction kinetics. For the conditions used in this work (diffusion coefficient $\sim 10^{-11} \text{ m}^2/\text{s}$ and inlet velocity ($\sim 10 \text{ } \mu\text{m}/\text{s}$) and also in typical protein detection system [234] the sensing performance of the device fall in transport-limited regime. Therefore, increasing the mass transport is the key for enhancing the detection time of these devices which is also consistent with the results obtained in literature [226, 231]. This was further illustrated by comparing the Damkohler number. The Damkohler number ($Da = k_{on}R_iH / D$), where H is the characteristic length equal to half the channel height, relates the rate of transport to target antigen on the surface to the rate of antigen-antibody binding. For $Da < 1$, the rate of binding is much slower than diffusion and the system is said to be reaction limited, while for $Da > 1$ the diffusion is much slower than the rate of reaction and the system is diffusion limited. The Da for sensing condition used in this work is about 10 ($\gg 1$), indicating that the binding of antigen-antibody complex is limited by diffusion.

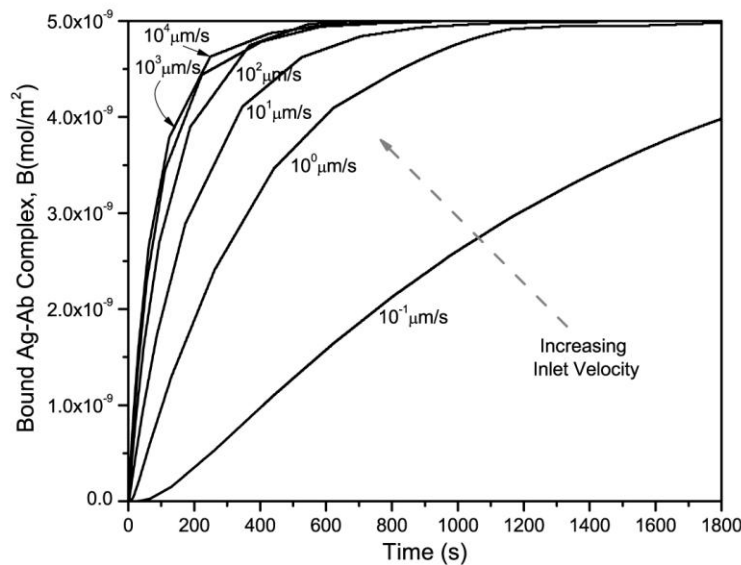


Figure 3.28 Effect of inlet flow velocity on the reaction kinetics of formation of antigen-antibody complex at the surface of microchannel. (Parameters: $c_0=10\text{nM}$, $R_T=10^{-8}\text{mol}/\text{m}^2$, $D=10^{-11} \text{ m}^2/\text{s}$, $k_{on}=10^3 \text{ m}^3/\text{mol.s}$, and $k_{off}=10^{-2} \text{ s}^{-1}$).

Furthermore, mass transport can also be increased by increasing the flow velocity of the incoming sample. In order to investigate the variation of inlet flow velocity on the formation of antigen-antibody MNP complex, inlet velocity was varied keeping all other parameters constants and the simulated results is presented in Figure 3.28. It can be seen that at low inlet velocity ($\sim 0.1 \mu\text{m}/\text{s}$), it takes longer time for the surface reaction to reach equilibrium because of insufficient mass transport of the target antigen towards the binding surface. Furthermore, as the inlet velocity is increased, it takes shorter time to reach equilibrium. However, further enhancement of time to reach equilibrium is less pronounced at very high inlet velocity (e.g., $u_0 = 10^3 \mu\text{m}/\text{s}$) as shown in Figure 3.28 and the reaction-limited region is reached [225]. The relative rate of the convective transport was compared with diffusional transport by non-dimensional shear Peclet number ($Pe_s = u_0 L^2 / HD$), where L is the length of sensing surface. The Pe_s number for current system (diffusion coefficient = $10^{-11} \text{ m}^2/\text{s}$ and inlet velocity = $10 \mu\text{m}/\text{s}$) is around 90, which implies that the diffusion of target molecule is slower than the convective transport. This further confirms that increasing the diffusional transport is the key for improving the sensing performance of these devices, findings that were consistent with the result described by Kim et al.[231].

3.3.3.4 Magnetic Nanoparticle Enhanced Reaction Kinetics

In order to increase the diffusion or refresh the consumed target molecule near the reactive surface we proposed a novel method of tagging antigens with magnetic nanoparticles and then using magnetic field near the sensing zone to attract antigens towards surface-bound antibodies. The magnetic nanoparticle will experience magnetic force which will attract them towards higher magnetic field gradient. This will also bring more antigens near the surface of reaction causing more formation of bound complex at faster rate. The magnetic field was generated using

different combination of four wires carrying 1A current each near the vicinity of the sensing surface inside the microchannel.

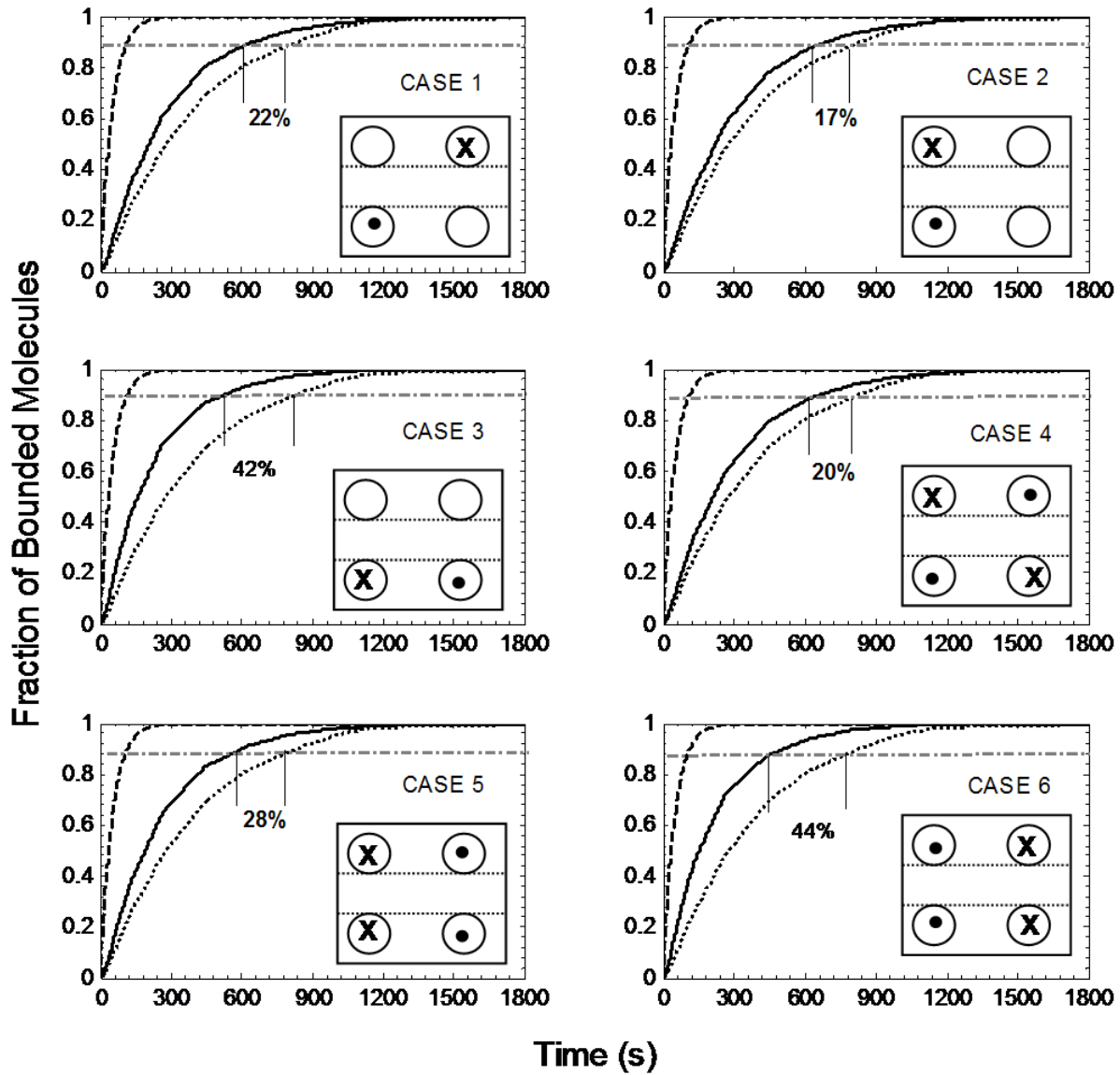


Figure 3.29 Effect of six different configuration of magnetic field on the reaction kinetics of magnetic nanoparticle tagged antigen-antibody complex at the surface of microchannel. Dash line represents (“upper bound”) and corresponds to analytical solution without mass transfer. Solid lines represent kinetic profiles when there is mass transfer with magnetic field effect and dotted line represent (“lower bound”) and correspond to scenario when there is mass transfer as well as reaction kinetics but no magnetic field. Schematic representations of six different cases of circular current carrying wires near the channel are also shown. X and dot represent current into and out of the plane.

Several combination of current in four wires could be possible but we investigated the six most feasible combinations in the simulations. The diffusion coefficient, D (10^{-11} m²/s) and inlet velocity, u_0 (10 μ m/s) was kept constant throughout the simulations. Figure 3.29 shows the effect of different combination of magnetic field on the detection performance of the microfluidic system. The detection time was assumed to be taken at 90% of equilibrium value (grey dash-dotted line in Figure 3.29) of bound molecules. The most ideal scenario is the “upper bound” and corresponds to the fastest binding event between antigen and antibody. Convection and diffusion effects tend to slow down the kinetics. The analytical expression given by Eq. 3.44 is used to calculate the “upper bound” kinetic curves and corresponds to the ideal case. The “lower bound” kinetic curves correspond to reaction rate with mass transport and no magnetic field effect is compared with the kinetic profiles that are obtained when magnetic field is used. In Figure 3.29, schematic representations of six different combinations of circular current carrying wires near the channel are also shown. The wires with cross and dot sign indicates the direction of current which is in and out of the wires respectively. The wire without any sign indicates that there is no current. It is observed that magnetic field enhances the reaction kinetics when magnetic nanoparticles are tagged with antigens and magnetic force is used. Under, “lower bound” scenario, there is no antigen focusing on sensor area due to magnetic force acting on antigen-MNP complex, chemical binding locally depletes the suspended antigen concentration in the microchannel. Because convection and diffusion are the only transport mechanism, the depleted region surrounding the reactive surface increases with time and reduces the rate of antigen-antibody binding. On contrary, when magnetic field is applied, the antigen-MNP complex experience magnetic force and are pulled towards the surface bound antibodies, which causes circulation that redistributes the depleted concentration throughout the domain. The immobilized

antibodies effectively see higher suspended antigen concentration, resulting in a higher binding rate. It can be also seen from Figure 3.29 that, Case 3 and 6 under magnetic field configuration decreased the detection time by almost 42% and 44% respectively. It's worthwhile to note that Case 5 and Case 6 are symmetrical with respect to magnitude of magnetic field (magnetic field gradient) but it's the direction which plays a critical role in enhancing the sensing performance. For Case 5, the direction of magnetic field is away from sensing surface therefore it tends to bring smaller amount of target antigen-MNP towards surface for binding as compared with Case 6 where magnetic field is directed towards the sensing surface and brings more target to the surface and overall enhance the performance. Case 3 was chosen as the most optimized configuration because it utilizes only two wires which means less power requirement for sensing as compared to four wires in Case 6.

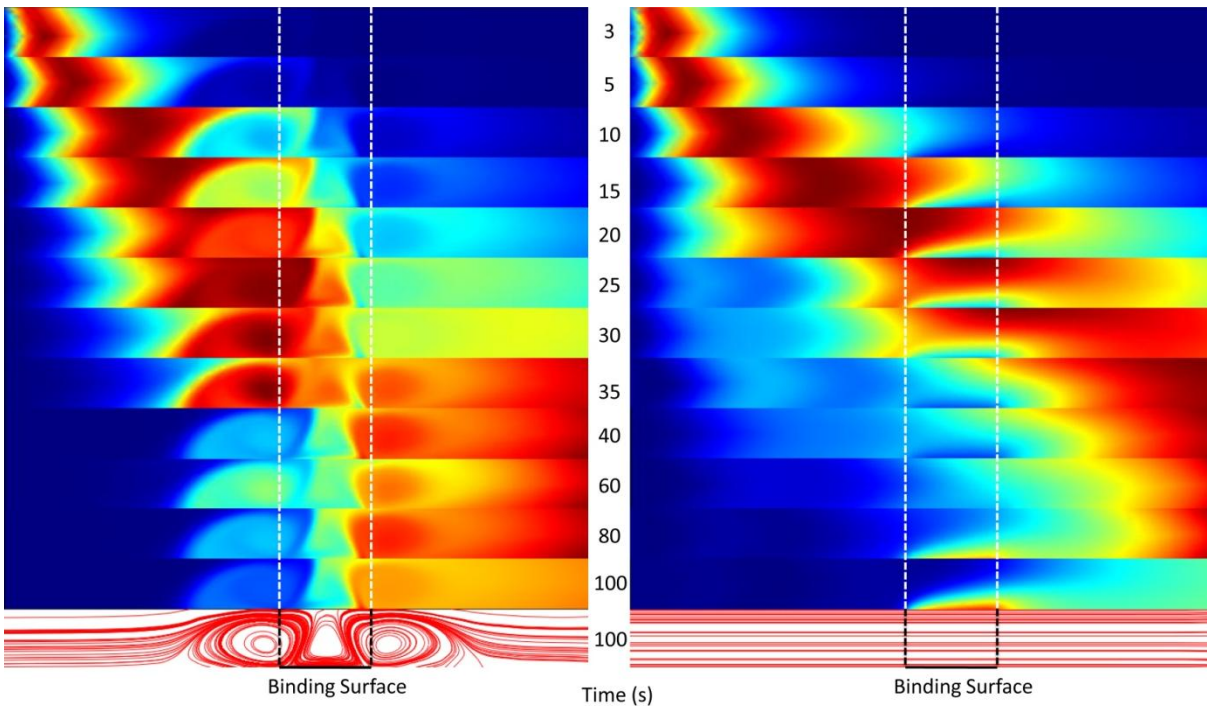


Figure 3.30 Snapshots of microchannel taken at different times with (left) and without (right) magnetic field effect on the concentration on target antigen. White dash line indicates the sensing zone and black solid line shows the position of binding surface in the microchannel. A streamline plot at $t=100s$ shows the velocity field with (left) and without (right) magnetic field effect. Magnetic field effect causes circulation near the sensing surface (left).

The results obtained above shows that magnetic field enhances the binding kinetics by focusing target antigen in the sensing zone. This is further illustrated in Figure 3.30 where Case 3 configuration is used to cause magnetic field in the sensing zone. The antigen-MNP complex is introduced as a “burst” of concentration ($c_0=10\text{nM}$) for 0.5 seconds and then its supply is stopped. The journey of the antigen-MNP complex is studied inside the channel. It is observed that magnetic force seems to focus antigen-MNP complex on the reactive surface and retain it in the microchannel for longer duration when compared with the scenario when there is no magnetic field. It is further observed from Figure 3.30 that there is more concentration of target antigen near the sensing zone even after 30s in the microchannels with the magnetic field as compared to microchannels without magnetic field. Therefore, there is more focusing or more supply of antigen towards the sensing surface which resulted in overall enhancement of the rate of surface reaction. This is further proved quantitatively in Figure 3.31.

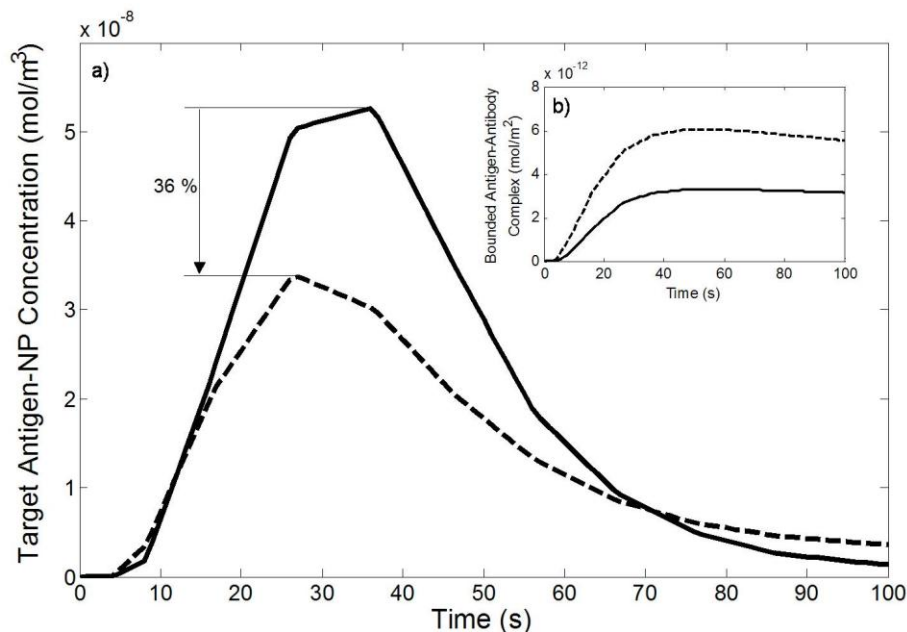


Figure 3.31(a) Outlet concentration of target antigen tagged with magnetic nanoparticles as a function of time, (b) binding concentration of antigen-antibody complex on the sensing surface as a function of time. Solid line represents when there was no magnetic field near the sensing zone whereas dashed line represents when there was the magnetic field.

It is clearly seen that there is 36 % reduction in the outlet concentration of target antigen-MNP complex as shown in Figure 3.31a when magnetic field is used. This clearly demonstrates that the binding concentration is almost two-fold higher (see Figure 3.31b) when magnetic field is used and illustrates that magnetic nanoparticle under the influence of magnetic field causes more mixing, focusing and provides enhanced binding of target antigen with the surface bound antibodies.

3.3.3.5 Influence of Magnetic Nanoparticle size and Diffusivity on magnetically enhanced binding

In order to account for change in magnetically enhanced binding due to variation in magnetic nanoparticle size and diffusivity two sets of simulation were performed keeping all other parameters ($u_0 = 10 \mu\text{m} / \text{s}$; $c_0 = 10 \text{nM}$; $k_{on} = 10^3 \text{ m}^3 / \text{mol.s}$; $k_{off} = 10^{-2} \text{ s}^{-1}$) constant throughout.

In the first set of simulations magnetic nanoparticle diameter was varied from 10nm to 250nm whereas the diffusivity was assumed to vary slightly and was kept constant at $10^{-11} \text{ m}^2/\text{s}$, for second set of simulations, nanoparticle diameter was kept constant at 50nm whereas diffusivity was varied in between 10^{-13} - $10^{-9} \text{ m}^2/\text{s}$. The results of these simulations are given in Figure 3.32 where the time to reach 90% of binding (t_{90}) was evaluated for different values of diffusivity and nanoparticle diameter. It was observed that as the nanoparticle size was increased, the time to reach 90% binding initially decreased but later started increasing for nanoparticle size of more than 100nm. Therefore, nanoparticle size between 50-100 nm were identified as the most optimum for the simulated system that gave the least amount of time to reach 90% binding. This can be explained in terms of forces, magnetic force due to magnetic field and drag force due to fluid flow, acting on magnetic nanoparticles in the microchannel. As the diameter of magnetic nanoparticles increases, the magnetic force acting on nanoparticles also increases and bring more

magnetic nanoparticle tagged antigen towards sensing surface whereas we also know that drag force due to fluid flow is also proportional to the size of particles and also increases.

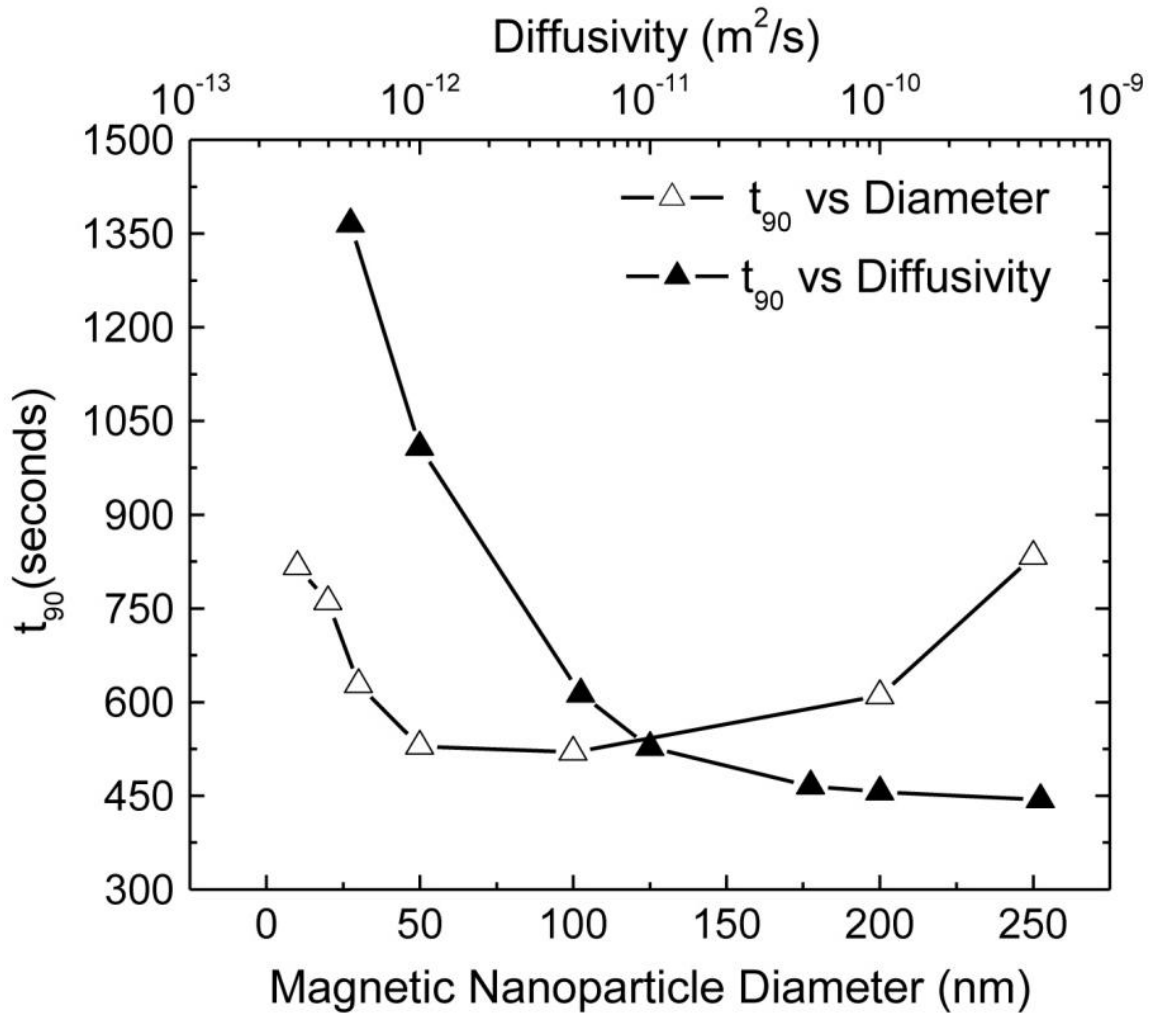


Figure 3.32 Variation of binding time (t_{90} , time at 90% binding) with change in nanoparticle size and diffusivity. These values were comparable to the values used in literature [65, 232-234] for similar systems.

When the size of nanoparticle is below 100 nm, drag forces are smaller and do not influence path of magnetic nanoparticle tagged antigen whereas when the size increase beyond 100nm the drag forces influences the profile and sweeps away more target antigen from the surface and consequently results in higher 90% binding time. In the second set of simulation, the nanoparticle size was kept constant at 50nm and diffusivity was varied, it can be observed from

Figure 3.32 that 90% binding time decrease with increasing the diffusivity but reaches a saturation beyond which there is no influence of diffusivity or we can say that the system has entered the reaction limited regime in which increasing the mass transfer would have no affect on binding reaction. A diffusion coefficient around 10^{-11} m²/s and nanoparticle size of 50nm was identified as the optimum values for this particular system which enhanced the magnetically driven binding kinetics.

3.3.3.6 Comparison of Magnetic Force and Passive Mixing based Strategies

We further investigate and compare passive mixing method with the magnetic nanoparticle enhanced reaction kinetics as shown in Figure 3.33. For passive mixing we add a bluff body (Figure 3.33b) to the top of channel. This is done to reduce the diffusion length and provide better contact between the target antigen and surface bound antibody. The binding concentration of antigen-antibody complex is predicted for three different scenarios including standard straight microchannel without magnetic field and bluff body, microchannel with bluff body, and microchannel with magnetic field effect. Even though passive method enhanced the binding kinetics and reduced the detection time by 7%, it can be seen that magnetic nanoparticle provides better enhancement of binding kinetics and resulted in almost 35% more reduction in detection time when compared with passive mixing. The numerical simulations results reported here indicate that magnetic nanoparticle-based strategy can be a useful technique for increasing binding rates in heterogeneous assays, particularly for diffusion-limited reactions and can be used for developing rapid and sensitive microfluidic biosensors.

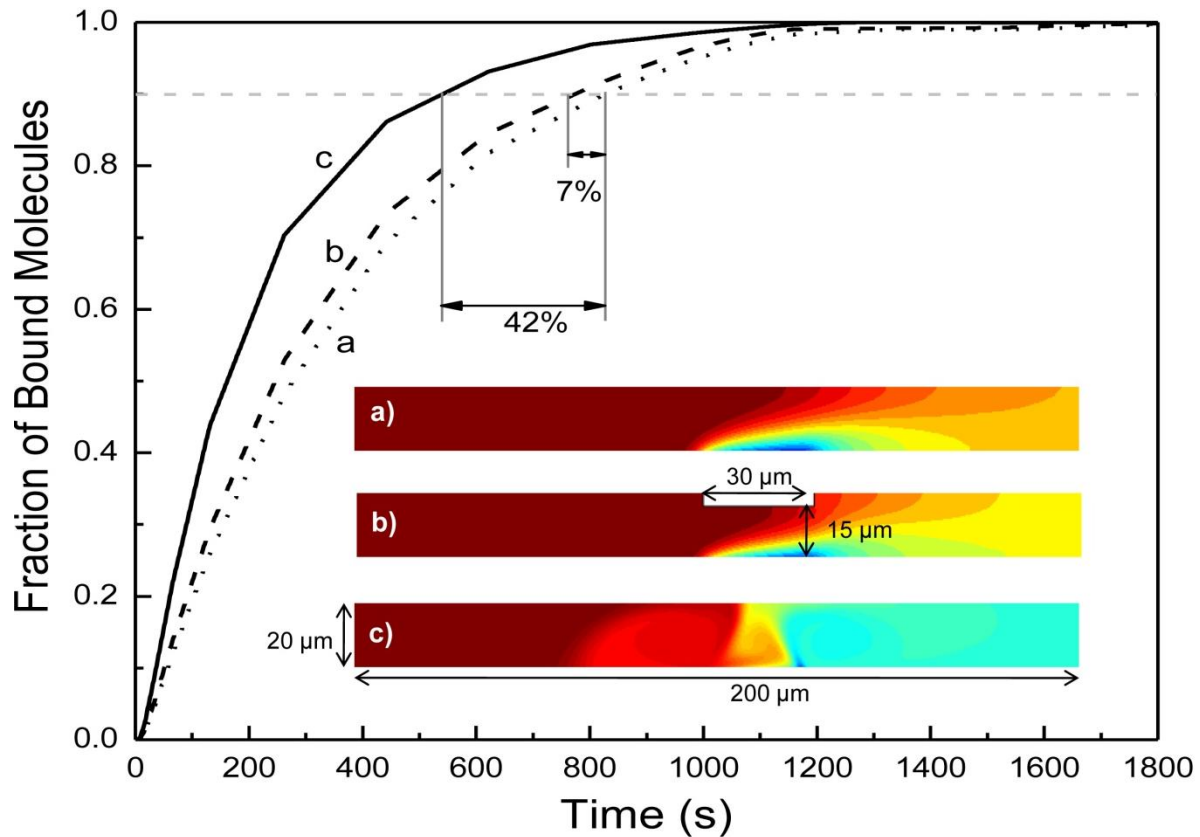


Figure 3.33 Binding concentration of antigen-antibody complex on the sensing surface as a function of time. Three different scenarios (a) straight channel without magnetic field, (b) channel with bluff body on the top without the magnetic field, and (c) straight channel with the magnetic field are shown. The target antigen concentration profile is also shown inside the channel for all the three scenarios.

3.3.4 Conclusion

A finite element mathematical model for demonstrating magnetic nanoparticle-based generic strategy for enhancing the performance of surface-based bio-assay on a microfluidic platform was successfully developed. The effect of convection, diffusion, binding reaction, and magnetic field on the binding kinetics of surface-based antigen-antibody reaction was studied. The detection time was found more sensitive to diffusion process and in order to maximize local concentration of antigen, it was tagged with magnetic nanoparticles and then focused on sensing site by magnetic force. Different configurations of magnetic field around the microchannel were simulated and the most optimized configuration was predicted. Furthermore, it was quantified

that the detection time was reduced by almost 42% when magnetic nanoparticle were combined with target antigens. This also resulted in more efficient binding between antigen and antibody when compared with physical enhancement methods. Overall, the simulation performed using the developed “numerical prototype” provided an excellent estimate of the potential to use magnetic nanoparticles for designing and developing faster integrated surface-based biosensors and biochips for detecting biomolecules.

3.4 Magnetically actuated scheme for tagging biomolecules with magnetic nanoparticles in a microfluidic system

3.4.1 State of the Art

Microfluidics combined with nanotechnology has played a major role in developing micro-total-analysis-systems (μ TAS) or lab-on-a-chip systems. The idea is to bring chemical or biological analysis from laboratories to microchips. These miniaturized systems have found profound great application in medical diagnostics, chemical and biological analysis, forensic analysis and even immunoassays and toxicity monitoring [4, 5, 172, 187, 188, 235, 236]. Miniaturization has offered numerous advantages including shorter analysis times, reduced sample and reagent volume, as well as high selectivity and sensitivity[237]. Recently, functionalized magnetic micro/nanoparticles[37, 61] are advantageously combined with microfluidics for separation and detection of biomolecules [45, 60], immunoassay of proteins [48, 172], purification of DNA [31, 50], and cell separation [52, 53, 238]. These devices are based on a very simple principle of isolating biomolecules of interest from the bulk mixture by attaching them to small magnetic micro/nanoparticles and then steering it by using an external magnetic field [29, 207]. Numerous microfluidic systems based on magnetic isolation techniques have been developed in the last few years [36, 45, 48, 50, 172, 176, 178, 239]. The combination of magnetic micro/nano particles together with microfluidic has offered added significant benefits [29, 37, 61] such as, easy implementation and automation, higher surface to volume ratio for chemical binding, superparamagnetic nature i.e., zero magnetization in absence of magnetic field helps them to stay suspended in carrier liquid without agglomerating, and no harmful effect on internal solution containing biomolecules. However, prior to separation and detection analysis, the biomolecules should be tagged with magnetic nanoparticles using specific antigen-antibody chemistry [157,

184, 240] in-situ before realizing its advantages in a lab-on-a-chip system typically developed for point-of-care analysis. Most of the microfluidic systems developed so far were based on tagging process done in laboratory settings before putting the samples on microfluidic devices. Tagging involves bulk phase reaction between MNPs and biomolecules which greatly depends on the quality of mixing. Due to extremely small channel size the tagging process on chip is quite challenging, mostly due to the flow regimes that are typically laminar. This results in diffusion being the rate limiting process and overall affects mixing, reaction rates, biomolecule accumulation times and ultimately, separation or detection sensitivities of these devices. Moreover, enormous time is needed for the biomolecules to be thoroughly mixed and combined with MNPs for further application on chips. Numerous external/internal actuation strategies have been designed in order to enhance the mixing either in an actively or passively. Some of them include splitting and injecting of fluid flows[84], disturbing the fluid flows with microchannel structures [99] and confining the species in droplets [18, 87, 91, 104, 105]. Other active methods are by inducing external energies including mechanical [104, 105], electrical [113-115, 118, 189, 197], acoustic[200], ultrasonic [111] or thermal [201] in the microchannel flow. Although these methods have produced excellent results but often require complicated fabrication protocols or energies that can potentially damage cell, biomolecules or DNA[202].

To circumvent this problem, magnetic nanoparticles together with local alternating magnetic field can be used in the microfluidic channels. This novel strategy can produce enhanced mixing which is simple and can be easily integrated on lab-on-a-chip devices for tagging biomolecules of interest with magnetic particles for further processing. However, a more quantitative understanding of the dynamics and kinetics involved in this process is required which will also play a key role in optimizing, designing, and finally fabricating devices that are based on

magnetic particle actuation. Several groups have reported both numerical and analytical models [138, 209-211, 213] on the motion of magnetic particles in microfluidic systems though useful these studies did not take into account the multiphysics approach, where magnetic field, fluid flow, mass transfer, and reaction kinetics were considered together to simulate the tagging process. Moreover, these studies focused on microparticles or microbeads and were confined to only simple magnetic field configurations without a detailed analysis and optimization strategies. Therefore, in this work a finite-element COMSOL based multi-physics model is developed to investigate a wide range of design parameters involved in the development of novel time-dependent magnetically actuated tagging process on chip. The model takes into account coupling of magnetic nanoparticle transport in the presence of magnetic field with reaction kinetics of tagging process. It is demonstrated that a time-dependent magnetic body forces are produced due to the electrodes embedded in the device substrate beneath the microchannel. These forces disturbs the MNPs flow regime causing agitation in the surrounding fluid that otherwise follow laminar profile and overall speeds up the reaction kinetics of the tagging process. This strategy is easy to implement and can be integrated on a lab-on-a-chip system especially for point-of-care analysis. The model was employed to quantitatively as well as qualitatively investigate the effect of fluid flow, magnetic nanoparticle size, and frequency of magnetic actuation on the tagging performance and subsequently optimize the process. Also, magnetic actuation strategy was compared with passive method to enhance reaction kinetics of tagging process. Overall, the developed COMSOL model demonstrates that time-dependent magnetic actuation is an efficient tool to mix or tag MNPs with biomolecules in situ for the development of efficient point-of-care microfluidic systems.

3.4.2 Model Development

In this work MNPs are used together with time-dependent magnetic field to enhance the mixing and consequently improve kinetics of tagging process. A schematic of the microfluidic system together with integrated copper electrodes for generating time-dependent magnetic field, along with corresponding co-ordinates and dimensions, is shown in Figure 3.34. On application of current in the electrodes, large magnetic force and magnetic field gradients are created that disturbs the MNP solution flowing within the microchannel.

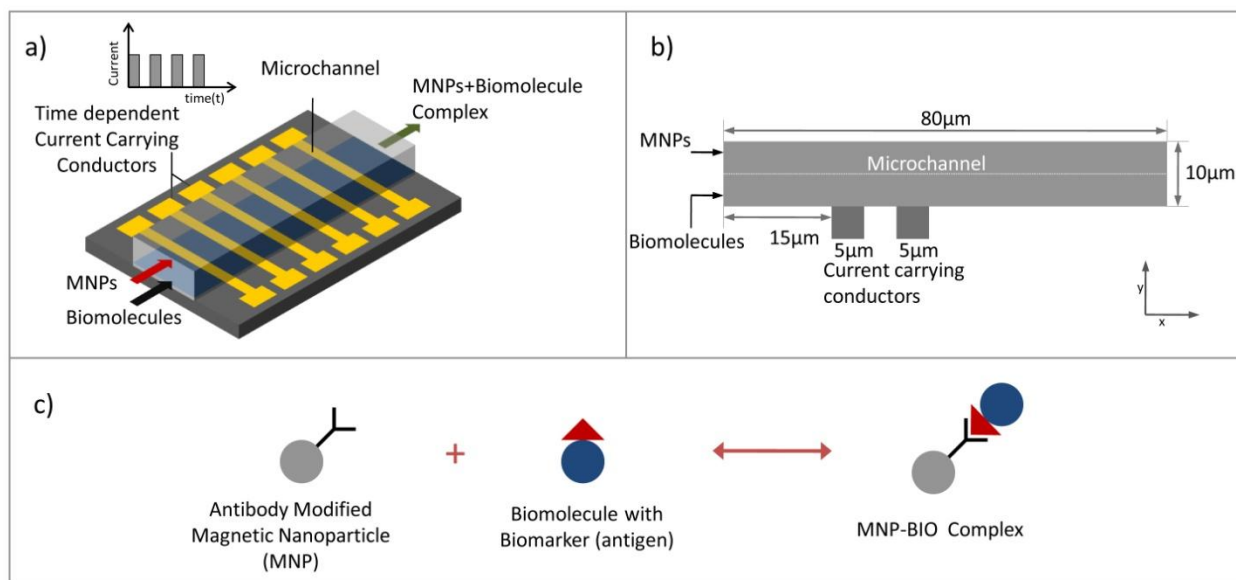


Figure 3.34 Schematic of time dependent magnetic tagging process: a) a three-dimensional conceptual representation of the microfluidic system, b) a 2D cross-sectional view used to develop finite element COMSOL model, and c) binding reaction between MNPs and biomolecule using antigen-antibody chemistry.

The disturbances are periodically created by turning the current on/ off through the conductors causing agitation in the flow thereby increasing the mixing and consequently improving the tagging kinetics. It is assumed that the variation in mass transport will be negligible in the direction perpendicular to the x-y plane due to high aspect ratio [214] of the system modeled. This will reduce the 3D geometry to a 2D thereby significantly decreasing the computational time and memory. Moreover, a 2D model will serve as a simple, fast, and relatively accurate

guideline for designing and optimizing magnetic microfluidic systems for tagging process. Carrier fluid (water) containing MNPs is loaded from top whereas biomolecule solution flows from bottom inlet. In all the simulations, it is considered that both the fluids flow with a constant laminar flow velocity from left to right. It is considered that both the magnetic nanoparticle and biomolecule solution is transported by convective flow towards the outlet and is also free to diffuse. The transport of a magnetic nanoparticles in a carrier fluid (water) is governed by; a) the magnetic force, arising from transient magnetic field, b) the viscous drag, due to movement of magnetic nanoparticles with respect the surrounding fluid, (c) fluid-particle interactions, due to perturbations produced in the flow field , (d) gravity/buoyancy, (e) thermal kinetics (Brownian motion), and (h) inter-particle or particle-particle effects It is assumed in the simulation that a low concentration of MNPs were used therefore inter-particle or particle-particle effects were neglected in the analysis. Moreover, the sizes of MNPs used in the analysis are extremely small therefore gravity effects were neglected but Brownian motion [214] was included in the simulation by incorporating a drift-diffusion. The equations and theory developed are based on Navier-Stokes equations for solving flow field of carrier fluid in this case it is assumed water, drift diffusion equation for mass transport of MNPs and Maxwell's equations to predict magnetic field and magnetic force in the microchannel. The model basically solves the Maxwell's equation for a transient magnetic field. The computed magnetic force is coupled to fluid flow by using the magnetic volume force term acting on the nanoparticles in the Navier-Stokes equations, which account for the momentum transfer from the MNPs to the fluid (particle-fluid interaction). A drift-diffusion equation was used to predict the nanoparticle concentration which was dependent on flux contributions from diffusion, advection, and magnetic force-based migration. A surface modified MNPs containing antibody as a receptor were considered in the simulation that binds

with biomolecules (receptor-antigen) by utilizing specific antigen-antibody chemistry [240-242] with a known rate constants. It is assumed that the reaction between MNPs and biomolecules is homogeneous reaction without taking in account the heterogeneity of surface reaction between the linker molecules (antigen-antibody). The detailed explanation of the equations and theory used in the model are described in the following sections.

3.4.2.1 Magneto-Static Equations

The static magnetic field is calculated using Maxwell-Ampere's law given by;

$$\nabla \times H = J \quad (3.46)$$

Where H is the magnetic field vector (A/m) and J is the current density vector (A/m^2),

According to Gauss law for magnetic flux density, B (Vs/m^2)

$$\nabla \cdot B = 0 \quad (3.47)$$

In order to describe a relation between B and H a constitutive relation given by the following equation is used in the model.

$$B = \mu(H + M) \quad (3.48)$$

Where, μ is the magnetic permeability and M is the magnetization vector. The magnetic permeability can also be expressed as $\mu_0\mu_r$ where μ_r is the relative permeability of magnet (=1)

and is assumed to be constant in all the simulations and μ_0 is the permeability in vacuum ($\mu_0 = 4\pi \times 10^{-7} N/A^2$). A magnetic vector potential A is described [180] according to the following equation

$$\nabla \times A = B; \nabla \cdot A = 0 \quad (3.49)$$

After substitution of Eq. 3.49 in Eq. 3.49, 3.47, and 3.48 the following vector equation is obtained;

$$\nabla \times \left(\frac{1}{\mu_0 \mu_r} \nabla \times A - M \right) = J \quad (3.50)$$

It is assumed that the magnetic vector potential has a nonzero component only perpendicular to the plane A_z which basically simplifies the 2D; the externally applied current density J is calculated for the 40 x 40 μm copper conductor. A square-shaped current with a set frequency is used to replicate the on/off behavior of current in the conductor. Heaviside step function of COMSOL is used to generate a square current pulse similar to the one produced by experimental pulse generator. The step function is expressed as $\text{flc2hs}(x, 0.1)$ and it smoothes within the interval $-0.1 < x < 0.1$. In order to implement time-dependent control signal for generating pulsating magnetic field, the following equation is used.

$$J = \frac{I_0}{A} [\text{flc2hs}(\sin(2\pi ft), 0.1)] \quad (3.51)$$

Where, I_0 is the current supplied to the conductors which is equal to 1 A for all simulations, A is the surface area of the copper conductors, and f is the switching frequency in hertz. It was assumed based on literature [122] that the temperature rise inside the microchannel will be negligible when current between 0.5A-1A is used. Magnetic field is actuated from left to right meaning when the current in left conductor is ON, the current in the right conductor is OFF and vice versa. This is done by having a phase difference of 180° in the alternating current supplied to the conductors. The above equations are solved in magnetostatic module of COMSOL Multiphysics software and the pulsating magnetic field is obtained. Magnetic force that is exerted on the magnetic nanoparticles is calculated using the following equation [180]:

$$F_m = (1 - N_d) \mu_0 \mu_r \alpha V_{MNP} (H \cdot \nabla) H \quad (3.52)$$

Where, N_d is the demagnetizing factor (0.33 for a sphere), V_{MNP} is the volume of a magnetic nanoparticles, and α is the ratio of iron oxide content which is 0.8 for the magnetic nanoparticles used in this work.

3.4.2.1.1 Boundary Conditions

A magnetic insulation boundary condition ($A_z = 0$) is applied along the system boundary. The interior boundaries between the copper conductors and the air only assume continuity, corresponding to a homogeneous Neumann condition.

3.4.2.2 Fluid Flow Equation

The magnetic nanoparticles (MNPs) were assumed to be dispersed in the fluid of viscosity η ($10^{-3} \text{ kg / m} \cdot \text{s}$) and density ρ (10^3 kg / m^3) equal to that of water. The aqueous solution of MNPs is injected from top into the microchannel with a parabolic velocity. The magnetic force acting on MNPs due to external magnetic field transfers momentum to the surrounding fluid leading to a disturbance in flow profile of carrier liquid. The flow velocity u for this incompressible fluid ($\nabla \cdot u = 0$) is described using Navier-Stokes equation,

$$\rho \frac{\partial u}{\partial t} + \rho(u \cdot \nabla)u = -\nabla p + \eta \nabla^2 u + F_{vol} \quad (3.53)$$

Where, u is the carrier fluid velocity field (m/s), p is the pressure (N/m^2), and F_{vol} is the volume force (N/m^3). The momentum transfer from MNPs to the fluid is incorporated by setting the volume force term equal to the magnetic force acting on a single MNP multiplied with MNP number density, α , which is the number of MNP per unit volume. Therefore, the volume force acting on fluid is given by;

$$F_{vol} = \alpha F_m \quad (3.54)$$

Eq. 3.54 couples the fluid flow equation with the magnetic field equation and depends on the instantaneous concentration of MNP solution in the microchannel which is described in more detail later section. MNP number density (α) is calculated using Eq. 3.55.

$$\alpha = \frac{6CM_{Fe_3O_4} \times 10^{-3}}{\rho_m \pi d_p^3} \quad (3.55)$$

Where, C is the concentration of MNPs (μM), $M_{Fe_3O_4}$ is the molar mass of Fe_3O_4 (g/mol), ρ_m is the density of MNPs (g/cm^3), and d_p is the diameter of MNPs (cm). It is also assumed that there is no particle-particle interaction (e.g.: Van der Waals forces) and even the sedimentation effects will have negligible influence on the overall mass transport due to extremely small size of MNPs.

3.4.2.2.1 Boundary Conditions

The flow of fluid at the inlet is assumed to be parabolic and moves in the direction of x-axis with zero velocity in y-direction. The average flow velocity of carrier fluid is u_0 . No slip condition ($u = v = 0$) is applied along the walls of microfluidic system and at the outlet, pressure condition is set equal to zero.

3.4.2.3 Drift-Diffusion Equation

The spatial and temporal variation of the MNP solution inside the microfluidic channel is described using the drift-diffusion equation where Brownian motion due to extremely small size of nanoparticle is also taken into account [180] Specifically, C the concentration of MNP solution is governed by the following equation,

$$\frac{\partial C}{\partial t} + \nabla \cdot J = 0 \quad (3.56)$$

Where $J = J_D + J_A$ is the total flux of nanoparticles, which includes a contribution from diffusion, $J_D = -D\nabla C$, and a contribution $J_A = u_p C$, due to the advection of the nanoparticles under the influence of applied forces. The drift velocity u_p of MNPs is obtained using classical Newtonian particle motion equation [209] as described below.

$$m_p \frac{\partial u_p}{\partial t} = F_m + F_g + F_D \quad (3.57)$$

In the limit of negligible inertia ($m_p \frac{\partial u_p}{\partial t} \rightarrow 0$) and zero gravitational force, F_g Eq. 3.57 results in Eq. 3.58,

$$F_m + F_D = 0 \quad (3.58)$$

Where F_m and F_D are magnetic and drag forces respectively. According to Stokes' law of viscous drag, $F_D = -6\pi\eta r_p (u_p - u)$ where u_p and r_p is the MNPs velocity and radius respectively, u is the fluid velocity of viscosity η ($10^{-3} \text{ kg/m}\cdot\text{s}$). Therefore, from Eq. 3.58,

$$F_m - 6\pi\eta r_p (u_p - u) = 0 \quad (3.59)$$

Since the mobility of the particle is given by $\gamma = 1/6\pi\eta r_p$ Eq. 3.59 can be re-written as;

$$u_p = u + \gamma F_m \quad (3.60)$$

Substituting equation 3.60 in flux, J_A Eq. 3.56 can be re-written as;

$$\frac{\partial C}{\partial t} = D\nabla^2 C - u\nabla C - (\gamma F_m)\nabla C \quad (3.61)$$

Where diffusion coefficient D is calculated using Nernst-Einstein relation $D = \gamma kT$

3.4.2.3.1 Boundary Conditions

An initial unmixed concentration of MNP solution is injected into the microchannel on the right boundary. Convective flux is set at the outlet boundary on the left, keeping insulation/symmetry in all the other boundaries.

3.4.2.4 Tagging Kinetics Equation

The tagging reaction is assumed to be a bulk reaction between the magnetic nanoparticles C (mol/m^3) and the biomolecules C_{BIO} (mol/m^3) facilitated due to surface immobilized antibody and antigen on MNPs and biomolecules respectively, resulting in MNP-biomolecule complex, $C_{MNP-BIO}$ (mol/m^3). The schematic of the reaction process is shown in Fig.1 (c) and can be described by following reversible bulk reaction;



The tagging kinetics of biomolecule with nanoparticle will also depend on the number of tagging sites that are available on the surface of nanoparticles that in turn will be influenced by the size of the particle as well as of the biomolecule. It is therefore important to include a factor in the model that accounts for biomolecule and nanoparticles interaction on the kinetic rate constant. Assuming that each bound biomolecule as a sphere physically in contact with the nanoparticle surface, the correct number of tagging sites for the biomolecule is given by the ratio between the extended nanoparticle surface and the cross-section of the biomolecule [241] as shown in Eq.3.63.

$$n = \frac{(R_{MNP} + R_{BIO})^2}{(R_{BIO})^2} \quad (3.63)$$

Where, R_{MNP} is the magnetic nanoparticle radius, and R_{BIO} is the biomolecule radius. The model biomolecule investigated in this work is a high density lipoprotein (HDL) which is a complex

composed of different proteins, phospholipids, cholesterol and triglycerides found in human blood. The properties of biomolecule such as radius of HDL (~5nm), and rate constant ($k_{on} = 3 \times 10^4 M^{-1} s^{-1}$, $k_{off} = 3 \times 10^{-5} s^{-1}$) were obtained from literature [241]. The number of binding sites per biomolecule was included in the association rate constant, to serve as correction factors accounting for biomolecule-magnetic nanoparticle interaction. Assuming law of mass action kinetics, the tagging kinetics can be modeled by following set of ordinary differential equations (ODEs) describing the reaction rate.

$$\frac{\partial C_{MNP-BIO}}{\partial t} = (n \times k_{on} C \times C_{BIO}) - (k_{off} C_{MNP-BIO}) \quad (3.64)$$

Where, k_{on} is the association rate constant ($M^{-1} s^{-1}$), and k_{off} is the dissociation rate constant (s^{-1}) as described earlier.

3.4.2.5 Numerical Simulation

A finite element software package, COMSOLTM Multiphysics (COMSOL AB., Stockholm, Sweden) is used to solve the two-dimensional partial differential Equations obtained in our model. The finite element model developed in COMSOL consisted of three application modes: incompressible Navier-Stokes mode and magnetostatics mode to predict the convective velocity of fluids with and without the influence of magnetic field force, a convection-diffusion mode to predict the concentration of MNPs, biomolecules, and MNPBIO complex solution within the microchannel. A bulk phase reaction term is used in the convection and diffusion mode to realize interaction between MNPs and biomolecules based on antigen-antibody chemistry. The meshing within the microchannel was kept at 10^{-6} except near the centre point of inlet where point meshing parameter of 10^{-7} with growth rate of 1.1 is selected. The model is solved in transient mode in one step using time-dependent solver.

In order to quantify the tagging performance, mixing cup concentration (C_{MC}) of MNP-biomolecule (MNPBIO) complex is computed. Mixing cup concentration is defined as the concentration of fluid if the flow was emptied to a cup that was well stirred, basically it determines how well the concentrations of MNP tagged biomolecule is mixed. It is given by Eq.3.65.

$$C_{MC} = \frac{\int_A u C_{MNP-BIO}(x, y) dx dy}{\int_A u dx dy} \quad (3.65)$$

Where, $C_{MNP-BIO}(x, y)$ is the instantaneous concentration of MNPBIO complex and u is the x-directed flow velocity.

3.4.2.6 Magnetic Force Validation

Prior to more detailed analysis and optimization, the magnetic force calculation in the COMSOLTM finite element model described was validated using the experimental and numerical results from literature [122]. Accurate prediction of magnetic field and consequently magnetic force on the nanoparticles in the microchannel is the most critical first step in coupling the microfluidic flow and mass transfer with magnetic force tagging process therefore its correct estimation is essential. In order to compare results, a volume of $2.16 \times 10^{-9} m^3$ corresponding to $0.7 \mu m$ magnetic particles and a $40 \times 40 \mu m$ copper conductor carrying 1A was considered in the COMSOLTM model. The model setup is shown in the inset of Fig 2. The fluid with magnetic particles flows in the microchannel whereas at the bottom the copper conductors are used to generate magnetic field. The magnetic field force as described in Eq. 3.52 on magnetic particles are calculated along different lines that are parallel to the x-axis ($y=1, 5, 10, \text{ and } 20 \mu m$) starting from $180 \mu m$ from the left of microchannel (central point between two conductors) and going

toward right for a distance of 100 μm (see Figure 3.34). The location $x=20\mu\text{m}$ and $x=60\mu\text{m}$ corresponds to the inner and outer edges of the right conductor respectively. It can be seen from Figure 3.35 that as we move away from bottom of microchannel the x-component of magnetic force tends to decrease as well as oscillates around the central axis of the microchannel and peaks at the edges of the conductor, responsible for the oscillatory motion of the magnetic particles within the microchannel. Moreover, the computed magnetic force profiles along different planes within the microchannel as well as the range of maximum magnetic forces (e.g.; 0.1-0.3 pN) obtained, agree reasonably well with experimental and simulation work performed by [122].

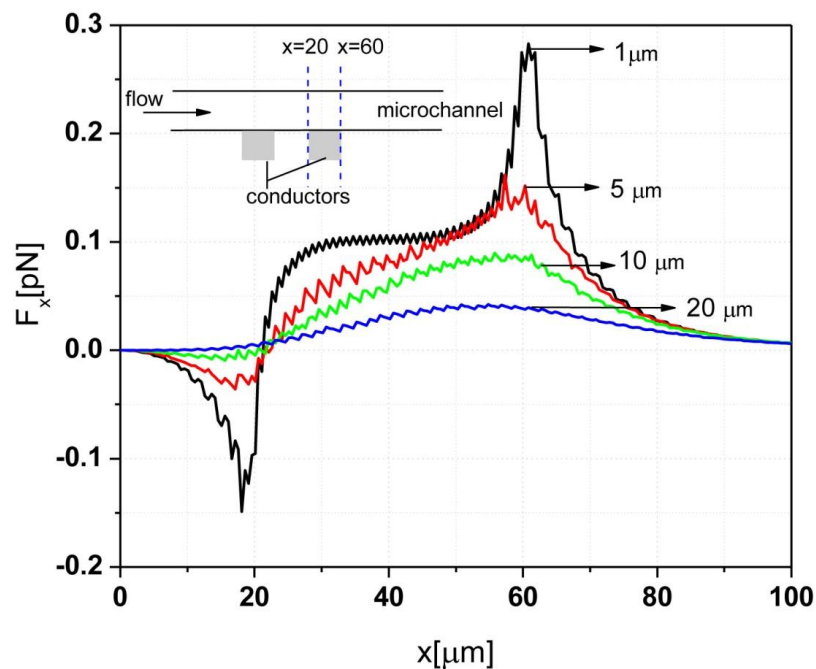


Figure 3.35 Magnetic body force along the z-lines above the current carrying conductor. The location $x=20\mu\text{m}$ and $x=60\mu\text{m}$ corresponds to the inner and outer edges of the right conductor respectively.

3.4.3 Results & Discussion

In this section, we present the dynamic analysis of time-dependent MNP-enhanced tagging process in the microchannel. Time-dependent finite element results were obtained using the above described model and the performance of tagging was predicted and optimized using mixing cup concentration as described earlier in section 3.4.2. Effect of magnetic nanoparticle size, and frequency of applied current used to generate magnetic field was investigated together with fluid flow. The novel strategy of using magnetic field assisted tagging process was compared against passive methods of enhancing bulk phase reaction kinetics. In magnetic field equation average current of 1A is considered throughout the simulations. The diffusivity of DNA, protein, cells, etc. as reported in literature ranges from 10^{-11} – 10^{-14} m²/s, therefore in mass transfer equation, a diffusion coefficient of $D=10^{-11}$ m²/s is used throughout the simulations. Other parameters such as fluid viscosity η (10^{-3} kg / m · s) and density ρ (10^3 kg / m³) are kept constant throughout. The affinity constant, $K_a (= k_{on} / k_{off})$ is kept constant at 10^9 M⁻¹ with $k_{on} = 3 \times 10^4$ M⁻¹ s⁻¹, $k_{off} = 3 \times 10^{-5}$ s⁻¹ throughout the simulations. The effect of various parameters on the tagging performance is described in more detail in the following sections.

3.4.3.1 Effect of Switching Frequency and Magnetic Nanoparticle Size

In the schematic shown in Figure 3.34, time-dependent magnetic field that turns on and off at certain frequency produces magnetic forces on MNPs that disturbs the parallel streamline flow in the otherwise highly ordered laminar flow. These disturbances causes vertical momentum (in y-direction) to the fluid solution and stretching/folding of streamlines resulting in enhanced mixing and higher tagging performance. Therefore, the switching frequency of the electric current supplied to the electrodes together with magnetic nanoparticle sizes are one of the most important parameters in this system. Switching frequency and magnetic nanoparticle sizes can

result in either very fast or very slow modulating magnetic forces of varying strength; therefore they need to be optimized. The effect of switching frequency on the reaction kinetics of tagging process is analyzed for four different diameters of MNPs (50nm, 80nm, 100nm, and 150nm) using six different switching frequencies ranging from 0.1 Hz to 15 Hz, keeping the other parameters such as inlet flow velocity (50 $\mu\text{m/s}$), and current through the conductor (1 A) constant throughout the simulations. The simulations were run for 5s and mixing cup concentrations (C_{MC}) of MNP-biomolecule (MNPBIO) complex were computed as described by Eq. 3.65. It can be seen from Figure 3.36 that time-dependent magnetic actuation enhances the mixing process by stretching and folding the streamlines and overall enhances the tagging process as evident from increase in formation of MNP-BIO complex. However, for smaller magnetic nanoparticles ($\sim 50\text{nm}$) the enhancement is not profound and the reaction between MNPs and biomolecules mostly takes place near the interface of two streams (at the center of microchannel). This is because 50nm size MNPs were unable to agitate the fluid and most of the reaction takes place due to diffusion-based mixing (see Figure 3.36 (a-f)i). This is further evident from mixing cup concentrations (C_{MC}) data versus time as shown in Figure 3.37. For all the scenarios where 50nm MNPs were used, the mixing cup concentration (C_{MC}) of MNP-biomolecule (MNPBIO) complex resulting from tagging reaction was small. The effect of switching frequency can be seen even when 50nm MNPs were used but the migration of species was very small in vertical direction due to weak magnetic forces and resulted in maximum reaction only near the interfaces. Furthermore, we can see that as the size of magnetic nanoparticle increases, the strong magnetic forces tend to produce more migration of both MNPs and biomolecules resulting in enhanced reaction kinetics.

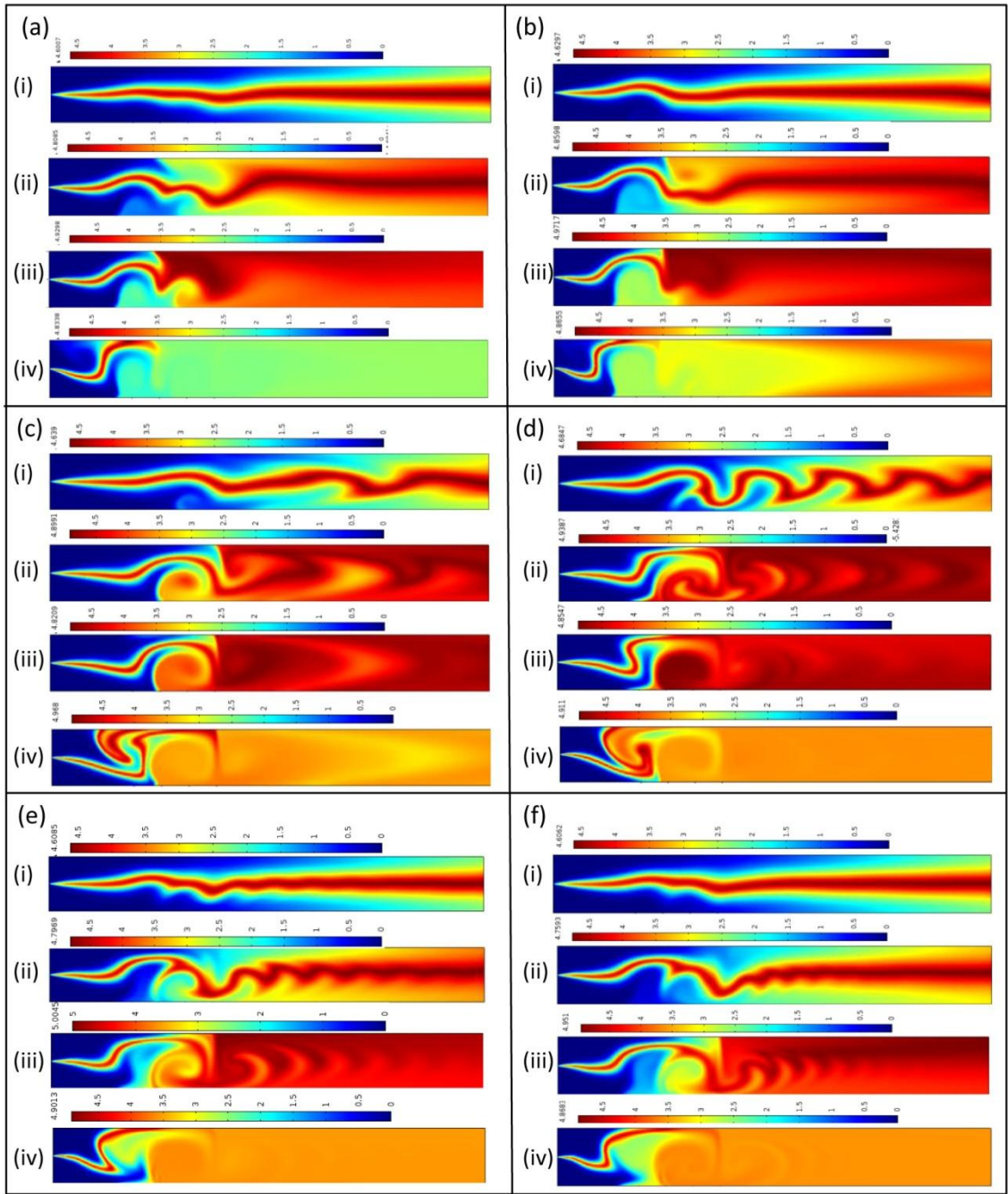


Figure 3.36 Simulated concentration profile of MNP-tagged-biomolecule complex formed during the bulk phase reaction between MNPs and biomolecules in the presence of magnetic actuation scheme (time of simulation=5s). The effect of switching frequency (a) 0.1 Hz, (b) 0.5 Hz, (c) 1 Hz, (d) 5 Hz, (e) 10 Hz, and (f) 15 Hz on the reaction kinetics of tagging process is analyzed for four different diameters of MNPs (i) 50nm, (ii) 80nm, (iii) 100nm, and (iv)150nm.

It can be seen from the results that performance of tagging process is greatly affected by the interplay of magnetic nanoparticle size and switching frequency. In general, MNPs will experience both magnetic force and drag force in the microchannel. If magnetic force is more

than the drag force exerted by fluid flow, MNPs will get deviated (move in lateral direction towards magnetic electrodes) from its original path. Again, if the magnetic force is switched off, MNPs will just flow with the fluid without any further deviation due to drag forces. Periodically switching the magnetic force on and off will disturb the path of MNPs which will also disturb the liquid and cause mixing.

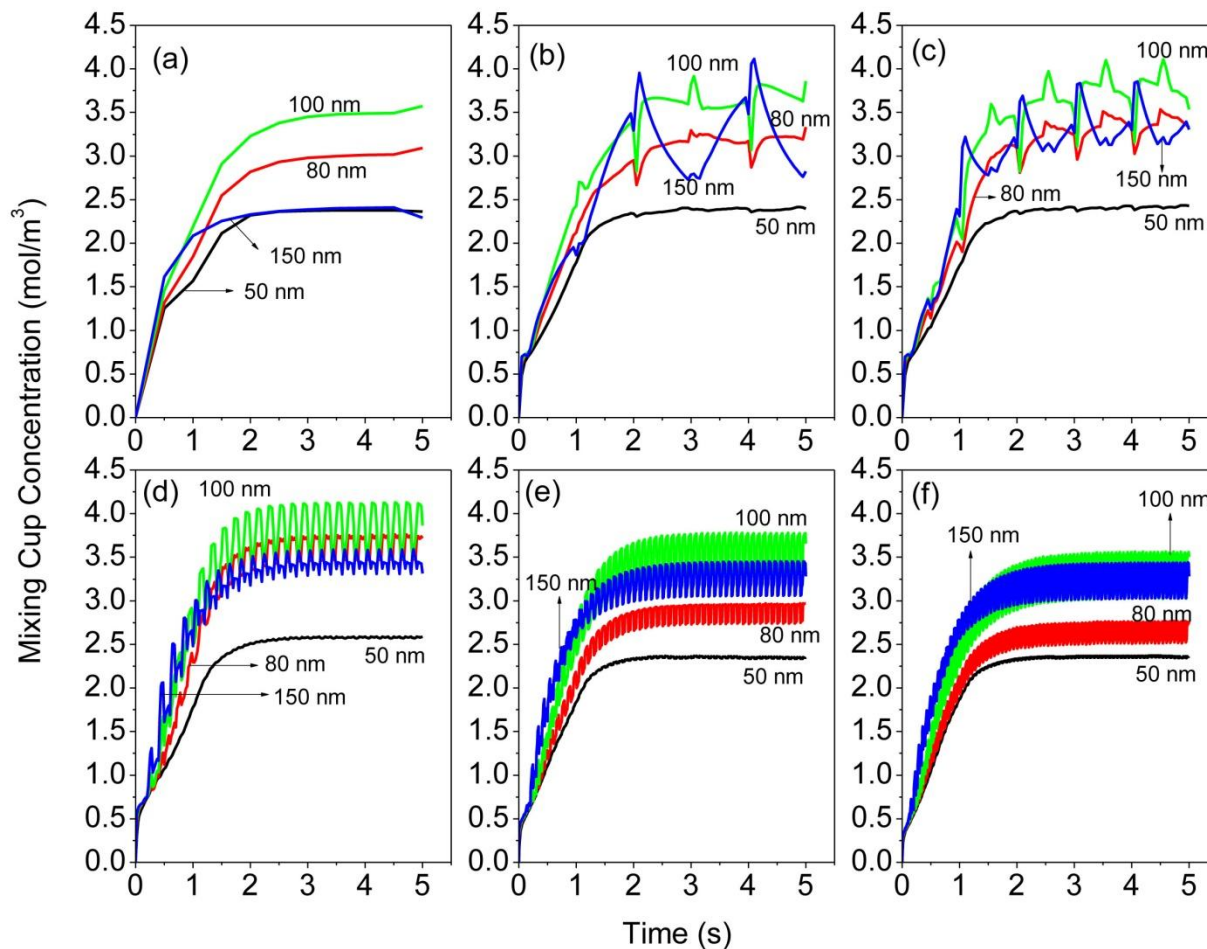


Figure 3.37 Variation of mixing cup concentration of MNP-tagged-biomolecule complex formed during the bulk phase reaction between MNPs and biomolecules in the presence of magnetic actuation scheme with time. The effect of switching frequency (a) 0.1 Hz, (b) 0.5 Hz, (c) 1 Hz, (d) 5 Hz, (e) 10 Hz, and (f) 15 Hz on the reaction kinetics of tagging process is analyzed for four different diameters of MNPs.

The distance travelled by MNPs both in vertical direction as well as in horizontal direction will be a function of magnetic as well as drag forces. In order to produce enhanced mixing it will be

desirable to produce more vertical and less horizontal movement of magnetic nanoparticles that is more oscillations. In these simulations the flow rate is fixed but the drag forces and magnetic forces can be very well controlled by magnetic nanoparticle size and switching frequency to induce high oscillations. Therefore, there is always a critical MNP size and switching frequency based on the dimensions of microchannel that will bring out optimum mixing and consequently enhanced bulk phase reactions for a given set of conditions. Based on the results given in Figure 3.36 and Figure 3.37 it can be seen that magnetic nanoparticle size of 100nm produces more MNP-biomolecule (MNPBIO) complex for all the frequencies used in the simulations. However, if the frequency is increased there is more oscillation in concentration of MNP-biomolecule (MNPBIO) complex seen. It can be also observed from Figure 3.36 (a&b) and quantitatively from Figure 3.37(a&b) that for low frequencies increasing the size of MNPs to 150nm resulted in very low formation of MNP-biomolecule (MNPBIO) complex. This again can be explained from the fact that the tagging process highly depends on the disturbance produced in the microchannel. Although, increasing the size of MNPs increases the magnetic forces but switching frequency was not optimum to produce a good balance of horizontal and vertical movement in order to produce maximum disturbance and resulted in less formation of MNP-biomolecule complex. From the above analysis it can be realized that tagging process in microchannel can be enhanced using magnetic actuation but it is a strong function of both magnetic nanoparticle size and switch frequency of magnetic field working together. Based on the results given in Figure 3.37 and for the geometrical configuration and flow condition used in the model, 100 nm MNPs together with 0.1 Hz switching frequency gave the most optimized tagging performance.

3.4.3.2 Effect of Inlet flow Velocity

Inlet flow velocity or flow rate also has significant effect on the tagging performance, a too high incoming flow rate will produce large drag forces that will overcome magnetic forces and consequently make the magnetic actuation strategy ineffective, Also a too small flow rate will result in less throughput and can affect the overall performance of lab-on-a-chip devices. Therefore, flow rates or inlet flow velocity needs to be optimized for a given configuration. In order to further understand the time-dependent magnetic field influenced tagging process and optimize it, simulations were performed to account for the effect of inlet flow velocity or Reynolds Number on the mixing cup concentration. MNPs of 100nm diameter are used together with magnetic field switching frequency of 0.1Hz. All the other parameters are kept constant as described in previous sections throughout the simulations that were run for 30s. Inlet flow was increased from 30 $\mu\text{m/s}$ to 120 $\mu\text{m/s}$ and mixing cup concentrations (C_{MC}) of MNP-biomolecule (MNPBIO) complex are computed. It can be seen from Figure 3.38 that as the flow velocity or Reynolds Number is increased; the time fluid element spent in the microchannel decreases resulting in less effective magnetically actuated tagging process (see Figure 3.38f). Therefore, an optimum flow velocity for magnetically actuated mixing needs to be identified. In general, if the system is operated at higher flow velocity ($\sim 120 \mu\text{m/s}$) larger magnetic field force is needed to bring out desired oscillation within the microchannel in order to enhanced reaction kinetics. This can be done either by increasing the current through the electrodes or choosing larger magnetic particles but both these conditions can have negative impact on overall process. Too high current can cause excessive heating and may damage cells, DNA's or biomolecules whereas increasing the size of MNPs can lead to clogging of microchannel for device size that is expected to be small.

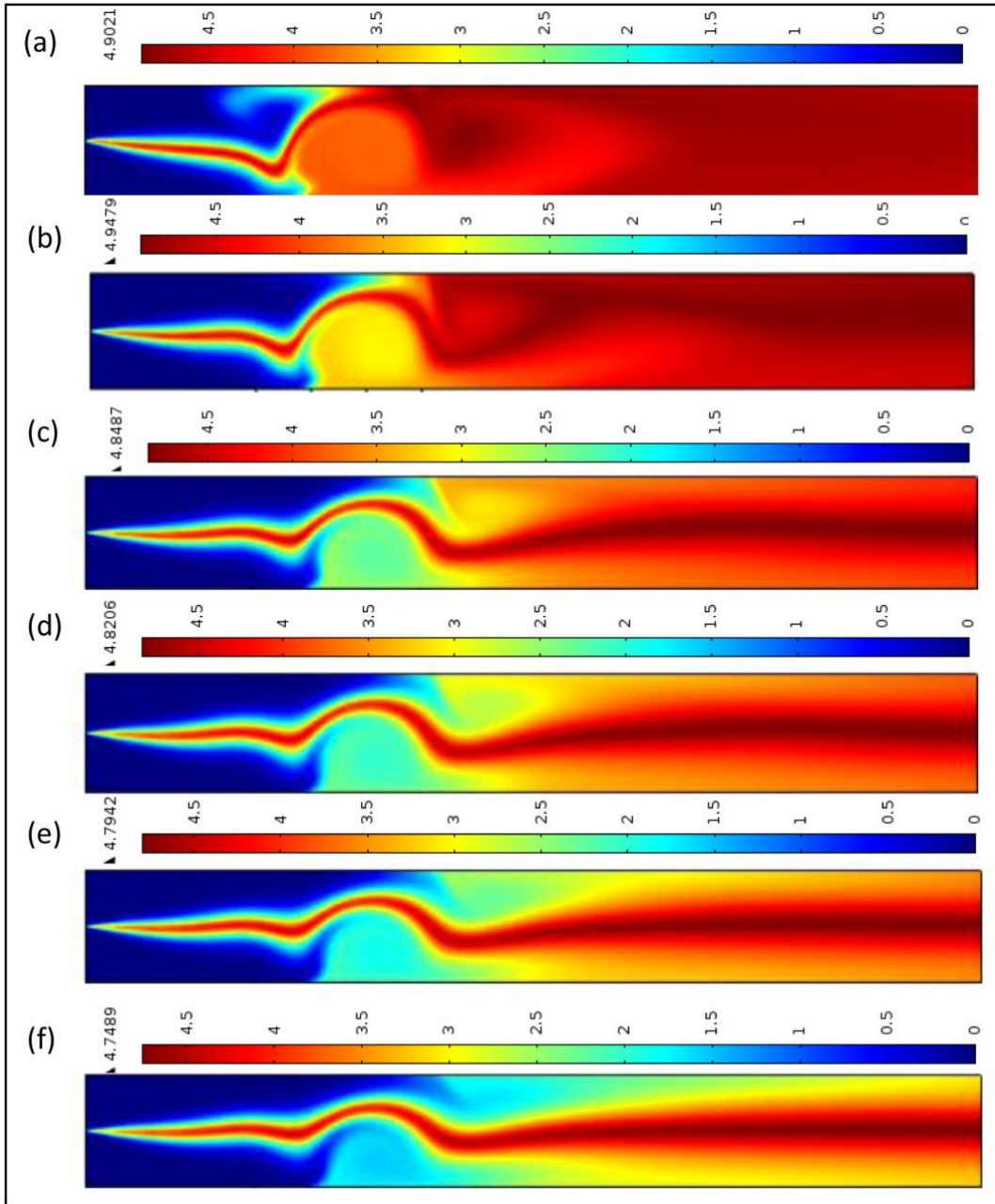


Figure 3.38 Simulated concentration profile of MNP-tagged-biomolecule complex formed during the bulk phase reaction between MNPs and biomolecules in the presence of magnetic actuation scheme after 30s. The effect of flow velocity (a) 30 $\mu\text{m/s}$, (b) 50 $\mu\text{m/s}$, (c) 80 $\mu\text{m/s}$, (d) 90 $\mu\text{m/s}$, (e) 100 $\mu\text{m/s}$, and (f) 120 $\mu\text{m/s}$ on the reaction kinetics of tagging process is analyzed.

As this method is envisioned to facilitate better tagging of biomolecules with MNPs in situ for lab-on-a-chip devices, the tagging process overall will be controlled by two important time scales, convection time scale, t_c and reaction time scale, t_r , that is the tagging process will

depend on how much time MNPs and biomolecules have to react. If the convection time, t_c is smaller than reaction time, t_r , biomolecules and MNPs will not get enough time to interact and they will just move out of the system without being tagged. Moreover, a high inlet flow velocity will increase the drag force and make magnetic force ineffective resulting in very small migration of MNPs in vertical direction and consequently most of the reaction only takes place at interface as seen in Figure 3.38f. On the other hand working with too low velocity produces large variation in MNP-biomolecule (MNPBIO) complex formation as seen in Figure 3.39. Therefore, working at optimum flow velocity ($Re \sim 5 \times 10^{-4}$) in this case with magnetic mixing will be needed to provide sufficient reaction time for tagging biomolecules with MNPs and also less oscillation in results. From the above analysis MNPs actuated tagging process seems to be more profound at an optimum inlet velocity of $50 \mu\text{m/s}$ for the geometry and conditions used in the simulations.

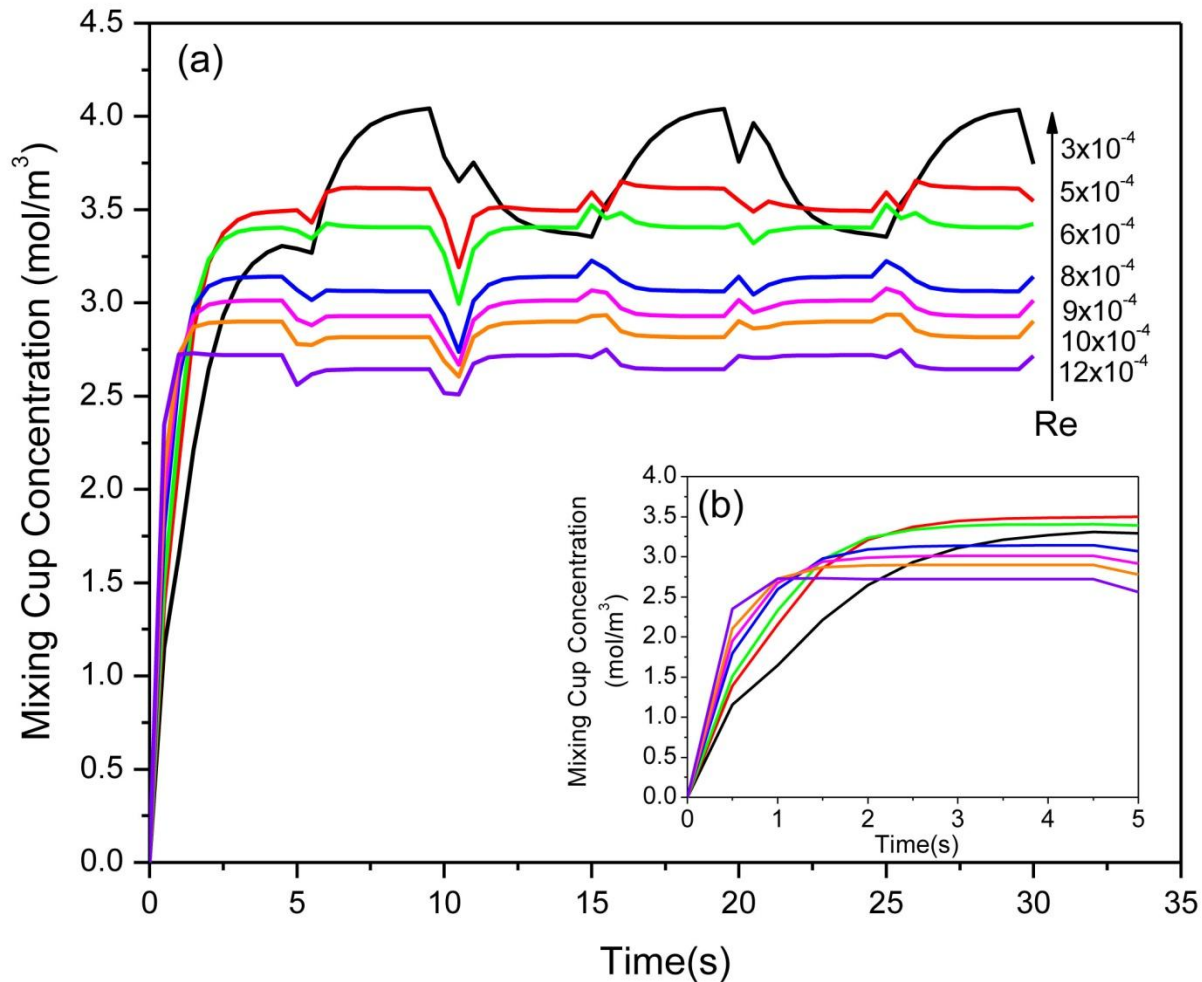


Figure 3.39 Variation of mixing cup concentration of MNP-tagged-biomolecule complex formed during the bulk phase reaction between MNPs and biomolecules in the presence of magnetic actuation scheme with time. Effect of Reynolds number (3×10^{-4} to 12×10^{-4}) on the reaction kinetics of tagging process is analyzed. Inset (b) shows that after 5s, working with $Re \sim 5 \times 10^{-4}$ provides optimum flow conditions ($\sim 50 \mu\text{m/s}$) for formation of MNP-biomolecule complex.

3.4.3.3 A Comparative Study

In this section the novel strategy of using magnetic actuation to enhance tagging process as described earlier is compared with passive mixing scheme and with scenario when no actuation strategy either passive or active is deployed. For passive method three bluff bodies (barriers) were added to the top of channel and two to bottom of the microchannel.

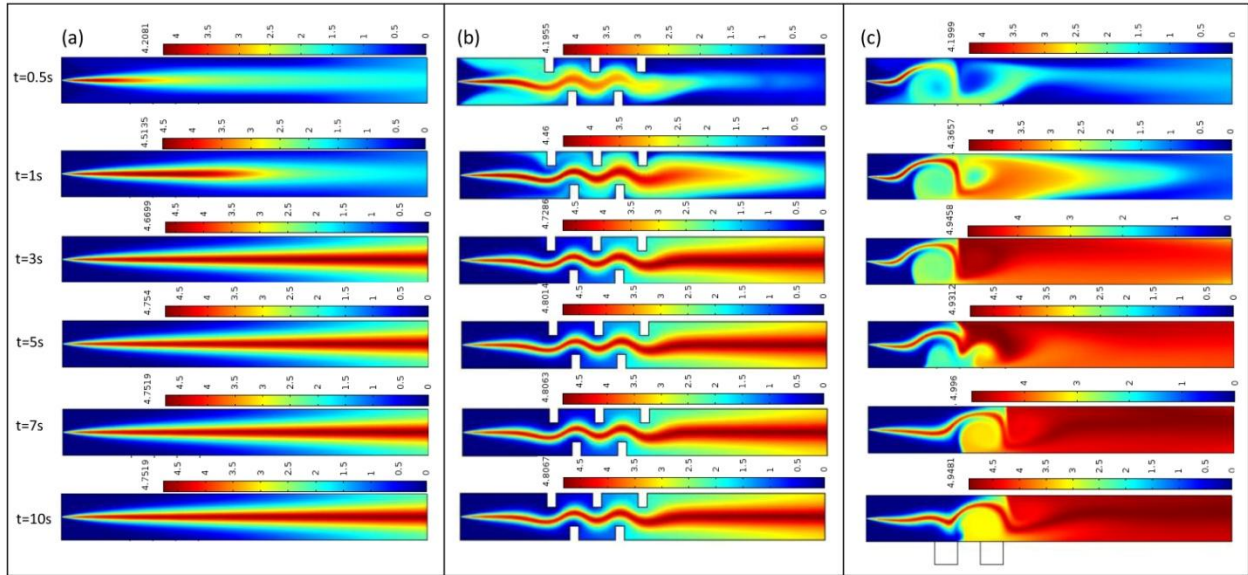


Figure 3.40 Simulated concentration profile of MNP-tagged-biomolecule complex after 10s formed during the bulk phase reaction between MNPs and biomolecules for three different scenarios (a) no active or passive mixing, (b) with passive barriers, and (c) with active magnetic actuation.

The barriers had width of $2\mu\text{m}$ and height of $3\mu\text{m}$ placed $3.5\mu\text{m}$ apart. This is done to reduce the diffusion length and create disturbances in streamlines with an objective to provide better contact between MNPs and biomolecule for tagging process. A flow velocity of $50\mu\text{m/s}$ is used for all three scenarios. For magnetic actuation, MNPs of 100nm diameter were used together with magnetic field switching frequency of 0.1Hz . All the other parameters are kept constant as described in previous sections throughout the simulations that run for 10s. The mixing cup concentrations (C_{MC}) of MNP-biomolecule (MNPBIO) complex is predicted for three different scenarios including standard straight microchannel without any actuation, microchannel with bluff bodies, and microchannel with magnetic field effect. Figure 3.40 shows the predicted concentration profile of MNP-biomolecule complex for three different scenarios at different time slots. It can be seen that for base scenario without any actuation strategy (see Figure 3.40a) the bulk phase reaction only takes place at the interface of MNPs and biomolecules due to diffusion limitation and no mixing.

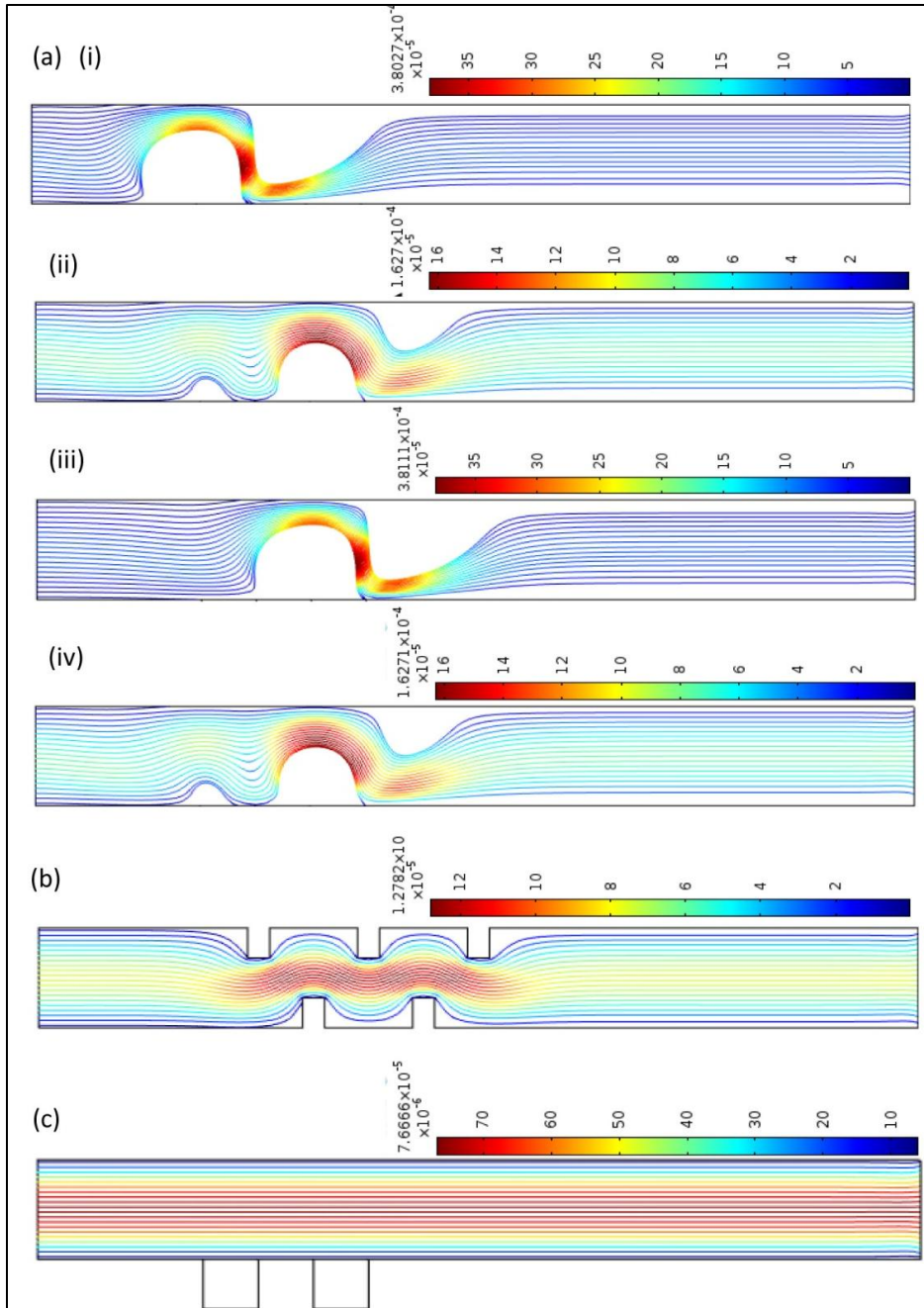


Figure 3.41 Streamline plots of velocity field of carrier fluid containing MNPs for three different scenarios (a) with active magnetic actuation at $t =$ (i) 4.5s, (ii) 5s, (iii) 5.5s, and (iv) 10s, (b) with passive barriers at $t = 10$ s, and (c) no active or passive mixing at $t = 10$ s. The plot shows that velocity field is varying for magnetic actuation scheme and therefore provides better mixing.

With the use of passive actuation scheme as shown in Figure 3.40b, an enhancement in binding can be observed due to slight stretching and folding of streamlines (see Figure 3.41b) due to presence of barriers. Even though passive method enhanced the tagging process as compared to

scenario when no actuation was used, but it was small as compared to scenario when magnetic actuation was deployed (see Figure 3.40c). Furthermore, magnetic nanoparticle actuation scheme produced large stretching and folding of stream lines that also dynamically changed with time as shown in Figure 3.41a resulting in enhanced mixing. It can also be seen quantitatively from Figure 3.42 that large increase in formation of mixing cup concentrations (C_{MC}) of MNP-biomolecule complex was observed when magnetic actuation is used in the tagging process.

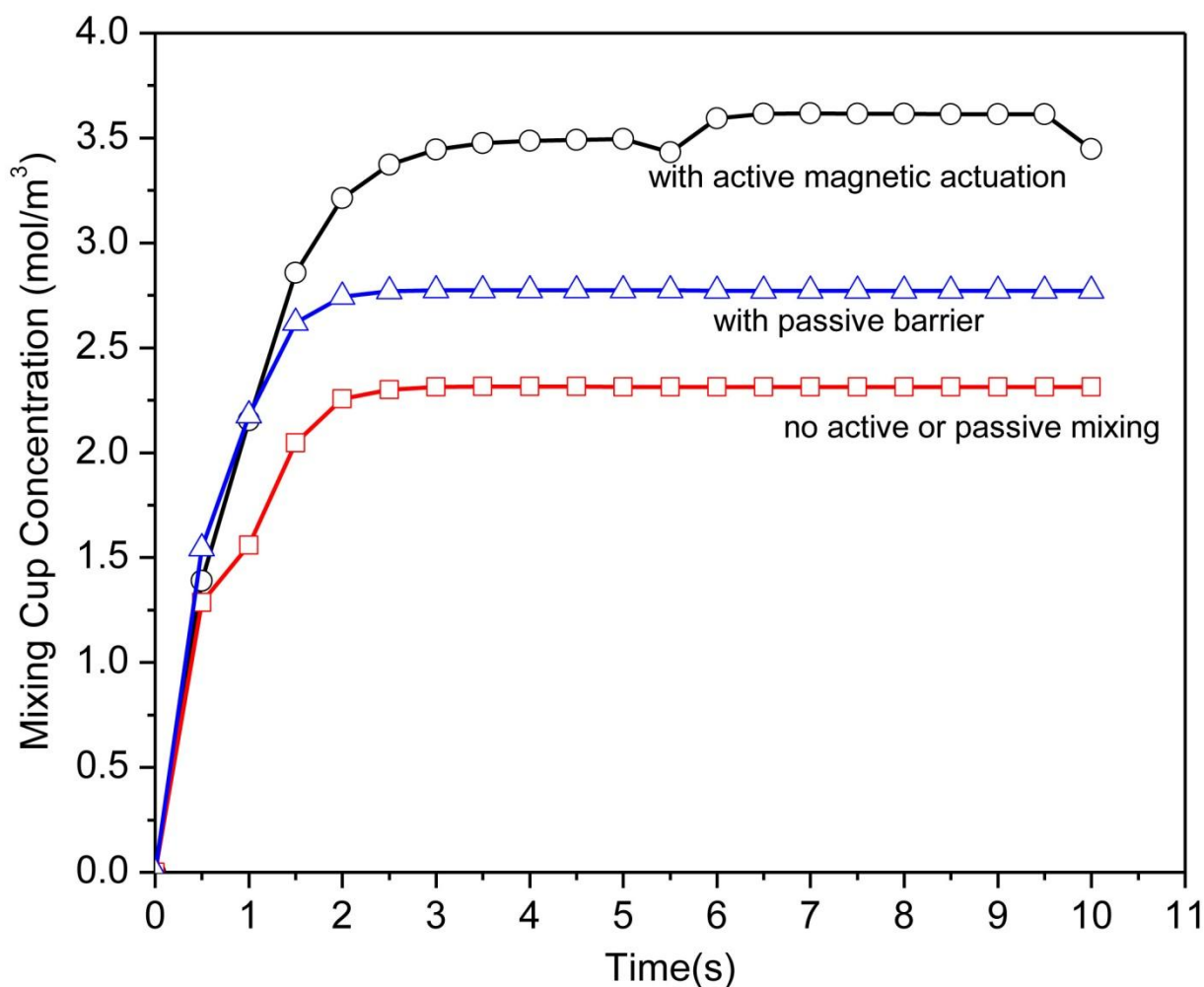


Figure 3.42 Comparative Study: Variation of mixing cup concentration of MNP-tagged-biomolecule complex formed during the bulk phase reaction between MNPs and biomolecules with time for three different scenarios (a) no active or passive mixing, (b) with passive barriers, and (c) with active magnetic actuation.

Overall, based on the mixing cup concentrations (C_{MC}) curves, a 20% increase in tagging process is observed when passive method is used whereas 49% increase in tagging performance is observed when magnetic nanoparticle together with magnetic actuation strategy is used in the system. The numerical simulations results reported here indicate that magnetic nanoparticle-based strategy performs better in all conditions and can be a useful technique for speeding up the reaction kinetics of the tagging process, particularly for diffusion-limited microfluidic systems. This strategy is easy to implement and can be very easily integrated on a lab-on-a-chip devices for developing rapid and sensitive micro-total analysis systems.

3.4.4 Conclusion

COMSOL-based multi-physics model is developed to demonstrate a novel magnetically actuated tagging process in microfluidic systems using magnetic nanoparticles. It is shown that oscillating electromagnetic body forces can be produced due to the electrodes embedded in the device substrate resulting in MNPs agitation causing enhanced mixing in the surrounding fluid. The strategy demonstrated here overall speeds up the reaction kinetics of the tagging process and can be easily integrated on lab-on-a-chip systems. The model was used to quantitatively as well as qualitatively investigate the effect of fluid flow, magnetic nanoparticle size, and frequency of magnetic actuation on the tagging kinetics and subsequently optimized parametric values were predicted. Furthermore, magnetic actuation strategy was compared with passive mixing method to enhance reaction kinetics of tagging process. A 49% increase in tagging performance was observed when magnetic nanoparticle together with magnetic actuation strategy was used as compared to passive method which resulted in only 20% increase in tagging process. The numerical simulations results reported here indicate that magnetic nanoparticle-based strategy performs better in all conditions and can be a useful technique for speeding up the reaction

kinetics of the tagging process, particularly for diffusion-limited microfluidic systems. Overall, the developed “numerical prototype” proves that time-dependent magnetic manipulation technique has an excellent potential to efficiently tag MNPs with biomolecules *in situ* for further processing and will be very useful in developing rapid and sensitive micro-total analysis systems.

4. PROOF-OF-CONCEPT EXPERIMENTATION & VALIDATION

4.1 Experimental Materials & Methods

4.1.1 Magnetic Microfluidic Platform Setup

A simple, low cost and generic magnetic microfluidic platform setup that consisted of microfluidic channel, magnetic nanoparticles (MNPs), and in-house assembled magnets is shown in Figure 4.1. The magnetic and microfluidic assembly can be divided into six main components: the microfluidic microchip, the magnetic nanoparticles, the fluidic connections, the imaging & analytical instrumentation, and the magnetic assembly. Design and fabrication of microfluidic chip together with synthesis of magnetic nanoparticles will be discussed in more detail in later section.

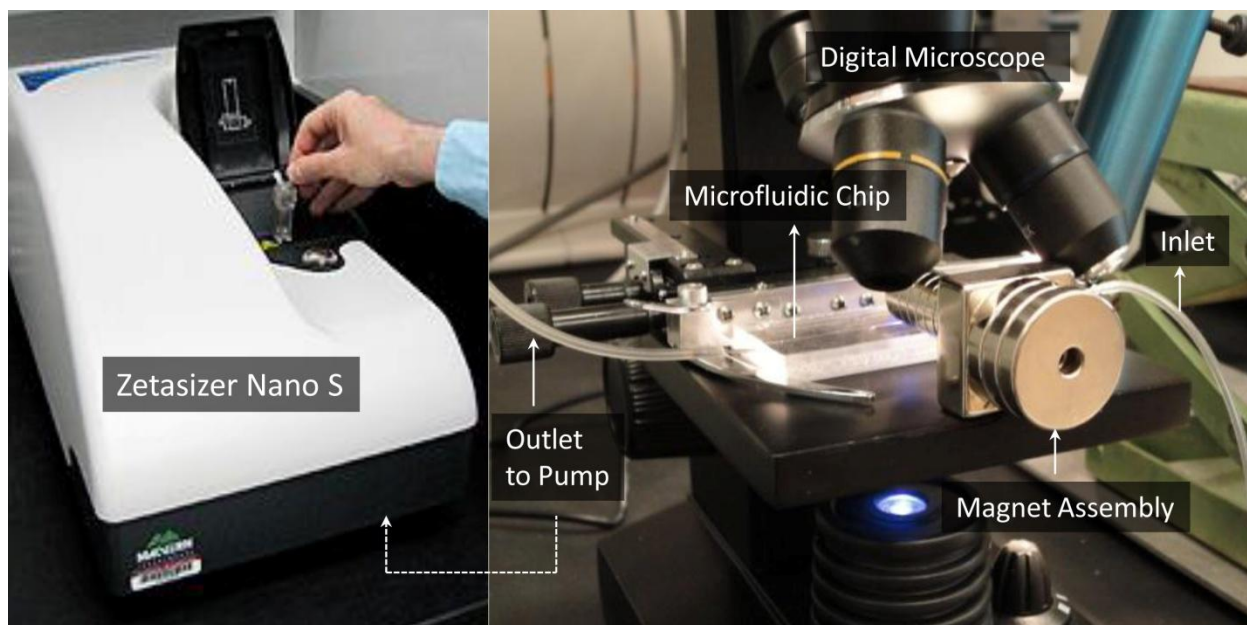


Figure 4.1 Microfluidic platform with inlet and outlet connections through tubings, permanent magnet in the vicinity of microfluidic chip, and the objective of microscope over the ROI for recording images. The sample from outlet is taken in Zetasizer Nano for concentration analysis.

The microchip for the retention and manipulation of magnetic nanoparticles in a sample flow relies on a simple and robust design. A unique microfluidic channel including a single inlet and a single outlet will be sufficient to perform mixing and separation analysis on chip. As shown in

Figure 4.1, the microfluidic channel was connected with inlet and outlet via flexible tygon tubing. In order to provide leak free connections a microsyringe tips made of stainless steel was embedded into the microchannel inlet/outlet for secure connections between the flexible tubes and the microfluidic chip.

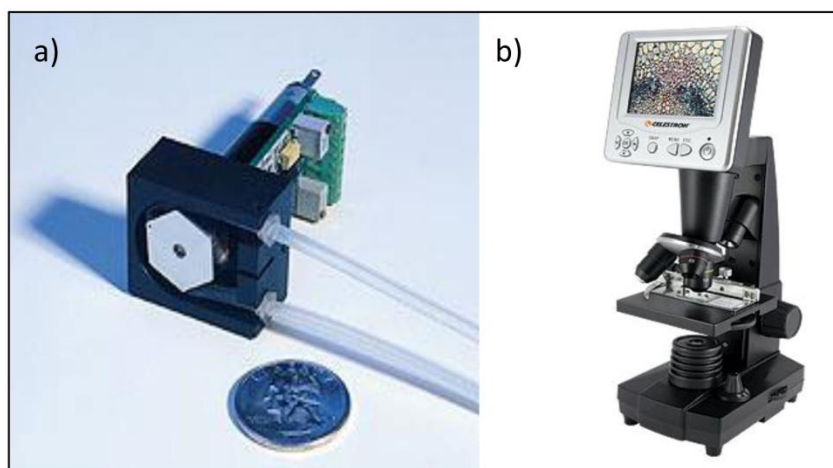


Figure 4.2 Components of Experimental Set up: a) Micro-peristaltic pump with inlet and outlet connections using tygon tubing, (b) LCD Digital microscope with translational stage for image acquisition.

The overall objective of the experiments were to capture optical images of the magnet nanoparticles as well collect samples for concentration analysis in the microfluidic channels under different magnetic actuation conditions. Therefore, a differential pressure drop is maintained inside the channel by connecting the outlet to peristaltic micropump (Instech P625) and inlet to reservoir containing magnetic solution. Flow rate can be varied using the precise-bi directional speed controller on the pump (see Figure 4.2). This simple method allows for a good control of the flow in the channel in suction mode.

In order to provide static magnetic field in the experimentation an assembly of permanent neodymium magnet purchased from KJ Magnetics were used. Most of the capturing and separation studies involved static magnetic field where as dynamic magnetic field used in mixing experiments was provided using in-house assembled electromagnet kit purchased from Arttec

Inc. (Arttec., Inc, Woolwich, Maine). The kit comes with few levels of assembly (soldering the parts onto the printed circuit board). The electromagnet was basically constructed from a 2700 turns of 33 gage wire on a 2" bolt and nut with a 60 Ohm coil measuring 1" x 1 1/4". The total air gap is about 3/8". The electromagnet requires a 12VDC at 200mA. The knob on the circuit board can be used to adjust the air gap by about 1/4" and also works as on/off switch for magnetic field. Magnetic assembly was placed near the vicinity of the microchannel and optical images were acquired using the digital microscope (Celestron 44340). The digital microscope used in the experiments is shown in Figure 4.2b. It consists of integrated LCD screen together with USB connection to PC. The translational stage of the microscope was used to place the microfluidic chip assembly such that the objective of camera can acquire images of the flowing nanoparticles both in static and in real time. The CCD camera can be connected to a computer for data acquisition. The translation stage could be adjusted in the horizontal direction for focusing the channel and in the vertical direction to investigate the flow inside the channel. Image acquisition was performed using ImageJ software (NIH, USA). Images were acquired from the region of interest (ROI) under Bright field lightning condition.

4.1.2 Microfluidic chip fabrication

Polydimethylsiloxane (PDMS) is widely used for the fabrication of microfluidic systems because it can readily be transferred into the desired shape, is easy to seal onto substrates, and is transparent thus permitting visualization of the sample. However, the fabrication of PDMS-based microfluidic devices requires a mold or mask that is often developed using photoresist (SU-8) and silicon lithography. This process requires clean room for photolithography and microfabrication methods, all of which are expensive and time consuming and beyond the reach of many researchers. Recently, rapid prototyping techniques that circumvent the requirement for

a clean room have been proposed, such as the use of double sided scotch tapes, but lack precision and control. Moreover, both rapid prototyping method and clean room method produce negative or positive stamp on PDMS which needs to be combined with glass or silicon using plasma. Combination of two pieces of element often leads to problem of leakage. In this work standard molding process was combined with novel rapid prototyping method to produce low cost microfluidic chip made of polydimethylsiloxane (PDMS). An Aluminum wire of known diameter was used as a mold. The size of each microchannel was adjusted by selecting different sizes of wires, and different branch architectures can also readily be fabricated. The wires are then simply removed from the PDMS replica leaving behind a network of microchannels. The fabrication starts by fixing an aluminum wire in the center and approximately at half the depth of the empty Petri dish. Small holes were created on the sides of petri-dish to hold the wire at half the depth, these holes were later sealed using adhesive tapes to remove substantial leakage. PDMS with a base and curing agent (Sylgard 184) kit was purchased from, Dow Corning. USA. The kit contains two parts: a liquid silicone rubber base and a catalyst or curing agent. The base and curing agent are typically mixed in a ratio of 10:1. Once mixed, the liquid mixture becomes a solid and cross-linked elastomer in a few hours. Heat will accelerate the crosslinking reaction. If the ratio of curing agent to base is increased, a harder and more cross-linked elastomer can be formed. The fabrication process includes following steps: weigh, mix, degas, dispense, spread, curing and peel off. PDMS with a base and curing agent mixed in a ratio of 10:1 was poured onto the mold (see Figure 4.3) and was degassed to remove any bubbles using desiccators. The uncured PDMS was baked in an oven (65 °C) for 1 h. The final step was to peel off the cured-PDMS containing the aluminium wire from the Petri dish. The sides of the cured PDMS were cut

using a razor blade, leaving a significant amount of the wire exposed outside. With the help of pliers the wire were carefully removed.

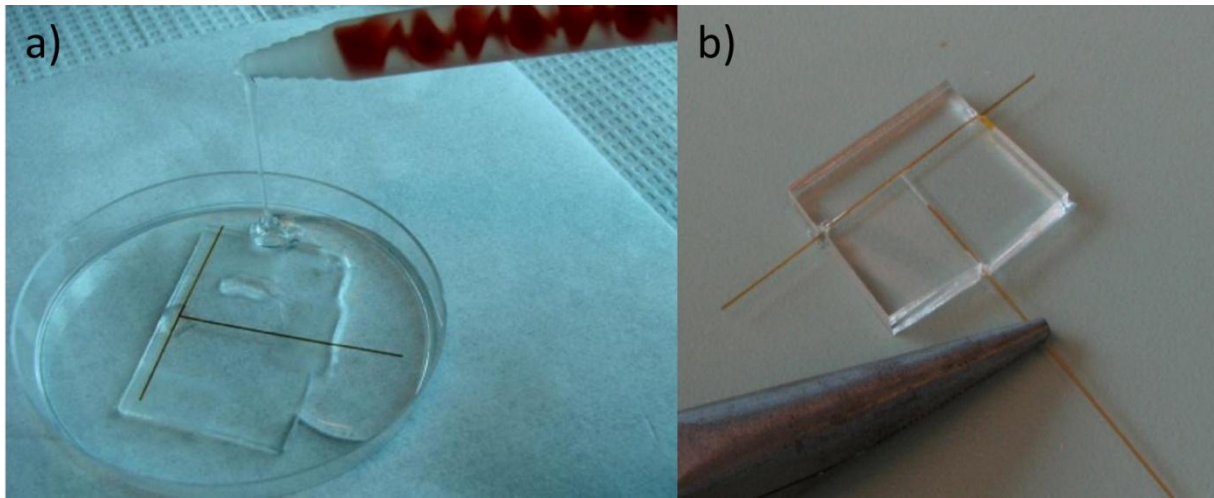


Figure 4.3 Fabrication Process for developing Microfluidic Channel, a) Pouring PDMS mix over the mold, and b) Cured microchannel with wires embedded in it.

To make this process easier, the microchannel were washed with acetone which swelled the PDMS and expanded the channels prior to pulling out the wires. The microchannel was connected with the tygon tubing as shown in Figure 4.4 using the stainless tip obtained from microsyringe. The tip was inserted into the microchannel to make leakage free connection.

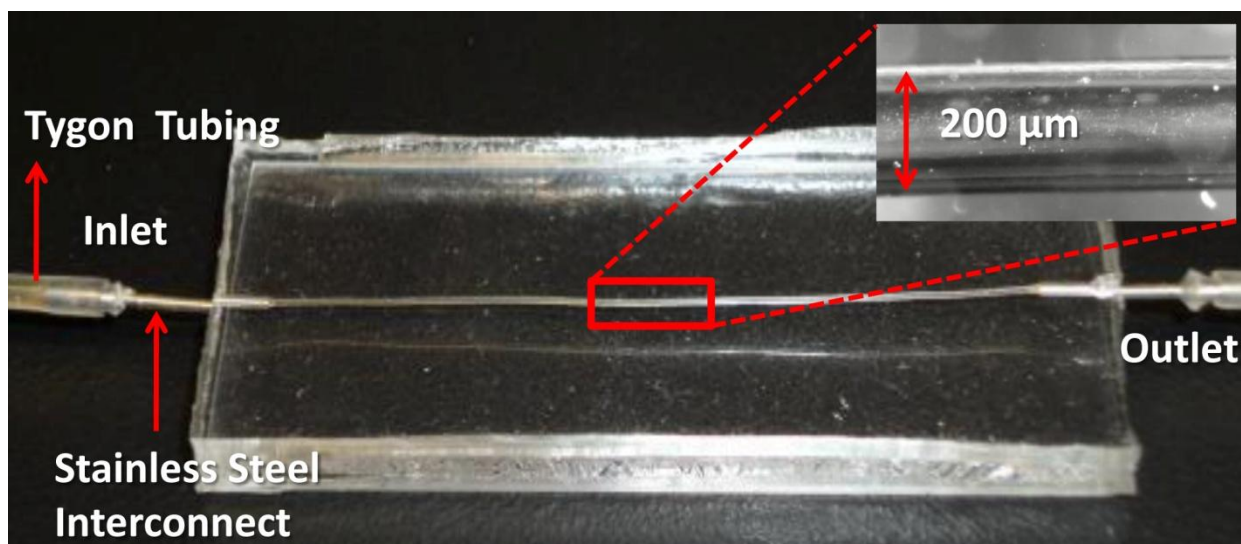


Figure 4.4 Straight Microchannel fabricated using PDMS and micromolding process with connection for inlet and outlet using tygon tubing and stainless steel tip as interconnect.

4.1.3 Magnetic Nanoparticles

Magnetic nanoparticles with diameters of 200 nm were obtained from Chemicell GMBH. These superparamagnetic nanoparticles as shown in Figure 4.5 are made of magnetic iron oxide core and covered with hydrophilic polymers which protect them against aggregation by foreign ions.

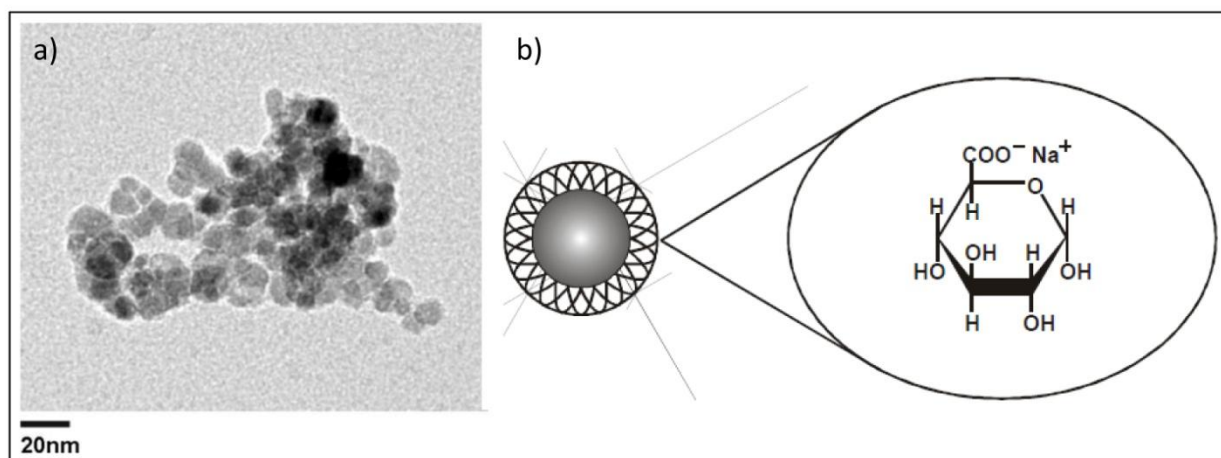


Figure 4.5 Magnetic Nanoparticles used in this work, a) TEM image of multi-domain magnetite core, and b) structure of magnetic nanoparticles with magnetic core surrounded by polysaccharide matrix.

Terminal functional groups such as ion-exchange groups or reactive groups for covalent immobilization can be used for binding to biomolecules. FluidMAG-ARA will be used in this work because it has terminal carboxyl group which can be easily attached to biomolecules of interest. The fluidMAG-ara particles (chemicell, Berlin, Germany) consist of small magnetite (Fe_3O_4) crystals with a diameter of approximately 12 nm, embedded in a biocompatible polysaccharide matrix. This enables stability and prevents biodegradation for several days up to weeks. Magnetite is known to be completely biocompatible. It does not show any toxicity (no L50 index) [207]. The shell allows for covalent binding of biomolecules of interest so that the particles can be functionalized. The average diameter of the particles is approximately 200 nm, whereas the volume fraction of magnetite within a composite particle is 80%. A composite particle is not a perfect sphere; it is randomly shaped due to the fact that the magnetite particles are held together only by a thin shell as seen in Figure 4.5b. The size distribution of the single crystals was determined by transmission electron microscopy (TEM). A TEM image of a composite particle is shown in Figure 4.5a. The single crystals are clearly visible, whereas the shell does not provide any contrast.

4.1.4 Calibration Curve

The concentration of MNPs solution in the effluent was estimated from in-house determined calibration curve. The calibration curves were generated from original stock of MNPs solution diluted to different concentrations. A dynamic light scattering instrument (Malvern Zetasizer Nano S, UK) as shown in Figure 4.1 was used. The Zetasizer Nano S measures the intensity of scattered light of various concentrations of sample at one angle; this is compared with the scattering produced from a standard (i.e. Toluene).

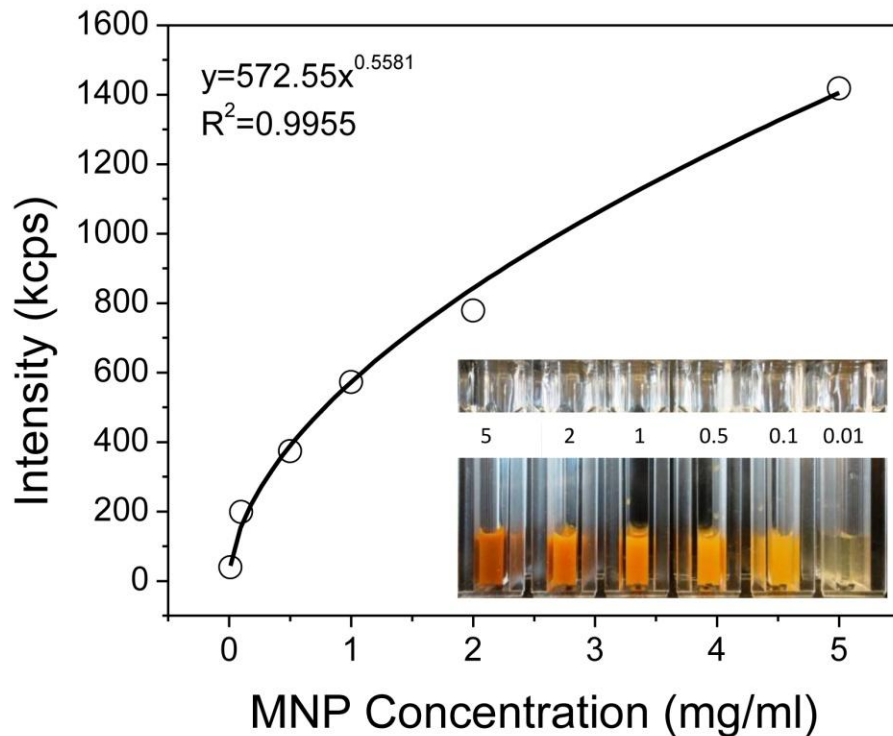


Figure 4.6 Calibration Curve obtained for MNPs using scattering intensity obtained from Zetasizer Nano S. Inset shows different concentrations of MNPs used in generating calibration curve($R^2=0.9908$).

In general, Zetasizer is used to measure the size of molecules but also the count rate can be used as a method of determining the relative concentration of a sample of stable size—as the count rate goes down, so does the concentration. While the Zetasizer software does not automatically spit out an estimated sample concentration from the count rate, it is actually a fairly stable value for the same sample over time, and therefore is used in this work as an estimate of concentration. Power law calibration curve of scattering intensity (kilocounts per second, kcps) versus concentration of magnetic nanoparticles (mg/ml) were obtained for 200nm particles ($R^2=0.9908$) (see Figure 4.6).

4.2 In situ analysis of capturing dynamics of magnetic nanoparticles in a microfluidic system

4.2.1 State of the Art

A Magnetic field-assisted separation of biomolecules in microfluidic systems has received increased attention in the last decade due to its vast applications in biomedical engineering research, clinical diagnostic and biotechnological sciences. The idea behind this innovative technology involves isolating biomolecules of interest from the bulk mixture by attaching them to magnetic particles and then recovering it using an external magnetic field [3, 29, 41, 61, 134, 207]. In the past few years, several microfluidic system incorporating magnetic-actuation have been successfully developed for separation and detection of biomolecules [45, 60], immunoassay of proteins [48, 172], purification of DNA [50], and cell separation [52]. Most of these system are based on functionalized magnetic beads or microparticles [29, 47, 52, 147], however there are relative few microfluidic systems [62] in literature that have employed magnetic nanoparticles (MNPs) for separation of biomolecules. Compared with microparticles, MNPs possess better properties that can advantageously be used in microfluidic devices, such as their extremely small size causes minimal disturbance to attached biomolecules [37]. MNPs also possesses higher surface to volume ratio [37, 61, 62] that can bring out efficient chemical binding and most importantly they are super-paramagnetic [37], i.e., their magnetization without a magnetic field is zero. The super-paramagnetic nature ensures that they stay suspended in carrier liquid when the magnetic field is removed without giving agglomeration issues as can be seen in microparticles or microbeads. This makes it easy for the removal or capture of tagged biomolecules of interest and better interaction with biomolecules like cells, proteins, DNA etc. Overall, inclusion of magnetic nanoparticles in microfluidic devices will greatly enhance the

device functionality and separation performance. The separation of biomolecules not only depends on the use of magnetic nanoparticles but is also a multiphysics phenomenon that involves interplay of various other parameters such as inlet velocity, MNP size, magnetic field strength and its orientation, geometry of the device etc. In order to design and develop more robust magnetic microfluidic system it is important to understand how these parameters influence each other. Proof of concept experiments together with mathematical modeling can reveal the dynamics of this process and will be very helpful in designing, optimizing and developing more efficient magnetic microfluidic bioseparation system. To date several groups have reported [138, 208-213] the study of the transport of magnetic particles in microfluidic system but most of these were focused on microparticles or microbeads. Moreover, only simple magnetic field configurations were considered without a detailed analysis and optimization strategies. Recent advances in MEMS technology has helped researcher to develop systems for manipulation of microparticles [[138, 208-213]. Experimental investigations have so far focused on qualitative demonstrations of capture [138, 208-213] or separation [138, 208-213] using microfabricated electromagnets. While useful, these investigations lack detailed quantitative analysis that can be used for designing more simple and robust systems. Moreover, these devices require expensive fabrication processes or clean room techniques in order to integrate the magnets with the microfluidic channels to achieve magnetic particles capturing and separation. A microfluidic system that allows a simple fabrication procedure while achieving the same functional purpose of magnetic based separation is also highly desirable.

In this work, a simple, low cost and generic microfluidic platform is assembled to study the dynamics of magnetic nanoparticle capturing process. Standard molding process combined with a novel rapid prototyping method is used to develop low cost polydimethylsiloxane (PDMS)

microchannel. The fabrication method used in this work circumvents the requirement for a clean room. It also eliminates the combination of two pieces of element, such as in standard fabrication method where negative or positive stamp on PDMS are combined with glass or silicon using plasma as a result overcomes the problem of leakage. Magnetic nanoparticle dynamics in microchannel is studied using an experimental setup containing a sub-microliter fluid volume surrounded permanent magnet systems for particle capturing. On the basis of MNPs concentration measurement using optical technique, capturing efficiency analysis is performed. Influence of flow rate conditions, magnetic field systems on the capturing efficiency is investigated. A finite-element-based mathematical model is also developed to predict the dynamics of the magnetic nanoparticle loaded fluid. The simulations are found to be in good agreement with the experimental results. Parametric investigations using both experiments and theoretical predictions illustrate the effects of flow and magnetic parameters on the MNPs capturing efficiency in the microchannel and agree very well with each other. Mathematical model is further used to enhance the performance of the proof-of-concept study performed using the experimental setup. A novel idea of incorporating a grooved iron bar in close proximity to a microfluidic channel is tested using the numerical simulation. The presence of external grooved shape iron bar altered the magnitude of the magnetic field density gradient inside the microchannel which results in an increase in capturing efficiency due to higher magnetic force acting on the MNPs. This work demonstrates that a simple low cost experimental proof-of-concept setup can be synchronized with advanced numerical simulation to design and improve the functional performance of magneto-fluidic bioseparation systems based on magnetic nanoparticles.

4.2.2 Materials & Methods

4.2.2.1 Microchannel Fabrication

The microfluidic channels with a diameter of 500 μ m and length of 75mm were fabricated by a low cost rapid micromolding technique. First, a mold was prepared by fixing an aluminum wire of 500 μ m diameter in the center and approximately at half the depth of the empty Petri dish. Polydimethylsiloxane (PDMS)(Sylgard 184, Dow Corning, USA) with a base and curing agent mixed in a ratio of 10:1 was poured onto the mold and was degassed to remove any bubbles using desiccators. The uncured PDMS was baked in an oven (65 °C) for 1 h. The final step was to peel off the cured-PDMS containing the aluminium wire from the Petri dish. The sides of the cured PDMS were cut using a razor blade, leaving a significant amount of the wire exposed outside. With the help of pliers the wire were carefully removed. To make this process easier, the microchannel were washed with acetone which swelled the PDMS and expanded the channels prior to pulling out the wires. The microchannel was connected with the tygon tubing using the stainless tip obtained from microsyringe. The tip was inserted into the microchannel to make leakage free connection.

4.2.2.2 Microfluidic System Setup

A schematic view together with experimental set-up to carry out magneto-hydrodynamic experiments is shown in Figure 4.7a and Figure 4.7b. The magnetic and microfluidic set-up may be divided in five main components: the microchannel, the magnetic nanoparticles solution, the fluidic connections, the imaging instrumentation, and the permanent magnet system. As shown in Figure 4.7, the microfluidic channel is connected with inlet and outlet via flexible tygon tubing. In order to provide leak free connections a microsyringe tips made of stainless steel are

embedded into the microchannel inlet/outlet for secure connections between the flexible tubes and the microfluidic chip.

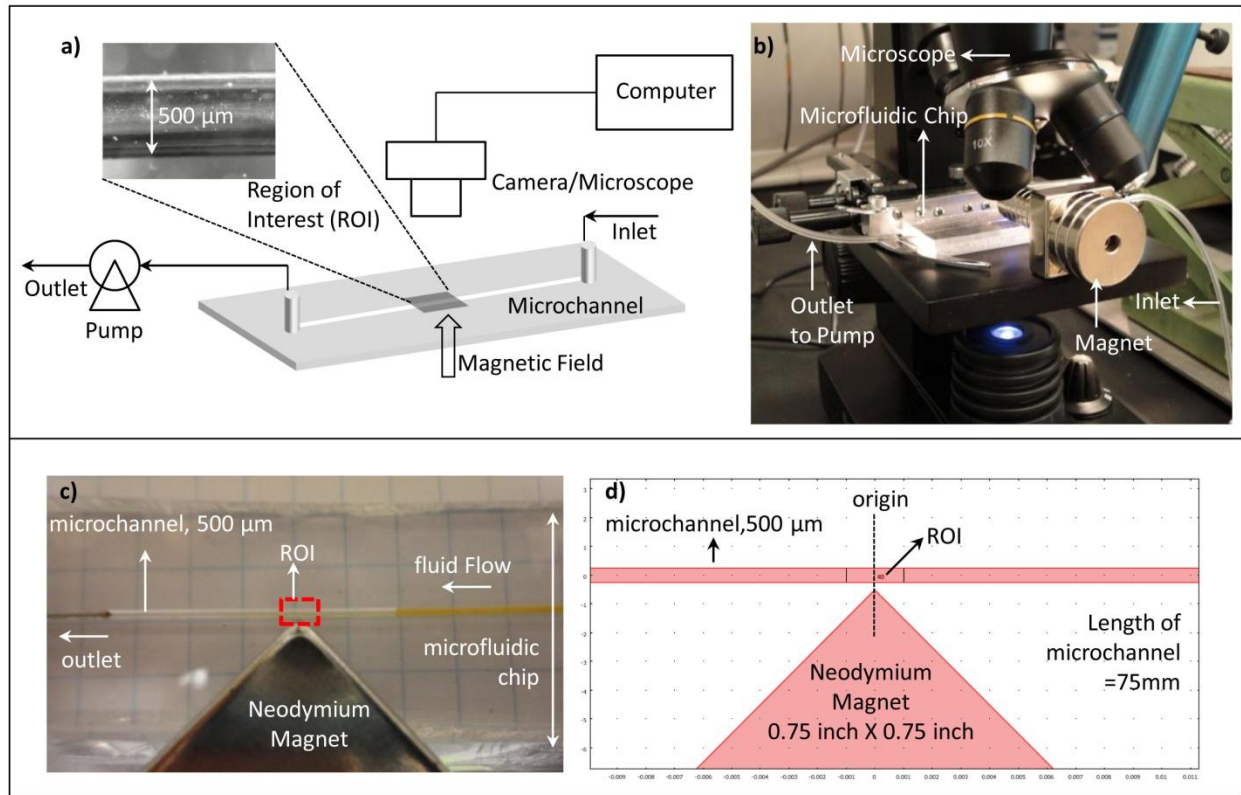


Figure 4.7 Microfluidic Magnetic Nanoparticle Capturing System; (a) schematic of the experimental setup, (b) snapshot of the setup showing microfluidic platform with inlet and outlet connections through tubings, permanent magnet in the vicinity of microfluidic chip, and the objective of microscope over the region of interest (ROI) for recording images. Inset shows the size of ROI and microchannel diameter, (c) experimental setup showing ROI within the microchannel with neodymium magnet placed at its edge (System 8), and (d) Finite Element Model setup in COMSOL for simulating the scenario given in (c). (Length of channel=75mm)

A differential pressure drop is maintained inside the channel by connecting the outlet of the microchannel to peristaltic micropump (P625 Peristaltic Pump, Instech, USA) and inlet to reservoir containing MNPs solution. Flow rate were varied using the precise-bi directional speed controller on the pump. This simple method allows for a good control of the flow in the channel in suction mode. Magnetic field is provided by assembly of permanent neodymium magnets (KJ Magnetics, USA). Magnetic system assembly comprising of different shapes and strength of neodymium magnets as illustrated in Table 4.1, were used in the vicinity of the microchannel.

The approximate strength of magnetic assemblies was calculated based on the finite element simulation described later in the section.

Table 4.1 Specification of Magnetic System Assembly used in Capturing MNPs

System	Specification(inch)				Effective Width ^a inch	Length inch	Magnetic Flux density Tesla (T)
	Square (0.75 X 0.75)	Circular (D=0.75)	Circular (D=0.50)	Rectangle (0.75x 0.375)			
1	0	14	0	0	0.75	1.75	0.236
2	1	14	0	0	0.75	2.5	0.276
3	0	0	22	0	0.5	1.375	0.229
4	0	0	0	20	0.375	1.25	0.138
5	1	0	0	20	0.375	1.5	0.177
6	1	14	0	20	0.75	3.25	0.264
7	1 (Flat)	0	0	0	0.75	0.75	0.45 ^b
8	1 (Edge)	0	0	0	0.75	0.75	0.645 ^b

^a Surface width of magnet close to the wall of microchannel

^b Magnet system is close to the wall of microchannel (0 mm)

Optical images in the region of interest (ROI) (see Figure 4.7a) were acquired using the digital microscope (Celestron 44340, Celestron Inc., USA). The translational stage of the microscope was used to place the microfluidic chip assembly such that the objective of camera acquires images of the flowing nanoparticles both in static and in real time. The CCD camera was connected to a computer for data acquisition. Image acquisition was performed using ImageJ software (NIH, USA) from the region of interest (ROI) under bright field lightning condition.

Magnetic nanoparticles (MNPs) of 200nm diameter (fluidMAG-ARA Chemicell GMBH, Germany) were suspended in de-ionized DI water and injected into the inlet. The magnetic nanoparticles consisted of an inner core made up of magnetite (Fe₃O₄) crystals of approximately 12 nm diameter, embedded in a biocompatible polysaccharide matrix for better stability that also prevented biodegradation. The overall diameter of the nanoparticles was approximately 200 nm,

whereas the volume fraction of magnetite within a composite particle is 80%. For different flow rates, effluent was collected at the outlets once all the solution has passed through the microchannel. The volume collected at the outlet was regularly verified to confirm the equal flow rates in the microchannel.

The concentration of MNPs solution in the effluent was estimated from in-house determined calibration curve. The calibration curves were generated from original stock of MNPs solution diluted to different concentrations. A dynamic light scattering instrument (Malvern Zetasizer Nano S, UK) was used. The Zetasizer Nano S measures the intensity of scattered light of various concentrations of sample at one angle; this is compared with the scattering produced from a standard (i.e. Toluene). In general, Zetasizer is used to measure the size of molecules but also the count rate can be used as a method of determining the relative concentration of a sample of stable size—as the count rate goes down, so does the concentration. While the Zetasizer software does not automatically spit out an estimated sample concentration from the count rate, it is actually a fairly stable value for the same sample over time, and therefore is used in this work as an estimate of concentration. Power law calibration curve of scattering intensity (kilocounts per second, kcps) versus concentration of magnetic nanoparticles (mg/ml) were obtained for 200nm particles ($R^2=0.9908$). In order to obtain capturing efficiency ($CE_{\text{experiment}}$) of the system under various condition of magnetic field strength and flow rate, the outlet sample from the effluent was taken in cuvette and placed in Zetsizer to obtain unknown scattering intensity (kcps) of the sample. Calibration curve was used to convert the scattering intensity into concentration (mg/ml). Since the inlet concentration of MNPs was known, capturing efficiency was calculated by subtracting the ratio of outlet to inlet concentration from 1.

4.2.2.3 Numerical Model

A finite element mathematical model was implemented keeping the following objective in mind; i) to investigate the interaction of external magnetic field with the flow of magnetic nanoparticles, ii) to predict and validate the experimental proof-of-concept study, and iii) to implement a novel idea in the system for enhancing the performance. The two-dimensional geometrical representation of a microfluidic channel with a permanent magnet as used in experiments is shown in Figure 4.7d. It was assumed that the mass transport variation under the influence of magnetic field will be negligible in the direction perpendicular to the x-y plane due to high aspect ratio [214] of the system modeled. This will reduce the 3D geometry to a 2D thereby significantly decreasing the computational overhead. Moreover, a 2D model will serve as a simple, fast, and relatively accurate guideline for designing and optimizing magnetic microfluidic systems for bioseparation.

The 2D model geometry as shown in Figure 4.7d consists of a microchannel which is 500 μm wide and 75mm long. A magnetic field assembly comprising of a 0.75 x 0.75 inch square neodymium magnet is placed closed to the microchannel with one of its edge very close to the microchannel. This geometry is chosen to represent the system 8 (see Table 4.1) magnetic field assembly. The magnetic nanoparticles are assumed to be dispersed in the water and flow from right to left. The transport of a magnetic nanoparticle in a carrier fluid (eg: water) is governed by the following major factors including a) the magnetic force, arising from magnetic field and strong magnetic field gradient created from external permanent magnet, b) the viscous drag, due to movement of magnetic nanoparticles with respect the surrounding fluid, (c) fluid-particle interactions, due to perturbations produced in the flow field , (d) gravity/buoyancy, (e) thermal kinetics (Brownian motion), and (h) inter-particle effects. In the experimentation a low

concentration of MNPs was used therefore particle/fluid interactions and inter-particle effects were neglected in the analysis. Moreover, the size of MNPs was extremely small (~200nm) therefore gravity effects were neglected but Brownian motion [214] was included by incorporating a drift-diffusion equation for simulating the behavior of a concentration of magnetic nanoparticles. The equations and theory developed are based on Navier-Stokes equations for solving flow field of carrier fluid (in this case it is assumed water), drift diffusion equation for mass transport of MNPs, and Maxwell's equations to predict magnetic field and magnetic force in the microchannel. The model basically solves the Maxwell's equation for a static magnetic field. The computed magnetic force is coupled to fluid flow by using the magnetic volume force term acting on the nanoparticles in the Navier-Stokes equations, which accounts for the momentum transfer from the MNPs to the fluid (particle-fluid interaction). A drift-diffusion equation was used to predict the nanoparticle concentration which was dependent on flux contributions from diffusion, advection, and magnetic force-based migration. The detailed explanation of the equations and theory used in the model are described in the following sections.

1.1.1.1. Magneto-Static Equations

The static magnetic field is calculated using Maxwell-Ampere's law given by;

$$\nabla \times H = J \quad (4.1)$$

Where H is the magnetic field vector (A/m) and J is the current density vector (A/m^2),

According to Gauss law for magnetic flux density, B (Vs/m^2)

$$\nabla \cdot B = 0 \quad (4.2)$$

In order to describe a relation between B and H , a constitutive relation given by the following equation is used in the model.

$$B = \mu(H + M) \quad (4.3)$$

Where, μ is the magnetic permeability and M is the magnetization vector. The magnetic permeability can also be expressed as $\mu_0\mu_r$ where μ_r is the relative permeability of magnet ($\mu_r = 1$) and is assumed to be constant in all the simulations and μ_0 is the permeability in vacuum ($\mu_0 = 4\pi \times 10^{-7} \text{ N/A}^2$). A magnetic vector potential A is described [180] according to the following equation

$$\nabla \times A = B; \nabla \cdot A = 0 \quad (4.4)$$

After substitution of Eq. 4.4 in Eq. 4.1, 4.2, and 4.3, the following vector equation is obtained;

$$\nabla \times \left(\frac{1}{\mu_0\mu_r} \nabla \times A - M \right) = J \quad (4.5)$$

It is assumed that the magnetic vector potential has a nonzero component only perpendicular to the plane A_z which basically simplifies the 2D and it has perpendicular current equals to zero.

Based on these assumptions Eq. 4.5 simplifies to following equation;

$$\nabla \times \left(\frac{1}{\mu_0\mu_r} \nabla \times A - M \right) = 0 \quad (4.6)$$

Given the magnetic field, H obtained using Eq. 4.6, magnetic force that is exerted on the magnetic nanoparticles is calculated using the following equation [180]:

$$F_m = (1 - N_d)\mu_0\mu_r\alpha V_{MNP}(H \cdot \nabla)H \quad (4.7)$$

Where, N_d is the demagnetizing factor (0.33 for a sphere), V_{MNP} is the volume of a magnetic nanoparticles, and α is the ratio of iron oxide content which is 0.8 for the magnetic nanoparticles used in this work.

4.2.2.3.1 Boundary Conditions

A magnetic insulation boundary condition ($A_z = 0$) was applied along the system boundary.

4.2.2.4 Fluid Flow Equation

The magnetic nanoparticles (MNPs) were assumed to be dispersed in the fluid of viscosity η ($10^{-3} \text{ kg/m}\cdot\text{s}$) and density ρ (10^3 kg/m^3) equal to that of water. The aqueous solution of MNPs is injected into the microchannel with a parabolic velocity. The magnetic force acting on MNPs due to external magnetic field transfers momentum to the surrounding fluid leading to a disturbance in flow profile of carrier liquid. The flow velocity u for this incompressible fluid ($\nabla \cdot u = 0$) is described using Navier-Stokes equation,

$$\rho \frac{\partial u}{\partial t} + \rho(u \cdot \nabla)u = -\nabla p + \eta \nabla^2 u + F_{vol} \quad (4.8)$$

Where, u is the carrier fluid velocity field (m/s), p is the pressure (N/m^2), and F_{vol} is the volume force (N/m^3). The momentum transfer from MNPs to the fluid is incorporated by setting the volume force term equal to the magnetic force acting on a single MNP multiplied with MNP number density, α , which is the number of MNP per unit volume. Therefore, the volume force acting on fluid is given by;

$$F_{vol} = \alpha F_m \quad (4.9)$$

Eq. 4.9 couples the fluid flow equation with the magnetic field equation and depends on the instantaneous concentration of MNP solution in the microchannel, which is described in more detail later section. MNP number density (α) is calculated using Eq. 4.10.

$$\alpha = \frac{6CM_{Fe_3O_4} \times 10^{-3}}{\rho_m \pi d_p^3} \quad (4.10)$$

Where, C is the concentration of MNPs (μM), $M_{Fe_3O_4}$ is the molar mass of Fe_3O_4 (g/mol), ρ_m is the density of MNPs (g/cm^3), and d_p is the diameter of MNPs (cm). It is also assumed that there is no particle-particle interaction (e.g.: Van der Waals forces) and even the sedimentation effects will have negligible influence on the overall mass transport due to extremely small size of MNPs.

4.2.2.4.1 Boundary Conditions

The flow of fluid at the inlet is assumed to be parabolic and moves in the direction of x-axis with zero velocity in y-direction. The average flow velocity of carrier fluid is u_0 . No slip condition ($u = v = 0$) is applied along the walls of microfluidic system and at the outlet, pressure condition is set equal to zero.

4.2.2.5 Drift-Diffusion Equation

The spatial and temporal variation of the MNP solution inside the microfluidic channel is described using the drift-diffusion equation where Brownian motion due to extremely small size of nanoparticle was also taken into account [180] Specifically, C the concentration of MNP solution is governed by the following equation [180],

$$\frac{\partial C}{\partial t} + \nabla \cdot J = 0 \quad (4.11)$$

Where $J = J_D + J_A$ is the total flux of nanoparticles, which includes a contribution from diffusion, $J_D = -D\nabla C$, and a contribution $J_A = u_p C$, due to the advection of the nanoparticles under the influence of applied forces. The drift velocity u_p of MNPs is obtained using classical Newtonian particle motion equation [19] as described below.

$$m_p \frac{\partial u_p}{\partial t} = F_m + F_g + F_D \quad (4.12)$$

In the limit of negligible inertia ($m_p \frac{\partial u_p}{\partial t} \rightarrow 0$) and zero gravitational force, F_g , equation 12 results in Eq. 4.13,

$$F_m + F_D = 0 \quad (4.13)$$

Where F_m and F_D are magnetic and drag forces respectively. According to Stokes' law of viscous drag, $F_D = -6\pi\eta r_p(u_p - u)$, where u_p and r_p is the MNPs velocity and radius respectively, u is the fluid velocity of viscosity η ($10^{-3} \text{ kg/m}\cdot\text{s}$). Therefore, from Eq. 4.13,

$$F_m - 6\pi\eta r_p(u_p - u) = 0 \quad (4.14)$$

Since the mobility of the particle is given by $\gamma = 1/6\pi\eta r_p$ Eq. 4.14 can be re-written as;

$$u_p = u + \gamma F_m \quad (4.15)$$

Substituting Eq. 4.15 in flux, J_A Eq.4.11 can be re-written as;

$$\frac{\partial C}{\partial t} = D\nabla^2 C - u\nabla C - (\gamma F_m)\nabla C \quad (4.16)$$

Where diffusion coefficient D is calculated using Nernst-Einstein relation $D = \gamma kT$

4.2.2.5.1 Boundary Conditions

An initial unmixed concentration of MNP solution is injected into the microchannel on the right boundary. Convective flux is set at the outlet boundary on the left, keeping insulation/symmetry in all the other boundaries.

4.2.2.6 Numerical Simulation

A finite element software package, COMSOLTM was used to solve the partial differential equations described above in the model. The model consisted of one geometry and three application modes including magnetostatics to obtain static magnetic field produced by the

permanent magnet, incompressible Navier-Stokes to predict velocity profile of carrier fluid, and convection diffusion to simulate spatial and temporal variation of the MNP solution inside the microfluidic channel. The meshing around the geometry was around 10 μm except for the channel inlet and outlet where more fine elements (1 μm) were used in order to resolve the domain. The model was solved in two steps using two different solvers. First the magnetic field and magnetic forces generated due to permanent magnet were solved using the magnetostatic application mode with a non-linear solver and then a time-dependent solver was used to solve incompressible Navier-Stokes application mode together with convection diffusion equation.

4.2.2.7 Capturing Efficiency ($CE_{\text{numerical}}$)

Magnetic nanoparticle concentration rate (mg/s) at the inlet and outlet of the microchannel was computed using the total normal flux (mg/m.s) multiplied by the cross-section length of the channel at the inlet and outlet. In order to obtain the incoming (M_{in}) and outgoing mass (M_{out}) of magnetic nanoparticles, a numerical integration method (trapezoidal rule) was used to approximate the integral or the area under a curve of magnetic nanoparticle concentration rate (mg/s) versus time. Capturing efficiency was later obtained using the following equation;

$$CE_{\text{numerical}} = \left(1 - \frac{M_{out}}{M_{in}}\right) \times 100 \quad (4.17)$$

4.2.3 Results & Discussion

4.2.3.1 Magnetic field measurements

Prior to more detailed parametric investigation, magnetic field strength for different permanent magnet assembly (see Table 4.1) was computed using the numerical model described for magneto-static equation in section 4.2.2. The magnetic flux density calculations were also validated using the well developed analytical expressions given by Furlani et al. [208].

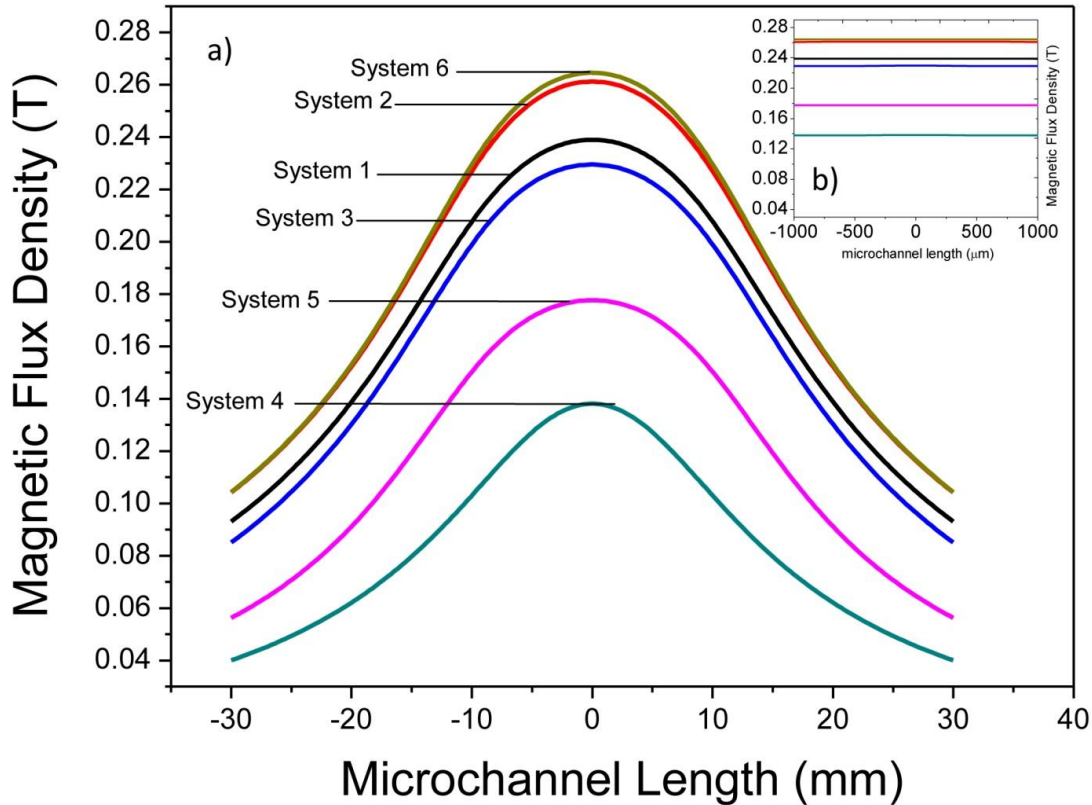


Figure 4.8 Calculated Magnetic Flux density at center of microchannel along the length of the microchannel, and (b) shows the magnetic flux density in the region of interest (ROI) for different magnetic systems.

The numerical results agree very well with the analytical solution and the range of magnetic flux density (0.12-0.2 Tesla) computed using the numerical model for different magnetic system assembly was also almost of same order of magnitude as reported in real microfluidic devices [37, 47, 139]. Computed Magnetic flux density at the center of microchannel along the x-axis for different magnetic system assemblies are given Figure 4.8. It can be seen that system 2 and system 6 produced maximum magnetic field with system 4 producing the least amount inside the microchannel. The magnetic field strength is dependent on shape, size, and grade of neodymium magnets used in the assembly. Systems 1-6 were placed 5mm away from microchannel and had a maximum energy product of 46 MGOe (N46 grade). Magnetic Systems 7-8 (not shown in Figure 4.8) produced much higher magnetic field inside the microchannel and were comprised of single

0.75x 0.75 x 0.25 inch neodymium magnet placed very close to the microchannel wall. These systems were made of higher grade neodymium magnet with a maximum energy product of 52MGOe (N52 grade). Magnetic field strength was found to be maximum at the center of microchannel in the region of interest (ROI) and gradually diminishes near the inlet and outlet.

In this work both a steady state and time-dependent operation of magnetic nanoparticle capturing process on a microfluidic platform were investigated. This simple setup employs an assembly of permanent magnets to attract nanoparticles in the microchannel continuously. The main design parameters of this multiphysics process are magnet field strength and gradient, magnetic nanoparticle size and properties; type of carrier fluid which translates to its viscosity and density, and most importantly microchannel dimensions. Based on the simple setup we have in this work, the operating parameters that were varied in this work are magnet field assembly which translates to magnetic field strength of the system, placement of permanent from microchannel and fluid flow rate. It is expected that these primary operating parameters can strongly influence the capturing process and were investigated. All experiments were conducted at room temperature and pressure with DI water and dilute magnetic nanoparticle concentrations.

4.2.3.2 Effect of Magnetic System Assembly on MNP Capturing

In this section the effect of magnetic field assembly on the capturing process is investigated. Magnetic system were assembled based on different sizes and shape of permanent neodymium magnet (see Table 4.1) and were placed near the lower wall of microchannel as seen in figure 1. The magnetic field strength of these systems were calculated based on numerical simulation and have been discussed in detail in section 4.2.2. In these experiments System 1-6 were only compared based on the capturing efficiency of MNPs as they were kept 5mm from the lower wall of the microchannel. A 50 μ L of MNPs solution with an initial concentration of 0.5 mg/mL

was injected at the inlet of the microchannel at a flow rate of 0.3 $\mu\text{L/s}$. The sample from the outlet is collected until all the solution has passed through the microchannel. It is taken in a cuvette and placed in Zetasizer to obtain unknown scattering intensity (kcps) of the sample. Previously determined calibration curve is used to convert the scattering intensity into unknown outlet concentration (mg/mL), which is used to compute the capturing efficiency of different magnetic system assemblies (System 1-6). Each experiment was performed in triplicates and average values together with standard deviation were reported. Figure 4.9 illustrate the effect of magnetic system assembly on the capturing of magnetic nanoparticles. It can be seen that system 2 and system 6 resulted in increased capturing of magnetic nanoparticles with capturing efficiency of 87% and 89.2 % respectively, whereas system 4 was not successful in capturing enough magnetic nanoparticles (CE~ 36.7 %) in the system. It can be seen that capturing process was not only dependent on the strength of magnetic field in the microchannel but also on the effective region in which the magnetic field was spread. For system 4 (see Table 4.1) the effective width of the magnet assembly is only 0.375 inch and magnetic field intensity is 0.138 T, therefore it produced maximum magnetic force only in a small region and the magnetic field decreased dramatically within $-10\text{mm} < x < 10\text{ mm}$ (see Figure 4.8) from the magnet and reached a steady state.

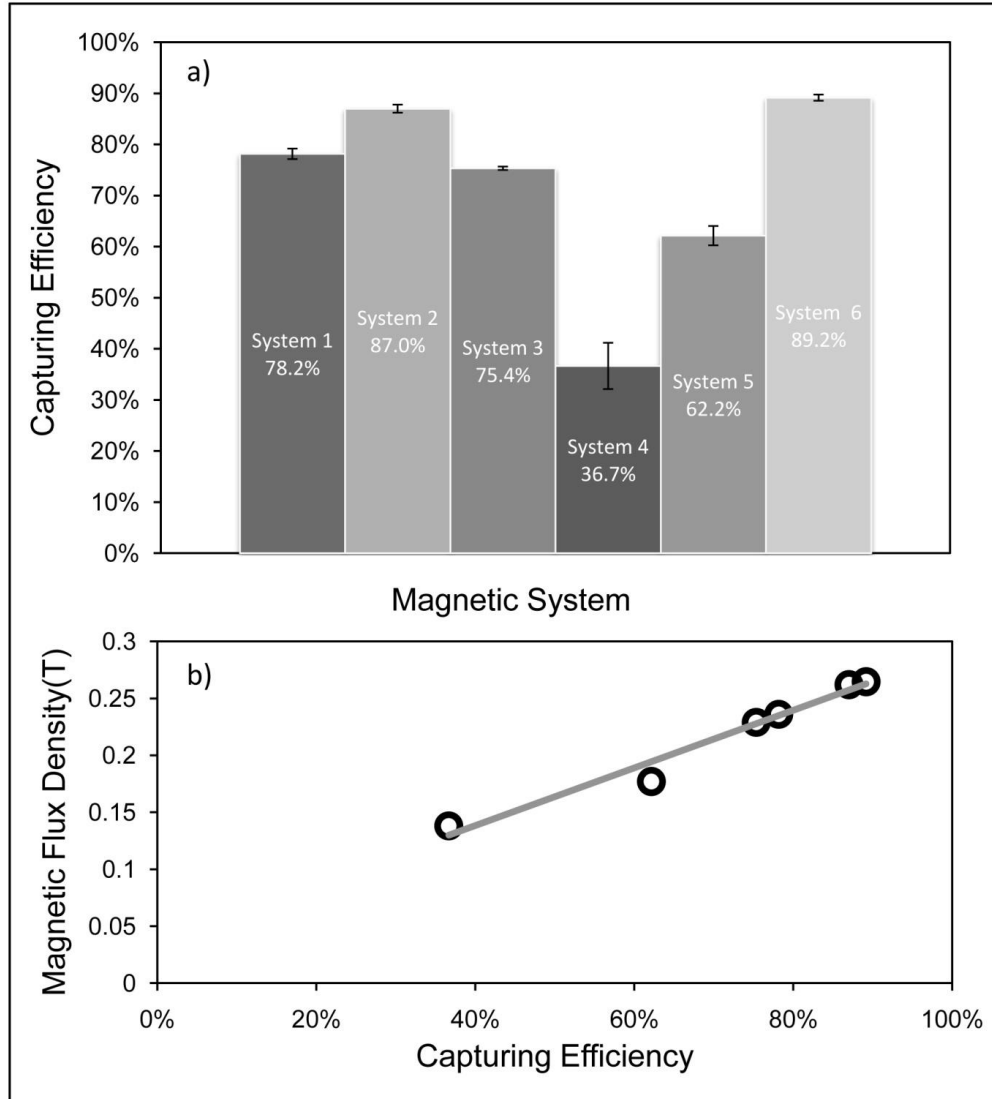


Figure 4.9 Capturing Efficiency Analysis, (a) Comparison of capturing efficiency of different magnetic systems, (b) Magnetic Flux density versus capturing efficiency plot shows that magnetic systems producing high magnetic flux density in the microchannel have higher efficiency for trapping MNPs.

This resulted in less capturing of magnetic nanoparticles in the system. Moreover, effective width across x-axis for system 3 increased to 0.5 inch, which resulted in more capturing of MNPs as compared to system 4. For system 5 the effective width (~0.375 inch) was same as system 4 but due to addition of a square magnet of 0.75 x 0.75 inch at the bottom of assembly a slightly increase in capturing of MNPs was observed. It can also be seen from Figure 4.9b that capturing efficiency was also largely dependent on the magnetic flux density produced within the

microchannel. A higher magnetic flux density over longer range will translate into maximum magnetic force that can be obtained in the microchannel and will result in more capturing of magnetic nanoparticles. Based on this analysis system 2 was selected to be used for other parametric investigations as it produced higher magnetic field strength over longer range.

4.2.3.3 Effect of Flow rates and placement of magnets on MNP Capturing

In this section the effect of inlet flow rate and placement of magnetic field assembly (system 2) on the capturing process is investigated. Magnetic system 2 was initially placed at a distance of 0 mm from lower wall of microchannel and later displaced by a distance of 5, 10, 15, and 20mm respectively. A 50 μL of MNPs solution with an initial concentration of 0.5 mg/mL was injected at the inlet of the microchannel at different flow rates and outlet sample was collected and analyzed using Zetasizer instrument. Five different flow rate conditions were used for each position of magnetic system assembly. Capturing efficiency was computed using the concentration values obtained at the outlet. It can be seen from Figure 4.10 that capturing efficiency increases with decrease in flow rates because decrease in flow rates will increase the residence time of magnetic nanoparticles in the microchannel which will allow the nanoparticles to diffuse more, and experience larger magnetic force as compared to drag force. This will result in more magnetic nanoparticles being captured in the microchannel. It can also be seen from Figure 4.10b that as we move the magnetic system away from microchannel, the effective magnetic force acting on the MNPs will decrease, which will lead to lesser capturing of magnetic nanoparticles.

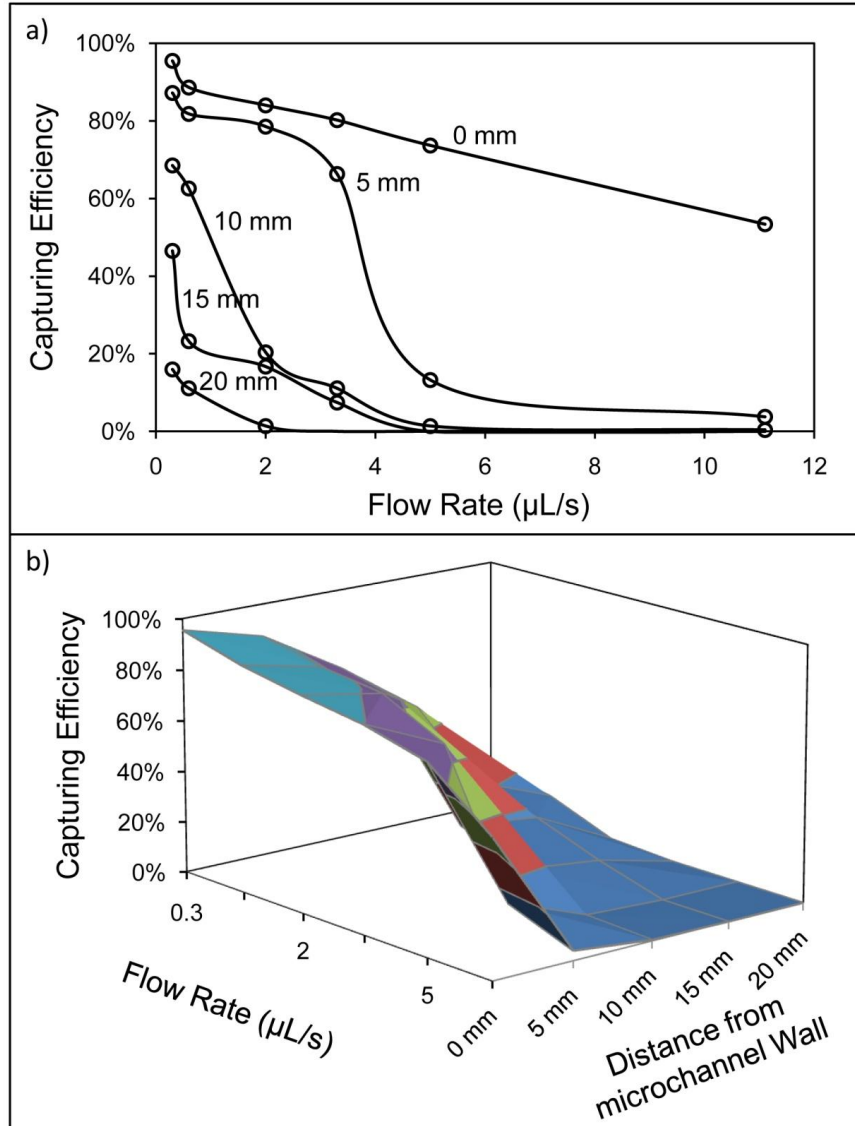


Figure 4.10 (a) Variation of capturing efficiency of MNPs with flow rate of MNPs and distance of magnet from the lower wall of microchannel, and (b) 3D plot gives the guideline for obtaining higher capturing efficiency. A lower flow rate and magnet being closer to the microchannel is desirable.

The effect of displacing the magnetic system away from the microchannel is more prominent at higher flow rates where magnetic nanoparticles follow the convection dominated regime and effective magnetic force acting on the magnetic nanoparticles is not enough to overcome drag force and cause capturing. Figure 4.10b provides a general guideline based on these experiments for effectively increasing the capturing efficiency. It can be seen that a lower flow rates and

magnetic system being more close to the microchannel is always desirable. In case that higher flow rates are needed to increase throughput, then choosing a system with higher magnet field strength in a longer range will be required.

4.2.3.4 Qualitative Capturing Analysis of MNPs

In this section qualitative analysis of the motion magnetic nanoparticles is performed with the aid of optical imaging using the digital microscope (Celestron 44340, Celestron Inc., USA). The translational stage of the microscope was used to place the microfluidic channel together with magnetic system assembly. Magnetic system 2 and 6, described earlier in the section were compared with magnetic system 7 and 8 (see Table 4.1.). The objective of camera acquired sequential images of the flowing magnetic nanoparticles at different times and transferred it to a computer for data acquisition. Image acquisition was performed using ImageJ software (NIH, USA) from the region of interest (ROI) under bright field lightning condition. A 50 ul of magnetic nanoparticle solution with a concentration of 0.5 mg/mL was injected from inlet at a flow rate of 0.3uL/s. It can be seen from Figure 4.11a that magnetic nanoaprticles get captured near the magnetic system assembly on the lower wall of the microchannels. As the time progress more and more MNPs get captured. From the pixel intensity curve (see Figure 4.11b) magnetic system 7 and 8 shows higher percentage of MNPs capturing as compared to system 2 and 6. The reason for more trapping of MNPs was due to the fact that system 7 & 8 comprised of much higher grade Neodymium magnet (N52) which produced relatively higher magnetic field intensity inside the microchannel and they were placed closer to microchannel wall. Moreover, by placing Neodymium magnet (N52) with edge close to microchannel wall (system 8) a slightly higher magnetic field strength together with more focusing of magnetic force was obtained. This eventually resulted in increased capturing of MNPs.

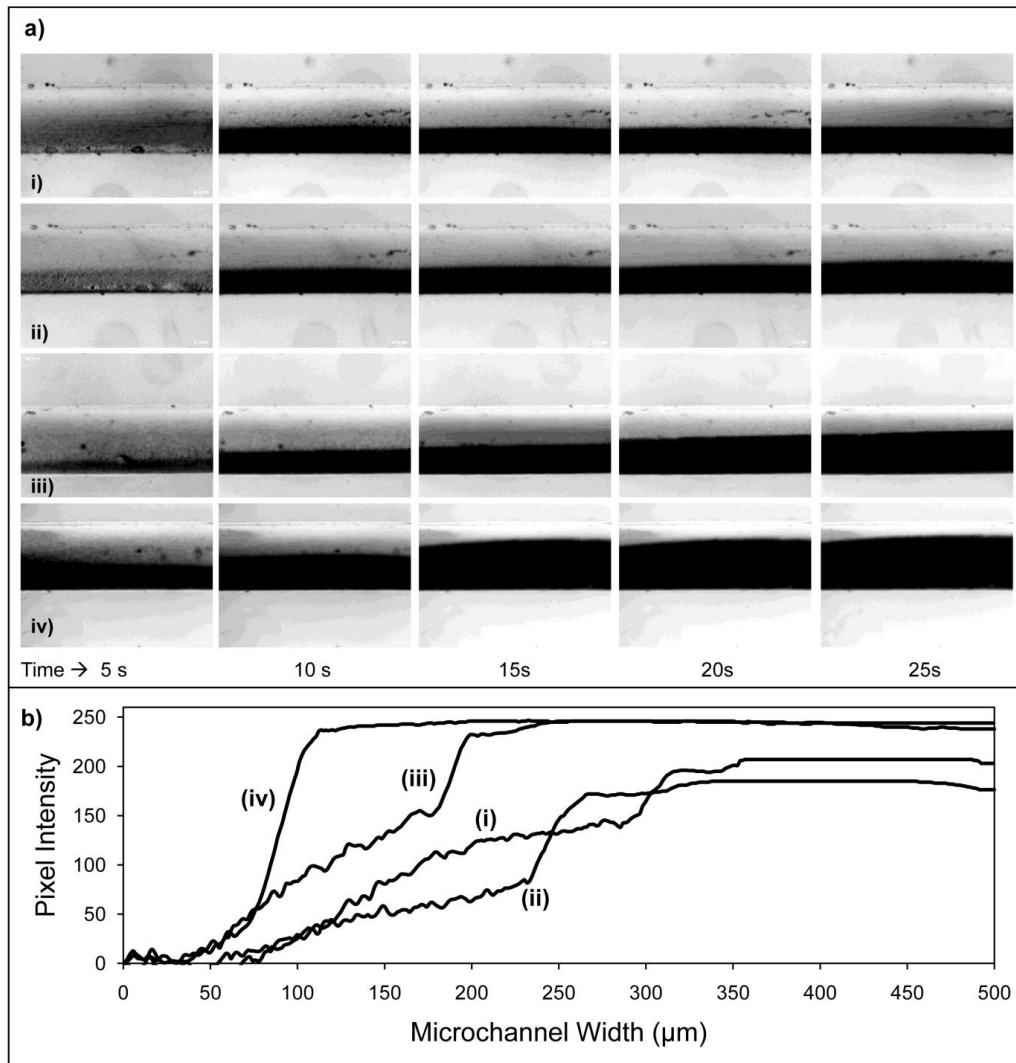


Figure 4.11 (a) Micrograph of Magnetic Nanoparticle capturing experiments in the region of interest (ROI) at different times for four different magnetic systems, i) system 2, ii) system 6, iii) system 7, and iv) system 8. Magnetic systems were placed near the lower wall of the microchannel. Systems 2 & 6 were placed at 5mm from the wall whereas Systems 7 & 8 was placed adjacent to the wall (0 mm), and (b) Pixel Intensity of the captured magnetic nanoparticles in ROI after 25s shows that system 8 has the highest amount magnetic nanoparticles captured in the microchannel.

From the analysis, it was found that system 8 produced the best results as overall it is easier to use higher grade Neodymium magnet and simple to assemble in the microfluidic setup when compared to system 2.

4.2.3.5 Numerical Simulation and Experimental Validation

To predict the dynamics of magnetic nanoparticle capturing and understand the underlying physics affecting the process, a finite-element COMSOL-based mathematical model was developed as described in section 4.2.2. Numerical simulations were performed for magnetic microfluidic system 8. 0.5 mg/ml of magnetic nanoparticles were injected at the inlet under varying flow rate conditions. The results were compared and validated with experiments performed using similar magnetic system assembly. Figure 4.12 shows the simulated magnetic nanoparticle concentration rate (mg/s) at the inlet and outlet for different flow rate conditions. It can be seen that at lower flow rate ($\sim 0.3 \mu\text{l/s}$) most of the nanoparticles gets trapped in the microchannel as a result only a small percentage exits the system. As the flow rate is increased more and more magnetic nanoparticles come out of the microchannel. Similar observation was made in the experiments. At higher flow rates drag forces acting on the magnetic nanoparticles dominates when compared to magnetic forces as a result it is expected that more nanoparticles will leave the system and will not get trapped. In order to validate the numerical prediction, experiments were performed as described in previous section using magnetic system 2 and 8 assembly for different flow rate conditions. A concentration 0.5 mg/ml of magnetic nanoparticles was injected into the microchannel and Zetasizer instrument was used to compute concentration exiting the system and finally the capturing efficiency. Magnetic system in both the scenarios was kept close to the microchannel ($\sim 0\text{mm}$). Figure 4.13 gives the qualitative comparison between experiments and numerical simulation for capturing of magnetic nanoparticle flowing at $1 \mu\text{l/s}$ inside the microchannel.

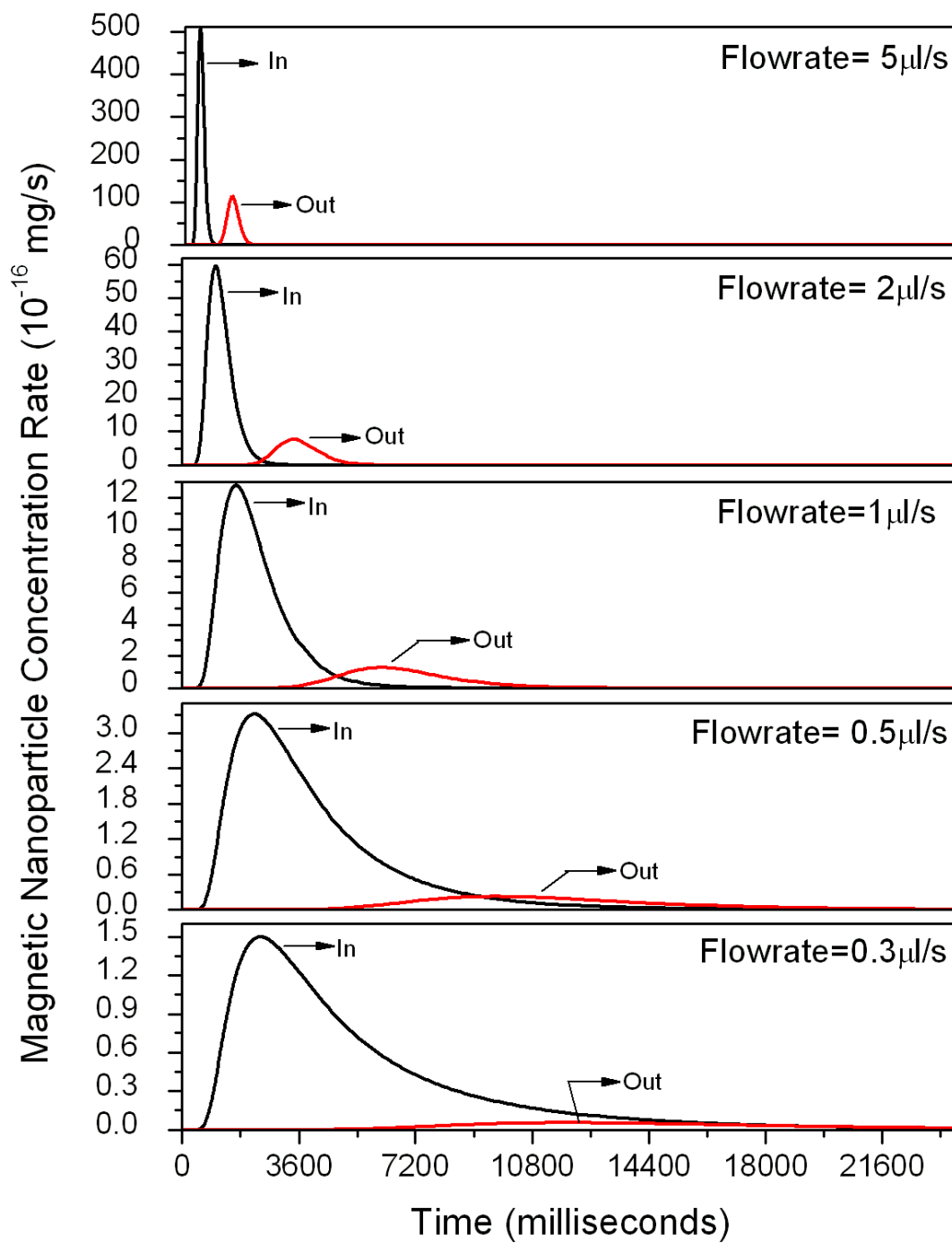


Figure 4.12 Simulated magnetic nanoparticle concentration rate (mg/s) at the inlet and outlet of the microchannel for different flow rate conditions. Magnetic system 8 with MNPs concentration of 0.5 mg/ml was used in the simulation.

Magnetic system 8 was used in both experiments and numerical simulation. The results agree very well except for the fact that model did not account for the migration of magnetic nanoparticle along the lower wall of microchannel after they have been trapped.

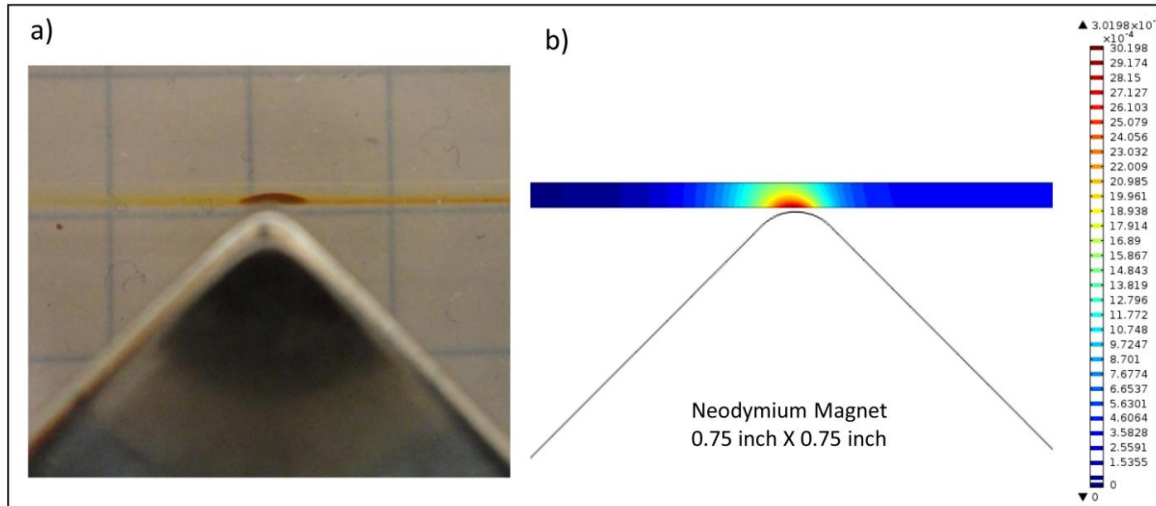


Figure 4.13 Qualitative comparison of experiments and numerical simulation for capturing magnetic nanoparticle flowing at $1 \mu\text{l/s}$ inside the microchannel using magnetic system 8. Initial concentration of 0.5 mg/ml was injected in the system from the right.

This obvious behavior could be due to particle-particle and particle-wall interaction, which makes some of magnetic nanoparticles leave the area of trapping and follow convective along the microchannel wall. Both particle-particle and particle-wall interaction was considered negligible in the simulation. Overall, the model was successful in predicting the spot or region where majority of magnetic nanoparticles were captured in the microchannel. Figure 4.14 gives the quantitative comparison of capturing efficiency of magnetic nanoparticles for both experiments and numerical simulation. It can be seen that numerical predictions were very close to experimental results. Slightly lower values were predicted by the mathematical model, this could be due to the incorrect magnetic force term in the model which did not take in account the surrounding medium that can very well influence magnetic field strength. Overall, the numerical

prediction followed the same trend as the experimental results with capturing efficiency decreasing for higher flow rate conditions.

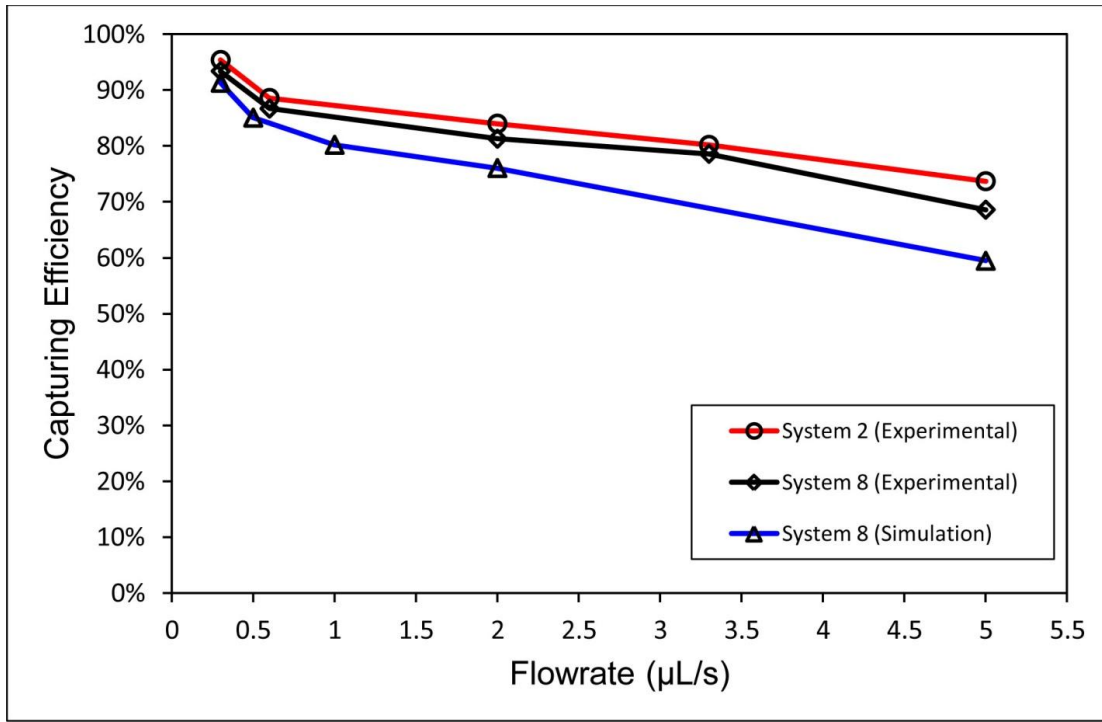


Figure 4.14 Comparison of experimental and theoretical results for capturing of magnetic nanoparticles under varying flow rate conditions. Initial concentration of MNPs injected at the inlet was 0.5mg/ml.

4.2.3.6 Numerical Prototype & Optimization

In this section the advantage of synchronizing numerical simulation with a simple low cost experimental proof-of-concept is highlighted. Numerical prototype and simulations can readily serve as “virtual experiments” and are used in this work to identify key design parameters and improve the functional performance of current magneto-fluidic capturing systems. It can be seen from previous experimental as well as theoretical results that the magnetic field strength, its orientation, effective range and magnetic field gradient are very important factors that influence the capturing of magnetic nanoparticles. Therefore, in order to enhance the performance magnetic field gradient was changed by placing a grooved iron bar on the opposite wall of the

microchannel as seen in Figure 4.15. The bar was 1mm wide and 4mm long with 8 grooves of about 0.25mm in diameter.

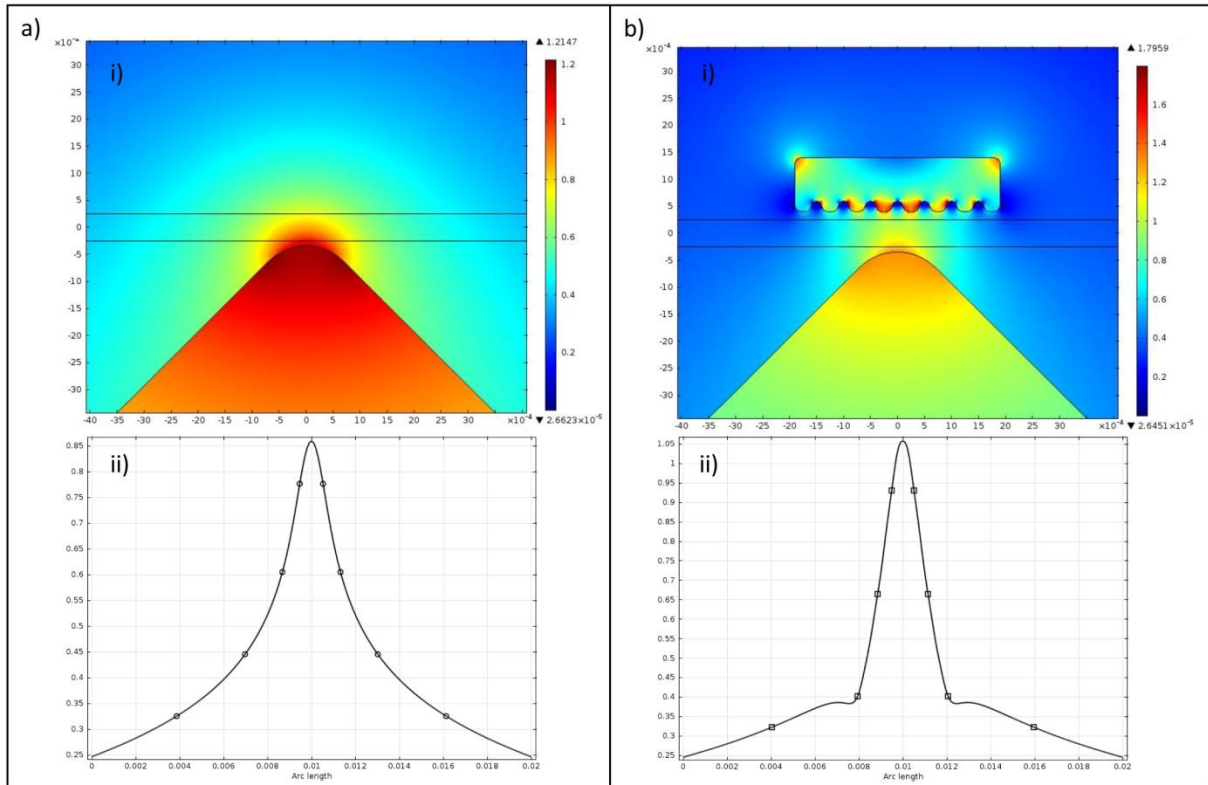


Figure 4.15 Simulated magnetic field intensity in Tesla (a) Magnetic System 8 (i) 2D surface plot of Magnetic field Intensity, (ii) Magnetic field intensity along the x-axis in the center of microchannel($y=0$), and b) System 8 with iron grooved bar (i) 2D surface plot of Magnetic field Intensity, (ii) Magnetic field intensity along the x-axis in the center of microchannel($y=0$)

In order to analyze the effect, virtual simulation were done and compared with base system comprising only of magnetic system 8 assembly. From Figure 4.15, we can see that by placing the groove structure the magnetic flux density increased from 0.85 to 1.05 Tesla (see Figure 4.15a(ii) & Figure 4.15b(ii)) at the center of microchannel. It can also be seen the magnetic field was more focused in the region of interest where magnetic nanoparticle are expected to be trapped. Figure 4.16 illustrate the effect of placing grooved iron bar on the inlet and outlet concentration rate of magnetic nanoparticles computed using the mathematical model. Initially,

0.5 mg/ml of MNPs were injected into the system at a flow rate of 1 $\mu\text{l/s}$. It can be seen that more magnetic nanoparticles gets trapped (see Figure 4.16b) when grooved iron bar is placed in the vicinity of microchannel since the outlet concentration rate was decreased when compared to system without grooved structure.

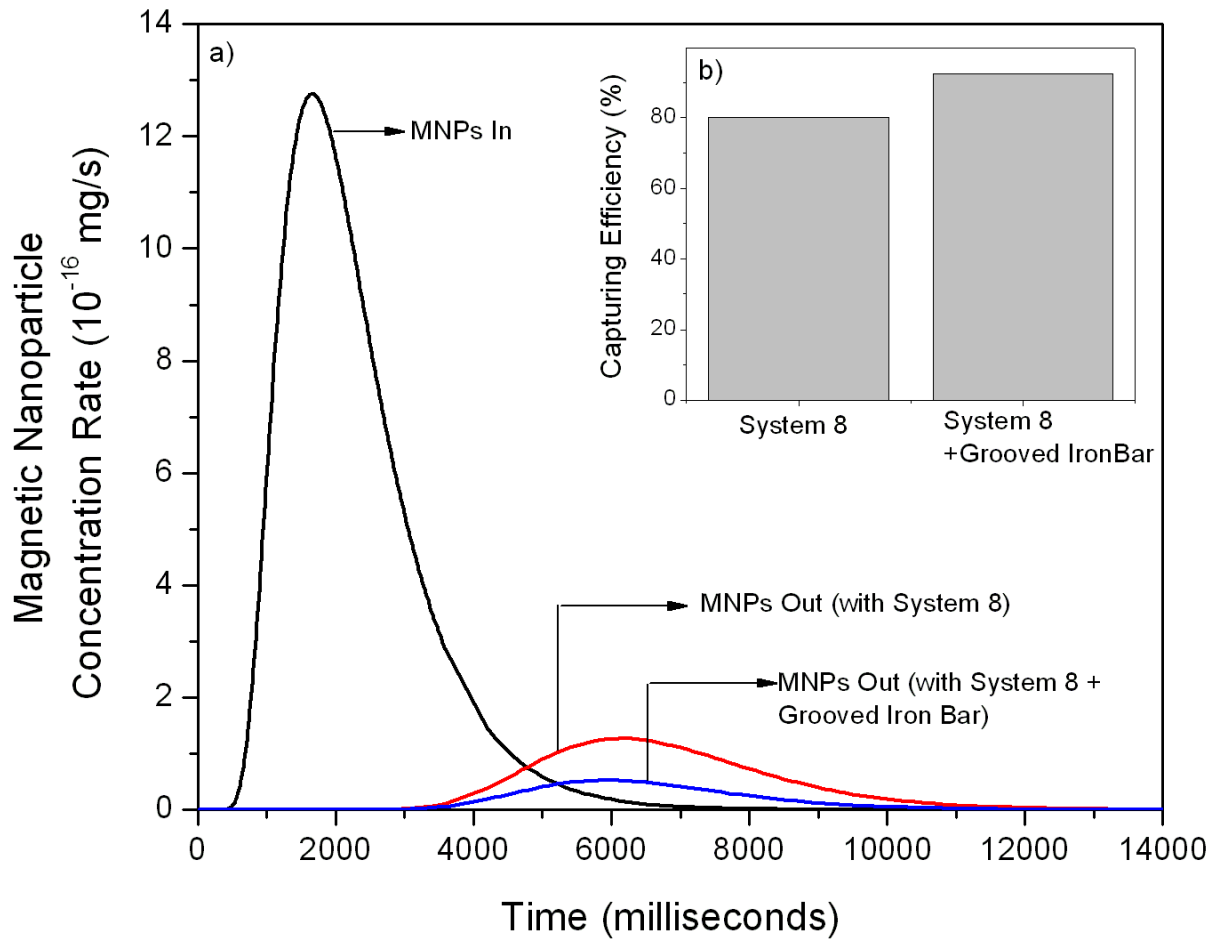


Figure 4.16 (a) Simulated magnetic nanoparticle concentration rate (mg/s) at the inlet and outlet of the microchannel for Magnetic system 8 with and without grooved-iron bar in the vicinity of microchannel. MNPs concentration of 0.5 mg/ml was used in the simulation, (b) Capturing efficiency computed based on incoming and outgoing mass of magnetic nanoparticles for both the system.

This proves that presence of grooved iron, close to the microchannel is able to induce a large magnetic field gradient which translates into an enhanced magnetic force on the magnetic nanoparticles. Capturing efficiency was computed as described in previous section and it was

found that there was 12% increase in trapping magnetic nanoparticles flowing at $1\mu\text{l/s}$ when grooved-iron bar was placed in vicinity. This strategy is very useful in enhancing the performance of magnetic microfluidic system in scenarios where higher flow rates conditions are required. Despite the successful demonstration of incorporating iron structure in the setup for magnetic nanoparticle capturing process, one should note that the current system can further be optimized in a number of ways. Other improvements which can be done to further enhance the device performance are parameters such as the geometries of the main channel as well as the flow rates for the carrier fluid, magnetic system assembly. These parameters are critical in dictating the resulting capturing efficiency and can very well be optimized using mathematical tool before implementing in the fabrication process and device development. Overall, the numerical simulation was helpful in testing one of the hypotheses without actually performing the experiments and identifying the key design parameters that will be very useful in enhancing the functional performance of magneto-fluidic capturing systems.

4.2.4 Conclusion

In this work, a simple, low cost and generic microfluidic platform is developed to study the dynamics of magnetic nanoparticle capturing process in microfluidic channel. Compared to the conventional MEMS fabrication technology, microfluidic channels were fabricated using a novel micromolding method that can be done without a clean room and at much lower cost and time. Proof-of-concept experiments were combined with finite element simulation based on drift-diffusion model to enhance the performance of the magnetic microfluidic system. Parametric investigations using both experiments and theoretical predictions were performed. It was found that flow rate and magnetic parameters influence the transport magnetic nanoparticles in the microchannel and control the capturing efficiency. Mathematical model was validated using the

experimental results and was further used to enhance the performance of the capturing process by introducing an iron-grooved bar in the virtual simulations. Overall, this work demonstrated that a simple low cost experimental proof-of-concept setup can be synchronized with advanced numerical simulation to design and improve the functional performance of magneto-fluidic bioseparation systems.

4.3 Investigation of magnetically actuated separation using tangential microfluidic channels and magnetic nanoparticles

4.3.1 State of the Art

Biomolecular separation using microfluidics technology involves capture, isolation, and release of target biomolecules from impure samples. It is used for purification, pre-concentration, and detection of biomolecules[45, 47], proteins[48, 172], DNA[31, 50], and cells[52, 126, 145, 243, 244] in clinical diagnostics, drug discovery, and microbiology. There are a number of techniques currently available on microfluidic platforms for particle separation, such as Electrophoresis [245, 246] and dielectrophoresis [247], size-based separation [132, 238, 248] , pinched flow fractionation [249, 250], acoustic separation[236], inertial separation [235, 251], and magnetic bioseparation[52, 131, 228, 252-255]. Among these techniques, magnetically actuated methods seem to be very promising because of the simplicity of design and ease of operation. This method utilizes surface-functionalized magnetic particles to trap target biomolecules through specific chemical binding followed by separation using magnetic manipulation. Magnetic bioseparation technique is dependent on the interaction of chemical bonds and therefore allows highly specific and selective biomolecular separation when compared to other techniques that rely on geometrical or physical properties of the species. Most of the magnetic bioseparation systems developed on microfluidic platform are based on magnetic micro-sized particles [29, 41, 47, 52, 147], however less intensively studied in microfluidic bioseparation[61, 62, 256] scheme are the emerging nanoscale magnetic particles. Compared with microparticles, nanoscale materials possess better properties that can be advantageously deployed in microfluidic devices. Higher surface to volume ratio [37] makes magnetic nanoparticles nearly ideal for the manipulation and detection of attached biomolecules [61, 207]. For example, it has been shown

that functionalized magnetic nanoparticles (MNPs) have enhanced detection of small molecules using Surface Plasmon Resonance (SPR) Spectroscopy[240]. MNPs have extremely small size as such they causes minimal disturbance to attached biomolecules [37] as well as provides enhanced interaction for chemical binding and tagging. Most importantly they are super-paramagnetic in nature [37] , i.e., their magnetization without a magnetic field is zero. The super-paramagnetic nature ensures that they stay suspended in carrier liquid when the magnetic field is removed. Unlike micrometer-sized particles, these particles do not irreversibly agglomerate or precipitate and can be repeatedly used subjected to magnetic fields of varying strength without causing any adverse effects. This also makes it easy for the removal or capture of tagged biomolecules of interest once the magnetic field is removed. Overall, the inclusion of magnetic nanoparticles in microfluidic devices for biomolecule separation, manipulation, and detection will not only enhance the device functionality and separation performance but also broaden the utility of these devices in real world applications. Separation of biomolecules using magnetic field actuation can be done either in conventional batch process or in continuous flow mode [133, 138, 208, 213]. In the batch process [243, 255, 257] magnetic particles tagged with target biomolecules are trapped or retained using magnetic field and subsequently released, after the removal of non-targets. A number of devices have been developed with various magnet designs [41, 42, 45] to accomplish magnetic bioseparation. Useful batch mode operation suffers from low separation efficiency, longer incubation and handling time, and, resulted in significant contamination due to nonspecific binding of impurities with magnetic beads[258]. More importantly, their incorporation in point-of-care microfluidic testing devices will require more complicated multi-step fluidic handling. On the other hand, continuous flow magnetic bioseparation processes overcome the above limitations because they employ magnetic

fractionation, i.e., continuous accumulative deflection of magnetic particles tagged to biomolecules. This method does not require multistep fluidic handling; Moreover higher magnetic field is also not a requisite because the process only depends on deflection rather than on complete trapping of magnetic particles. Continuous flow magnetic bioseparation can be distinguished into two types, one in which electromagnets or magnetic microstrips typically of alloy or ferromagnetic materials, are integrated on the device substrate to generate a magnetic field gradient that deflects magnetic beads [131, 253, 259-261] Substantial cost and effort is required to design and fabricate these systems. Alternatively, in the second type, a simple external permanent magnet assembly is used that provides greater flexibility and simplicity in device design to achieve higher magnetic field assisted bioseparation[262]. Development of continuous flow magnetic bioseparation scheme together with a simple low cost approach for selective injection or removal of biomolecules bound to magnetic nanoparticles is highly desirable to complement existing microfluidic technology available for bioseparation.

To circumvent this, a simple, low cost and generic microfluidic platform is assembled to demonstrate continuous flow magnetic bioseparation using tangential microfluidic channels and magnetic nanoparticles (MNPs). A major innovation of this setup lies in the fabrication of tangential microchannel which act as magnetic microfluidic switch to manipulate flows containing magnetic nanoparticles and can accomplish efficient bimolecular separation. Standard molding process combined with a novel rapid prototyping method is used in this work to develop low cost polydimethylsiloxane (PDMS) microchannel. The fabrication method used in this work circumvents the requirement for a clean room. It also eliminates the combination of two pieces of element, such as in standard fabrication method where negative or positive stamp on PDMS are combined with glass or silicon using plasma as a result eliminates the problem of leakage. In

this work continuous switching/separation of magnetic nanoparticle in a sub-microliter fluid volume surrounded by neodymium permanent magnet is studied. On the basis of MNPs concentration measurement using optical technique, separation efficiency is analyzed for scenarios with and without magnetic field. Separation performance of the setup is also studied for a mixture containing non-magnetic polystyrene (PS) particles and magnetic nanoparticles (MNPs). Effect of flow rate on continuous flow separation of MNPs in tangential microchannel is also investigated. This work demonstrates that a simple low cost magnetic switching scheme using tangential microchannel together with MNPs can be potentially of great utility for separation and detection of biomolecules and cells in lab-on-a-chip systems and can further improve the functional performance of magneto-fluidic bioseparation systems.

4.3.2 Materials & Methods

4.3.2.1 Microchannel Fabrication

Low cost rapid micromolding technique was used to develop 75mm long and 800 μ m diameter tangential microfluidic channels. The steps used in fabricating the microchannels are shown in Figure 4.17. The first step in preparing these channels involved development of mold which was prepared using aluminium wires each of 800 μ m diameters. The wires were placed in the center and approximately at half the depth of the empty Petri dish such that they overlap each other at an angle of 30⁰. In order to that, small holes were drilled using the stainless steel syringe which was later closed using adhesive tapes. It was also made sure that they touch each other approximately at the center. Polydimethylsiloxane (PDMS) (Sylgard 184, Dow Corning, USA) with a base and curing agent mixed in a ratio of 10:1 was poured onto the mold and was degassed to remove any bubbles using desiccators. The uncured PDMS was baked in an oven (65 °C) for 1 h. The final step was to peel off the cured-PDMS containing the aluminum wires from

the Petri dish. The sides of the cured PDMS were cut using a razor blade, leaving a significant amount of the wire exposed outside. With the help of pliers the wires were carefully removed. To make this process easier, the microchannel were washed with acetone which swelled the PDMS and expanded the channels prior to pulling out the wires. An internal access area was created at the center of overlap where the wires touched each other making the only connection between two microchannels. The microchannels were then connected with the tygon tubing using the stainless tip obtained from microsyringe. The tip was inserted into the microchannels to make leakage free connection.

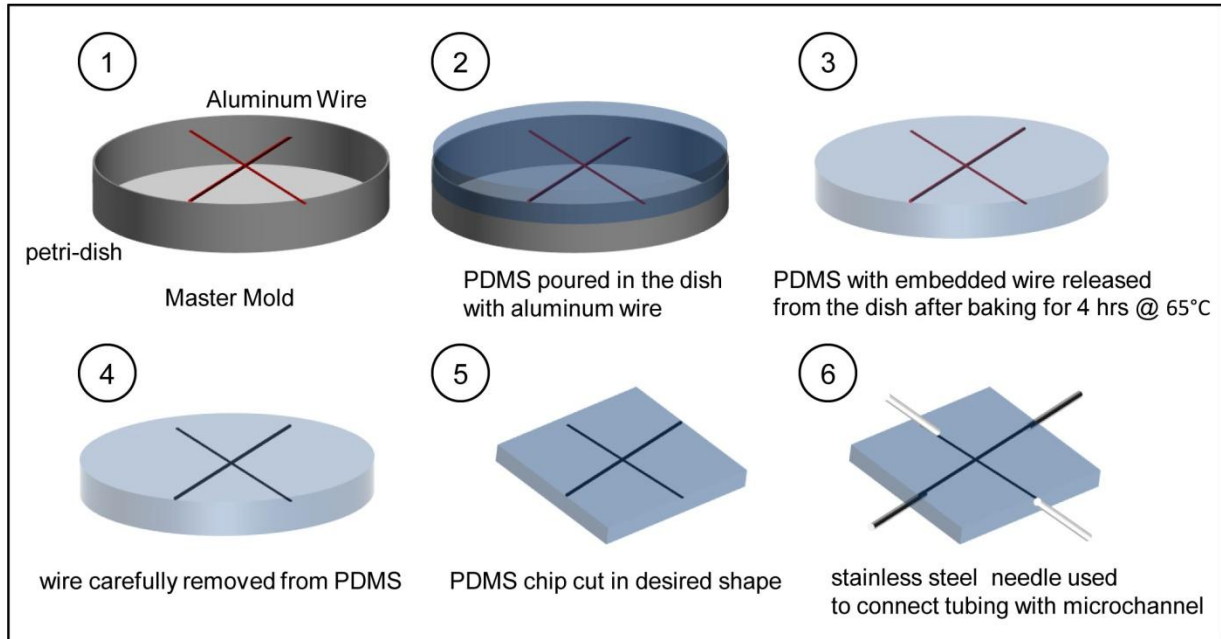


Figure 4.17 Fabrication step used in developing leak-proof microfluidic channels.

4.3.2.2 Microfluidic System Setup

A simple experimental set-up to carry out magneto-hydrodynamic experiments is shown in Figure 4.18. As shown in the figure, the microfluidic channels are connected with inlet and outlet via flexible tygon tubing. Lower microchannel inlet (LT1) is used to transport magnetic nanoparticle solution whereas DI-water flows from the upper channel inlet (UT1). In order to

provide leak free connections a microsyringe tips made of stainless steel are embedded into the microchannel inlet/outlet for secure connections between the flexible tubes and the microfluidic chip.

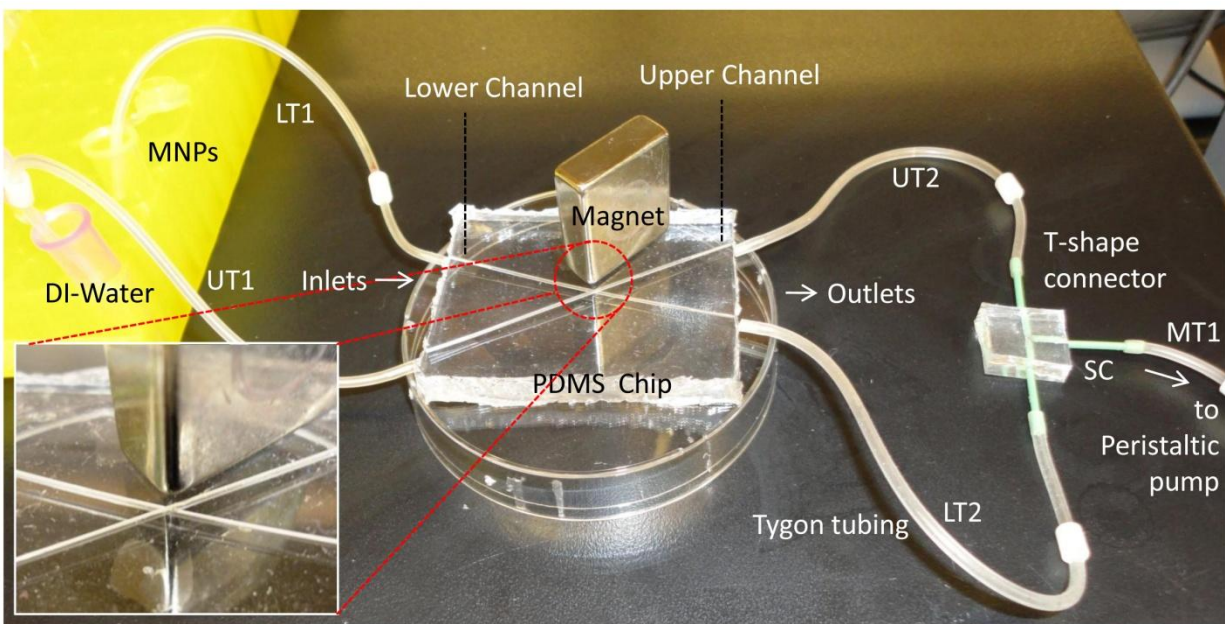


Figure 4.18 Experimental Setup of magnetic field based bio-separation using tangential microchannels and magnetic nanoparticles. Inset shows the close-up of tangential microchannel with neodymium magnet where magnetic field forces are focused in order to switch the path of magnetic nanoparticles.

A differential pressure drop is maintained inside the channels by connecting the outlet of the microchannels (LT2 & UT2) to peristaltic micropump (P625 Peristaltic Pump, Instech, USA) using an in house developed PDMS T-shaped connector. Flow rate were varied using the precise-bi directional speed controller on the pump. This simple method allows for a good control of the flow in the channels in suction mode. An upward magnetic pull force was obtained using permanent neodymium magnets (KJ Magnetics, USA) as shown in Figure 4.18(inset) near the access hole where the upper microchannel was connected to the lower microchannel. Optical images of the bio-separation experiments at different time points were obtained using the digital camera (Sony Cyber Shot DSC-W530, Sony Electronics Inc., USA). Magnetic nanoparticles

(MNPs) of 200nm diameter (fluidMAG-ARA Chemicell GMBH, Germany) with a concentration of 1mg/ml were transported through lower inlet. The magnetic nanoparticles consisted of an inner core made up of magnetite (Fe_3O_4) crystals of approximately 12 nm diameter, was embedded in a biocompatible polysaccharide matrix for better stability that also prevented biodegradation. The overall diameter of the nanoparticles was approximately 200 nm, whereas the volume fraction of magnetite within a composite particle is 80%. For different flow rates, effluent was collected at the outlets once all the solution has passed through the microchannels. The volume collected at the outlet was regularly verified to confirm the equal flow rates in both the microchannels. The concentration of MNPs solution in the effluent was estimated from in-house determined calibration curve. The calibration curves were generated from original stock of MNPs solution diluted to different concentrations. A dynamic light scattering instrument Zetasizer Nano S (Malvern Zetasizer Nano S, UK) was used. The Zetasizer Nano S measures the intensity of scattered light of various concentrations of sample at one angle; this is compared with the scattering produced from a standard (i.e. Toluene). In general, Zetasizer is used to measure the size of molecules but also the count rate can be used as a method of determining the relative concentration of a sample of stable size—as the count rate goes down, so does the concentration. While the Zetasizer software does not automatically spit out an estimated sample concentration from the count rate, it is actually a fairly stable value for the same sample over time, and therefore is used in this work as an estimate of concentration. Power law calibration curve of scattering intensity (kilocounts per second, kcps) versus concentration of magnetic nanoparticles (mg/ml) were obtained for 200nm particles ($R^2=0.9908$) (see Figure 4.19). In order to obtain the concentration of magnetic nanoparticles coming out of the system under various condition of flow rate, the outlet samples from the effluent was taken in cuvette and

placed in Zetasizer to obtain unknown scattering intensity (kcps) of the sample. Calibration curve was used to convert the scattering intensity into concentration (mg/ml). Since the inlet concentration of MNPs was known, percentage of magnetic nanoparticles separated was calculated.

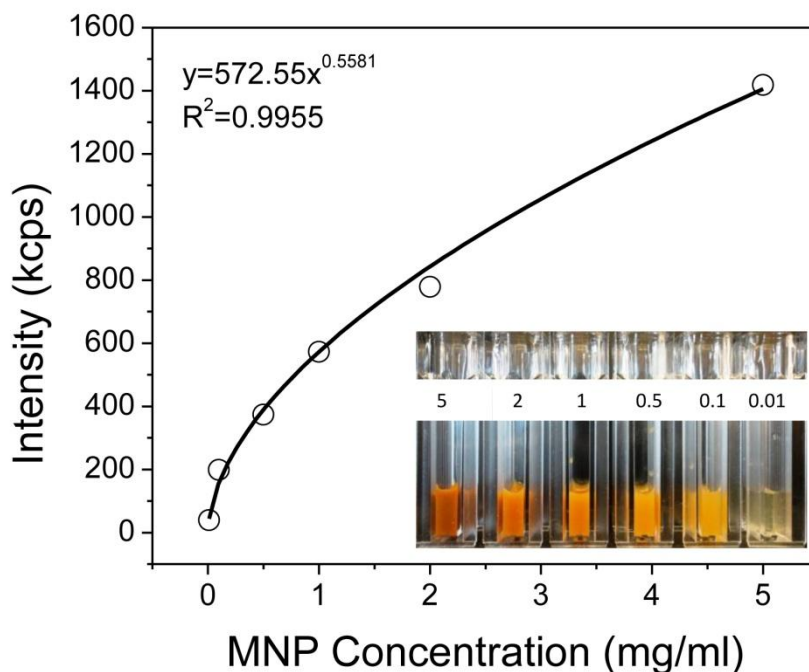


Figure 4.19 Calibration Curve obtained for MNPs using scattering intensity obtained from Zetasizer Nano S. Inset shows different concentrations of MNPs used in generating calibration curve.

4.3.3 Results & Discussion

4.3.3.1 Qualitative and Quantitative Analysis of MNPs Separation

Magnetic manipulation and switching of nanoparticles between two flow streams is a complementary way of separating biomolecules or cells in microfluidic devices when these biomolecules are tagged with nanoparticles. It is based on the attraction of the nanoparticles tagged biomolecules to regions with higher magnetic field intensity. In this section qualitative analysis of the switching or separation of magnetic nanoparticles is performed with the aid of imaging using a digital camera. The setup of the experiment is already described in previous

section. In order to examine magnetic nanoparticle movement within magnetic fields tangential PDMS microchannel were fabricated using a simple and inexpensive benchtop fabrication method as described earlier.

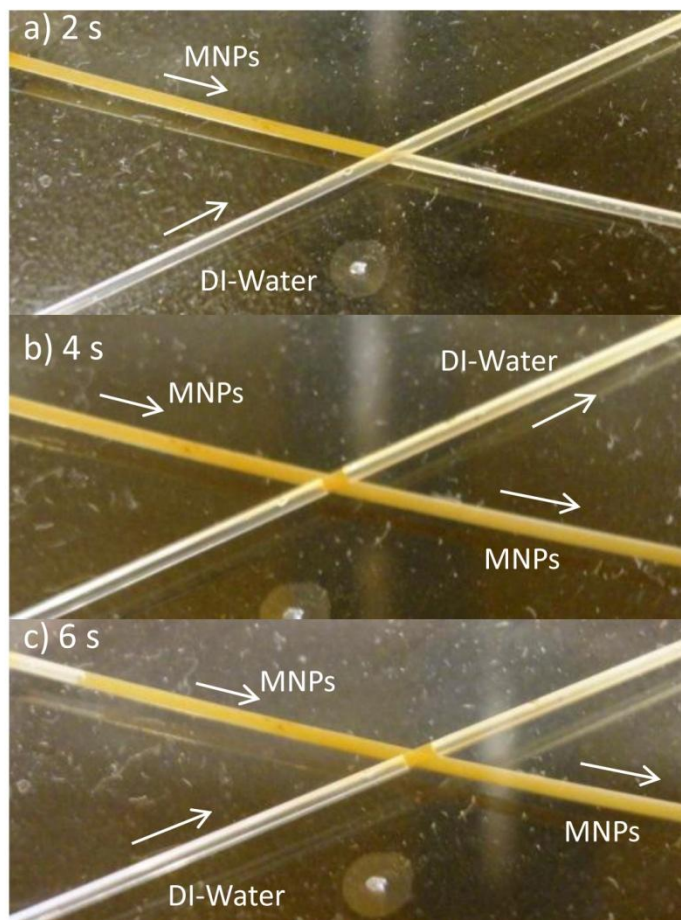


Figure 4.20 Flow of MNPs in the tangential microchannel in the absence of magnetic field. 100 μ l of MNP solution having a concentration of 1mg/ml was injected in the lower microchannel. It can be seen that no switch takes place in absence of magnetic force and MNPs enter and exit from lower channel.

It has been shown by Ismagilov et al. [68, 263] that the flow fields in tangential microchannels are independent of the contact area but strongly depends on the channel aspect ratio. A too low aspect ratio results in divergence of fluid from one channel into another channel, whereas at higher aspect ratio fluid exchange is minimal and fluid largely continues through the intersection within the same fluid stream. To minimize exchange of fluid between microchannels, we tested

many microchannels and found that microchannel with a diameter of $8\mu\text{m}$ produced best results. The Reynolds number used in the experiments remained less than 10 over the range of flow rates used ($0.3\text{-}11\ \mu\text{L/s}$), and thus, the flow within the microchannels was always laminar. To investigate the transport of magnetic nanoparticle solution in microchannels, we first examined the movement of the nanoparticles between the two tangential streams in the absence of any applied magnetic force. The flow rates of the two channels were same ($\sim 5\ \mu\text{L/s}$). A $100\ \mu\text{l}$ of MNP solution having a concentration of 1mg/ml were injected in the lower microchannel whereas DI-water flow was maintained in the upper microchannel. The transport of MNPs was recorded after every 2s and it can be seen from Figure 4.20 that after 6s almost all the solution continues through the intersection within the same flow stream with very small amount of solution transferring to upper stream due to diffusion across the interface.

In the next experiments, the movement of magnetic nanoparticles was investigated in the presence of magnetic field force. A Neodymium magnet (N52) was aligned on top of the intersection of the two microchannels such that the edge of the magnet is very close to intersection in order to provide maximum magnetic field force. The assembly of magnet is shown in Figure 1 and described in Table 4.1 in more detail. It was found that the distance between the intersection of the two microchannels and the edge of the neodymium magnet was approximately 2mm. The magnetic field intensity was computed using our in-house developed COMSOLTM numerical code [252, 264] which were also validated using the well developed analytical expressions given by Furlani et al. [208]. The magnetic flux density at this distance was computed to be in the range of 0.6-0.8 T. Mass transfer of $100\ \mu\text{l}$ of MNP solution having a concentration of 1mg/ml entering the lower microchannel was recorded after every 2s.

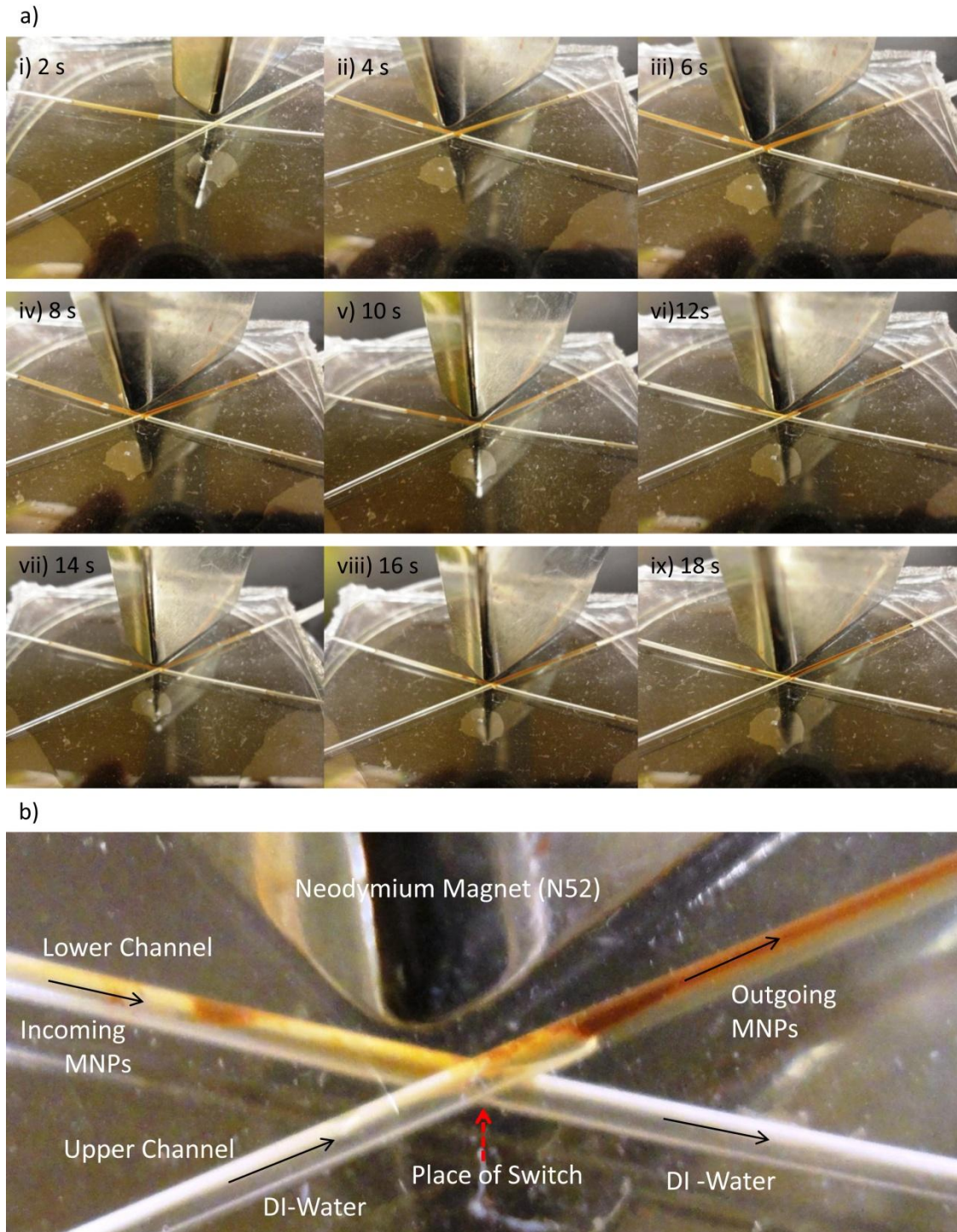


Figure 4.21 MNPs switching between microfluidic channels using Neodymium magnet. (a) Snapshot of tangential microchannel at different times. Magnetic Nanoparticles were injected in the lower microchannel, and (b) Closeup of tangential microchannel after 18s shows that due to magnetic field force generated by neodymium magnet magnetic nanoparticles switches its path and comes out from upper microchannel.

It can be seen from Figure 4.21a, that after 6s the magnetic nanoparticles preferentially move upward due to the magnetic force acting on them near the intersection and flows with the upward stream. A significant amount of MNPs switching was achieved near the intersection that can be seen in Figure 4.21b. Very small quantity of magnetic nanoparticles still emerges from lower stream, which could be due to moderate turbulent mixing arising from imperfect channel geometry. In order to further investigate the performance of separation or switching of magnetic nanoparticles, Zetasizer experiments were performed to evaluate the concentration of MNPs exiting both outlets. The sample from the outlets is collected until all the solution has passed through the microchannel. It is taken in a cuvette and placed in Zetasizer to obtain unknown scattering intensity (kcps) of the sample. Previously determined calibration curve is used to convert the scattering intensity into unknown outlet concentration (mg/mL). Each experiment both in the presence and absence of permanent magnet was performed in triplicates and average values together with standard deviation were reported. 100 μ l of magnetic nanoparticle solution having a concentration of 1mg/ml was injected in lower microchannel with a flow rate of 5 μ L/s. It can be seen from Figure 4.21b that when magnetic field is not deployed magnetic nanoparticles preferentially follows the same flow stream with concentration of MNPs exiting the lower microchannel was approximately 0.88 mg/mL. The concentration of MNPs found in upper microchannel was negligible (\sim 0.064 mg/mL approximately). This proves that no switching or separation takes place in the absence of magnetic field. It was also found that around 5.5% MNPs were not found either in the upper or lower microchannel. This could be due to the fact that some of the MNPs got trapped within the microchannel and never exited the system. Some of this error could also arise from instrumental error due to the correlation made between scattering intensity and concentration. However, when magnetic field was used as seen

from data given in Figure 4.22, approximately 0.90 mg/mL of the magnetic nanoparticles were switched from lower to upper microchannel as calculated from calibration curve for the scattering intensity data obtained from upper outlet. This was due to the fact that these magnetic nanoparticles experience magnetic pull force near the area of intersection and were transferred into upward flow stream. A very small amount (~ 0.067 mg/mL) was found in the lower microchannel with approximately 3% not found either in upper or lower microchannel. It was seen that out of 3% some of these magnetic nanoparticles got trapped on the inner walls of microchannel due to strong magnetic force. From the above analysis it can be demonstrated that 90% separation of magnetic nanoparticles was achieved using tangential microfluidic channels.

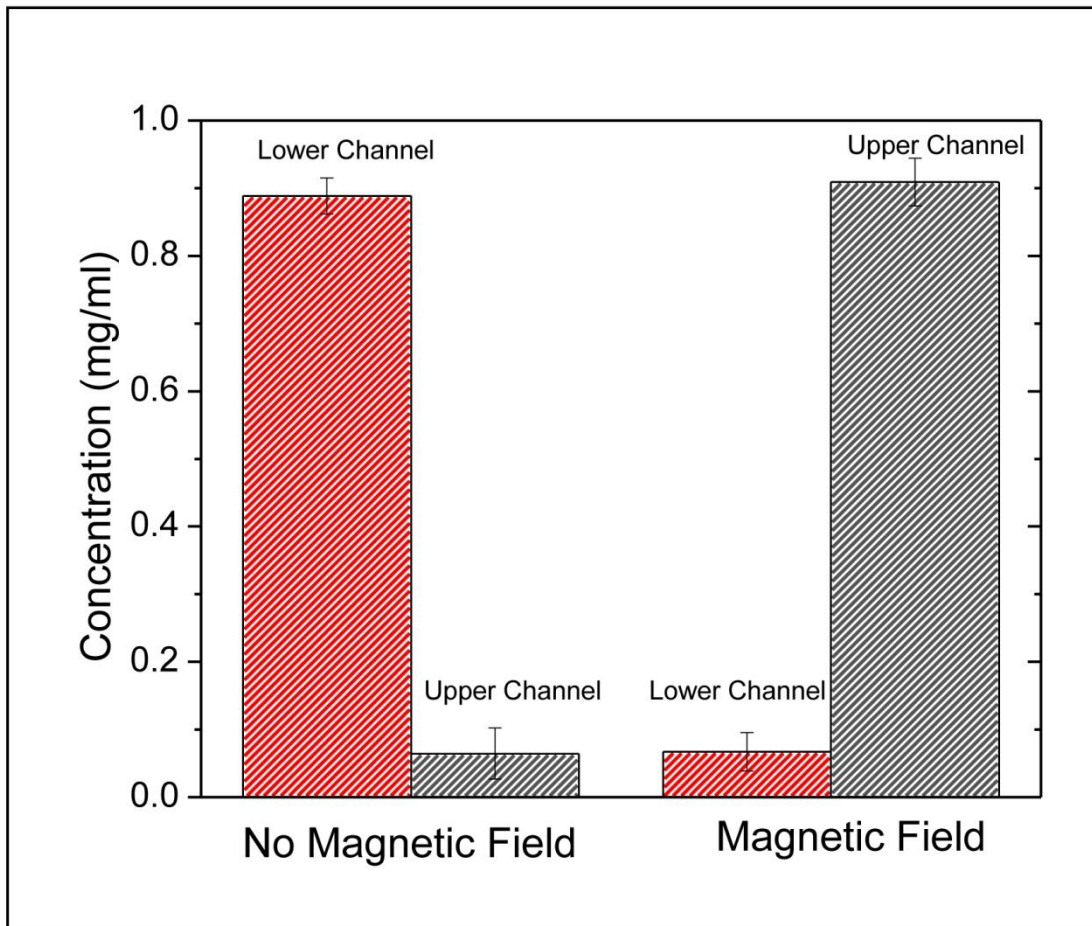


Figure 4.22 Concentration of MNPs eluted from upper and lower microchannel when 100 μ L of 1mg/ml MNPs were injected through lower microchannel at flow rate of 5 μ L/s in the absence and presence of magnetic field (Neodymium magnet, N52).

4.3.3.2 Effect of Flow rate on MNPs Separation

In this section the effect of flow rate on the magnetic nanoparticle separation in tangential microchannel is investigated. Variation of solvent flow rates impacts the residence time of magnetic nanoparticles within the microchannels as well as the drag and magnetic forces acting on these particles. A longer residence time means smaller flow rates that translate to lower drag forces therefore if the particles are exposed to higher magnetic force there will be strong tendency that these particles will eventually be pulled across the interface and into the other microchannel. To test the role of flow velocity on magnetic switching or separation, a series of

experiments were performed using a constant magnetic field and varied flow rates. MNPs with an initial concentration of 1mg/ml and volume of 100 μ l were injected from lower microchannel at varying flow rates. The concentration of magnetic nanoparticles that exited the intersection in the upper and lower microchannels was detected using Zetasizer instrument together with the procedure described in previous section. Each experiments both in the presence and absence of permanent magnet was performed in triplicates and average values together with standard deviation were reported. Since the inlet concentration of MNPs was known, percentages of magnetic nanoparticles separated between two tangential microchannels were calculated. It can be seen from Figure 4.23, that switching of magnetic nanoparticles takes place when magnetic field is used. A higher percentage of magnetic nanoparticles were pulled from lower microchannel to upper microchannel at lower flow velocity ($<5 \mu\text{L/s}$). However, when the flow velocity was increased beyond $5 \mu\text{L/s}$, a linear decrease in magnetic nanoparticle switching was observed. This is due to the fact that at lower flow velocity, the drag force acting on the magnetic nanoparticles was small as compared to magnetic force as such more number of MNPs was pulled in the upper flow stream from lower microchannel.

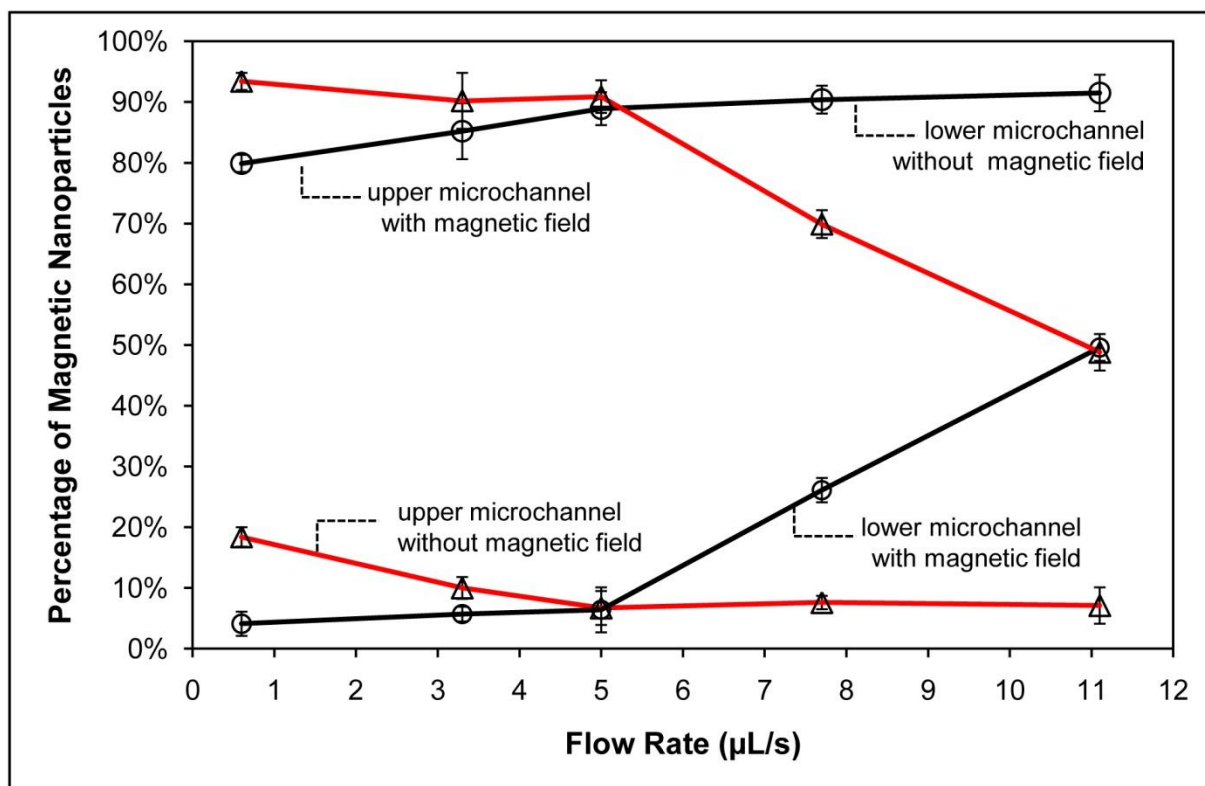


Figure 4.23 Variation of percentage of MNPs eluting from lower (O) and upper (Δ) microchannel at different flow rates in the presence and absence of magnetic field. MNPs initial concentration was 1mg/ml and 100 μ l of the sample was injected from lower microchannel. Error bar represent the standard deviation obtained after three injections.

This was not the case when flow velocity was increased due to larger drag forces acting on the magnetic nanoparticles. Another interesting observation was made in the absence of magnetic field when the flow rates were smaller than 5 μ L/s. It was found that a very low flow rates (\sim 0.6 μ L/s) some of the magnetic nanoparticles (\sim 18%) were pulled in the upper channel. This could be due to extremely large residence time which allowed magnetic particles to diffuse upward. This trend was minimized as the flow rate was increased. From these experiments it was illustrated that application of the magnetic field causes the magnetic nanoparticles to move from lower microchannel to upper microchannel. However, the percentage of magnetic nanoparticles that can be magnetically as well as non-magnetically transported into the upper microchannel is

dramatically influenced by the flow rate of both fluid streams. As the flow rate decreases from 11 μ L/s to 0.6 μ L/s under magnetic field, the percentage of magnetic nanoparticles eluting from the upper microchannel increases from 48.8% to 93.4% with more drastic change found in between flow rates of 5 μ L/s to 11 μ L/s. The improved separation achieved at lower flow rates was not simply a result of the increased residence time but is a function of both drag and magnetic force acting on these magnetic nanoparticles. By carefully calibrating the fluid flow an optimum value of flow rate can be achieved to provide maximum switching of magnetic nanoparticles together with higher throughput essential for bioseparation application.

4.3.3.3 Magnetic separation of a mixture of magnetic & non-magnetic particles

Magnetically actuated switching of biomolecules tagged with magnetic nanoparticles from one fluid stream into another, while leaving behind nonmagnetic particles, is an excellent strategy to achieve microfluidic-based separation of biomolecules continuously. This strategy was demonstrated and tested in this section. A mixture of 1mg/ml of Polystyrene (60nm) and 1mg/ml of MNPs (200nm) with a 1:1 volume ratio was injected from lower microchannel in the presence of magnetic field. The total volume of the mixture was 100 μ l and the injection rate of 5 μ l/s was maintained in both upper and lower microchannels. Samples from the outlets were collected and analyzed using Zetasizer. Both the size as well concentration measurement was performed using the instrument. Figure 4.24(a&b) gives the histogram of the size distribution of the particles eluting from upper and lower channel. It can be seen from results that the average size of particles eluting from upper channel and lower channel were around 273.1nm and 68.75nm respectively. This illustrate that most of the magnetic nanoparticles where pulled in upper microchannel due to magnetic force leaving behind non-magnetic polystyrene particles in the lower microchannel. A slight error in size estimation could be due to presence of magnetic

nanoparticles in lower and polystyrene upper microchannel. Based on the particle size histograms, it is evident that application of the magnetic field preferentially removed the magnetic nanoparticles from the lower microchannel.

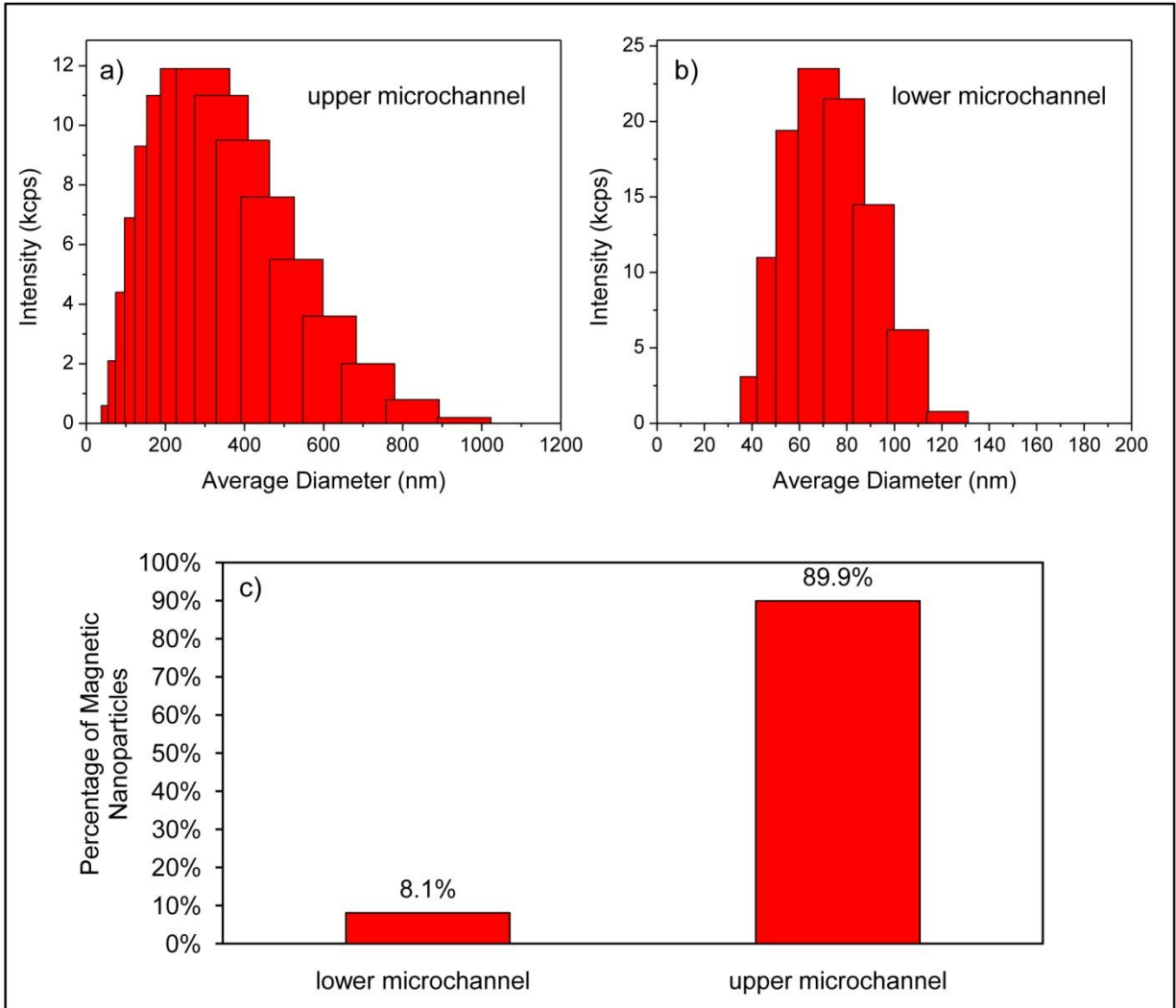


Figure 4.24 Magnetic field based separation of a mixture of Polystyrene (60nm) and MNPs (200nm) injected from lower microchannel at a flow rate of 5 μ l/s, (a) average diameter of sample eluted from upper microchannel, (b) average diameter of sample eluted from lower microchannel, and (c) Percentage of MNPs eluted from upper and lower microchannel.

In order to investigate separation or switching efficiency, concentration of magnetic nanoparticles was computed using the method described in earlier sections. It can be seen from Figure 4.24c that 89.9% of magnetic nanoparticles were pulled in upper microchannel from a

mixture of magnetic nanoparticles and polystyrene flowing in lower microchannel. From the above analysis it is evident that magnetic field assisted preferential switching of magnetic nanoparticles can be efficiently utilized in separating biomolecules in microfluidic devices.

4.3.4 Conclusion

Magnetic fields can be effectively used to manipulate the movement of magnetic nanoparticles together with biomolecules (cells, DNA, antibodies etc.) attached on their surfaces. In this work a continuous switching/separation of magnetic nanoparticles in a sub-microliter fluid volume surrounded by neodymium permanent magnet is studied. A simple, low cost and generic microfluidic platform is developed for proof-of-concept experiments to illustrate the idea of using tangential microfluidic channels for magnetic field-assisted bioseparation. On the basis of MNPs concentration measurement the movement of the nanoparticles between the two tangential streams in the absence and presence of applied magnetic force was investigated. It was found that negligible switching or separation of MNPs takes place in the absence of magnetic field whereas 90% of switching was observed when magnetic field was employed. Flow rate of MNPs solution had dramatic impact on separation performance. A too high flow rate resulted in decrease in switching of magnetic nanoparticles whereas too low flow rate did not significantly improve the separation efficiency. It was observed that by carefully calibrating the fluid flow, an optimum value of flow rate can be found to provide maximum switching of magnetic nanoparticles together with higher throughput essential for bioseparation application. Separation performance was also studied for a mixture containing non-magnetic polystyrene (PS) particles and magnetic nanoparticles (MNPs). It was found that magnetic nanoparticles preferentially moved from lower microchannel to upper microchannel resulting in efficient separation from non-magnetic particles. The proof-of-concept experiments performed in this work further

demonstrates that microfluidic-based separation of biomolecules can be efficiently achieved using functionalized magnetic nanoparticles, together with tangential microchannels, appropriate magnetic field strength and optimum flow rates. This work further demonstrates that a simple low cost magnetic switching scheme can be potentially of great utility for separation and detection of biomolecules and cells in lab-on-a-chip systems.

4.4 Investigation of magnetic nanoparticle-assisted mixing strategy in a microfluidic channel using residence time distribution (RTD) analysis

4.4.1 State of the Art

Lab-on-a-chips systems have received increased attention in the last decade due to its vast applications in engineering, research, and development. Some of the areas that have benefited include medical diagnostic, biomedical engineering, pharmaceuticals and biotechnological sciences. They are now being realized for vast array of analysis including DNA, proteomics, forensic, immunoassays, and toxicity monitoring [4-7, 172, 187, 188]. However, the development lab-on-a-chip systems have its own share of difficulties and one area that need to be focused is mixing. The characteristic laminar flow field that occurs in micro-scale channels makes mixing a very challenging operation in lab-on-a-chip devices and therefore needs to be tackled.

In a typical Lab-on-a-chip microfluidic system, mixing of two or more liquids mainly occurs by molecular diffusion, which is often much slower than convection and reaction and overall slows down the separation or detection capabilities of the devices [252, 264]. In order to overcome that external or internal fluid manipulation techniques are required to enhance mass transfer and consequently mixing. Numerous experimental and theoretical strategies have been demonstrated in the past [43, 66, 76, 81, 89, 92, 104, 108, 113, 115, 116, 119, 124, 189, 195, 199, 200, 265-267] to enhance mixing. These strategies include both active and passive methods for instance: internal passive mixing by disturbing the fluid flows with microchannel structures [99, 100] or by splitting and injecting the fluid flows [84, 191, 193], or by confining the species in droplets [19, 194]. Some of the external active mixing strategies include fluid actuation by inducing energies including electrical [196-198], acoustic [200], mechanical [104, 105], ultrasonic[111,

267] or thermal [201] in the microchannel. Even though, these strategies are useful but they are limited by fabrication cost, complexities of setup or integration, and some form of active mixing strategies that require energies can damage cells, biomolecules or DNA [202]. Moreover, there exist no universal conventional method(s) that can evaluate and compare the performance of these strategies. Certain mixing characterization methods are available based on flow visualization [99, 266], chemical reaction [268, 269] and Poincare section [270, 271] but require complicated experimental setup. Therefore, simple mixing strategy together with easy to use, low cost characterization technique(s) for the quantitative evaluation of mixing patterns in microfluidic channels still pose some challenges [69] and needs to be addressed.

The objective of this work is to demonstrate a simple strategy of mixing and evaluate and optimize its performance using a universal characterization method that is easy to setup and can provide fast and reliable data for characterization. Therefore, in this work the classical theory of residence time distribution analysis (RTD) [185, 186] is used as a characterization tool to evaluate the mixing performance of a novel and simple scheme of mixing using magnetic nanoparticles (MNPs) and time-dependent magnetic field pulse in a microfluidic channel. RTD is a well established technique in chemical industry for characterizing mixing in macro-scale mixers/reactors but its application in microfluidic systems is still new [204-206, 272] has successfully demonstrated that RTD methods can be used to characterize mixing in microfluidic environment but his work was limited to passive actuation strategies that required complicated fabrication protocol and clean room. In this work, magnetic nanoparticles are used instead of magnetic microparticles or magnetic beads because of its superior properties such stability over time, high surface to volume ratio, minimum disturbance caused by the attached biomolecules

because of their extremely small size, and superparamagnetic nature that helps them to get re-suspended in fluid when magnetic field is removed without any agglomeration.

The novel active mixing scheme is demonstrated in this work using a simple, low cost and generic microfluidic platform setup that consisted of microfluidic channel, magnetic nanoparticles (MNPs), and in-house assembled electromagnet. It will be shown that periodic switching of magnetic field between on and off position produces oscillation in magnetic nanoparticles travelling in the channel. This causes chaos and agitation in the fluid flow and overall enhances the mixing process. Effect of flow condition on mixing performance is evaluated using RTD analysis and optimized values will be predicted. Overall, the proof-of-concept experimental setup in conjunction with RTD characterization tool deployed in this work proves that a simple time-dependent magnetic actuation scheme employing magnetic nanoparticles can be effectively used to mix micro volume of fluids in microfluidic lab-on-a-chip systems.

4.4.2 Materials & Method

4.4.2.1 Microchannel Fabrication

The microfluidic channels with a diameter of 800 μ m and length of 75mm were fabricated by a low cost rapid micromolding technique as shown in Figure 4.25. First, a mold is prepared by fixing an aluminum wire of 800 μ m diameter in the center and approximately at half the depth of the empty Petri dish. Polydimethylsiloxane (PDMS)(Sylgard 184, Dow Corning, USA) with a base and curing agent mixed in a ratio of 10:1 is poured onto the mold and is degassed to remove any bubbles using desiccators.

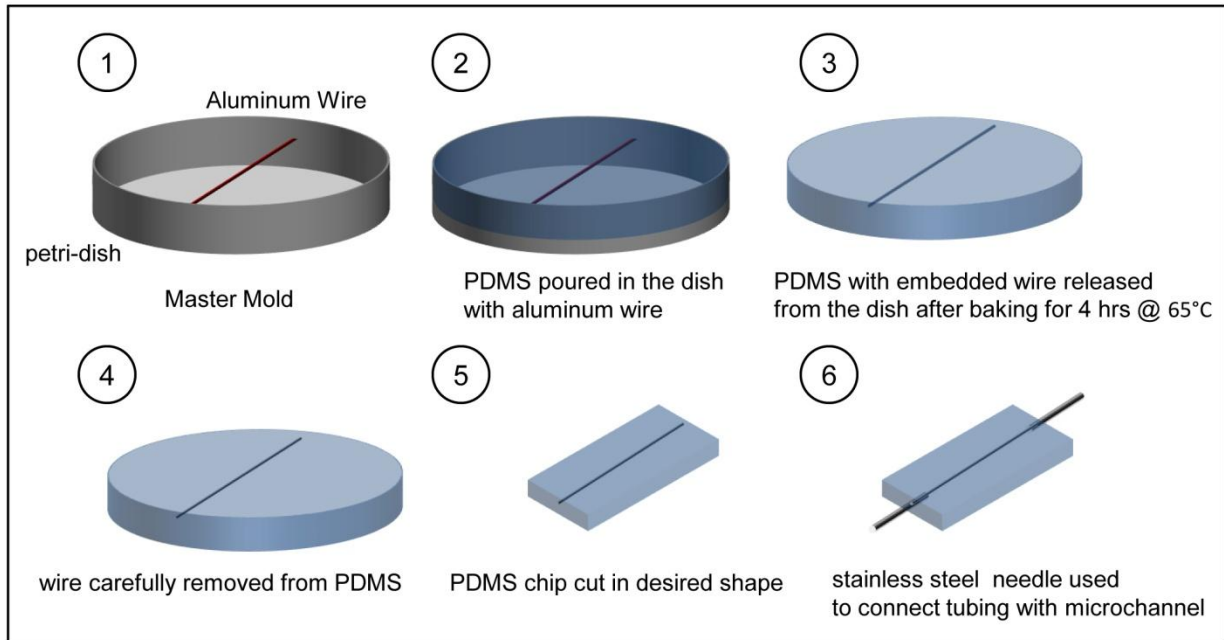


Figure 4.25 Fabrication step used in developing leak-proof microfluidic channels.

The uncured PDMS is baked in an oven (65 °C) for 1 h. The final step is to peel off the cured-PDMS containing the aluminium wire from the Petri dish. The sides of the cured PDMS are cut using a razor blade, leaving a significant amount of the wire exposed outside. With the help of pliers the wire are carefully removed. To make this process easier, the microchannel are washed with acetone which swells the PDMS and expand the channels prior to pulling out the wires. The microchannel was connected with the tygon tubing using the stainless tip obtained from microsyringe. The tip was inserted into the microchannel to make leakage free connection.

4.4.2.2 Microfluidic System Setup

A schematic view together with experimental set-up to carry out magneto-hydrodynamic mixing experiments is shown in Figure 4.26. The magnetic and microfluidic set-up can be divided into five main components: the microchannel, the magnetic nanoparticle solution, the fluidic connections, the imaging instrumentation, and the electromagnet system.

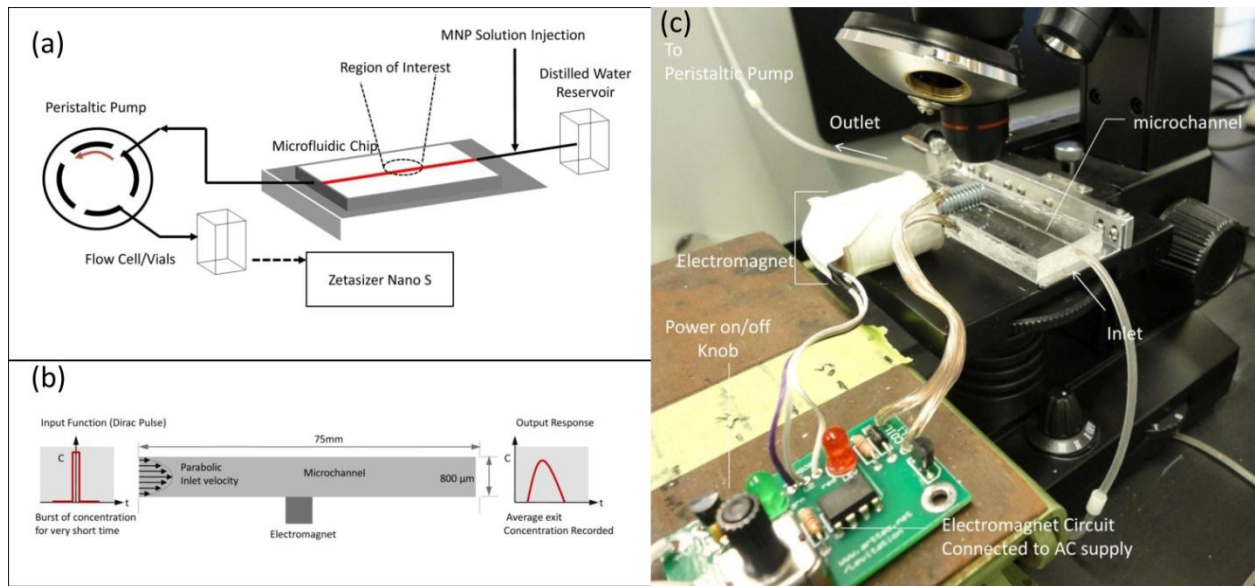


Figure 4.26 Microfluidic Magnetic Nanoparticle Mixing System: (a) Schematic representation of the setup showing the microchannel with electromagnet for generating magnetic field. The MNP solution is injected near the inlet from the right and flows under laminar conditions. The samples are collected at discrete time values and analyzed using Zetasizer Nano to obtain concentration-time curves, (b) In order to generate RTD curves, MNP with known concentration is injected for a very short time interval (Dirac pulse) into the microchannel from inlet and the response function is recorded at the microchannel output, and (c) snapshot of the setup showing microfluidic platform with inlet and outlet connections through tubings, electromagnet assembly in the vicinity of microfluidic chip with power switch to control magnetic field, and the objective of microscope over the region of interest (ROI) for recording images.

As shown in Figure 4.26c, the microfluidic channel is connected with inlet and outlet via flexible tygon tubing. In order to provide leak free connections a microsyringe tips made of stainless steel are embedded into the microchannel inlet/outlet for secure connections between the flexible tubes and the microfluidic chip. A differential pressure drop is maintained inside the channel by connecting the outlet of the microchannel to peristaltic micropump (P625 Peristaltic Pump, Instech, USA) and inlet to a reservoir containing distilled water. A steady state flow of distilled water is maintained in the microchannel. Flow rate was measured by collecting known sample of distilled water at the outlet at different times. It was also varied using the precise-bi directional speed controller on the pump. This simple method allows for a good control of the flow in the channel in suction mode. A micro- volume solution of magnetic nanoparticles was then introduced as a pulse input into the steady state flow of water using a 10mL syringe with

stainless steel needle. The sample is injected very close to the microchannel inlet so as to avoid any axial dispersion in tubing. The pulse input-response method was preferably chosen in this work to determine RTD because it is more robust and the data obtained using injection technique usually yield more reliable RTD analysis compared to step input-response method or other methods [206].

Magnetic field is controlled using electromagnet kit purchased from Arttec Inc. (Arttec., Inc, Woolwich, Maine). The kit comes with few levels of assembly (soldering the parts onto the printed circuit board). The electromagnet was basically constructed from a 2700 turns of 33 gage wire on a 2" bolt and nut with a 60 Ohm coil measuring 1" x 1 1/4". The total air gap is about 3/8". The electromagnet requires a 12VDC at 200mA. The knob on the circuit board can be used to adjust the air gap by about 1/4" and also works as on/off switch for magnetic field. Magnetic flux density (B) inside a solenoid can be found by multiplying magnetic permeability ($\mu_0\mu_r$) of core, turn density (n) and current flowing in the solenoid (I). The magnetic permeability is expressed as $\mu_0\mu_r$, where μ_r is the relative permeability of iron (=200) and is assumed to be constant, and μ_0 is the permeability in vacuum ($\mu_0 = 4\pi \times 10^{-7} \text{ N/A}^2$). For a solenoid of length L with N turns, the turn density is $n = N/L$ (turns/m). If the current in the solenoid is I (~200mA) and the relative permeability of the core $\mu_0\mu_r$, then the magnetic field at the center of the solenoid is given by:

$$B = \mu_0\mu_r \times n \times I \quad (4.18)$$

Based on Eq. 4.18, the magnetic field intensity of the electromagnet was approximately 5 Tesla. Optical images in the region of interest (ROI) (see Figure 4.26a) were acquired using the digital microscope (Celestron 44340, Celestron Inc., USA). The translational stage of the microscope

was used to place the microfluidic chip assembly such that the objective of camera acquires images of the flowing nanoparticles in real time. The CCD camera was connected to a computer for data acquisition. Magnetic nanoparticles (MNPs) of 200nm diameter (fluidMAG-ARA Chemicell GMBH, Germany) were suspended in de-ionized water and injected into the inlet. The magnetic particles consisted of small magnetite (Fe_3O_4) crystals with a diameter of approximately 12 nm, embedded in a biocompatible polysaccharide matrix which enabled stability and prevented biodegradation. The average diameter of the particles was approximately 200 nm, whereas the volume fraction of magnetite within a composite particle is 80%. For different flow rates, effluent was collected at the outlets at a number of discrete time intervals. The volume collected at the outlet was regularly verified to confirm the equal flow rates in the microchannel and the concentration of each MNPs sample collected in the effluent at different times was estimated from our in-house determined calibration curve. The calibration curves were generated from original stock of MNPs solution diluted to different concentrations. A dynamic light scattering instrument (Malvern Zetasizer Nano S, UK) was used. The Zetasizer Nano S measures the intensity of scattered light of various concentrations of sample at one angle; this is compared with the scattering produced from a standard (i.e. Toluene). In general, Zetasizer is used to measure the size of molecules but also the count rate can be used as a method of determining the relative concentration of a sample of stable size—as the count rate goes down, so too does the concentration. While the Zetasizer software does not automatically spit out an estimated sample concentration from the count rate but it is actually a fairly stable value for the same sample over time, and therefore used in this work as an estimate of concentration. Power law calibration curve of scattering intensity (kilocounts per second, kcps) versus concentration of magnetic nanoparticles (mg/ml) were obtained for 200nm particles ($R^2=0.9908$). In order to

obtain residence time distribution (RTD) curves for various condition of flow rate, the outlet sample from the effluent was taken in cuvette and placed in Zetsizer to obtain unknown scattering intensity (kcps) of the sample. Calibration curve was used to convert the scattering intensity into concentration (mg/ml). After the acquisition of the concentration–time data at a number of discrete time values, RTD curves were generated using the trapezoidal rule.

4.4.3 Results & Discussion

4.4.3.1 Residence-Time Distribution Function

The Residence-time distribution (RTD) curve is obtained after the acquisition of the concentration–time data at a number of discrete time values. MNP solution is injected for a very short time interval (Dirac pulse) at the inlet of the microchannel, and then the concentration of MNP at the outlet is recorded as a function of time using the method described in the section above. The RTD function also known as exit age-distribution $E(t)$ is defined quantitatively from the concentration–time data. The $E(t)$ function basically tells quantitatively, how much time different fluid elements have spent in a continuous flow system such that $E(t) \cdot dt$ is the fraction of MNP solution exiting the microchannel that have spent a time between t and $t + dt$ in the microchannel [186]. The RTD function, $E(t)$ is given by Eq.4.19, where $C(t)$ is the MNP solution concentration at the outlet, as a function of time. Experiments were performed in triplicates and the average value of MNP concentrations is used as $C(t)$.

$$E(t) = \frac{C(t)}{\int_0^{\infty} C(t) dt} \cong \frac{C(t_i)}{\sum_{i=0}^{\infty} C(t_i) \cdot \Delta t_i} \quad (4.19)$$

where, $\Delta t_i (= t_{i+1} - t_i)$ is the time steps used in the simulation.

After the RTD function is obtained, parameters that are used to quantify the mixing performance are calculated based on the methods given in literature[186]. These statistical parameters are mean residence time t_m , which gives the average time the exiting fluid element spend in the microchannel; variance σ^2 , which is the measure of the spread of the distribution; and coefficient of variance or normalized variance, which provides the relative standard deviation of the distribution. These statistical parameters are mathematically given by Eqs. 4.20-4.22.

$$t_m = \frac{\int_0^{\infty} tE(t)dt}{\int_0^{\infty} E(t)dt} = \int_0^{\infty} tE(t)dt \cong \sum_{t=0}^{\infty} tE(t)\Delta t \quad (4.20)$$

$$\text{since } \int_0^{\infty} E(t)dt = 1$$

$$\text{Variance} = \sigma^2 = \int_0^{\infty} (t - t_m)^2 E(t)dt \cong \sum_{t=0}^{\infty} (t - t_m)^2 E(t)\Delta t \quad (4.21)$$

$$\text{Normalized Variance} = \frac{\sigma^2}{t_m} \quad (4.22)$$

The RTD of the microchannel with magnetic actuation will deviate from an ideal plug flow mixer depending on the magneto-hydrodynamics with the microchannel. Based on computation a variance of zero would mean complete plug-flow mixing while a non-zero value will imply mixing due to non-uniform or laminar velocity and molecular diffusion. In this work normalized variance values given by Eq. 4.22 will be calculated for different flow conditions, a smaller normalized variance value will mean narrower RTD curve, closer distribution to mean residence time, and higher mixing performance. In this way, mixing performance for all the conditions including magnetic and no magnetic field assisted mixing will be computed, compared and optimized conditions will be predicted.

4.4.3.2 Qualitative Analysis of Mixing

Magnetically actuated mixing scheme demonstrated in this work relies on the periodic switching of magnetic field between on and off position. Turning the magnetic field on will attract the MNPs to regions with higher magnetic field intensity whereas turning off will again force them to follow the fluid flow due to drag forces acting on them. This will eventually create chaos and a means to oscillate MNPs that result in mixing of fluid. In order to see this affect images were acquired at discrete time steps (~ 5 s) using a digital camera embedded in our laboratory microscope. The details of the setup are already described in previous section. At a time, $t=0$ s, a 30 μ l of a 200nm MNP solution having a concentration of 1mg/ml is injected for a very short time period into the deionized (DI) water flowing at a rate of 0.6 μ l/s near the inlet. Magnetic field is manually turned on and off after 30s. It is turned on for 5s and then turned off for next 5s giving a total of four pulses of magnetic field (see Figure 4.27b) within a span of 35s. Figure 4.27a shows the snapshot of microchannel in the region of interest at different time intervals. It can be seen that initially at $t=30$ s when no magnetic field is used MNP solutions flows with the carrier fluid with a perfect parabolic flow profile, i.e. maximum velocity at the center indicated by higher concentration of MNPs in the center at $t=30$ s.

When magnetic field is turned on at $t=35$ s, MNPs tend to attract towards the region of higher magnetic field intensity, generating spikes as can be seen in the Figure 4.27a. When the magnetic field is turned off again the MNPs relaxes and goes with the drag force exerted by fluid flow. Periodically switching the magnetic field on/off, creates chaos and oscillation in MNPs as seen in Figure 4.27b at time $t=40$ s to $t=75$ s. The disturbance of MNPs using external electromagnet source can be effectively used to mix fluids and it can be seen from time $t=80$ & 85s that after the sudden burst of magnetic actuation pulses the MNPs solutions seems to flow more like a plug

flow with less variation in concentration across the cross-section of the microchannel and better mixing. Quantitative evaluation of mixing performance is done using RTD analysis and is presented in next section together with the affect of flow rate on the mixing.

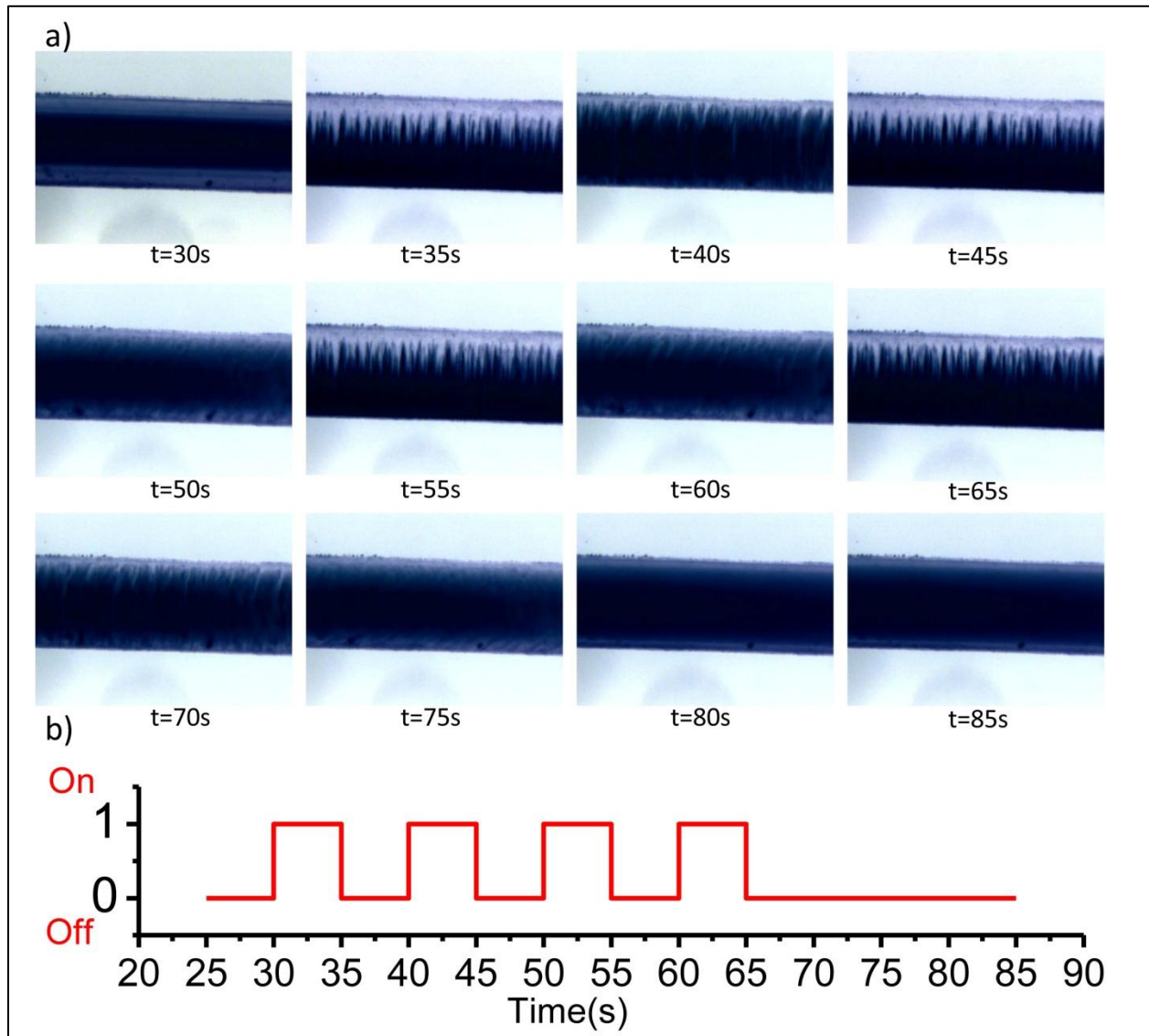


Figure 4.27 (a) Micrograph of magnetic nanoparticle concentration in the region of interest (ROI) with the microchannel at discrete time intervals, and (b) Oscillating magnetic field in the form of square-wave that is turned on and off at different times. Four pulses of magnetic field are generated to cause disturbances in MNP solution coming from right and moving towards left.

4.4.3.3 Effect of Flow Conditions

Flow rate of carrier fluid in this case it is DI-water also has significant effect on the mixing performance and needs to be optimized. RTD curves were obtained as described earlier in the sections. At a time, $t=0s$, a $30\ \mu\text{l}$ of a 200nm MNP solution having a concentration of 1mg/ml is injected for a very short time period into the de-ionized (DI) water flowing at rates of 0.3 , 0.6 , and $1\ \mu\text{l/s}$.

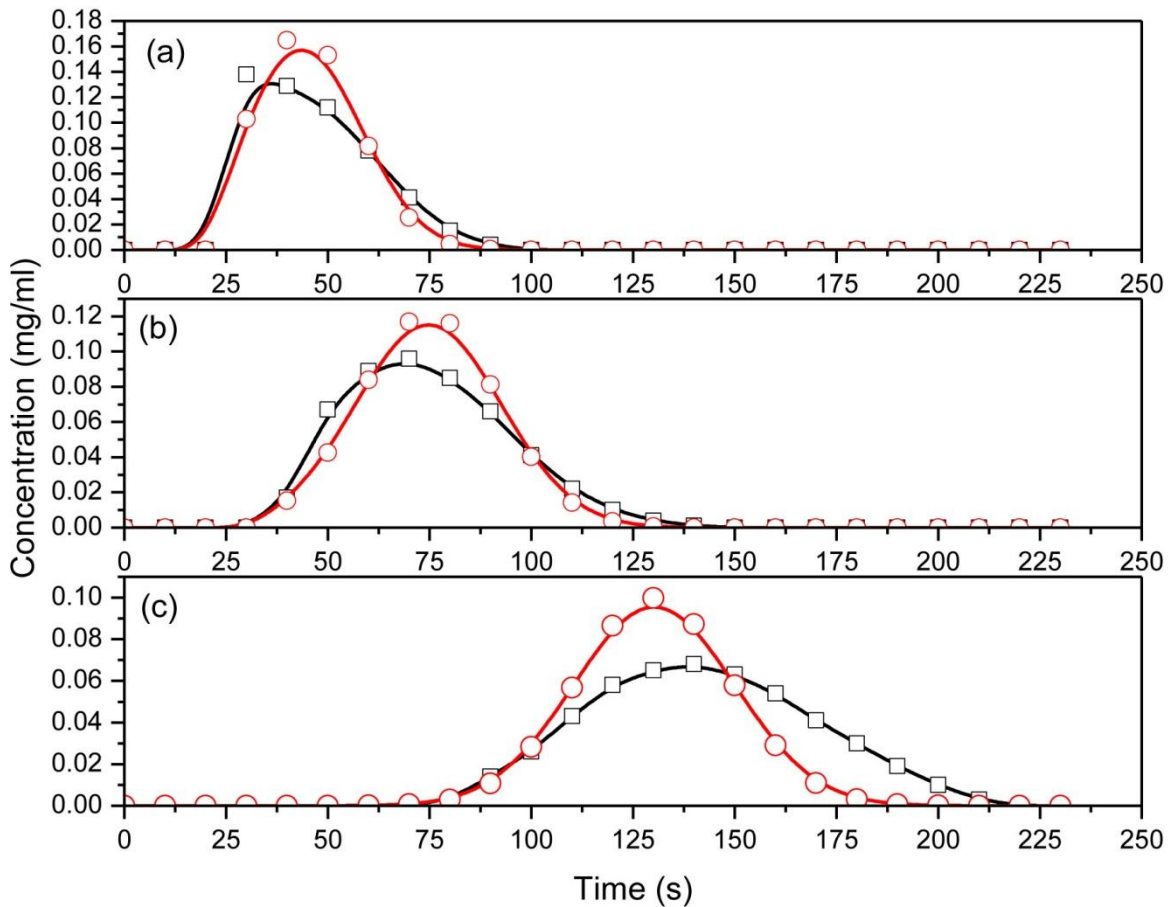


Figure 4.28 Concentration-time curves of magnetic nanoparticle solution obtained with (circle) and without (square) magnetic actuation. MNP solution was injected for a very short time period into the de-ionized (DI) water flowing at rates of (a) $1\ \mu\text{l/s}$, (b) $0.6\ \mu\text{l/s}$, and (c) $0.3\ \mu\text{l/s}$

The injection point is kept close to the inlet so as to minimize the axial dispersion of the pulse.

The time-dependent concentration data was obtained for each flow rates using the method

described in previous section. Briefly, the outlet sample from the effluent was taken in a cuvette after every 10s and placed in Zetasizer to obtain unknown scattering intensity (kcps) of the sample. Calibration curve was used to convert the scattering intensity into concentration (mg/ml). Three replicates of experiments were performed for each flow rate investigated to establish high repeatability of data both with and without magnetic actuation. From the concentration-time curves given in Figure 4.28, it can be seen that when the flow conditions are changed, the time fluid element spent in the microchannel also changes; therefore as the flow rate is increased the mean residence time decreases which may also decrease the effectiveness of magnetically actuated mixing. Therefore, an optimum flow rate for magnetically actuated mixing needs to be identified. From Figure 4.28, it can be seen that for all conditions of flow rate the mixing is enhanced when magnetic field actuation is deployed. The effectiveness of magnetic actuation is more pronounced at lower flow rates ($\sim 0.3 \mu\text{l/s}$). RTD curves were generated based on the concentration-time data shown in Figure 4.28 for both with and without magnetic actuation. It can be seen from Figure 4.29 that the RTD curves for magnetic scenario when compared to no magnetic scenario becomes less spread out and the computed normalized variance values are also lower than their counterpart.

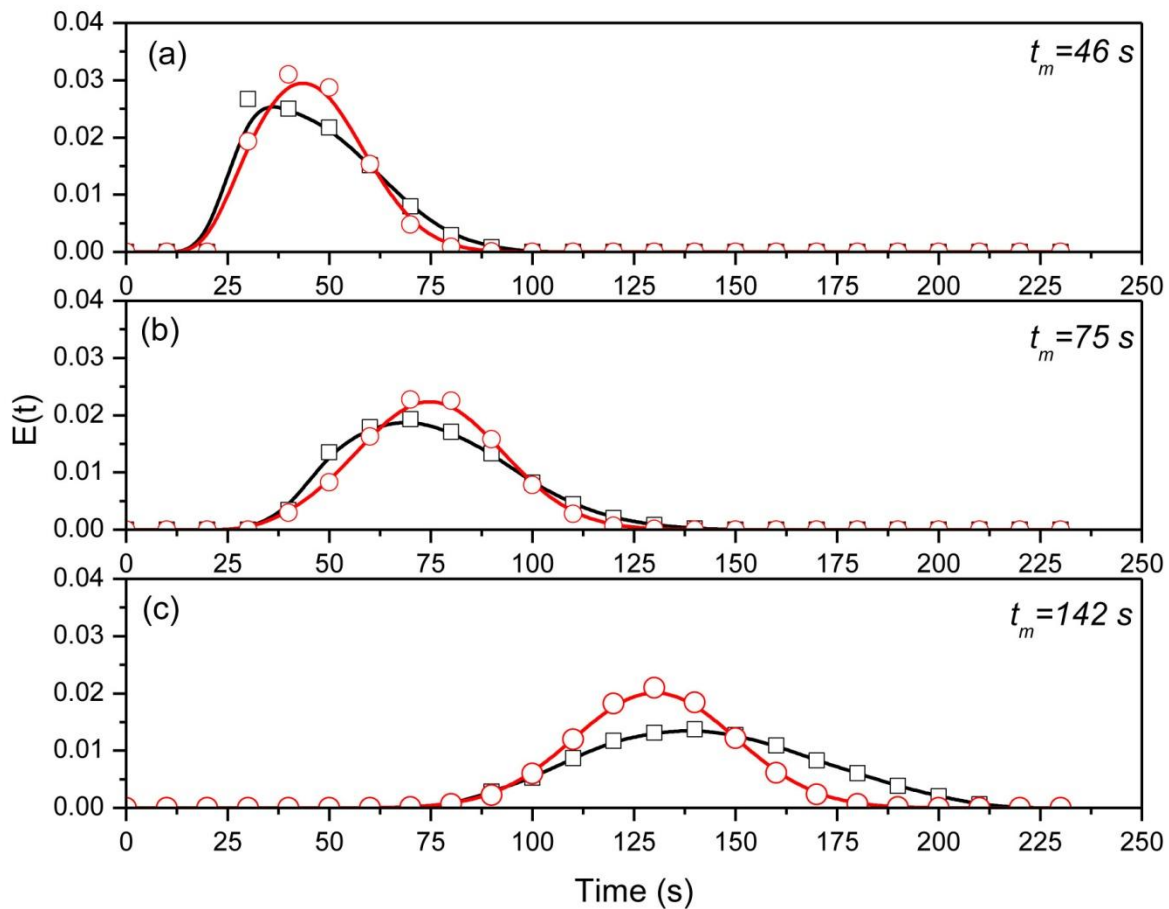


Figure 4.29 Residence time distribution (RTD) curves of magnetic nanoparticle solution obtained with (circle) and without (square) magnetic actuation. MNP solution was injected for a very short time period into the de-ionized (DI) water flowing at rates of (a) 1 $\mu\text{l/s}$, (b) 0.6 $\mu\text{l/s}$, and (c) 0.3 $\mu\text{l/s}$

This shows that mixing is enhanced due to the presence of magnetic actuation. Basically a narrower RTD curve means a closer distribution of species to mean residence time, and higher mixing performance. The mixing seems to be more pronounced with low flow rates. In order to evaluate that normalized variance were also computed for different flow conditions within the microchannel for both magnetic and non-magnetic scenarios. As seen from Figure 4.30, the effect of magnetic actuation largely depends on the flow condition. At higher flow rates the normalized variance difference between non magnetic and magnetic scenario decreases. For both

0.6, and 1 $\mu\text{l/s}$, there was approximately 30% decrease in normalized variance that translates to approximately 30% increase in mixing due to the presence of magnetic field actuation.

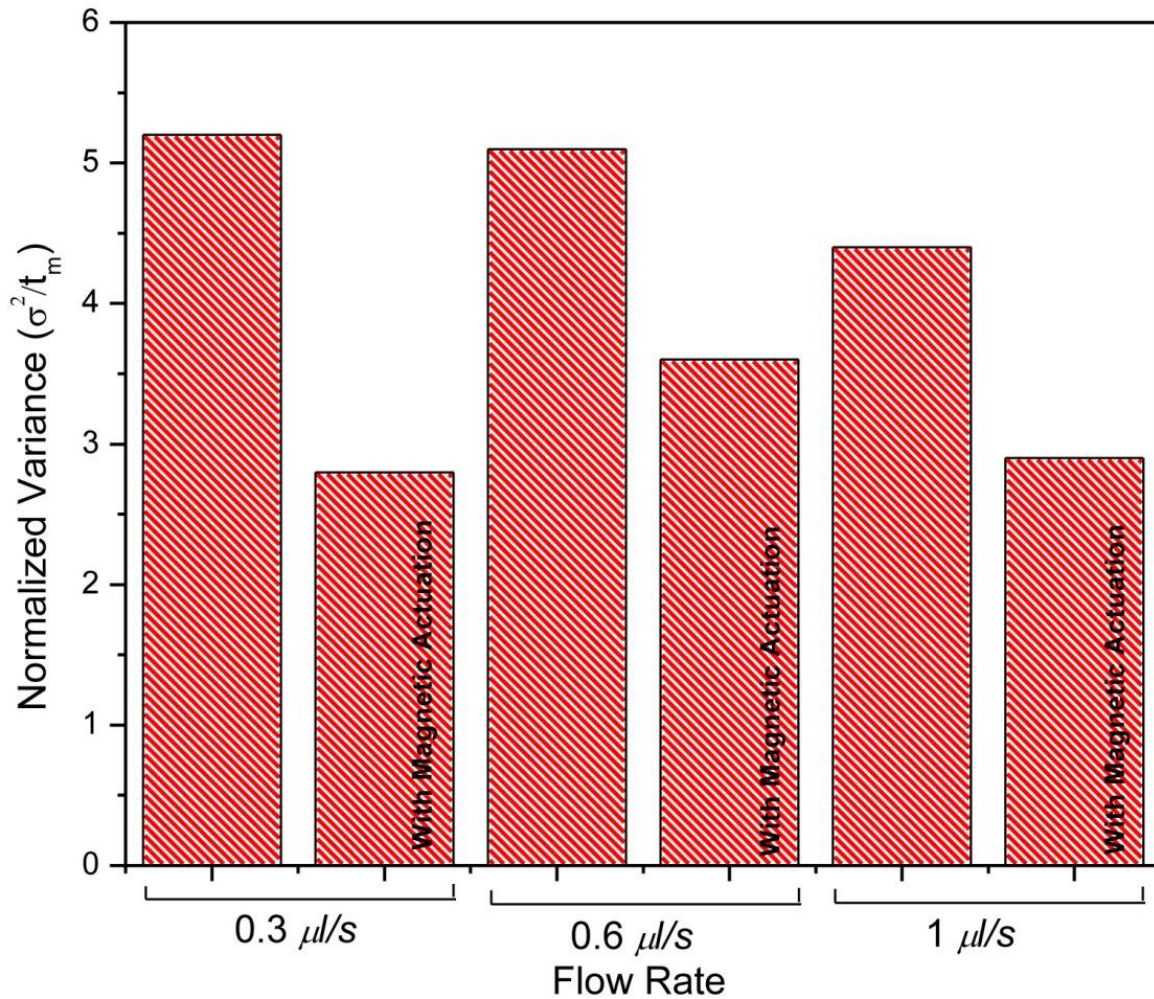


Figure 4.30 Normalized variance plot for three flow rate conditions with and without magnetic actuation.

Whereas at much lower flow rate of 0.3 $\mu\text{l/s}$, there was approximately 50% decrease in normalized variance or effectively 50% enhancement in mixing due to the presence of magnetic field actuation. Therefore for the magnetic field strength and conditions used in these experiments, it would be ideal to operate the system with a flow rate of 0.3 $\mu\text{l/s}$. However, if the system needs to be operated at higher flow rates larger magnetic field force is needed to bring

out desired disturbance within the microchannel in order to enhance mixing and this can be done by increasing the magnetic field strength of electromagnet. From the RTD analysis above, it can be concluded that magnetically actuated mixing scheme is easy to set up and can be effectively used to mix small volumes of fluid in microchannels useful for separation and detection systems.

4.4.4 Conclusion

A proof-of-concept experimental study to demonstrate an innovative time-dependent magnetically actuated mixing scheme is successfully demonstrated. Residence-time distribution (RTD) analysis, for the first time, is used to study the dynamics of this novel mixing scheme as well as investigate the affect of flow conditions. A low cost generic microfluidic platform is assembled using electromagnet that comprises of copper wire and iron core and microfluidic channels that were fabricated from a novel micromolding technique that can be done without a clean room. Both qualitative and quantitative findings reveals that periodic switching of magnetic field between on and off position produces oscillation in magnetic nanoparticles and overall enhances the mixing process. Based on RTD analysis and computation of normalized variance of MNPs concentration at the outlet of microchannel, approximately 50% enhancement in mixing was achieved by working at lower flow rate of 0.3 $\mu\text{l/s}$. The enhancement decreased to 30% when flow rates were increased. Overall, the proof-of-concept experiments in conjunction with RTD analysis done in this work reveals that a simple time-dependent magnetic actuation scheme employing magnetic nanoparticles can be effectively used to mix micro volume of fluids *in situ* and can be potentially of great utility for separation and detection of biomolecules in microfluidic lab-on-a-chip systems.

5. CONCLUSION

In this work magnetically actuated system comprising of microfluidic channel and superparamagnetic nanoparticles is designed and developed. Advanced mathematical model comprising of mass and momentum transport, convection & diffusion, and magnetic field interaction was combined with proof-concept experiments performed using an assembled simple low cost generic microfluidic platform that consisted of microfluidic channels, magnet assembly, flow system and characterization protocols. It was found that the combination of magnetic fields with microfluidics simplified the complexity of the present generation devices and showed that biomolecules can be precisely captured, separated or detected with high efficiency and ease of operation by tagging them with magnetic nanoparticles. The presence of MNPs together with time-dependent magnetic actuation also demonstrated that high mixing can be achieved with ease within the microchannel. The numerical simulations were helpful in testing and optimizing key design parameters and demonstrated that fluid flow rate, magnetic field strength, and magnetic nanoparticle size had dramatic impact on the performance of magnetic microfluidic systems studied. The main focus of this research was to understand the physical phenomena and behavior of magnetic particles and how this novel technique be used for efficient separation and detection of biomolecules. This work also emphasizes on the importance of considering magnetic nanoparticles interactions for a thorough design of magnetic nanoparticle-based LOC devices where all the laboratory unit operations can be easily integrated. This new approach allows for versatile chip design rules and provides a simple approach to integrate external elements for enhancing separation and detection of biomolecules. The present system may be of interest for many on-chip bio-analytical applications and in particular for magneto-microfluidic bio assays. Indeed, when using magnetic nanoparticles with functionalized surfaces, dynamic actuation of

the MNPs increases the efficiency of analyte capture in a sample flow. Moreover, when the magnetic field is removed, the superparamagnetic nature of the MNPs prevents clustering and permits easy release from the system for further processing and detection downstream. Suggestions regarding future steps and expansion needed to further improve and develop such systems are also provided. The vast applications of the novel concepts studied in this work demonstrate its potential of to be applied to devices for point-of care diagnostics especially in resource-limited settings.

6. OUTLOOK

In this section we will discuss about the future direction with respect to development of magnetically actuated components such as mixer, separator, and detector for microfluidic application and discuss the feasibility of using the results obtained in this work. The first thing we can focus on is the physics of the system and whether the multiphysics model developed in this work is successful in translating the real world phenomenon of magnetic nanoparticle interaction in microchannels. Needless to say that the developed mathematical model was successful in predicting the phenomenon to a certain extent but there will be instances when further improvement will be necessary. For example, the scenarios considered in this work were dedicated to low concentration of magnetic nanoparticles (MNPs) although useful for most of the cases but in some situation we will need to consider buffers containing a high concentration of the MNPs, in these scenarios the mutual interactions of particle will play a critical role and must be taken into account. Also, use of higher concentrations of MNPs may be advantageous. Firstly, increased number of the MNPs will improve the ratio of the tagged target biomolecules and therefore, can enhance the efficiency of the separation or detection. Secondly, concentrated MNP solution can be used to perform liquid-liquid mixing. It is worth noting that liquid-liquid mixing will be much easier than solid particles disturbing the fluid flow and will eventually require lower magnetic field. A high concentration of MNPs can be considered as two-phase system where particle-particle interaction can be considered using Euler-Euler approximation. However, simulation of such scenario will call for further improvement in mathematical model and computational resources. Therefore, the next step could be development of mathematical model that can take into account both low and high concentration of MNPs and the new particle tracing module of COMSOL Multiphysics software will be worth exploring.

When developing magnetically actuated microfluidic system, the most important aspect is the choice of magnetic assembly i.e. if the system should be active or passive. A time-dependent magnetic actuation for mixing demonstrated in this work will require active magnetic assembly. Active systems can use electromagnets or soft magnetic elements embedded on chip. The later will be difficult, expensive to fabricate, and can generate heat on-chip therefore not recommended. Use of external electromagnets can provide both sufficient magnetic field and time-dependent magnetic actuation but one has to keep in mind the size of electromagnet when developing such system.

If the device needs to only capture or switch magnetic particles for continuous separation, passive systems consisting of permanent magnet should be chosen. Several passive systems have been designed and tested in this thesis. The advantage of using permanent magnet-based system is two-fold, first they are simple, low cost and easy to assemble and secondly they provide higher magnetic fields. The disadvantages of placing magnets near the microchannel would be the inability to use optical system for characterization. The light scattering-based characterization technique used in this study is more robust and can be very well be used in such situations.

In this work, an in-house developed micromolding technique is used to develop PDMS microchannels. This is an in-expensive fabrication procedure and do not require clean room but may result in microchannels that are not precise with respect to width and length. It is worth noting that objective of this work is to demonstrate the strategy of magnetic actuation and this work was successful in doing it. In future, however it is recommended to have precise dimension of microchannels that can be fabricated using clean room-based soft lithography techniques. However, these fabrication methods should be further developed and tested.

The characterization technique used in this study was based on light-scattering instrument which required development of calibration curve. It is also recommended that magnetic microfluidic system should be evaluated through various other techniques based on availability. One interesting characterization method is by recording the motion of the MNPs using PIV (Particle Image Velocimetry) or PTV (Particle Tracking Velocimetry) techniques which will be really helpful in analyzing chaotic systems.

Finally, in this work the focus has been to characterize MNPs manipulation and understand the physics thoroughly in order to determine how well they work and what makes them work well so that they can be deployed in mixing, separation, and detection system. The next step can be development of various components by considering the interaction of MNPs with target biomolecules. Mixing can be integrated with separation or detection to see how biomolecules interact with surface functionalized MNPs. As we envisioned, this will eventually lead to the development of magnetic nanoparticle-based Lab-on-a-chip system for field applications.

7. REFERENCES

- [1] M. J. Madou, *Fundamentals of Microfabrication: The Science of Miniaturization*, 2 ed.: CRC Press, 2002.
- [2] G. T. A. Kovacs, *Micromachined Transducers – Sourcebook*: McGraw-Hill, New York, 1998.
- [3] A. Manz, N. Graber, and H. M. Widmer, "Miniaturized total chemical analysis systems: A novel concept for chemical sensing," *Sensors and Actuators B-Chemical*, vol. 1, pp. 244-248, Jan 1990.
- [4] M. A. Burns, B. N. Johnson, S. N. Brahmaandra, K. Handique, J. R. Webster, M. Krishnan, T. S. Sammarco, P. M. Man, D. Jones, D. Heldsinger, C. H. Mastrangelo, and D. T. Burke, "An integrated nanoliter DNA analysis device," *Science*, vol. 282, pp. 484-487, Oct 1998.
- [5] L. Cao, S. Mantell, and D. Polla, "Design and simulation of an implantable medical drug delivery system using microelectromechanical systems technology," *Sensors and Actuators a-Physical*, vol. 94, pp. 117-125, Oct 2001.
- [6] F. Vinet, P. Chaton, and Y. Fouillet, "Microarrays and microfluidic devices: miniaturized systems for biological analysis," *Microelectronic Engineering*, vol. 61-2, pp. 41-47, Jul 2002.
- [7] T. Vo-Dinh, G. Griffin, D. L. Stokes, and A. Wintenberg, "Multi-functional biochip for medical diagnostics and pathogen detection," *Sensors and Actuators B-Chemical*, vol. 90, pp. 104-111, Apr 2003.
- [8] Y. N. Xia and G. M. Whitesides, "Soft lithography," *Annual Review of Materials Science*, vol. 28, pp. 153-184, 1998.
- [9] C. M. Ho and Y. C. Tai, "Micro-electro-mechanical-systems (MEMS) and fluid flows," *Annual Review of Fluid Mechanics*, vol. 30, pp. 579-612, 1998.
- [10] E. Belloy, A. Sayah, and M. A. M. Gijs, "Oblique powder blasting for three-dimensional micromachining of brittle materials," *Sensors and Actuators a-Physical*, vol. 92, pp. 358-363, Aug 2001.
- [11] P. Abgrall and A. M. Gue, "Lab-on-chip technologies: making a microfluidic network and coupling it into a complete microsystem - a review," *Journal of Micromechanics and Microengineering*, vol. 17, pp. R15-R49, May 2007.
- [12] C. Hansen and S. R. Quake, "Microfluidics in structural biology: smaller, faster... better," *Current Opinion in Structural Biology*, vol. 13, pp. 538-544, Oct 2003.
- [13] S. Haeberle and R. Zengerle, "Microfluidic platforms for lab-on-a-chip applications," *Lab on a Chip*, vol. 7, pp. 1094-1110, 2007.
- [14] D. Mark, S. Haeberle, G. Roth, F. von Stetten, and R. Zengerle, "Microfluidic lab-on-a-chip platforms: requirements, characteristics and applications," *Chemical Society Reviews*, vol. 39, pp. 1153-1182, 2010.
- [15] C. W. Li, C. N. Cheung, J. Yang, C. H. Tzang, and M. S. Yang, "PDMS-based microfluidic device with multi-height structures fabricated by single-step photolithography using printed circuit board as masters," *Analyst*, vol. 128, pp. 1137-1142, 2003.
- [16] M. Reches, K. A. Mirica, R. Dasgupta, M. D. Dickey, M. J. Butte, and G. M. Whitesides, "Thread as a Matrix for Biomedical Assays," *ACS Applied Materials & Interfaces*, vol. 2, pp. 1722-1728, Jun 2010.

- [17] P. J. Bracher, M. Gupta, and G. M. Whitesides, "Patterned paper as a template for the delivery of reactants in the fabrication of planar materials," *Soft Matter*, vol. 6, pp. 4303-4309, 2010.
- [18] R. Mukhopadhyay, "Diving into droplets," *Analytical Chemistry*, vol. 78, pp. 1401-1404, Mar 2006.
- [19] R. B. Fair, A. Khlystov, T. D. Taylor, V. Ivanov, R. D. Evans, P. B. Griffin, V. Srinivasan, V. K. Pamula, M. G. Pollack, and J. Zhou, "Chemical and biological applications of digital-microfluidic devices," *Ieee Design & Test of Computers*, vol. 24, pp. 10-24, Jan-Feb 2007.
- [20] R. B. Fair, "Digital microfluidics: is a true lab-on-a-chip possible?," *Microfluidics and Nanofluidics*, vol. 3, pp. 245-281, Jun 2007.
- [21] J. El-Ali, P. K. Sorger, and K. F. Jensen, "Cells on chips," *Nature*, vol. 442, pp. 403-411, Jul 2006.
- [22] E. Verpoorte, "Beads and chips: new recipes for analysis," *Lab on a Chip*, vol. 3, pp. 60N-68N, 2003.
- [23] F. E. Regnier, B. He, S. Lin, and J. Busse, "Chromatography and electrophoresis on chips: critical elements of future integrated, microfluidic analytical systems for life science," *Trends in Biotechnology*, vol. 17, pp. 101-106, Mar 1999.
- [24] G. M. Whitesides and A. D. Stroock, "Flexible methods for microfluidics," *Physics Today*, vol. 54, pp. 42-48, Jun 2001.
- [25] A. Manz, C. S. Effenhauser, N. Burggraf, D. J. Harrison, K. Seiler, and K. Fluri, "Electroosmotic pumping and electrophoretic separations for miniaturized chemical analysis systems," *Journal of Micromechanics and Microengineering*, vol. 4, pp. 257-265, Dec 1994.
- [26] P. J. Asiello and A. J. Baeumner, "Miniaturized isothermal nucleic acid amplification, a review," *Lab on a Chip*, vol. 11, pp. 1420-1430, 2011.
- [27] D. R. Reyes, D. Iossifidis, P. A. Auroux, and A. Manz, "Micro total analysis systems. 1. Introduction, theory, and technology," *Analytical Chemistry*, vol. 74, pp. 2623-2636, Jun 2002.
- [28] P. A. Auroux, D. Iossifidis, D. R. Reyes, and A. Manz, "Micro total analysis systems. 2. Analytical standard operations and applications," *Analytical Chemistry*, vol. 74, pp. 2637-2652, Jun 2002.
- [29] N. Pamme, "Magnetism and microfluidics," *Lab on a Chip*, vol. 6, pp. 24-38, 2006.
- [30] H. A. Stone, A. D. Stroock, and A. Ajdari, "Engineering flows in small devices: Microfluidics toward a lab-on-a-chip," *Annual Review of Fluid Mechanics*, vol. 36, pp. 381-411, 2004.
- [31] S. W. Yeung and I. M. Hsing, "Manipulation and extraction of genomic DNA from cell lysate by functionalized magnetic particles for lab on a chip applications," *Biosensors & Bioelectronics*, vol. 21, pp. 989-997, Jan 2006.
- [32] K. E. McCloskey, J. J. Chalmers, and M. Zborowski, "Magnetic cell separation: Characterization of magnetophoretic mobility," *Analytical Chemistry*, vol. 75, pp. 6868-6874, Dec 2003.
- [33] F. Sauzedde, A. Elaissari, and C. Pichot, "Thermosensitive magnetic particles as solid phase support in an immunoassay," *Macromolecular Symposia*, vol. 151, pp. 617-623, Feb 2000.

- [34] M. Tudorache, M. Co, H. Lifgren, and J. Emneus, "Ultrasensitive magnetic particle-based immunosupported liquid membrane assay," *Analytical Chemistry*, vol. 77, pp. 7156-7162, Nov 2005.
- [35] H. Kuramitz, "Magnetic microbead-based electrochemical immunoassays," *Analytical and Bioanalytical Chemistry*, vol. 394, pp. 61-69, May 2009.
- [36] H. Chen, A. Abolmatty, and M. Faghri, "Microfluidic inverse phase ELISA via manipulation of magnetic beads," *Microfluidics and Nanofluidics*, vol. 10, pp. 593-605, Mar 2011.
- [37] M. A. M. Gijs, "Magnetic bead handling on-chip: new opportunities for analytical applications," *Microfluidics and Nanofluidics*, vol. 1, pp. 22-40, Nov 2004.
- [38] N. Pamme and A. Manz, "On-chip free-flow magnetophoresis: Continuous flow separation of magnetic particles and agglomerates," *Analytical Chemistry*, vol. 76, pp. 7250-7256, Dec 2004.
- [39] G. P. Hatch and R. E. Stelter, "Magnetic design considerations for devices and particles used for biological high-gradient magnetic separation (HGMS) systems," *Journal of Magnetism and Magnetic Materials*, vol. 225, pp. 262-276, Apr 2001.
- [40] M. Brzeska, M. Panhorst, P. B. Kamp, J. Schotter, G. Reiss, A. Puhler, A. Becker, and H. Bruckl, "Detection and manipulation of biomolecules by magnetic carriers," *Journal of Biotechnology*, vol. 112, pp. 25-33, Aug 2004.
- [41] C. H. Ahn, M. G. Allen, W. Trimmer, Y. N. Jun, and S. Erramilli, "A fully integrated micromachined magnetic particle separator," *Journal of Microelectromechanical Systems*, vol. 5, pp. 151-158, Sep 1996.
- [42] J. W. Choi, C. H. Ahn, S. Bhansali, and H. T. Henderson, "A new magnetic bead-based, filterless bio-separator with planar electromagnet surfaces for integrated bio-detection systems," 2000, pp. 34-39.
- [43] J. W. Choi and C. H. Ahn, "An active microfluidic mixer for mixing of microparticles and liquids," in *Microfluidic Devices and Systems III* vol. 4177, C. H. Mastrangelo and H. Becker, Eds., ed, 2000, pp. 154-161.
- [44] J. W. Choi, T. M. Liakopoulos, and C. H. Ahn, "An on-chip magnetic bead separator using spiral electromagnets with semi-encapsulated permalloy," *Biosensors & Bioelectronics*, vol. 16, pp. 409-416, Aug 2001.
- [45] J. W. Choi, K. W. Oh, J. H. Thomas, W. R. Heineman, H. B. Halsall, J. H. Nevin, A. J. Helmicki, H. T. Henderson, and C. H. Ahn, "An integrated microfluidic biochemical detection system for protein analysis with magnetic bead-based sampling capabilities," *Lab on a Chip*, vol. 2, pp. 27-30, 2002.
- [46] A. Rida, V. Fernandez, and M. A. M. Gijs, "Long-range transport of magnetic microbeads using simple planar coils placed in a uniform magnetostatic field," *Applied Physics Letters*, vol. 83, pp. 2396-2398, Sep 2003.
- [47] M. Q. Bu, T. B. Christensen, K. Smistrup, A. Wolff, and M. F. Hansen, "Characterization of a microfluidic magnetic bead separator for high-throughput applications," 2008, pp. 430-436.
- [48] Y. K. Hahn, Z. Jin, J. H. Kang, E. Oh, M. K. Han, H. S. Kim, J. T. Jang, J. H. Lee, J. Cheon, S. H. Kim, H. S. Park, and J. K. Park, "Magnetophoretic immunoassay of allergen-specific IgE in an enhanced magnetic field gradient," *Analytical Chemistry*, vol. 79, pp. 2214-2220, Mar 2007.

- [49] S. Bronzeau and N. Pamme, "Simultaneous bioassays in a microfluidic channel on plugs of different magnetic particles," *Analytica Chimica Acta*, vol. 609, pp. 105-112, Feb 2008.
- [50] U. Lehmann, C. Vandevyver, V. K. Parashar, and M. A. M. Gijs, "Droplet-based DNA purification in a magnetic lab-on-a-chip," *Angewandte Chemie-International Edition*, vol. 45, pp. 3062-3067, 2006.
- [51] A. Rida and M. A. M. Gijs, "Manipulation of self-assembled structures of magnetic beads for microfluidic mixing and assaying," *Analytical Chemistry*, vol. 76, pp. 6239-6246, Nov 2004.
- [52] N. Xia, T. P. Hunt, B. T. Mayers, E. Alsberg, G. M. Whitesides, R. M. Westervelt, and D. E. Ingber, "Combined microfluidic-micromagnetic separation of living cells in continuous flow," *Biomedical Microdevices*, vol. 8, pp. 299-308, Dec 2006.
- [53] C. W. Yung, J. Fiering, A. J. Mueller, and D. E. Ingber, "Micromagnetic-microfluidic blood cleansing device," *Lab on a Chip*, vol. 9, pp. 1171-1177, 2009.
- [54] S. X. Wang and G. Li, "Advances in giant magnetoresistance biosensors with magnetic nanoparticle tags: Review and outlook," *IEEE Transactions on Magnetics*, vol. 44, pp. 1687-1702, Jul 2008.
- [55] V. C. Martins, F. A. Cardoso, J. Germano, S. Cardoso, L. Sousa, M. Piedade, P. P. Freitas, and L. P. Fonseca, "Femtomolar limit of detection with a magnetoresistive biochip," *Biosensors & Bioelectronics*, vol. 24, pp. 2690-2695, Apr 2009.
- [56] M. Koets, T. van der Wijk, J. van Eemeren, A. van Amerongen, and M. W. J. Prins, "Rapid DNA multi-analyte immunoassay on a magneto-resistance biosensor," *Biosensors & Bioelectronics*, vol. 24, pp. 1893-1898, Mar 2009.
- [57] Q. Ramadan, V. Samper, D. Poenar, and C. Yu, "On-chip micro-electromagnets for magnetic-based bio-molecules separation," *Journal of Magnetism and Magnetic Materials*, vol. 281, pp. 150-172, Oct 2004.
- [58] Q. Ramadan, V. Samper, D. P. Poenar, and C. Yu, "An integrated microfluidic platform for magnetic microbeads separation and confinement," *Biosensors & Bioelectronics*, vol. 21, pp. 1693-1702, Mar 2006.
- [59] Q. Ramadan, C. Yu, V. Samper, and D. P. Poenar, "Microcoils for transport of magnetic beads," *Applied Physics Letters*, vol. 88, Jan 2006.
- [60] M. Q. Bu, T. B. Christensen, K. Smistrup, A. Wolff, and M. F. Hansen, "Characterization of a microfluidic magnetic bead separator for high-throughput applications," *Sensors and Actuators a-Physical*, vol. 145, pp. 430-436, Jul-Aug 2008.
- [61] Q. A. Pankhurst, J. Connolly, S. K. Jones, and J. Dobson, "Applications of magnetic nanoparticles in biomedicine," *Journal of Physics D-Applied Physics*, vol. 36, pp. R167-R181, Jul 2003.
- [62] P. H. Shih, J. Y. Shiu, P. C. Lin, C. C. Lin, T. Veres, and P. Chen, "On chip sorting of bacterial cells using sugar-encapsulated magnetic nanoparticles," *Journal of Applied Physics*, vol. 103, Apr 2008.
- [63] J. Atencia and D. J. Beebe, "Controlled microfluidic interfaces," *Nature*, vol. 437, pp. 648-655, Sep 2005.
- [64] E. R. G. Eckert and R. M. Drake, *Analysis of heat and mass transfer*. New York,: McGraw-Hill, 1971.
- [65] T. Gervais and K. F. Jensen, "Mass transport and surface reactions in microfluidic systems," *Chemical Engineering Science*, vol. 61, pp. 1102-1121, Feb 2006.

- [66] C. P. Jen, C. Y. Wu, and Y. C. Lin, "Design and simulation of the micromixer with chaotic advection in twisted microchannels," *Lab on a Chip*, vol. 3, pp. 77-81, 2003.
- [67] A. E. Kamholz, B. H. Weigl, B. A. Finlayson, and P. Yager, "Quantitative analysis of molecular interaction in a microfluidic channel: The T-sensor," *Analytical Chemistry*, vol. 71, pp. 5340-5347, Dec 1999.
- [68] R. F. Ismagilov, A. D. Stroock, P. J. A. Kenis, G. Whitesides, and H. A. Stone, "Experimental and theoretical scaling laws for transverse diffusive broadening in two-phase laminar flows in microchannels," *Applied Physics Letters*, vol. 76, pp. 2376-2378, Apr 2000.
- [69] N. T. Nguyen and Z. G. Wu, "Micromixers - a review," *Journal of Micromechanics and Microengineering*, vol. 15, pp. R1-R16, Feb 2005.
- [70] M. Q. Yi and H. H. Bau, "The kinematics of bend-induced mixing in micro-conduits," *International Journal of Heat and Fluid Flow*, vol. 24, pp. 645-656, Oct 2003.
- [71] S. H. Wong, M. C. L. Ward, and C. W. Wharton, "Micro T-mixer as a rapid mixing micromixer," *Sensors and Actuators B-Chemical*, vol. 100, pp. 359-379, May 2004.
- [72] M. Koch, H. Witt, A. G. R. Evans, and A. Brunnschweiler, "Improved characterization technique for micromixers," *Journal of Micromechanics and Microengineering*, vol. 9, pp. 156-158, Jun 1999.
- [73] V. Haverkamp, W. Ehrfeld, K. Gebauer, V. Hessel, H. Lowe, T. Richter, and C. Wille, "The potential of micromixers for contacting of disperse liquid phases," *Fresenius' Journal of Analytical Chemistry*, vol. 364, pp. 617-624, 1999.
- [74] Z. Wang, J. Taylor, A. B. Jemere, and D. J. Harrison, "Microfluidic devices for electrokinetic sample fractionation," *Electrophoresis*, vol. 31, pp. 2575-2583, Aug 2010.
- [75] A. Piruska, S. Branagan, D. M. Crokek, J. V. Sweedler, and P. W. Bohn, "Electrokinetically driven fluidic transport in integrated three-dimensional microfluidic devices incorporating gold-coated nanocapillary array membranes," *Lab on a Chip*, vol. 8, pp. 1625-1631, Oct 2008.
- [76] M. Long, M. A. Sprague, A. A. Grimes, B. D. Rich, and M. Khine, "A simple three-dimensional vortex micromixer," *Applied Physics Letters*, vol. 94, Mar 2009.
- [77] S. Y. Yang, J. L. Lin, and G. B. Lee, "A vortex-type micromixer utilizing pneumatically driven membranes," *Journal of Micromechanics and Microengineering*, vol. 19, Mar 2009.
- [78] J. B. Knight, A. Vishwanath, J. P. Brody, and R. H. Austin, "Hydrodynamic focusing on a silicon chip: Mixing nanoliters in microseconds," *Physical Review Letters*, vol. 80, pp. 3863-3866, Apr 1998.
- [79] K. Jensen, "Chemical kinetics - Smaller, faster chemistry," *Nature*, vol. 393, pp. 735-+, Jun 1998.
- [80] S. Hardt, K. S. Drese, V. Hessel, and F. Schonfeld, "Passive micromixers for applications in the microreactor and mu TAS fields," *Microfluidics and Nanofluidics*, vol. 1, pp. 108-118, May 2005.
- [81] J. Branebjerg, P. Gravesen, J. P. Krog, C. R. Nielsen, and Ieee, "Fast mixing by lamination," in *Ninth Annual International Workshop on Micro Electro Mechanical Systems, IEEE Proceedings - an Investigation of Micro Structures, Sensors, Actuators, Machines and Systems*, ed, 1996, pp. 441-446.

- [82] N. Schwesinger, T. Frank, and H. Wurmus, "A modulator microfluid system with an integrated micromixer," *Journal of Micromechanics and Microengineering*, vol. 6, pp. 99-102, Mar 1996.
- [83] J. Melin, G. Gimenez, N. Roxhed, W. van der Wijngaart, and G. Stemme, "A fast passive and planar liquid sample micromixer," *Lab on a Chip*, vol. 4, pp. 214-219, 2004.
- [84] R. Miyake, T. S. J. Lammerink, M. Elwenspoek, J. H. J. Fluitman, and Ieee, *MICRO MIXER WITH FAST DIFFUSION*, 1993.
- [85] J. Voldman, M. L. Gray, and M. A. Schmidt, "An integrated liquid mixer/valve," *Journal of Microelectromechanical Systems*, vol. 9, pp. 295-302, Sep 2000.
- [86] M. Q. Pan, Y. Tang, L. S. Lu, Z. P. Wan, X. K. Liu, and X. Q. Liu, "Design and numerical simulation of a three-dimensional nozzle microstructured mixer," in *Progress of Precision Engineering and Nano Technology*. vol. 339, S. Dong and Y. X. Yao, Eds., ed, 2007, pp. 343-347.
- [87] K. Hosokawa, T. Fujii, I. Endo, and I. Ieee, "Droplet-based nano/picoliter mixer using hydrophobic microcapillary vent," in *Mems '99: Twelfth Ieee International Conference on Micro Electro Mechanical Systems, Technical Digest*, ed, 1999, pp. 388-393.
- [88] K. Handique and M. A. Burns, "Mathematical modeling of drop mixing in a slit-type microchannel," *Journal of Micromechanics and Microengineering*, vol. 11, pp. 548-554, Sep 2001.
- [89] P. Paik, V. K. Pamula, and R. B. Fair, "Rapid droplet mixers for digital microfluidic systems," *Lab on a Chip*, vol. 3, pp. 253-259, 2003.
- [90] R. Sista, Z. S. Hua, P. Thwar, A. Sudarsan, V. Srinivasan, A. Eckhardt, M. Pollack, and V. Pamula, "Development of a digital microfluidic platform for point of care testing," *Lab on a Chip*, vol. 8, pp. 2091-2104, 2008.
- [91] H. Song, M. R. Bringer, J. D. Tice, C. J. Gerdt, and R. F. Ismagilov, "Experimental test of scaling of mixing by chaotic advection in droplets moving through microfluidic channels," *Applied Physics Letters*, vol. 83, pp. 4664-4666, Dec 2003.
- [92] Y. Lin, G. J. Gerfen, D. L. Rousseau, and S. R. Yeh, "Ultrafast microfluidic mixer and freeze-quenching device," *Analytical Chemistry*, vol. 75, pp. 5381-5386, Oct 2003.
- [93] H. Z. Wang, P. Iovenitti, E. Harvey, and S. Masood, "Optimizing layout of obstacles for enhanced mixing in microchannels," *Smart Materials & Structures*, vol. 11, pp. 662-667, Oct 2002.
- [94] V. Mengeaud, J. Josserand, and H. H. Girault, "Mixing processes in a zigzag microchannel: Finite element simulations and optical study," *Analytical Chemistry*, vol. 74, pp. 4279-4286, Aug 2002.
- [95] C. C. Hong, J. W. Choi, and C. H. Ahn, "A novel in-plane passive microfluidic mixer with modified Tesla structures," *Lab on a Chip*, vol. 4, pp. 109-113, 2004.
- [96] R. H. Liu, M. A. Stremler, K. V. Sharp, M. G. Olsen, J. G. Santiago, R. J. Adrian, H. Aref, and D. J. Beebe, "Passive mixing in a three-dimensional serpentine microchannel," *Journal of Microelectromechanical Systems*, vol. 9, pp. 190-197, Jun 2000.
- [97] S. J. Park, J. K. Kim, J. Park, S. Chung, C. Chung, and J. K. Chang, "Rapid three-dimensional passive rotation micromixer using the breakup process," *Journal of Micromechanics and Microengineering*, vol. 14, pp. 6-14, Jan 2004.
- [98] R. A. Vijayendran, K. M. Motsegood, D. J. Beebe, and D. E. Leckband, "Evaluation of a three-dimensional micromixer in a surface-based biosensor," *Langmuir*, vol. 19, pp. 1824-1828, Mar 2003.

- [99] A. D. Stroock, S. K. W. Dertinger, A. Ajdari, I. Mezic, H. A. Stone, and G. M. Whitesides, "Chaotic mixer for microchannels," *Science*, vol. 295, pp. 647-651, Jan 2002.
- [100] A. D. Stroock, S. K. Dertinger, G. M. Whitesides, and A. Ajdari, "Patterning flows using grooved surfaces," *Analytical Chemistry*, vol. 74, pp. 5306-5312, Oct 2002.
- [101] A. D. Stroock and G. M. Whitesides, "Controlling flows in microchannels with patterned surface charge and topography," *Accounts of Chemical Research*, vol. 36, pp. 597-604, Aug 2003.
- [102] H. Z. Wang, P. Iovenitti, E. Harvey, and S. Masood, "Numerical investigation of mixing in microchannels with patterned grooves," *Journal of Micromechanics and Microengineering*, vol. 13, pp. 801-808, Nov 2003.
- [103] J. Aubin, D. F. Fletcher, J. Bertrand, and C. Xuereb, "Characterization of the mixing quality in micromixers," *Chemical Engineering & Technology*, vol. 26, pp. 1262-1270, Dec 2003.
- [104] L. H. Lu, K. S. Ryu, and C. Liu, "A magnetic microstirrer and array for microfluidic mixing," *Journal of Microelectromechanical Systems*, vol. 11, pp. 462-469, Oct 2002.
- [105] K. S. Ryu, K. Shaikh, E. Goluch, Z. F. Fan, and C. Liu, "Micro magnetic stir-bar mixer integrated with parylene microfluidic channels," *Lab on a Chip*, vol. 4, pp. 608-613, 2004.
- [106] G. A. Mensing, T. M. Pearce, M. D. Graham, and D. J. Beebe, "An externally driven magnetic microstirrer," *Philosophical Transactions of the Royal Society a-Mathematical Physical and Engineering Sciences*, vol. 362, pp. 1059-1068, May 2004.
- [107] T. Fujii, Y. Sando, K. Higashino, and Y. Fujii, "A plug and play microfluidic device," *Lab on a Chip*, vol. 3, pp. 193-197, 2003.
- [108] I. Glasgow and N. Aubry, "Enhancement of microfluidic mixing using time pulsing," *Lab on a Chip*, vol. 3, pp. 114-120, 2003.
- [109] J. C. Rife, M. I. Bell, J. S. Horwitz, M. N. Kabler, R. C. Y. Auyeung, and W. J. Kim, "Miniature valveless ultrasonic pumps and mixers," *Sensors and Actuators a-Physical*, vol. 86, pp. 135-140, Oct 2000.
- [110] K. Yasuda, "Non-destructive, non-contact handling method for biomaterials in micro-chamber by ultrasound," *Sensors and Actuators B-Chemical*, vol. 64, pp. 128-135, Jun 2000.
- [111] G. G. Yaralioglu, I. O. Wygant, T. C. Marentis, and B. T. Khuri-Yakub, "Ultrasonic mixing in microfluidic channels using integrated transducers," *Analytical Chemistry*, vol. 76, pp. 3694-3698, Jul 2004.
- [112] R. H. Liu, R. Lenigk, R. L. Druyor-Sanchez, J. N. Yang, and P. Grodzinski, "Hybridization enhancement using cavitation microstreaming," *Analytical Chemistry*, vol. 75, pp. 1911-1917, Apr 2003.
- [113] A. O. El Moctar, N. Aubry, and J. Batton, "Electro-hydrodynamic micro-fluidic mixer," *Lab on a Chip*, vol. 3, pp. 273-280, 2003.
- [114] J. D. Zahn and V. Reddy, "Two phase micromixing and analysis using electrohydrodynamic instabilities," *Microfluidics and Nanofluidics*, vol. 2, pp. 399-415, Sep 2006.
- [115] F. Li, O. Ozen, N. Aubry, D. T. Papageorgiou, and P. G. Petropoulos, "Linear stability of a two-fluid interface for electrohydrodynamic mixing in a channel," *Journal of Fluid Mechanics*, vol. 583, pp. 347-377, Jul 2007.

- [116] H. H. Bau, J. H. Zhong, and M. Q. Yi, "A minute magneto hydro dynamic (MHD) mixer," *Sensors and Actuators B-Chemical*, vol. 79, pp. 207-215, Oct 2001.
- [117] C. H. Lin, L. M. Fu, and Y. S. Chien, "Microfluidic T-form mixer utilizing switching electroosmotic flow," *Analytical Chemistry*, vol. 76, pp. 5265-5272, Sep 2004.
- [118] Y. T. Zhang, H. Chen, I. Mezic, C. D. Meinhart, L. Petzold, and N. C. MacDonald, *SOI processing of a ring electrokinetic chaotic micromixer*, 2004.
- [119] N. Sasaki, T. Kitamori, and H. B. Kim, "AC electroosmotic micromixer for chemical processing in a microchannel," *Lab on a Chip*, vol. 6, pp. 550-554, 2006.
- [120] Z. L. Tang, S. B. Hong, D. Djukic, V. Modi, A. C. West, J. Yardley, and R. M. Osgood, "Electrokinetic flow control for composition modulation in a microchannel," *Journal of Micromechanics and Microengineering*, vol. 12, pp. 870-877, Nov 2002.
- [121] H. Suzuki, C. M. Ho, and I. Ieee, "A magnetic force driven chaotic micro-mixer," in *Fifteenth Ieee International Conference on Micro Electro Mechanical Systems, Technical Digest*, ed, 2002, pp. 40-43.
- [122] H. Suzuki, C. M. Ho, and N. Kasagi, "A chaotic mixer for magnetic bead-based micro cell sorter," *Journal of Microelectromechanical Systems*, vol. 13, pp. 779-790, Oct 2004.
- [123] W. H. Tan, Y. Suzuki, N. Kasagi, N. Shikazono, K. Furukawa, and T. Ushida, "A lamination micro mixer for mu-immunomagnetic cell sorter," *Jsme International Journal Series C-Mechanical Systems Machine Elements and Manufacturing*, vol. 48, pp. 425-435, Dec 2005.
- [124] Z. H. Wei, C. P. Lee, and M. F. Lai, "Magnetic Force Switches for Magnetic Fluid Micromixing," *Japanese Journal of Applied Physics*, vol. 49, 2010.
- [125] I. Safarik and M. Safarikova, "Use of magnetic techniques for the isolation of cells," *Journal of Chromatography B*, vol. 722, pp. 33-53, Feb 1999.
- [126] J. J. Chalmers, M. Zborowski, L. P. Sun, and L. Moore, "Flow through, immunomagnetic cell separation," *Biotechnology Progress*, vol. 14, pp. 141-148, Jan-Feb 1998.
- [127] J. J. Chalmers, M. Zborowski, L. Moore, S. Mandal, B. B. Fang, and L. P. Sun, "Theoretical analysis of cell separation based on cell surface marker density," *Biotechnology and Bioengineering*, vol. 59, pp. 10-20, Jul 1998.
- [128] P. Tartaj, M. D. Morales, S. Veintemillas-Verdaguer, T. Gonzalez-Carreno, and C. J. Serna, "The preparation of magnetic nanoparticles for applications in biomedicine," *Journal of Physics D-Applied Physics*, vol. 36, pp. R182-R197, Jul 2003.
- [129] A. S. Teja and P. Y. Koh, "Synthesis, properties, and applications of magnetic iron oxide nanoparticles," *Progress in Crystal Growth and Characterization of Materials*, vol. 55, pp. 22-45, 2009.
- [130] A. G. Roca, R. Costo, A. F. Rebolledo, S. Veintemillas-Verdaguer, P. Tartaj, T. Gonzalez-Carreno, M. P. Morales, and C. J. Serna, "Progress in the preparation of magnetic nanoparticles for applications in biomedicine," *Journal of Physics D-Applied Physics*, vol. 42, Nov 2009.
- [131] D. W. Inglis, R. Riehn, R. H. Austin, and J. C. Sturm, "Continuous microfluidic immunomagnetic cell separation," *Applied Physics Letters*, vol. 85, pp. 5093-5095, Nov 2004.
- [132] N. Pamme and C. Wilhelm, "Continuous sorting of magnetic cells via on-chip free-flow magnetophoresis," *Lab on a Chip*, vol. 6, pp. 974-980, 2006.
- [133] S. Miltenyi, W. Muller, W. Weichel, and A. Radbruch, " High gradient magnetic cell separation with MACS," *Cytometry*, vol. 11, pp. 231-238, 1990.

- [134] T. Deng, M. Prentiss, and G. M. Whitesides, "Fabrication of magnetic microfiltration systems using soft lithography," *Applied Physics Letters*, vol. 80, pp. 461-463, Jan 2002.
- [135] S. Ostergaard, G. Blankenstein, H. Dirac, and O. Leistiko, "A novel approach to the automation of clinical chemistry by controlled manipulation of magnetic particles," *Journal of Magnetism and Magnetic Materials*, vol. 194, pp. 156-162, Apr 1999.
- [136] J. W. Choi, C. H. Ahn, and H. T. Henderson, "Planar bio/magnetic bead separator with microfluidic channel," *Microfluidic Devices and Systems*, vol. 3515, A. B. Frazier and C. H. Ahn, Eds., ed, 1998, pp. 260-267.
- [137] K. S. Kim and J. K. Park, "Magnetic force-based multiplexed immunoassay using superparamagnetic nanoparticles in microfluidic channel," *Lab on a Chip*, vol. 5, pp. 657-664, 2005.
- [138] M. C. Kim, D. K. Kim, S. H. Lee, M. S. Amin, I. H. Park, C. J. Kim, and M. Zahn, "Dynamic characteristics of superparamagnetic iron oxide nanoparticles in a viscous fluid under an external magnetic field," *IEEE Transactions on Magnetics*, vol. 42(4), 2006, pp. 979-982.
- [139] K. S. Kim and J. K. Park, "Superparamagnetic nanoparticle-based nanobiomolecular detection in a microfluidic channel," *Current Applied Physics*, vol. 6(6), 2006, pp. 976-981.
- [140] C. S. Lee, H. Lee, and R. M. Westervelt, "Microelectromagnets for the control of magnetic nanoparticles," *Applied Physics Letters*, vol. 79, pp. 3308-3310, Nov 2001.
- [141] R. Wirix-Speetjens, W. Fyen, K. D. Xu, J. De Boeck, and G. Borghs, "A force study of on-chip magnetic particle transport based on tapered conductors," *IEEE Transactions on Magnetics*, vol. 41, pp. 4128-4133, Oct 2005.
- [142] B. B. Yellen, R. M. Erb, H. S. Son, R. Hewlin, H. Shang, and G. U. Lee, "Traveling wave magnetophoresis for high resolution chip based separations," *Lab on a Chip*, vol. 7, pp. 1681-1688, 2007.
- [143] K. H. Han and A. B. Frazier, "Continuous magnetophoretic separation of blood cells in microdevice format," *Journal of Applied Physics*, vol. 96, pp. 5797-5802, Nov 2004.
- [144] K. H. Han and A. B. Frazier, "Diamagnetic capture mode magnetophoretic microseparator for blood cells," *Journal of Microelectromechanical Systems*, vol. 14, pp. 1422-1431, Dec 2005.
- [145] K. H. Han and A. B. Frazier, "Paramagnetic capture mode magnetophoretic microseparator for high efficiency blood cell separations," *Lab on a Chip*, vol. 6, pp. 265-273, Feb 2006.
- [146] R. Rong, J. W. Choi, and C. H. Ahn, "An on-chip magnetic bead separator for biocell sorting," *Journal of Micromechanics and Microengineering*, vol. 16, pp. 2783-2790, Dec 2006.
- [147] K. Smistrup, T. Lund-Olesen, M. F. Hansen, and P. T. Tang, "Microfluidic magnetic separator using an array of soft magnetic elements," *Journal of Applied Physics*, vol. 99, Apr 2006.
- [148] C. X. Liu, L. Lagae, R. Wirix-Speetjens, and G. Borghs, "On-chip separation of magnetic particles with different magnetophoretic mobilities," *Journal of Applied Physics*, vol. 101, Jan 2007.
- [149] E. Druet, P. Mahieu, J. M. Foidart, and P. Druet, "Magnetic solid-phase enzyme immunoassay for the detection of anti-glomerular basement membrane antibodies," *Journal of Immunological Methods*, vol. 48, pp. 149-157, 1982.

- [150] A. Bhattacharyya and C. M. Klapperich, "Design and testing of a disposable microfluidic chemiluminescent immunoassay for disease biomarkers in human serum samples," *Biomedical Microdevices*, vol. 9, pp. 245-251, Apr 2007.
- [151] Y. Jiang, P. C. Wang, L. E. Locascio, and C. S. Lee, "Integrated plastic microfluidic devices with ESI-MS for drug screening and residue analysis," *Analytical Chemistry*, vol. 73, pp. 2048-2053, May 2001.
- [152] M. A. Holden and P. S. Cremer, "Microfluidic tools for studying the specific binding, adsorption, and displacement of proteins at interfaces," *Annual Review of Physical Chemistry*, vol. 56, pp. 369-387, 2005.
- [153] J. Wang, D. K. Xu, and R. Polsky, "Magnetically-induced solid-state electrochemical detection of DNA hybridization," *Journal of the American Chemical Society*, vol. 124, pp. 4208-4209, Apr 2002.
- [154] M. Wolf, B. Michel, P. Hunziker, and E. Delamarche, "Simultaneous detection of C-reactive protein and other cardiac markers in human plasma using micromosaic immunoassays and self-regulating microfluidic networks," *Biosensors & Bioelectronics*, vol. 19, pp. 1193-1202, May 2004.
- [155] D. Altschuh, S. Oncul, and A. P. Demchenko, "Fluorescence sensing of intermolecular interactions and development of direct molecular biosensors," *Journal of Molecular Recognition*, vol. 19, pp. 459-477, Nov-Dec 2006.
- [156] J. L. Wang and H. S. Zhou, "Aptamer-based Au nanoparticles-enhanced surface plasmon resonance detection of small molecules," *Analytical Chemistry*, vol. 80, pp. 7174-7178, Sep 2008.
- [157] J. L. Wang, A. Munir, and H. S. Zhou, "Au NPs-aptamer conjugates as a powerful competitive reagent for ultrasensitive detection of small molecules by surface plasmon resonance spectroscopy," *Talanta*, vol. 79, pp. 72-76, Jun 2009.
- [158] E. Palecek and M. Fojta, "Magnetic beads as versatile tools for electrochemical DNA and protein biosensing," *Talanta*, vol. 74, pp. 276-290, Dec 2007.
- [159] O. A. Sadik, S. K. Mwilu, and A. Aluoch, "Smart electrochemical biosensors: From advanced materials to ultrasensitive devices," *Electrochimica Acta*, vol. 55, pp. 4287-4295, May 2010.
- [160] J. S. Ko, H. C. Yoon, H. S. Yang, H. B. Pyo, K. H. Chung, S. J. Kim, and Y. T. Kim, "A polymer-based microfluidic device for immunosensing biochips," *Lab on a Chip*, vol. 3, pp. 106-113, 2003.
- [161] C. Situma, M. Hashimoto, and S. A. Soper, "Merging microfluidics with microarray-based bioassays," *Biomolecular Engineering*, vol. 23, pp. 213-231, Oct 2006.
- [162] M. Varshney, Y. B. Li, B. Srinivasan, and S. Tung, "A label-free, microfluidics and interdigitated array microelectrode-based impedance biosensor in combination with nanoparticles immunoseparation for detection of Escherichia coli O157 : H7 in food samples," *Sensors and Actuators B-Chemical*, vol. 128, pp. 99-107, Dec 2007.
- [163] H. Z. Huang, P. X. Ran, and Z. G. Liu, "Impedance sensing of allergen-antibody interaction on glassy carbon electrode modified by gold electrodeposition," *Bioelectrochemistry*, vol. 70, pp. 257-262, May 2007.
- [164] Y. T. Lim, M. Y. Cho, B. S. Choi, J. M. Lee, and B. H. Chung, "Paramagnetic gold nanostructures for dual modal bioimaging and phototherapy of cancer cells," *Chemical Communications*, pp. 4930-4932, 2008.

- [165] J. P. Brody and P. Yager, "Diffusion-based extraction in a microfabricated device," *Sensors and Actuators a-Physical*, vol. 58, pp. 13-18, Jan 1997.
- [166] B. H. Weigl and P. Yager, "Microfluidics - Microfluidic diffusion-based separation and detection," *Science*, vol. 283, pp. 346-347, Jan 1999.
- [167] A. Hatch, A. E. Kamholz, K. R. Hawkins, M. S. Munson, E. A. Schilling, B. H. Weigl, and P. Yager, "A rapid diffusion immunoassay in a T-sensor," *Nature Biotechnology*, vol. 19, pp. 461-465, May 2001.
- [168] M. U. Kopp, A. J. de Mello, and A. Manz, "Chemical amplification: Continuous-flow PCR on a chip," *Science*, vol. 280, pp. 1046-1048, May 1998.
- [169] A. T. Woolley, D. Hadley, P. Landre, A. J. deMello, R. A. Mathies, and M. A. Northrup, "Functional integration of PCR amplification and capillary electrophoresis in a microfabricated DNA analysis device," *Analytical Chemistry*, vol. 68, pp. 4081-4086, Dec 1996.
- [170] K. Sato, M. Tokeshi, T. Odake, H. Kimura, T. Ooi, M. Nakao, and T. Kitamori, "Integration of an immunosorbent assay system: Analysis of secretory human immunoglobulin A on polystyrene beads in a microchip," *Analytical Chemistry*, vol. 72, pp. 1144-1147, Mar 2000.
- [171] C. T. Lim and Y. Zhang, "Bead-based microfluidic immunoassays: The next generation," *Biosensors & Bioelectronics*, vol. 22, pp. 1197-1204, Feb 2007.
- [172] M. A. Hayes, N. A. Polson, A. N. Phayre, and A. A. Garcia, "Flow-based microimmunoassay," *Analytical Chemistry*, vol. 73, pp. 5896-5902, Dec 2001.
- [173] F. Lacharme, C. Vandevyver, and M. A. M. Gijs, "Magnetic beads retention device for sandwich immunoassay: comparison of off-chip and on-chip antibody incubation," *Microfluidics and Nanofluidics*, vol. 7, pp. 479-487, Oct 2009.
- [174] S. A. Peyman, A. Iles, and N. Pamme, "Mobile magnetic particles as solid-supports for rapid surface-based bioanalysis in continuous flow," *Lab on a Chip*, vol. 9, pp. 3110-3117, 2009.
- [175] M. Herrmann, E. Roy, T. Veres, and M. Tabrizian, "Microfluidic ELISA on non-passivated PDMS chip using magnetic bead transfer inside dual networks of channels," *Lab on a Chip*, vol. 7, pp. 1546-1552, 2007.
- [176] J. Do and C. H. Ahn, "A polymer lab-on-a-chip for magnetic immunoassay with on-chip sampling and detection capabilities," *Lab on a Chip*, vol. 8, pp. 542-549, 2008.
- [177] W. C. Lee, K. Y. Lien, G. B. Lee, and H. Y. Lei, "An integrated microfluidic system using magnetic beads for virus detection," *Diagnostic Microbiology and Infectious Disease*, vol. 60, pp. 51-58, Jan 2008.
- [178] U. Lehmann, S. Hadjidj, V. K. Parashar, C. Vandevyver, A. Rida, and M. A. M. Gijs, "Two-dimensional magnetic manipulation of microdroplets on a chip as a platform for bioanalytical applications," *Sensors and Actuators B-Chemical*, vol. 117, pp. 457-463, Oct 2006.
- [179] C. S. a. C. SH, *Physics of Magnetism*. New York: Wiley, 1964.
- [180] R. RE, *Ferrohydrodynamics*. New York: Dover Publication Inc., 1997.
- [181] T. Jonsson, P. Nordblad, and P. Svedlindh, "Dynamic study of dipole-dipole interaction effects in a magnetic nanoparticle system," *Physical Review B*, vol. 57, pp. 497-504, Jan 1998.

- [182] A. H. Lu, E. L. Salabas, and F. Schuth, "Magnetic nanoparticles: Synthesis, protection, functionalization, and application," *Angewandte Chemie-International Edition*, vol. 46, pp. 1222-1244, 2007.
- [183] A. H. Latham and M. E. Williams, "Versatile routes toward functional, water-soluble nanoparticles via trifluoroethylester-PEG-thiol ligands," *Langmuir*, vol. 22, pp. 4319-4326, Apr 2006.
- [184] K. E. McCloskey, J. J. Chalmers, and M. Zborowski, "Magnetophoretic mobilities correlate to antibody binding capacities," *Cytometry*, vol. 40, 2000, pp. 307-315.
- [185] P. V. Danckwerts, "Continuous flow systems. Distribution of residence times (Reprinted from Chem Engng Sci, vol 2, pg 1-13, 1953)," *Chemical Engineering Science*, vol. 50, pp. 3857-3866, Dec 1995.
- [186] F. HS, *Elements of Chemical Reaction Engineering*, 4th ed.: Prentice Hall, 2005.
- [187] T. Vo-Dinh and B. Cullum, "Biosensors and biochips: advances in biological and medical diagnostics," *Fresenius Journal of Analytical Chemistry*, vol. 366, pp. 540-551, Mar-Apr 2000.
- [188] T. A. Franke and A. Wixforth, "Microfluidics for Miniaturized Laboratories on a Chip," *Chemphyschem*, vol. 9, pp. 2140-2156, Oct 2008.
- [189] V. Hessel, H. Lowe, and F. Schonfeld, "Micromixers - a review on passive and active mixing principles," *Chemical Engineering Science*, vol. 60, pp. 2479-2501, Apr-May 2005.
- [190] S. H. Lee, H. J. Kang, and B. Choi, "A study on the novel micromixer with chaotic flows," *Microsystem Technologies-Micro-and Nanosystems-Information Storage and Processing Systems*, vol. 15, pp. 269-277, Feb 2009.
- [191] F. Schonfeld, V. Hessel, and C. Hofmann, "An optimised split-and-recombine micromixer with uniform 'chaotic' mixing," *Lab on a Chip*, vol. 4, pp. 65-69, 2004.
- [192] L. L. Wang and J. T. Yang, "An overlapping crisscross micromixer using chaotic mixing principles," *Journal of Micromechanics and Microengineering*, vol. 16, pp. 2684-2691, Dec 2006.
- [193] Y. C. Lin, Y. C. Chung, and C. Y. Wu, "Mixing enhancement of the passive microfluidic mixer with J-shaped baffles in the tee channel," *Biomedical Microdevices*, vol. 9, pp. 215-221, Apr 2007.
- [194] V. Srinivasan, V. K. Pamula, and R. B. Fair, "Droplet-based microfluidic lab-on-a-chip for glucose detection," *Analytica Chimica Acta*, vol. 507, pp. 145-150, Apr 2004.
- [195] X. L. Mao, B. K. Juluri, M. I. Lapsley, Z. S. Stratton, and T. J. Huang, "Milliseconds microfluidic chaotic bubble mixer," *Microfluidics and Nanofluidics*, vol. 8, pp. 139-144, Jan 2010.
- [196] J. G. Santiago, "Electroosmotic flows in microchannels with finite inertial and pressure forces," *Analytical Chemistry*, vol. 73, pp. 2353-2365, May 2001.
- [197] E. Biddiss, D. Erickson, and D. Q. Li, "Heterogeneous surface charge enhanced micromixing for electrokinetic flows," *Analytical Chemistry*, vol. 76, pp. 3208-3213, Jun 2004.
- [198] X. C. Xuan and D. Q. Li, "Electroosmotic flow in microchannels with arbitrary geometry and arbitrary distribution of wall charge," *Journal of Colloid and Interface Science*, vol. 289, pp. 291-303, Sep 2005.
- [199] C. C. Chang and R. J. Yang, "Electrokinetic mixing in microfluidic systems," *Microfluidics and Nanofluidics*, vol. 3, pp. 501-525, Oct 2007.

- [200] R. H. Liu, J. N. Yang, M. Z. Pindera, M. Athavale, and P. Grodzinski, "Bubble-induced acoustic micromixing," *Lab on a Chip*, vol. 2, pp. 151-157, 2002.
- [201] J. H. Tsai and L. W. Lin, "Active microfluidic mixer and gas bubble filter driven by thermal bubble micropump," *Sensors and Actuators a-Physical*, vol. 97-8, pp. 665-671, Apr 2002.
- [202] M. A. McClain, C. T. Culbertson, S. C. Jacobson, and J. M. Ramsey, "Flow cytometry of Escherichia coli on microfluidic devices," *Analytical Chemistry*, vol. 73, pp. 5334-5338, Nov 2001.
- [203] M. Zolgharni, S. M. Azimi, M. R. Bahmanyar, and W. Balachandran, "A numerical design study of chaotic mixing of magnetic particles in a microfluidic bio-separator," *Microfluidics and Nanofluidics*, vol. 3, pp. 677-687, Dec 2007.
- [204] J. T. Adeosun and A. Lawal, "Mass transfer enhancement in microchannel reactors by reorientation of fluid interfaces and stretching," *Sensors and Actuators B-Chemical*, vol. 110, pp. 101-111, Sep 2005.
- [205] J. T. Adeosun and A. Lawal, "Numerical and experimental mixing studies in a MEMS-based multilaminated/elongational flow micromixer," *Sensors and Actuators B-Chemical*, vol. 139, pp. 637-647, Jun 2009.
- [206] J. T. Adeosun and A. Lawal, "Numerical and experimental studies of mixing characteristics in a T-junction microchannel using residence-time distribution," *Chemical Engineering Science*, vol. 64, pp. 2422-2432, May 2009.
- [207] C. C. Berry and A. S. G. Curtis, "Functionalisation of magnetic nanoparticles for applications in biomedicine," *Journal of Physics D-Applied Physics*, vol. 36, pp. R198-R206, Jul 2003.
- [208] F. EP, *Permanent Magnet and Electromechanical Devices : Materials, Analysis and Applications*. New York: Academic Press Inc., 2001.
- [209] E. P. Furlani, "Analysis of particle transport in a magnetophoretic microsystem," *Journal of Applied Physics*, vol. 99, Jan 2006.
- [210] E. P. Furlani and K. C. Ng, "Analytical model of magnetic nanoparticle transport and capture in the microvasculature," *Physical Review E*, vol. 73, Jun 2006.
- [211] E. P. Furlani, Y. Sahoo, K. C. Ng, J. C. Wortman, and T. E. Monk, "A model for predicting magnetic particle capture in a microfluidic bioseparator," *Biomedical Microdevices*, vol. 9, pp. 451-463, Aug 2007.
- [212] J. R. Brauer, D. L. Cook, and T. E. Bray, "Finite-element computation of magnetic force densities on permeable particles in magnetic separators," *IEEE Transactions on Magnetics*, vol. 43, pp. 3483-3487, Aug 2007.
- [213] L. Clime, B. Le Drogoff, and T. Veres, "Dynamics of superparamagnetic and ferromagnetic nano-objects in continuous-flow microfluidic devices," 2007, pp. 2929-2931.
- [214] S. P. Sullivan, B. S. Akpa, S. M. Matthews, A. C. Fisher, L. F. Gladden, and M. L. Johns, "Simulation of miscible diffusive mixing in microchannels," *Sensors and Actuators B-Chemical*, vol. 123, pp. 1142-1152, May 2007.
- [215] C. M. Oldenburg, S. E. Borglin, and G. J. Moridis, "Numerical simulation of ferrofluid flow for subsurface environmental engineering applications," *Transport in Porous Media*, vol. 38, pp. 319-344, Mar 2000.
- [216] C. J. a. R. JF, *Chemical Engineering Vol. 2: Particle Technology and Separation Processes*, 5th ed.: Butterworth-Heinemann, 2002.

- [217] J. C. McDonald, D. C. Duffy, J. R. Anderson, D. T. Chiu, H. K. Wu, O. J. A. Schueller, and G. M. Whitesides, "Fabrication of microfluidic systems in poly(dimethylsiloxane)," *Electrophoresis*, vol. 21, pp. 27-40, Jan 2000.
- [218] B. Goldstein, D. Coombs, X. Y. He, A. R. Pineda, and C. Wofsy, "The influence of transport on the kinetics of binding to surface receptors: application to cells and BIAcore," *Journal of Molecular Recognition*, vol. 12, pp. 293-299, Sep-Oct 1999.
- [219] M. Abrantes, M. T. Magone, L. F. Boyd, and P. Schuck, "Adaptation of a surface plasmon resonance biosensor with microfluidics for use with small sample volumes and long contact times," *Analytical Chemistry*, vol. 73, pp. 2828-2835, Jul 2001.
- [220] H. P. Jennissen and T. Zumbink, "A novel nanolayer biosensor principle," *Biosensors & Bioelectronics*, vol. 19, pp. 987-997, Apr 2004.
- [221] V. Haverkamp, W. Ehrfeld, K. Gebauer, V. Hessel, H. Lowe, T. Richter, and C. Wille, "The potential of micromixers for contacting of disperse liquid phases," *Fresenius Journal of Analytical Chemistry*, vol. 364, pp. 617-624, Aug 1999.
- [222] G. X. Li, V. Joshi, R. L. White, S. X. Wang, J. T. Kemp, C. Webb, R. W. Davis, and S. H. Sun, "Detection of single micron-sized magnetic bead and magnetic nanoparticles using spin valve sensors for biological applications," *Journal of Applied Physics*, vol. 93, pp. 7557-7559, May 2003.
- [223] D. G. Myszka, X. He, M. Dembo, T. A. Morton, and B. Goldstein, "Extending the range of rate constants available from BIACORE: Interpreting mass transport-influenced binding data," *Biophysical Journal*, vol. 75, pp. 583-594, Aug 1998.
- [224] M. C. Kim, D. K. Kim, S. H. Lee, M. S. Amin, I. H. Park, C. J. Kim, and M. Zahn, "Dynamic characteristics of superparamagnetic iron oxide nanoparticles in a viscous fluid under an external magnetic field," *IEEE Transactions on Magnetics*, vol. 42, pp. 979-982, Apr 2006.
- [225] M. Zimmermann, E. Delamarche, M. Wolf, and P. Hunziker, "Modeling and optimization of high-sensitivity, low-volume microfluidic-based surface immunoassays," *Biomedical Microdevices*, vol. 7, pp. 99-110, Jun 2005.
- [226] D. Friedrich, C. Please, and T. Melvin, "Optimisation of analyte transport in integrated microfluidic affinity sensors for the quantification of low levels of analyte," *Sensors and Actuators B-Chemical*, vol. 131, pp. 323-332, Apr 2008.
- [227] J. A. Benn, J. Hu, B. J. Hogan, R. C. Fry, L. D. Samson, and T. Thorsen, "Comparative modeling and analysis of microfluidic and conventional DNA microarrays," *Analytical Biochemistry*, vol. 348, pp. 284-293, Jan 2006.
- [228] C. JW, "Fabrication of Micromachined Magnetic Particle Separators for Bioseparation in Microfluidic Systems," in *Methods in Molecular Biology*. vol. 321, H. P. Inc., Ed., II ed Totowa, NJ, 2006, pp. 65-81.
- [229] W. Zhang, H. A. Stone, and J. D. Sherwood, "Mass transfer at a microelectrode in channel flow," *Journal of Physical Chemistry*, vol. 100, pp. 9462-9464, May 1996.
- [230] P. E. Sheehan and L. J. Whitman, "Detection limits for nanoscale biosensors," *Nano Letters*, vol. 5, pp. 803-807, Apr 2005.
- [231] D. R. Kim and X. L. Zheng, "Numerical Characterization and Optimization of the Microfluidics for Nanowire Biosensors," *Nano Letters*, vol. 8, pp. 3233-3237, Oct 2008.
- [232] G. Q. Hu, Y. L. Gao, and D. Q. Li, "Modeling micropatterned antigen-antibody binding kinetics in a microfluidic chip," *Biosensors & Bioelectronics*, vol. 22, pp. 1403-1409, Feb 2007.

- [233] O. D. Hendrickson, A. V. Zherdev, A. P. Kaplun, and B. B. Dzantiev, "Comparative analysis of models describing interactions between antibodies and liposomal antigens," *Applied Biochemistry and Microbiology*, vol. 39, pp. 75-81, Jan-Feb 2003.
- [234] K. A. Heyries, M. G. Loughran, D. Hoffmann, A. Homsy, L. J. Blum, and C. A. Marquette, "Microfluidic biochip for chemiluminescent detection of allergen-specific antibodies," *Biosensors & Bioelectronics*, vol. 23, pp. 1812-1818, Jul 2008.
- [235] S. S. Kuntaegowdanahalli, A. A. S. Bhagat, G. Kumar, and I. Papautsky, "Inertial microfluidics for continuous particle separation in spiral microchannels," *Lab on a Chip*, vol. 9, pp. 2973-2980, 2009.
- [236] J. Nam, H. Lim, D. Kim, and S. Shin, "Separation of platelets from whole blood using standing surface acoustic waves in a microchannel," *Lab on a Chip*, vol. 11, pp. 3361-3364, 2011.
- [237] R. Ehrnstrom, "Miniaturization and integration: challenges and breakthroughs in microfluidics," *Lab on a Chip*, vol. 2, pp. 26N-30N, 2002.
- [238] X. Chen, D. F. Cui, C. C. Liu, H. Li, and J. Chen, "Continuous flow microfluidic device for cell separation, cell lysis and DNA purification," *Analytica Chimica Acta*, vol. 584, pp. 237-243, Feb 2007.
- [239] Y. S. Huh, T. J. Park, E. Z. Lee, W. H. Hong, and S. Y. Lee, "Development of a fully integrated microfluidic system for sensing infectious viral disease," *Electrophoresis*, vol. 29, pp. 2960-2969, Jul 2008.
- [240] J. L. Wang, A. Munir, Z. Z. Zhu, and H. S. Zhou, "Magnetic Nanoparticle Enhanced Surface Plasmon Resonance Sensing and Its Application for the Ultrasensitive Detection of Magnetic Nanoparticle-Enriched Small Molecules," *Analytical Chemistry*, vol. 82, pp. 6782-6789, Aug 2010.
- [241] D. Dell'Orco, M. Lundqvist, C. Oslakovic, T. Cedervall, and S. Linse, "Modeling the Time Evolution of the Nanoparticle-Protein Corona in a Body Fluid," *Plos One*, vol. 5, Jun 2010.
- [242] T. Cedervall, I. Lynch, S. Lindman, T. Berggard, E. Thulin, H. Nilsson, K. A. Dawson, and S. Linse, "Understanding the nanoparticle-protein corona using methods to quantify exchange rates and affinities of proteins for nanoparticles," *Proceedings of the National Academy of Sciences of the United States of America*, vol. 104, pp. 2050-2055, Feb 2007.
- [243] V. I. Furdyi and D. J. Harrison, "Immunomagnetic T cell capture from blood for PCR analysis using microfluidic systems," *Lab on a Chip*, vol. 4, pp. 614-618, 2004.
- [244] T. Zheng, H. M. Yu, C. M. Alexander, D. J. Beebe, and L. M. Smith, "Lectin-modified microchannels for mammalian cell capture and purification," *Biomedical Microdevices*, vol. 9, pp. 611-617, Aug 2007.
- [245] F. K. Liu, Y. Y. Lin, and C. H. Wu, "Highly efficient approach for characterizing nanometer-sized gold particles by capillary electrophoresis," *Analytica Chimica Acta*, vol. 528, pp. 249-254, Jan 2005.
- [246] X. Y. Xu, K. K. Caswell, E. Tucker, S. Kabisatpathy, K. L. Brodhacker, and W. A. Scrivens, "Size and shape separation of gold nanoparticles with preparative gel electrophoresis," *Journal of Chromatography A*, vol. 1167, pp. 35-41, Oct 2007.
- [247] M. Durr, J. Kentsch, T. Muller, T. Schnelle, and M. Stelzle, "Microdevices for manipulation and accumulation of micro- and nanoparticles by dielectrophoresis," *Electrophoresis*, vol. 24, pp. 722-731, Feb 2003.

- [248] M. Yamada, K. Kano, Y. Tsuda, J. Kobayashi, M. Yamato, M. Seki, and T. Okano, "Microfluidic devices for size-dependent separation of liver cells," *Biomedical Microdevices*, vol. 9, pp. 637-645, Oct 2007.
- [249] A. Jain and J. D. Posner, "Particle dispersion and separation resolution of pinched flow fractionation," *Analytical Chemistry*, vol. 80, pp. 1641-1648, Mar 2008.
- [250] M. Yamada, M. Nakashima, and M. Seki, "Pinched flow fractionation: Continuous size separation of particles utilizing a laminar flow profile in a pinched microchannel," *Analytical Chemistry*, vol. 76, pp. 5465-5471, Sep 2004.
- [251] D. Di Carlo, D. Irimia, R. G. Tompkins, and M. Toner, "Continuous inertial focusing, ordering, and separation of particles in microchannels," *Proceedings of the National Academy of Sciences of the United States of America*, vol. 104, pp. 18892-18897, Nov 2007.
- [252] A. Munir, J. Wang, and H. S. Zhou, "Dynamics of capturing process of multiple magnetic nanoparticles in a flow through microfluidic bioseparation system," *Iet Nanobiotechnology*, vol. 3, pp. 55-64, Sep 2009.
- [253] J. D. Adams, U. Kim, and H. T. Soh, "Multitarget magnetic activated cell sorter," *Proceedings of the National Academy of Sciences of the United States of America*, vol. 105, pp. 18165-18170, Nov 2008.
- [254] S. Bucak, D. A. Jones, P. E. Laibinis, and T. A. Hatton, "Protein separations using colloidal magnetic nanoparticles," *Biotechnology Progress*, vol. 19, pp. 477-484, Mar-Apr 2003.
- [255] C. M. Earhart, R. J. Wilson, R. L. White, N. Pourmand, and S. X. Wang, "Microfabricated magnetic sifter for high-throughput and high-gradient magnetic separation," *Journal of Magnetism and Magnetic Materials*, vol. 321, pp. 1436-1439, May 2009.
- [256] A. J. Kell, K. Somaskandan, G. Stewart, M. G. Bergeron, and B. Simard, "Superparamagnetic nanoparticle-polystyrene bead conjugates as pathogen capture mimics: A parametric study of factors affecting capture efficiency and specificity," *Langmuir*, vol. 24, pp. 3493-3502, Apr 2008.
- [257] C. M. Earhart, E. M. Nguyen, R. J. Wilson, Y. A. Wang, and S. X. Wang, "Designs for a Microfabricated Magnetic Sifter," *IEEE Transactions on Magnetics*, vol. 45, pp. 4884-4887, Oct 2009.
- [258] J. Wunderlich, "Cell-Separation - Methods and Selected Application, vol. 2 - Pretlow, TG, Pretlow, TP," *Analytical Biochemistry*, vol. 140, pp. 304-304, 1984.
- [259] M. Berger, J. Castelino, R. Huang, M. Shah, and R. H. Austin, "Design of a microfabricated magnetic cell separator," *Electrophoresis*, vol. 22, pp. 3883-3892, Oct 2001.
- [260] B. Le Drogoff, L. Clime, and T. Veres, "The influence of magnetic carrier size on the performance of microfluidic integrated micro-electromagnetic traps," *Microfluidics and Nanofluidics*, vol. 5, pp. 373-381, Sep 2008.
- [261] Y. J. Liu, S. S. Guo, Z. L. Zhang, W. H. Huang, D. M. Baigl, Y. Chen, and D. W. Pang, "Integration of minisolenoids in microfluidic device for magnetic bead-based immunoassays," *Journal of Applied Physics*, vol. 102, Oct 2007.
- [262] M. A. Espy, H. Sandin, C. Carr, C. J. Hanson, M. D. Ward, and R. H. Kraus, "An instrument for sorting of magnetic microparticles in a magnetic field gradient," *Cytometry Part A*, vol. 69A, pp. 1132-1142, Nov 2006.

- [263] R. F. Ismagilov, D. Rosmarin, P. J. A. Kenis, D. T. Chiu, W. Zhang, H. A. Stone, and G. M. Whitesides, "Pressure-driven laminar flow in tangential microchannels: an elastomeric microfluidic switch," *Analytical Chemistry*, vol. 73, pp. 4682-4687, Oct 2001.
- [264] A. Munir, J. L. Wang, Z. H. Li, and H. S. Zhou, "Numerical analysis of a magnetic nanoparticle-enhanced microfluidic surface-based bioassay," *Microfluidics and Nanofluidics*, vol. 8, pp. 641-652, May 2010.
- [265] B. He, B. J. Burke, X. Zhang, R. Zhang, and F. E. Regnier, "A picoliter-volume mixer for microfluidic analytical systems," *Analytical Chemistry*, vol. 73, pp. 1942-1947, May 2001.
- [266] T. N. T. Nguyen, M. C. Kim, J. S. Park, and N. E. Lee, "An effective passive microfluidic mixer utilizing chaotic advection," *Sensors and Actuators B-Chemical*, vol. 132, pp. 172-181, May 2008.
- [267] Z. Yang, S. Matsumoto, H. Goto, M. Matsumoto, and R. Maeda, "Ultrasonic micromixer for microfluidic systems," *Sensors and Actuators a-Physical*, vol. 93, pp. 266-272, Oct 2001.
- [268] W. Ehrfeld, K. Golbig, V. Hessel, H. Lowe, and T. Richter, "Characterization of mixing in micromixers by a test reaction: Single mixing units and mixer arrays," *Industrial & Engineering Chemistry Research*, vol. 38, pp. 1075-1082, Mar 1999.
- [269] S. Panic, S. Loebbecke, T. Tuercke, J. Antes, and D. Boskovic, "Experimental approaches to a better understanding of mixing performance of microfluidic devices," *Chemical Engineering Journal*, vol. 101, pp. 409-419, Aug 2004.
- [270] M. Engler, N. Kockmann, T. Kiefer, and P. Woias, "Numerical and experimental investigations on liquid mixing in static micromixers," *Chemical Engineering Journal*, vol. 101, pp. 315-322, Aug 2004.
- [271] F. Trachsel, A. Gunther, S. Khan, and K. F. Jensen, "Measurement of residence time distribution in microfluidic systems," *Chemical Engineering Science*, vol. 60, pp. 5729-5737, Nov 2005.
- [272] D. Boskovic and S. Loebbecke, "Modelling of the residence time distribution in micromixers," *Chemical Engineering Journal*, vol. 135, pp. S138-S146, Jan 2008.